Title

The Strength-Toughness Combination of the Aluminum-Lithium Alloys 2090 and 2091 at Cryogenic Temperatures

Author

Glazer, J.

Publication Date

1989-07-01

LBL-27607

Center for Advanced Materials

CAM

The Strength-Toughness Combination of the Aluminum-Lithium Alloys 2090 and 2091 at Cryogenic Temperatures

J. Glazer
(Ph.D. Thesis)

July 1989

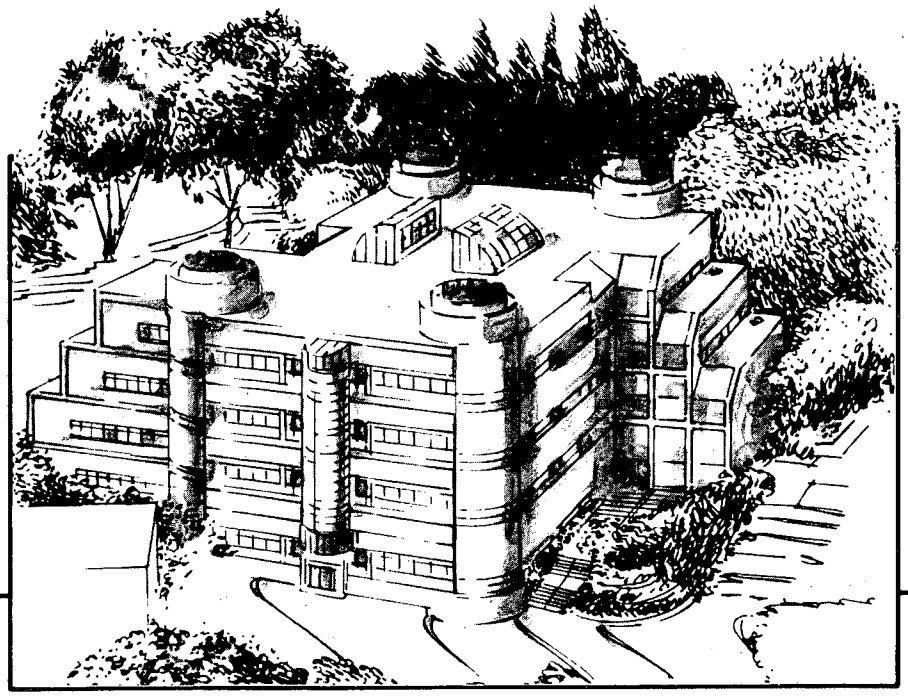

Materials and Chemical Sciences Division

Lawrence Berkeley Laboratory • University of California

ONE CYCLOTRON ROAD, BERKELEY, CA 94720 • (415) 486-4755

Prepared for the U.S. Department of Energy under Contract DE-AC03-76SF00098

DISCLAIMER

LBL-27607

The Strength-Toughness Combination of the Aluminum-Lithium Alloys 2090 and 2091 at Cryogenic Temperatures

Judith Glazer

PhD Dissertation

Department of Materials Science and Mineral Engineering,
University of California

and

Center for Advanced Materials
Materials and Chemical Sciences Division
Lawrence Berkeley Laboratory
1 Cyclotron Road
Berkeley, California 94720

July 1989

Portions of this study were funded by the Aluminum Company of America, Lockheed Missiles and Space Company and the Director, Office of Energy Research, Office of Basic Energy Science, Material Sciences Division of the U.S. Department of Energy under Contract No. DE-AC03-76SF00098. J. Glazer was supported by an AT&T Bell Laboratories PhD Scholarship.

THE STRENGTH-TOUGHNESS COMBINATION OF THE ALUMINUM-LITHIUM ALLOYS 2090 AND 2091 AT CRYOGENIC TEMPERATURES

Judith Glazer

PhD Thesis

ABSTRACT

The strength-toughness combination of the aluminum-lithium alloys 2090 (nominal composition Al-2.7 Cu-2.2 Li-0.1 Zr in wt. %) and 2091 (Al-2.2 Cu-2.0 Li- 1.5 Mg- 0.1 Zr) plate at cryogenic temperatures was investigated. Aluminum-lithium alloys have lower density and higher stiffness than conventional aluminum alloys and were developed for aircraft applications. This study was motivated by the possibility of using aluminum-lithium alloys for cryogenic tankage of spacecraft, an application in which light weight, weldability and good cryogenic mechanical properties are at a premium.

Alloy 2090-T81 has a strength-toughness combination that improves with decreasing temperature between 300 and 4 K under some conditions. This improvement is accompanied by an increase in the tensile elongation and strain hardening rate, but the large increase in fracture toughness is not reflected in the primary fracture mode. The goal of this study was to develop an understanding of the mechanisms responsible for the increase in fracture toughness at cryogenic temperatures. The mechanical properties of alloy 2090 in other metallurgical conditions and a second alloy, 2091, were also considered.

Several mechanisms for interpreting the increased toughness in in-plane orientations at low temperatures were considered. When there is a change in the primary fracture mode with test temperature, this change dominates the fracture toughness behavior. When the fracture mode is unchanged at low temperature, the results of this study lead to the conclusion that the toughness increases because of the increase in strength, stiffness and strain hardening rate. Crack-dividing splitting, which occurs in these alloys, may play a role in determining the level of toughness and in preserving the fracture mode through a large temperature range, but does not appear to be responsible for the improvement in fracture toughness. These conclusions suggest that understanding the deformation and strain hardening behavior of these alloys at low temperature will be important to improving their fracture behavior. Some initial results toward this end are also presented.

Table of Contents

1. INTRODUCTION

1.1. Motivations for study of aluminum-lithium alloys

As a class, aluminum-lithium alloys are of considerable interest because they offer the potential of mechanical properties comparable to standard high-strength aerospace aluminum alloys coupled with 7-10% lower density and 10-12% higher elastic modulus. The goal of aluminum-lithium alloy development is to produce alloys that allow these property advantages due to the presence of lithium to be realized in the form of decreased aircraft structural weight. In the last few years, four commercial alloys with varying combinations of mechanical properties, corrosion resistance and density have been registered: 2090, 2091, 8090 and 8091. These alloys are intended to replace conventional high strength aircraft alloys such as 2024 and 7075. A fifth alloy, Weldalite™, that is intended to replace 2219 for cryogenic applications, has also been announced recently. The nominal compositions and densities of these alloys are given in Table 1.1. Common temper designations are given in Appendix 1. The specific thermal and mechanical processing of the alloys investigated in this work is given in Section 2. Much of the work on the development of aluminum-lithium alloys over the last ten years is summarized in the proceedings of five international conferences [Aluminum-Lithium Alloys I-V, 1982-1989].

These first generation aluminum-lithium alloys were initially billed as one-for-one replacements for existing aerospace alloys; for example, 2090 was designed to replace 7075-T6. However, they have a different complex of mechanical, chemical and physical properties even when the strength and fracture toughness are the same under some conditions. This fact has necessitated reevaluation of standard tests used to provide a database for design. In some cases, formerly irrelevant differences in test procedure have proven to be important. In others, formerly predictive accelerated tests have been shown to correlate poorly to service experience. Yet a third class of differences comes from the increased microstructural and mechanical anisotropy found in these alloys, particularly in unrecrystallized wrought material. This anisotropy is most vividly expressed in the poor short-transverse properties of the material, including its tendency to delaminate along the large planar boundaries. The extent of these differences has made extending the base of underlying mechanistic information that supports alloy design and application crucial to reliable use of these alloys [James and Rioja, 1989].

One of the first major applications of aluminum-lithium alloys may be in space structures, in which the driving force for weight reduction is even greater than in conventional aircraft structures. The majority of these applications will be at cryogenic rather than ambient temperatures (although elevated temperature response may be important as well). Both the cryogenic applications for high-strength aluminum alloys and the generally well-behaved mechanical behavior at low temperatures of aluminum alloys and aluminum-lithium alloys in particular will be discussed in the following sections. However, it is important to note that with the notable exception of Weldalite™ none of these alloys was developed with cryogenic applications in mind. One result of this design strategy is that although some of these alloys have good cryogenic properties, they are not optimized for cryogenic properties. Since the determinants of good cryogenic properties are poorly understood,

another consequence is that modifications that improve ambient temperature mechanical properties will have unknown, and perhaps deleterious, effects on the cryogenic properties.

Table 1.1. Nominal compositions (center of registered composition range) in weight percent (atomic percent in parentheses) and calculated densities of commercial aluminum alloys. In older alloys, Mn or Cr was added instead of Zr to inhibit recrystallization.

Alloy (lb/in^3)	Al	Cu	Li	Mg	Zr	other	Density, gm/cm^3
2090	bal	2.7	2.2	-	0.12	-	2.58 (0.093)
		(1.1)	(8.1)	-	(0.04)	-	
2091	bal	2.2	2.0	1.5	0.12	-	2.57 (0.092)
		(0.9)	(7.4)	(1.6)	(0.03)	-	
8090	bal	1.3	2.4	1.0	0.12	-	2.54 (0.092)
		(0.5)	(8.8)	(1.0)	(0.03)	-	
8091	bal	1.9	2.6	0.9	0.12	-	2.53 (0.091)
		(0.8)	(9.6)	(0.9)	(0.03)	-	
Weldalite	bal	4.5-6.3	1.3	0.4	0.14	0.4 Ag[1]	2.68-2.71
		(1.9-2.7)	(5.0)	(0.4)	(0.04)	(0.1)	(0.097-0.098)
2219	bal	6.3	-	-	0.30 Mn	- [2]	2.79 (0.103)
		(2.8)	-	-	(0.15)	-	
7075	bal	1.6	-	2.5	0.23 Cr	5.6 Zn	2.80 (0.101)
		(0.7)	-	(2.7)	(0.12)	(2.3)	

[1] 0.03 Ti added for grain size control.
[2] 0.06 Ti added for grain size control.

1.2. Cryogenic applications for high-strength aluminum alloys

Interest in the cryogenic properties of aluminum alloys has, historically, been driven by specific technological needs that have arisen, for example, in the development of transportation systems for liquified natural gas (LNG) and cryogenic tankage for spacecraft. Because these applications have been relatively small in total volume, alloys have been selected from among preexisting commercial alloys rather than designed with cryogenic use in mind. As a consequence, the published information on the cryogenic properties of commercial alloys consists almost exclusively of tabulations of mechanical properties with little or no discussion of microstructure or mechanisms. The work includes a considerable effort in the early 1970's on extremely tough, low-to-moderate strength alloys such as 5083-O (nominal composition, in weight percent, Al-4.4Mg-0.7Mn), since

these were of interest for use in LNG tankers (111 K) [McHenry, 1983; Tobler, 1977; Kelsey, 1975; Hirose, 1982]. A second body of work was spurred by the development of the space shuttle, whose external tank is constructed of 2219-T87 (nominally Al-6.4Cu). Both applications involve welded cryogenic tanks, and hence stimulated research on the weldability of aluminum alloys for cryogenic use [Kaufman, 1963; Meister and Martin, 1967]. Much of the available data is summarized by McHenry [1983], who includes cryogenic mechanical properties for most commercial alloys that have been measured, although 4 K toughness data remains scarce. More fundamental research on aluminum alloys at low temperature has addressed their tensile properties almost exclusively, and has focussed on pure aluminum or simple alloys that have very little microstructural behavioral similarity to the commercial alloys of technological importance [e.g. Cottrell and Stokes, 1955; Chin, et al. 1964; Reed, 1972].

In the last few years there has been a resurgence of research on the cryogenic properties of high strength aluminum alloys that is driven by the simultaneous appearance of new programs in advanced aerospace systems and new high strength aluminum alloys with particularly promising properties. The most important of the new alloys are the advanced Al-Li alloys, although a 2219 modification, 2519 was introduced recently (nominal composition Al-5.8 Cu-0.15 Mg-0.24 Mn-0.12 Zr-0.19 Fe-0.03 Zn-0.08 Si-0.05 Ti) [Marinaro, 1989]. The density advantage of aluminum-lithium alloys is especially great in this application since 2219 is an exceptionally heavy alloy. In addition to the improvements in density and stiffness due to the presence of lithium, early work on binary aluminum-lithium alloys and on the Al-Cu-Li alloy 2090-T81 (Al-2.7Cu-2.2Li-0.1Zr) showed that the fracture toughness of aluminum-lithium alloys may improve significantly at low temperatures for at least some alloys, orientations and test procedures. Alloy 2090-T81 improves dramatically as temperature decreases [Glazer, 1986; Dorward, 1986]; the strength-toughness combination (L and L-T orientations, respectively) at 4-77 K is substantially superior to that of any other commercially available aluminum alloy. The important potential applications include cryogenic tankage for advanced aerospace systems and cryogenic structures for high energy physics devices.

Aerospace cryogenic tankage. The aerospace cryogenic structures of greatest current interest include expendable tanks for space vehicles such as the space shuttle, which are currently made of alloy 2219-T87, and integral tanks for future hypersonic aircraft. The fuels in both cases are liquid hydrogen (20 K) and liquid oxygen (100 K). The alloys for expendable, external tanks require high strength and toughness at 20 K, low density, and high stiffness. The alloys must be weldable, and, because of the need for low overall weight, must be formable or machineable into relatively complex shapes. Detailed property requirements are being developed as part of the NASA Advanced Launch System (ALS) program in the United States. The properties required for integral tankage in hypersonic vehicles depend on whether the tank is parasitic or part of the aircraft structure. Alloy strength is more important in the latter case. An integral tank also requires a more durable and damage tolerant design; the fatigue and corrosion resistance and elevated temperature stability all take on increased importance in the alloy selection. Current design activities in hypersonic vehicles include the National Aerospace Plane (NASP) in the United States and HOTOL in Europe [Gwynne, 1986; Robinson, 1987]. Japan is also studying the

development of a space plane, the Hope or H2 orbiting plane. Because of the variety of potential designs and manufacturing approaches, there is no general consensus on the optimum mix of properties for a cryogenic tankage alloy.

High energy physics devices. Advanced accelerators and magnetic fusion energy devices operate at 4 K so that they can use large superconducting magnets. The magnet case materials must have good mechanical properties at cryogenic temperature. Because of its physical properties (e.g. coefficient of thermal expansion) and light weight aluminum is sometimes selected over much higher strength cryogenic steels. An example is the Nb_3Sn force-cooled conductor magnet built by Westinghouse for the Large Coil program in the US [Westinghouse superconducting magnet coils contract report], which had an external case made of alloy 2219-T87. Aluminum alloys are now being considered for magnet collars for the Superconducting Supercollider (SSC) in the US. These may be made of 7075-T6 or 2090-T81 (for strength). Potential applications at the European high energy physics facility at CERN include shrink-fitted rings and collars of alloys 2014 and 5083. Cryogenic aluminum alloys may also be used in "radiation-thin" superconducting detector magnets and beam vacuum chambers [Lebrun, 1987; Lebrun, et al., 1988]. These designs require high strength, moderate toughness and good fatigue resistance.

Among the other past and potential cryogenic applications for aluminum alloys are LNG tankers, cryogenic wind tunnels, missiles and other space structures including telescopes.

Manufacturing issues may be paramount in the eventual alloy selection for all of these applications. The importance of weldability for an alloy to be used for cryogenic tankage was already alluded to. Superplastic forming, which allows the manufacture of parts with complex shapes without any joining, is another important technology. The fact that many aluminum-lithium alloys can be processed to be superplastic increases the likelihood of their application. Both welding and superplastic forming generally entail some decrease in the peak properties available from the material. Obviously it is desirable to minimize this loss to the extent possible and there is considerable research in this direction.

1.3. Cryogenic mechanical properties of fcc alloys

An examination of the literature suggests the behavior of aluminum alloys is a subset of the broader problem of generating a unified picture of the mechanical behavior at low temperatures of f.c.c. alloys in general. Austenitic steels and nickel-based alloys also show a wide range of low temperature behavior ranging from much improved to much deteriorated from their room temperature properties. It is likely that the mechanisms of improved low temperature behavior are common to all of these alloy systems. For this reason some comparisons are drawn in the discussion below between aluminum and other f.c.c. alloys. Because the f.c.c. alloys have widely disparate strengths, comparisons between them are difficult. Since the shear modulus G is a scaling factor in theoretical quantities related to strength, the data should be scaled by G or the elastic modulus E. Relative to their stiffness, high strength commercial aluminum alloys are as strong as the

highest strength steels. An aluminum alloy with a yield strength of 500 MPa (~70 ksi) is equivalent to a steel with a strength of about 1400 MPa (~200 ksi).

As mentioned previously, it is difficult to find both tensile and toughness data in the literature across the temperature range 300 K to 4 K for most alloys, and even more unusual to find accompanying microstructural and fractographic information. The following brief review of the available information emphasizes high strength aluminum alloys.

1.3.1. Elastic properties

The variation of elastic properties with temperature is one of the few areas of mechanical behavior that has been well characterized and is at least partially understood. Aluminum alloys show an increasing elastic modulus and decreasing Poisson's ratio with decreasing temperature. The change in these properties relative to their values at room temperature appears to be constant for all aluminum alloys even though their room temperature elastic properties are different (e.g. Al-Li alloys are 7-10% stiffer than conventional Al alloys). A compilation of elastic properties of cryogenic structural materials has been published by Ledbetter [1981]. With the exception of Invar (36Ni-64Fe), the percentage variation in stiffness with temperature is of about the same magnitude for aluminum and other f.c.c. alloys.

1.3.2. Strength

The variation in yield strength and ultimate tensile strength with temperature has been documented for a number of alloys in the range 300-4 K. The variation in yield strength with temperature for a selection of f.c.c. alloys is illustrated in Figure 1.1 [Chan and Morris, 1987]. However, most of the low temperature data is for a few discrete temperatures: at 4 K (LHe), 20 K (LH_2), 77 K (LN_2) and 200 K (dry ice in ethyl alcohol). A few studies have examined a much larger number of temperatures. The yield and ultimate strengths generally increase with decreasing temperature, but the detailed studies have indicated that they are not necessarily smoothly varying; peaks and plateaus are observed [e.g. Saji, et al., 1987; Niinomi, et al., 1988]. In addition, strength anisotropies between the L and LT orientations are not necessarily maintained through this temperature range and may even reverse. This is perhaps particularly surprising with respect to yield strengths. Ultimate tensile strength variations are more easily explained in the sense that work hardening is a complicated phenomenon, influenced by many factors that may have different temperature dependences (e.g. ease of cross-slip, which depends on texture). This cross-over effect is quite strong in 2090 and 2091 (Al-2.2Cu-2.0Li-1.5Mg-0.1Zr), both of which have a relatively anisotropic grain structure and are strongly textured.

1.3.3. Fracture toughness

In most materials, strength and toughness at a given temperature may be varied by processing and are inversely related. Since strength increases with decreasing temperature, it would perhaps be most easily explicable if the toughness decreased with decreasing

temperature along the same strength-toughness relation that holds for the material at room temperature. This type of behavior has been observed in Fe-Mn alloys [Yoshimura, et al., 1982]. This result might be expected to hold more generally if the fracture mode remains unchanged with temperature; conversely, a dramatic decrease in toughness should be observed if the fracture mode changes to a lower energy mode (i.e. a ductile-brittle transition such is observed in many b.c.c. steels). However, neither of these scenarios is the case for the aluminum alloys 2219 and 2090, or for a number of steels and nickel alloys that remain ductile to 4 K. In fact, upper shelf toughness can increase with decreasing temperature and increasing strength in alloys which do show a ductile-brittle transition [Ritchie, Server and Wullaert, 1979].

The strength-toughness combination for aluminum alloys 2090 and 2219 is illustrated in Figure 1.2 [Glazer et al., 1986]. The principal source of the improvement is the substantial increase in fracture toughness at low temperature; the yield strength is only slightly affected. As Figure 1.3 illustrates, this behavior is atypical, even for aluminum alloys. Other alloys show either an improvement in strength at relatively constant toughness or a deterioration in the toughness as the temperature drops. Both 2219 and 2090 also have improved tensile elongation at low temperature. Although 2219 has been used in cryogenic applications for some time little is known about the mechanism behind its improved properties at low temperature. The behavior of 2090 is a focus of this study and of other recent work; the possible mechanisms at work will be discussed in detail in later sections. The improvement is not simply due to the presence of lithium, since other aluminum-lithium alloys do not show improvements as striking as those in 2090 [Glazer and Morris, 1989; Rao, et al., 1989; Verzasconi, 1989].

1.3.4. Elongation

Although strain-to-failure is dependent on stress state, tensile elongation represents an important point on the forming limit curve. As shown in Figure 1.4, many f.c.c. alloys (2000 series (Cu-containing) aluminum alloys, OFHC copper, etc.) show an increase in tensile elongation at low temperature which may be a reflection of the increased strain hardening rate that can be maintained at low temperature. Not all of these alloys show improved toughness, but many of them do. In order to understand the significance of measured uniform and total elongations it makes sense to distinguish between those alloys that display necking behavior prior to failure and those that do not.

1.4. Overview of physical metallurgy of aluminum-lithium alloys

The microstructure of aluminum-lithium alloys is expressed in the properties of these alloys primarily at two levels. On the macroscopic level, the highly elongated grain structure found in unrecrystallized commercial alloys has a marked effect on the fracture and fatigue behavior of the material and probably also on its response to deformation. On the microscopic level, the precipitate types and distribution determine the strength, strain hardening ability and deformation behavior of the material and may strongly influence the

fracture behavior by concentrating deformation or providing nucleation sites for voids or cracks (through either precipitate free zones or large grain boundary precipitates).

Macrostructure. The highly elongated grain structure of most commercial aluminum-lithium alloys arises from the addition of about 0.12 Zr (weight percent). The Zr is incorporated in coherent Al_3Zr precipitates (β') that form at high temperature. These precipitates strongly inhibit recrystallization and grain coarsening by exerting a high drag force on the grain boundary due to the low diffusivity of Zr at processing and aging temperatures and the coherence of the original interface, which would be lost during recrystallization [Starke and Sanders, 1981]. The large planar grain boundaries in the resulting structure fail relatively easily and are often observed to delaminate in in-plane fracture toughness tests, where they are perpendicular to the main crack plane and crack front. The resulting fracture mode typifies many aluminum-lithium alloys and consists of these intergranular delaminations linked by regions of transgranular shear. The influence of the grain structure and this delamination phenomenon on the fracture and deformation behavior of the material will be discussed in Chapters 6 and 7.

There are a number of reasons for the low fracture strength in the ST direction that causes these delaminations to occur. Clearly, the presence of large planar boundaries creates a strong tendency for intergranular fracture; however, the proximate cause of fracture remains in question. Mechanical fibering of second phase particles, grain boundary precipitation and high local stresses caused by planar slip have all been suggested. Miller et al. [1987] have argued that there is Li segregation at the grain boundaries that makes them inherently brittle. However, the large shears in the immediate vicinity of the grain boundary observed by other investigators [Meyer, et al., 1987] again point to the potentially dominant influence of grain shape and texture.

Precipitate microstructure. Several precipitates contribute to the strength of Al-Li, Al-Cu-Li and Al-Cu-Mg-Li alloys. Some of the important phases are described in Table 1.2. It should be noted that the exact compositions and crystallography of some of these phases and the existence of precursor phases have been disputed; the information in this table is intended as a guide only. The composition ranges and corresponding strengthening phases present in commercial alloys are illustrated in Figure 1.5.

Many of the deformation properties of aluminum-lithium alloys that differ from other aluminum alloys come from the hardening precipitate in the binary aluminum-lithium system, δ' (Al_3Li). This precipitate has the $L1_2$ ordered fcc structure and is coherent with the matrix with an extremely low misfit. These precipitates are easily shearable. Because they are ordered, the passage of a dislocation creates an antiphase boundary. A second dislocation restores order. One consequence of this process is that superdislocation pairs tend to form; a second is that the sheared plane is softer because the diameter of the precipitates is reduced. This work softening partially counteracts the hardening influence of dislocation-dislocation interactions. The result is highly planar slip that can cause local stress concentrations. The low ductility and fracture toughness observed in binary aluminum-lithium alloys are attributed chiefly to planar slip.

Table 1.2. Important strengthening phases in commercial (aged) aluminum-lithium alloys [Flower and Gregson, 1987].

Phase	Composition	Crystal structure	Morphology and Habit Plane
δ'	Al_3Li	$L1_2$ (fcc)	spherical or on β', θ' or T_2 surfaces
β'	Al_3Zr	$L1_2$	spherical
T_1	Al_2CuLi	hexagonal	plate, {111}
T_2	Al_5CuLi_3	icosahedral	plate, {100}
θ'	Al_2Cu	tetragonal	plate, {100}
S'	Al_2CuMg	orthorhombic	lath, {021}, <100> growth direction

Al-Cu-Li alloys are both stronger and tougher than the binary alloys. The addition of 1-2 atomic percent copper makes possible the formation of plate-like Al-Cu-Li phases that simultaneously provide greater strength and promote slip homogenization. These phases are T_1 and θ' (which may have lithium incorporated); T_2 may form as an equilibrium phase. In alloys with a high copper to lithium ratio θ' replaces T_2. The δ' precipitate is present in two morphologies, as a spherical precipitate and on the faces of the θ' platelets. In general, slip line traces indicate that slip remains relatively coarse and planar. The T_1 phase seems to provide the maximum strengthening effect per Li atom. Because of the relatively high nucleation barrier, in solution heat treated and aged material a relatively high concentration of T_1 is found at grain boundaries while the grain interiors have relatively larger volume fractions of θ' and δ' and relatively little T_1. For this reason a tensile stretch of 2-6% is usually applied between the solution heat treatment and aging steps. The stretch introduces a homogeneous distribution of dislocations that act as heterogeneous nucleation sites for T_1 in the grain interior. The dislocations promote nucleation of T_1 at the expense of δ' and make it possible to achieve high strength without excessive grain boundary precipitation and with a minimum amount of the δ' precipitate that promotes planar slip.

The addition of Mg tends to further promote slip homogenization and cross slip. The Mg-containing alloys are strengthened by a combination of T_1 and the orthorhombic S' phase that forms as rods, or after further aging, laths with a {021} habit and a <100> growth direction. This phase also nucleates heterogeneously on dislocations. Its presence promotes cross-slip [Miller, White and Lloyd, 1988] because there are no close-packed planes parallel to the aluminum slip planes along which it can be readily sheared, even at very high stresses. The proportions of S' and T_1 phase depend on the composition of the alloy. In compositions with 2-3 wt% Li that are also rich in Cu and Mg, the S' phase predominates over the T_1 phase and θ' does not form [Flower and Gregson, 1987]. The δ' phase is also present, but precipitates independently of the other strengthening phases. At sufficiently high Cu and Mg contents S' can nucleate homogeneously [Peel et al., 1984]

although the required supersaturation is much higher than in Al-Cu-Mg alloys, probably due to the high lithium-vacancy binding energy [Gregson and Flower, 1985].

1.5. Cryogenic mechanical properties of aluminum-lithium alloys

The cryogenic mechanical properties of aluminum-lithium alloys have been studied by several investigators since 1984. Most of this work was ongoing during the course of the present study, much of which has been previously published [Glazer, et al., 1986; Glazer, et al. 1987abc; Glazer, et al., 1988; Morris and Glazer, 1988; Glazer and Morris, 1989]. The work described herein influenced the investigations reported in the literature and was in turn influenced by it. Accordingly, the bulk of the discussion of the relevant literature will be left for the discussion. The following provides some background on binary aluminum-lithium alloys and a brief resumé of the work on commercial and semi-commercial alloys designed to place the goals of the current study into context.

1.5.1. Initial studies.

The first study of cryogenic properties of aluminum-lithium alloys was performed by Webster [1984], who investigated the properties of several binary Al-Li extrusions using blunt notched Charpy impact specimens. This and other studies [Webster, 1986; Webster, 1987] showed that in L-T notched specimens the Charpy impact toughness generally was flat or increased with decreasing test temperature between 373 and 77 K. This behavior contrasts with results for 2224 (nominal composition Al-4.4 Cu-1.5 Mg-0.6 Mn) and 7175 (a higher purity version of 7075), which display generally decreasing Charpy impact energy with decreasing test temperature. Webster also obtained similar results for Al-Cu-Li-Mg-Zr alloys. In both cases, the increase in fracture toughness was not always monotonic; a dip between 300 K and 200K was often observed. The significance of this dip will be discussed below in the section on models for cryogenic toughness. In later work, he showed that in overaged alloys the toughness decreased significantly between room temperature and 77 K. These early indications that aluminum-lithium alloys had good cryogenic fracture toughness combined with the obvious benefit of using a low density alloy in space applications spawned the investigations described below of commercial and near-commercial alloys.

1.5.2. 2090-T81.

Several investigators have focussed on the high strength commercial alloy 2090-T8E41, more recently referred to as 2090-T81. (The -T81 processing is specific to this alloy and involves solution heat treatment followed by a 6-8% tensile stretch and aging to peak strength at 163°C for 24 hours.) This work has been reviewed by Morris and Glazer [1988] and Dorward [1989]. The initial results reported by Glazer, et al. [1986] showed that the strength-toughness relation improved with decreasing test temperature, dramatically in the L-T orientation and to a somewhat lesser extent in the T-L orientation. These improvements were paralleled by an increase in the tensile elongation and were later shown to be accompanied by an increase in the strain hardening rate at low temperatures. The

toughness results were qualitatively confirmed by Dorward [1986]. Dorward [1986] and Rao, et al. [1988] also examined other crack orientations; a small decrease in S-L and S-T toughness is observed between 295 and 77 K, while L+45 specimens display an increase of similar magnitude to the other in-plane orientations. Dorward also examined an underaged temper, with similar results. Fractographic studies have shown the primary fracture mode to be unchanged at all test temperatures. However, in the in-plane specimens intergranular, crack-dividing, delaminations are also present. The number and depth of these splits are clearly greater at 77 K than at room temperature. The fracture mode in the in-plane specimens is characterized by intergranular splits linked by regions of transgranular shear. In the S-L and S-T orientations the fracture is intergranular and intermetallic particles are visible on the fracture surface. In keeping with the low fracture toughnesses in these orientations, there is very little deformation around these particles. Jata and Starke [1988] also examined 2090-T8 (2% stretch), 2090-T6 and 8090-T8. They found an increase at 77 K over 295 K in the values of fracture toughness and strain hardening rate as well as yield strength, ultimate tensile strength and tensile elongation.

1.5.3. Other commercial alloys.

The cryogenic mechanical properties of other commercial alloys have also been studied, although none in as much detail as 2090. Many of these alloys and tempers also show improved low temperature fracture toughness. Rao, et al. [1989] studied 2091-T8X, 8090-T351 and 8091-T351, all of which failed by ductile rupture at room temperature.[1] At 77 K the fracture was characterized by intergranular delaminations linked by regions of transgranular shear (similar to 2090-T81). This fracture mode transition was associated with a decrease in fracture toughness. Alloys 2091-T351, 8090-T8X and 8091-T8X, which like 2090-T81 fractured by the transgranular shear mode at room temperature, all showed an increase in fracture toughness between 295 and 77 K. Glazer and Morris [1989] studied a 2091-T8 material which behaved similarly. Niinomi et al. [1988] studied the strength-toughness relationship of an Al-Cu-Li-Mg-Zr using tensile and instrumented Charpy tests. In the T6 temper, both the strength and toughness increased between 295 K and 77 K. The fracture mode was again intergranular delaminations linked by regions of transgranular shear. Some of these alloys showed an increase in elongation at low temperature, while others did not.

Dew-Hughes et al. [1988] have investigated the tensile behavior (including fracture stress) of 8090-T351 and -T651. They found that the yield stress and fracture stress generally increased with decreasing test temperature for all three orientations tested (L,LT,ST). The effect of temperature on the tensile elongation depended on the temper and test orientation. For the T651 temper, the L elongation increased, the ST elongation was flat and the LT

---

[1] Heat treatments used by Rao, et al. corresponding to these temper designations are:

-T351 Solution heat treat, stretch 3%, age at room temperature

-T8X Solution heat treat, stretch 3%, peak-age under the following conditions

2091-T8X aging 135°C/10 hours

8090-T8X aging 190°C/16 hours

8091-T8X aging 190°C/16 hours

elongation decreased with decreasing test temperature. In the naturally aged T351 temper, the elongation increased with decreasing temperature in the L and LT orientations, while in the ST orientation it was constant between room temperature and 115 K and then declined significantly at 77 K. The failure appearance of the T651 tensile specimens was typical of aluminum-lithium alloys — failure along grain boundaries parallel to the loading direction linked by transgranular shear. An increased amount of interboundary failure was observed for specimens tested at lower temperatures. The ST failures appeared to follow subgrain boundaries. In the underaged material, the LT specimens failed by ductile void linkage at room temperature, but at low temperature splitting was observed and the failure was similar to that of the T651 material. A transition from ductile to flat fracture was observed in the underaged ST specimens that correlated to the decrease in elongation. Dew-Hughes et al interpret their results as suggesting that the matrix strength increases with decreasing test temperature more rapidly than the grain boundary strength, thus promoting increased intergranular failure.

Saji et al. [1987] studied an Al-Cu-Li-Mg-Zr alloy (grain aspect ratio in μm (70-100):(50-70):(10-15)). This study examined tensile behavior between 7 and 295 K using 10 K intervals between 7 and 70 K. In both underaged and peak-aged material, the yield and ultimate tensile strengths, uniform elongation, reduction in area and strain hardening rate increased to a maximum at 20-30 K, where serrations from adiabatic heating became prominent. The post-uniform elongation displayed the opposite trend; a minimum was observed at 20-30 K. The effect of temperature on the strain hardening rate and elongation was somewhat greater for the underaged material, which has a higher matrix solute content, than for the peakaged material. Saji et al. observed delamination in their specimens. The maximum amount of delamination occurred at about 30 K, leading them to conclude the delamination had little effect on the mechanical properties, although it would seem that the opposite conclusion could just as easily be drawn.

1.5.4. Superplastic modifications.

The properties of superplastic modifications of these alloys have also been studied. Because the superplastic alloys have a fine equiaxed grain structure, their fracture behavior is different. In sheet form, these alloys generally show an increase in tensile elongation but a decrease in fracture toughness with decreasing temperature [Glazer et al., 1988; Verzasconi, 1989].

1.5.5. Binary alloys.

A number of studies of monocrystalline and polycrystalline binary Al-Li alloys have been conducted. In single crystals containing 2.9 weight percent (10 atomic percent) lithium, Miura, Yusu, Furukawa and Nemoto [1987] have found a positive temperature dependence of the yield strength in the range 77 - 373 K, i.e. increasing strength with increasing temperature. They attribute the increased strength to a greater resistance of the precipitate to shear caused by Kear-Wilsdorf locking, a process by which the mobility of screw dislocations is greatly decreased because one of the dislocations forming the superdislocation pair undergoes thermally activated cross slip to a {100} plane to reduce

the antiphase boundary energy associated with the pair. This mechanism has been used to explain a similar temperature dependence of the yield strength in Ni_3Al [e.g. Thornton et al., 1970]. Similar observations have been made by Tamura, Mori and Nakamura [1973] for single crystals containing large δ' precipitates. In polycrystalline alloys (11 at %, 3 wt %) Furukawa, Miura and Nemoto [1985] found that the positive temperature dependence was retained when the δ' precipitates were sheared (presumably again due to Kear-Wilsdorf locking), but was reversed when Orowan looping was the dominant bypassing process. They also found that at lower test temperatures peak strength occurred after longer aging treatments (i.e. at larger precipitate sizes). They interpret the shift as a consequence of the opposite temperature dependences of the shearing and looping stresses.

1.5.6. Mechanistic models.

The results of these studies of the cryogenic mechanical properties of aluminum-lithium alloys may be summarized briefly as follows. The predominant failure mode of commercial alloys with an elongated grain structure is intergranular delamination at large planar grain boundaries followed by transgranular shear. The amount of delamination at 77 K is greater than at 300 K. Materials with this failure mode at both temperatures generally show an increase in fracture toughness at low temperature. Alloys that fail by ductile rupture at 300 K, fail intergranularly or by the mechanism described above at low temperature and generally have a lower fracture toughness at 77 K. In most, but not all, of the alloys the tensile elongation increases with decreasing test temperature, especially in the longitudinal orientation.

These studies have resulted in four mechanistic models to explain the observed variation in fracture toughness with test temperature:

1) primary fracture mode

When the primary fracture mode changes from a ductile mode at one test temperature to a more brittle one at another, the fracture toughness decreases. Examples are the transitions at low temperature from ductile dimple rupture to transgranular shear observed by Rao et al. [1989] and from ductile shear to intergranular failure in superplastic 2090-T6 observed by Glazer et al. [1988].

2) liquid phases

Webster [1986, 1987] has postulated that Na, K, Cs, Rb and other impurities difficult to separate from Li can form low melting point phases that lower the toughness of these alloys by a liquid embrittlement mechanism. He postulates that these phases freeze out at lower temperatures, resulting in increased fracture toughness. However, none of the phases he suggests are liquid at 77 K or below.

3) crack-dividing splitting

Intergranular cracks perpendicular to the crack plane and perpendicular to the crack front may help to increase the fracture toughness by partially relaxing the triaxiality of the stress state. By analogy to the increase in fracture toughness observed in plane stress over plane strain, the splitting is expected to result in an increase in the apparent plane strain toughness. Since splitting is more prevalent in these materials at 77 K than at 295 K, it has been suggested that splitting is responsible for the increased fracture toughnesses measured at low test temperatures.

4) material properties (effect of yield strength and strain hardening rate)

There are numerous theories of ductile strain-controlled fracture. Although their functional forms differ, all predict a positive dependence of the K_{Ic} on the yield strength, elastic modulus, elongation and strain hardening rate. Thus if no fracture mode transition is observed, these theories predict the observed increase in toughness with decreasing test temperature. As discussed above, this behavior is observed in a number of fcc alloys.

1.6. Objective

The objective of this work is to develop a mechanistic understanding of the strength-toughness relationship in commercial aluminum-lithium alloys, with special emphasis on understanding the improved in-plane fracture toughness of 2090-T81 between room temperature and 4 K. It is hoped that this knowledge will provide useful input into the alloy design process in two ways. Firstly, since neither 2090 nor any other existing commercial aluminum alloy was optimized for cryogenic properties, the understanding gained here may provide insight into processing or compositional modifications that could lead to improved cryogenic properties. By the same token, some understanding of the source of the current good properties may enable the alloy designer to avoid inadvertently adversely affecting the cryogenic properties of the material. Accordingly, the discussion of mechanisms that follows is oriented toward providing these kinds of alloy design guidelines.

Commercial alloys were selected for this work because there is considerable likelihood that the failure mechanisms of laboratory alloys would be significantly different from those of commercial alloys. There are three main reasons for this expectation. One is that it is difficult to cast aluminum-lithium alloys of high quality due to the high reactivity of lithium. A second reason is that high reduction ratios are difficult to achieve in laboratory plate. As the previous discussion has highlighted the elongated grain structure found in unrecrystallized alloys plays an important role in their fracture and deformation behavior. A third problem is the difficulty of performing the tensile stretch that is common in commercial practice. This stretch promotes nucleation of strengthening phases other than δ'.

2. EXPERIMENTAL PROCEDURES

2.1. Materials and microstructures

The materials investigated in this study are individually described below. The composition and processing for each alloy and temper are given in the individual sections. These are 2090-T81 and -T4 plate, 2091-T8 plate, superplastic 2090-T6 sheet and an aluminum-lithium binary alloy. With the exception of the superplastic thermomechanically processed 2090-T6, which was manufactured by Reynolds Metals Co. and processed by Reynolds and Lockheed Missiles and Space Co., all of the experimental materials were provided by the Aluminum Company of America (Alcoa). Most of the emphasis in this section and in the study as a whole is on the 2090-T81 and 2091-T8 plate materials.

To examine the evolution of the microstructure, optical microscopy was performed at various stages of the processing on specimens polished to 0.05μm and etched using Keller's reagent (2.5% HNO_3, 1.5% HCl, 0.5% HF (40%), balance H_2O).

2.1.1. 2090-T81, -T4

The 2090 material was provided by Alcoa in the form of 12.7 mm (0.5 in) plate in the T81 condition. This temper is also referred as T8E41 in early publications. It is a proprietary process that includes a stretch of 6-8% after solution heat treatment and peak aging at 163°C for approximately 24 hours. The material used in this study is from a lot that has been extensively tested by a number of corporate and government laboratories.[2] Newer "vintages" of this alloy are now available in which the variability of properties though the plate thickness and tendency toward short-transverse delamination are much reduced. The nominal composition of 2090 is Al-2.7Cu-2.2Li-0.1Zr in weight percent. The actual composition of the plate, as determined by atomic emission (Cu) and atomic absorption (balance) spectroscopy, is Al-2.86Cu-2.05Li-0.12Zr (also in weight percent). Levels of Fe, Si, Mg, Mn and Ti were all 0.02 weight percent or less. The density of this material was measured to be 2.589 g/cm^3.

The microstructure of this material has been extensively characterized (e.g. Rioja and Ludwiczak, Huang and Ardell, Tosten, Vasudévan and Howell, [1986, 1988]). There are three principal precipitates, δ', T_1 ({111} habit plane) and θ' ({100} habit plane). Al_3Zr particles that pin the grain boundaries and inhibit recrystallization are also present. Figure 2.1 is an optical micrograph that shows the grain structure of the alloy. The grains in this material are highly elongated since it does not recrystallize at any time during the rolling process from ingot to plate. The mean grain size is approximately 2200 x 400 x 25 μm. Subgrains with relatively low misorientation with respect to one another are found within the grains; these are 3-10 μm in size.

---

2 "Cooperative Test Program on Al-Li Alloy 2090-T8EXX Plate, Sheet and Extruded Products," Naval Air Systems Command, Contract N•0921-84-C-0078.

To investigate the effect of the precipitates and matrix solute content on the properties, the 2090-T81 plate described above was re-processed and designated 2090-T4. This material was prepared by solution heat treating at 550°C for 30 minutes followed by a cold water quench and natural aging. The process does not substantially change either the grain or the subgrain structure from that of the original plate.

2.1.2. 2091-T8

2091 plate was received from Alcoa in the form of 38 mm (1.5 in) plate in the as-fabricated (F) temper. In this condition the material contains many large second phase particles of spherical and plate morphologies. The nominal composition of 2091 is Al-2.2Cu-2.0Li-1.5Mg-0.12Zr. The actual composition of the plate is Al-1.99Li-2.02Cu-1.34Mg-0.12Zr in weight percent. The microstructure after solution heat treatment is illustrated in Figure 2.2. The mean grain size was approximately 1400 x 400 x 70 μm.

The solution heat treatment temperature was initially determined from DSC (differential scanning calorimetry) behavior. A small dissolution reaction was observed at about 540°C followed by general melting at 575°C. Accordingly a solution heat treatment temperature of 550°C / 1 hour was selected. The longer time was chosen to allow for the greater distances over which homogenization is required in thicker plate.

Ashton et al. [1986] have demonstrated the importance of deformation prior to artificial aging to the mechanical properties of similar alloys (8091 and Al-2.3Li-2.1 Cu-0.7 Mg-0.1 Zr). The S' (Al_2CuMg) precipitate has a large coherency strain, so its nucleation is promoted by the presence of a homogeneous distribution of dislocations. A 3% stretch provides considerable benefit; a 7% stretch provides a greater, but not proportionately greater, benefit. Ashton et al. also found that the lowest practical aging temperature was preferable; the number of grain boundary precipitates, the width of the grain boundary precipitate free zone and the size of the matrix precipitates are all minimized.

The processing considerations mentioned above led to the following procedure. In order to allow deformation prior to aging, the 38 mm (1.5 in) plate was split in half. Both surfaces were machined to make pieces 0.625 in thick. These pieces were solution heat treated, cold water quenched and rolled 6% in one pass (to make the deformation as uniform as possible) within 15 minutes after quenching. The sample temperature during solution heat treatment was monitored using a thermocouple place in a small hole in the plate. The heat treatment time was 1 hour from the time the plate reached 540°C. Due to furnace overshoot the maximum sample temperature was 564°C rather than 550°C. After quenching, the exterior of the specimen appeared dark grey. Some blistering was evident on the surface and some small cracks visible at the edges. The samples cracked significantly during rolling. The crack planes seemed to be oxidized in the specimen interior; the cracking probably indicates local melting.

The solution heat treatment was modified to prevent cracking on quenching. In order to develop a successful procedure samples were heat treated at 530°C and 550°C and quenched into room temperature and 93°C (200°F) water. Only the 550°C/23°C (73°F)

combination resulted in blistering and obvious cracking. The final process selected was 530°C/1 hr followed by a 65°C (150°F) water quench. The peak sample temperature during heat treatment was 541°C. These specimens did not crack during rolling. Specimens were flattened after rolling using a second rolling pass with a very small additional reduction in thickness. The uniformity of the rolling deformation was checked by performing a series of hardness tests across the thickness. The hardness variation was small, suggesting that the extent of cold work was relatively uniform. Small edge cracks were still sometimes evident after aging, but these were readily machined away. The susceptibility of this material to cracking probably indicates non-equilibrium melting of insoluble phases that do not dissolve during the 30 minute heating time to the solution heat treatment temperature. Lowering this temperature greatly decreases the likelihood of such melting, while raising the quench temperature reduces the residual stresses introduced by the thermal gradient set up during cooling. In combination, these processing changes greatly decrease the likelihood of crack at weak interfaces such as large planar grain boundaries in the L-T plane [Aluminum, 1984].

Aging curves were generated at both 160°C and 190°C. Peak strength at 190°C was reached after approximately 24 hours; the maximum appeared to be very broad, with relatively little additional hardening after 8 hours and little tendency toward overaging. At 160°C, the hardness did not reach this value even after 64 hours of heat treatment.

Transmission electron microscopy of the peak-aged alloy showed that the δ', S' and T_1 precipitate phases were present. Considering that this particular 2091 plate is relatively lean in Mg, this combination of phases is in reasonable agreement with the literature results summarized in Figure 1.5. Both S' and T_1 were found at the grain boundaries as well as homogeneously distributed through the grain interiors. The distribution of precipitates is illustrated in Figure 2.3. The S' precipitates exhibited a rod morphology; apparently further aging is required to develop laths. The subgrains were about 3-10 μm in size and were demarcated by a narrow δ' precipitate free zone.

2.1.3. Thermomechanically-processed superplastic 2090-T6

The details of material preparation, the thermomechanical processing (TMP) of 2090 sheet to obtain superplasticity, and the actual forming process have been described in detail [Henshall, 1987] and are only reviewed briefly here since all thermomechanical processing took place before the material was received. The tensile behavior of TMP 2090-T6 at cryogenic temperature has also been reported previously [Glazer, Morris and Nieh, 1987]. The material was induction cast, homogenized 24 hours at 538°C and scalped after cooling to room temperature. The ingot was then hot rolled in two steps to 20 mm thickness. The chemical composition of the sheet was analyzed to be Al-2.6Cu-2.4Li-0.18Zr in weight percent.

Superplastic forming and subsequent processing. The TMP which led to optimum superplasticity in this alloy is a four-step (overage) procedure. The initial step is a solution heat treatment followed by a rapid quench to create a microstructure of a coarse-grained matrix containing ~0.1μm Al_3Zr particles. The second step, a severe overaging, leads to a

uniform distribution of large diameter (≥ 0.5μm) equilibrium second phase particles. Warm rolling is carried out in the third step, to create intense deformation bands of high local defect densities around these large second phase particles. The alloy is recrystallized in the fourth step to complete the procedure. During recrystallization the large second phase particles dissolve. Growth of newly-recrystallized grains is inhibited by the pinning action of the fine Al_3Zr particles. The result of this procedure is the development of a very fine-grained structure. For alloy 2090, the actual procedure was to solution heat treat at 538°C/1 hour, cold water quench, overage at 400°C/16 hours, air cool to 290°C and isothermally roll to 2 mm (true strain $\varepsilon = -2.3$) and, finally, recrystallize at the superplastic forming temperature, 485°C.

The excellent superplastic properties of the 2090 alloy in uniaxial tension [Wadsworth et al., 1985] led to an evaluation of its formability under production conditions. Superform USA carried out the forming on specially processed sheet provided by Reynolds Metals Company. The sheet was superplastically formed at 485°C (905°F) into a headbox, a hat-shaped piece with a rectangular cross section. The part was formed by using gas pressure to form the sheet into a bubble into which a male tool was inserted. The pressure was then gradually reversed to form the sheet around the top of the tool [Henshall et al., 1987].

All material (formed or not) was solution heat treated 0.5 hours, quenched in 5% glycol in cold water, and aged to approximately peak strength at 190°C (375°F) for 8 hours and air cooled. The choice of aging time and characterization of the initial microstructure have been described by Henshall [1987] and by Glazer [1987]. An optical micrograph showing the fine grain size of the material after thermomechanical processing (2-5 μm) is shown in Figure 2.4.

2.1.4. Al-Li binary

A small number of tests were performed on a pseudo-binary alloy, Al-2.4Li-0.1Zr by weight. This alloy was received as 12.7 mm (0.5 in) plate hot-rolled from an 11 kg (25 lb) ingot, solution heat treated at 555°C for one hour, cold water quenched and stretched 2% in tension. Aging curves in this condition were determined and the material was aged to peak strength by heat treating at 190°C/7 hours. Only the L orientation was studied. The grain size of this material was approximately 1000 x 250 x 45 μm; the subgrain size was 1-5 μm.

2.2. Mechanical testing

With the exception of the elastic constant measurements, testing was conducted at four discrete temperatures: room temperature (~ 300 K), dry ice in ethyl alcohol (~ 200 K), liquid nitrogen (77 K) and liquid helium (4 K). Tests were performed using a servo-hydraulic testing machine equipped for cryogenic testing.

2.2.1. Test matrix.

Since not all materials were tested at all four test temperatures and toughness was evaluated only for some conditions, a test matrix is provided as Table 2.1. Several different tensile specimens and toughness measurement techniques were utilized. These are referred to in the table for summary purposes and will be described in more detail in sections 2.2.3 and 2.2.4, which discuss tensile and fracture toughness testing, respectively.

TABLE 2.1. Test matrix for mechanical properties evaluation.
(Plain text: Tensile properties measured only.)
(Underlined: Tensile and fracture properties measured.)

Alloy, orientation and test location[1]			Test temperatures	Specimen[2]
2090-T81	L	T/2	300,77,4	2.6a
	LT		300,77,4	2.6a
2090-T81	L	T/4	300,200,77,4	2.6b
	LT		300,200,77	2.6b
2090-T81	ST	n/a	200,77,4	2.7
2090-T4	L	T/4	300,200,77,4	2.6b
	LT		300,77	2.6b
2091-T8	L	T/4	300,200,77,4	2.6c
	LT		300,200,77,4	2.6c
2090-T6spf			300,77,4[3]	2.6d
Al-2.4Li	L	T/2	300,77	2.6b

1 T/2, T/4 refer to location of specimen within plate thickness (See section 2.2.3).

2 Tensile specimen design (Numbers correspond to figure numbers).

3 Toughness measured using Kahn tear specimens only.

2.2.2. Determination of elastic modulus

Elastic constant measurements of 2091-T8 and -T4 were performed at the National Bureau of Standards by Dr. H. M. Ledbetter and his colleagues using ultrasonic (10 MHz) pulse techniques at 5° temperature intervals between 4 and 300 K [Glazer, Morris, Kim, Austin and Ledbetter, 1987]. The experimental procedure is described in detail elsewhere [Naimon, Ledbetter and Weston, 1975; Ledbetter, Frederick and Austin, 1980]. Except for high-strain cases, dynamic elastic constants equal static elastic constants within the usual uncertainty of the latter. For the dynamic values, the uncertainty is estimated to be about 0.1%. Static and dynamic values should show essentially identical temperature behavior. Results are given in Figure 2.5 and Table 2.2 below. The longitudinal and transverse sound wave velocities give rise to the longitudinal and transverse moduli, C_l and

C_t. C_t is the shear modulus G. C_l is equivalent to B + (4/3)G, where B is the bulk modulus.

TABLE 2.2. Elastic constants of 2090-T81 at specific temperatures. E, B, G, C_l and ν are the elastic, bulk, shear and longitudinal moduli and Poisson's ratio, respectively.

Elastic Constant		Temperature (K)				
		295	200	77	20	4
E	(GPa)	78.3	82.5	86.9	87.6	87.6
	(10^6 psi)	11.36	12.03	12.60	12.70	12.70
B	(GPa)	72.6	74.0	75.3	75.6	75.7
	(10^6 psi)	10.52	10.73	10.92	10.96	10.96
G	(GPa)	29.6	31.4	33.3	33.5	33.5
	(10^6 psi)	4.29	4.55	4.83	4.86	4.86
C_l	(GPa)	112.1	115.8	119.7	120.3	120.4
	(10^6 psi)	16.26	16.79	17.36	17.45	17.45
ν		0.320	0.314	0.308	0.307	0.307

The elastic constants c_{ij} of 2090-T81 and 2090-T4 are compared in Table 2.3. The variations between elastic constants that would be equal in a macroscopically isotropic polycrystal are due to texture. The constants for the -T4 temper are very close to those for the -T8 temper. These results suggest that the elastic stiffening due to lithium results from solid-solution effects rather than from the precipitates or precipitate-matrix interactions.

TABLE 2.2 Polycrystalline elastic constants of 2090-T8 and 2090-T4 at 295 K. All values in GPa. Directions 1, 2 and 3 correspond to the L, LT and ST directions in the plate.

Constant	2090-T81	2090-T4
c_{11}	112.1	111.1
c_{22}	113.1	112.0
c_{33}	111.1	110.1
c_{44}	29.62	29.35
c_{55}	30.28	30.00
c_{66}	29.04	28.74

2.2.3. Evaluation of tensile properties

2.2.3.1. Specimens

Various tensile specimens were used to perform tests on specific materials. Because mechanical properties vary though the plate thickness, the specimen location with respect to the plate thickness T is designated in each case, e.g. T/2 for a specimen centered on the mid-plane of the plate. The orientation code for tensile and compact tension specimens is illustrated in Appendix 1. The majority of the tensile specimens were flat, both because this facilitates cryogenic testing and because it allowed observation of surface slip patterns after testing. Elongations less than 20% were measured using an extensometer on a 1.0 in (2.54 cm) gauge. Reduction in area was not determined as most specimens necked very little. With the exception of short-transverse tensile tests, all tests were conducted using a crosshead displacement speed of 2.1×10^{-3} cm/sec (0.05 in/min) which corresponds to a strain rate of $\sim 8 \times 10^{-4}$ sec^{-1} for a 2.54 cm (1 inch) gauge length.

The longitudinal (L) and long-transverse (LT) tensile data were obtained using several different types of specimens. The 2090-T81 T/2 tensile data was measured using pairs of standard round tensile specimens of the type shown in Figure 2.6a. The crosshead displacement rate was 0.05 in/min which represents a strain rate of 8×10^{-4} s^{-1}. The 2090-T81 and -T4 T/4 tensile data were measured using pairs (and occasionally triples) of the flat tensile specimens diagrammed in Figure 2.6b. The specimens were mechanically polished to 0.05 μm prior to straining to facilitate observation of slip line patterns on the surface. Elongation was measured over a 2.54 cm (1.0 in) gauge using an extensometer except when the elongation exceeded 20%, when stroke data was used instead. So that it would be possible to follow the development of the deformation substructure, some tests were interrupted at predetermined engineering strains. The 2091-T8 tensile data were measured using the standard flat subsize tensile specimens shown in Figure 2.6c. All specimens were taken from the mid-thickness of the heat treated plate, which corresponds to T/4 with respect to the original 38 mm plate.

The small amount of superplastically formed TMP 2090-T6 severely restricted the testing procedure. Tensile specimens were cut from the flange of the hat (superplastic forming true strain $\varepsilon = 0$) and from the sides and top of the hat which were 0.5 mm (0.020 in) and 0.75 mm (0.30 in) thick ($\varepsilon = -1.1$ and -0.9, respectively). Control specimens were cut from the unformed sheet which was approximately 2 mm (0.080 in) thick. The specimens were subsize flat tensile specimens with a 2.54 cm (1.0 in) gauge length (see Figure 2.6d) and were cut parallel to the original rolling direction. All results are from duplicate tests except for the 0.75 mm, 4 K datum.

The short-transverse tensile behavior of 2090-T81 was also measured. Due to the small thickness of the plate, specimens were manufactured by electron beam welding grip sections onto the top and bottom surfaces of the plate. The welding parameters were as follows: current - 10.8 mA; voltage - 80 kV; travel speed - 16.9 mm/s; electrode to work distance - 280 mm; vacuum pressure - 2×10^{-4} Torr. The specimen design is illustrated in Figure 2.7. Because of the low strength of the fusion zone and heat affected zone, the

reduced section was located in the plate interior and was very narrow to ensure failure inside the gauge. The reduced section had a gauge length of approximately 4 mm and a gauge width of 1.3 mm. The specimens were 2.3 mm (0.090 in) thick. Because of the short length of the gauge section, it was not possible to use an extensometer and elongation values could not be determined with useful accuracy, but were between 1 and 4% for all specimens. These tests were conducted at a strain rate of 10^{-3}.

2.2.3.2. r-value measurements

Mechanical anisotropy of the materials in tensile tests was characterized in two ways, by determining standard tensile properties in both the L and LT orientations and by determining r-values. The r-value is a measure of the plastic strain anisotropy that is often cited in the forming literature. It is given by the plastic strain ratio

$$r = \varepsilon_w/\varepsilon_t$$

where ε_w and ε_t are the strains in the width and thickness directions, respectively. The r-value may be a function of the longitudinal strain, but because only an extensometer was used to measure strain only the final value at the close of uniform elongation was determined. This value was determined by measuring the initial and final width and thickness of the specimen away from the failure region. Under the constant volume assumption the r-value can also be determined using the tensile elongation and either one of the other two strain values. A low value of r indicates a tendency toward thinning that leads to poor formability of sheet.

2.2.3.3. Strain hardening rate measurements

Necking in tension occurs when

$$d\sigma/d\varepsilon = \sigma \qquad (2.1)$$

where σ and ε are the true stress and true strain, respectively, and $d\sigma/d\varepsilon$ is the instantaneous strain hardening rate. When this relation is satisfied (and the strain hardening rate continues to drop further below the true stress), uniform elongation is no longer stable and deformation begins to localize in a neck, leading to a triaxial stress state, large local stresses and strains, and final fracture. The relation between σ and $d\sigma/d\varepsilon$ at failure can be used to distinguish between cases of premature (brittle) fracture ($d\sigma/d\varepsilon > \sigma$) and failure due to the macroscopic geometric instability ($d\sigma/d\varepsilon \leq \sigma$). Examples of both cases were found even in specimens that did not apparently neck. In the engineering stress-strain curve the necking criterion is satisfied at the peak of the curve; however, when the curve is very flat it is difficult to locate this point, so a numerical method is useful.

Engineering stress and strain data was collected by digitizing the test record (2090) or by collecting the data in digital form using a computer (2091). The computer-collected data was smoothed and compressed before further computation. The engineering stress and strain values were then converted to true stress σ and true strain ε values. When the tensile

elongation was greater than the range of the extensometer, the load-gauge displacement curve collected using the extensometer was used to subtract the machine compliance from load-crosshead displacement curve. Stress-strain curves measured at 4 K showed the serrated yielding behavior due to adiabatic heating typically observed at very low temperatures. For these tests, the upper envelope of the stress-strain curve was used to determine the strain hardening rate behavior. The strain hardening rate $d\sigma/d\varepsilon$ was computed by fitting the data using a sliding five-point fit to the parabolic Hollomon relation

$$\sigma=K\varepsilon^{n}. \tag{2.2}$$

As illustrated in Figure 2.8, the overall stress-strain curve deviated substantially from the parabolic form and the values of K and n were found to be a function of stress and strain. This discrepancy highlights the advantages of examining the strain hardening rate directly rather than investigating correlations with an n-value calculated on the assumption that the stress-strain curve fits equation (2.2). An alternate form

$$\sigma = \sigma_y + K\varepsilon^{n} \tag{2.3}$$

did not give a substantially better fit. The strain hardening rates determined as described above were plotted as a function of true strain and compared to the values of the true stress to check for satisfaction of the necking criterion (equation 2.1). The curves were also compared among themselves to investigate for systematic trends in strain hardening rate with test temperature, temper and alloy. The initial strain hardening rate during the yielding process approaches the elastic modulus; it then declines rapidly during the initial straining.

n-values. The instantaneous n-value determined using the sliding fit varied with stress and strain. The n-value immediately after yielding was often lower than the value at intermediate strains; the n-value generally declined slowly at the largest strains. Most theoretical models of the relation between fracture toughness and material parameters assume a constitutive relation of the form given by (2.2). So that the data could be compared to the predictions of these models, the n-value was determined by fitting relation 2.2 to the data for stresses greater than half the sum of the yield and ultimate tensile stresses. The value obtained for this latter part of the stress-strain curve was sometimes as much as fifty percent greater than the value obtained from a fit to the entire plastic region (even though the square of the correlation coefficient was generally greater than 0.9 for the fit to the entire curve). In a few cases, the square of the correlation coefficient was less than 0.99 for the fit to the second half of the stress-strain curve; in these instances the n-value was recalculated using a larger initial stress so that a good fit was achieved. It should be noted that since the n-value is sensitive to the way in which it is determined, it is not a good substitute for the strain hardening rate over the whole stress-strain curve unless the materials being compared tend to behave quite similarly. The value of n is related to the strain hardening rate by

$$n = \frac{d\sigma}{d\varepsilon}\left(\frac{\varepsilon}{\sigma}\right). \tag{2.4}$$

2.2.4. *Fracture toughness measurements and indicators*

The principal measure of fracture toughness considered in this work was the J_{Ic} test, a fracture mechanics test. The J_{Ic} test was selected since it not possible to perform valid K_{Ic} tests in all cases. Although a fracture mechanics test is far preferable, in many engineering situations toughness indicator tests are used. These tests generally measure crack initiation and propagation energies for a machined notch of small root radius, rather than a fatigue precrack. The behavior of 2090 in several of these tests was examined. Blunt (machined) and sharp (fatigue-precracked) notch test may give qualitatively different toughness results; these differences are discussed in Section 7.

2.2.4.1. *J_{Ic} tests*

Fracture toughness of the 2090 and 2091 plate was measured by determining J_{Ic} for standard 0.5 in (12.5 mm) thick compact tension specimens with W = 50.8 mm (2.0 in) according to ASTM Standard E813 (1981 standard for 2090; 1987 standard for 2091) using the single specimen compliance technique. The specimen is illustrated in Figure 2.9. The chief difference between these standards is the procedure used to fit the J-Δa curve so that the point of crack initiation can be defined. Several 2090 tests were recalculated; the 1987 standard gave slightly higher values. For a few 2091 tests, the results were quite different; differences in the rules for defining valid data points resulted in much higher results under the 1987 standard. The J - Δa curve for a typical test is shown in figure 2.10. The logarithmic fit used in the 1987 standard provides a better fit to the data for crack lengths beyond the valid region, but is not substantially different from the linear fit in the valid region. Where apparent initial "negative crack growth" was observed at low temperatures, the curve was shifted to higher Δa values so that all positive crack growth data was included in the evaluation.[3] $K_{Ic}(J)$ values were calculated using the value of the elastic modulus E at the test temperature. Since values for E as a function of temperature are unknown for 2091, the values for 2090 were also used for 2091. This procedure is reasonable since the lithium contents of the two alloys are similar. Fatigue precracking was performed in accordance with the ASTM standard at maximum loads of less than 40% of the limit load.

2.2.4.2. *Blunt notch tests*

Kahn tear test. Toughness of the superplastic 2090 sheet was assessed using a Kahn-tear type specimen. This test has been used to determine the relative toughness of various aluminum alloys in the past [Kaufman and Holt, 1965a, 1965b]. The test specimen is rectangular and contains a machined notch of small root radius that is not fatigue precracked. The loading line is coincident with the notch tip. Its selection was suggested by the small amount of material available. The tests were conducted in displacement control. The results of the test are reported as the tear strength, i.e. the load required to

---

[3] The only extant standard for J_{Ic} testing of structural materials at 4 K is "Proposed standard method for Fracture Toughness Testing of Austenitic Stainless Steels at Liquid Helium Temperatures," Fifth draft, September, 1987; U.S.-Japan Cooperative Program Committee on Test Methodology.

initiate crack growth from a sharp notch, and the unit propagation energy (UPE), which is the total energy required to propagate the crack. A moderately large data base exists for this test; however, direct comparisons with data obtained at other laboratories is difficult because variations in machine compliance and control mode appear to have a large effect on the results, particularly on the UPE. The test specimens, procedures and comparability of tests are discussed in greater detail by Verzasconi [1989]. Because of the difficulty of obtaining samples of uniform processing from the headbox, only the unformed superplastic sheet was examined. Single specimens machined to 1.6 mm (0.063 in) thickness were taken from the sheet parallel to and perpendicular to the final rolling direction and tested at room temperature and 77 K.

Charpy impact tests. Charpy impact toughness was measured using standard v-notched Charpy bars. Alloy 2090-T81 was tested between room temperature and 77 K in the L-T orientation.

Notched tensile tests. As a final measure of estimating toughness, sharp notched round tensile specimens were tested for 2090-T81 at T/2. The specimens were 0.5 in (12.7 mm) in outer diameter and 0.353 inches (9 mm) in diameter at the notch root and were threaded at each end. The notch was cut at a 60° angle and had a root radius of less than 0.001 inches. The test results are reported as a notched tensile strength/yield strength ratio. It should be noted that this test is highly sensitive to machine alignment. It is difficult to align the cryogenic testing apparatus used for this research to high precision when using threaded specimens.

2.3. Characterization

2.3.1. Slip lines

Slip line behavior was characterized by light microscopy, i.e. by examining the surfaces of deformed specimens polished prior to tensile straining. Both 2090-T8,-T4 (T/4) and the binary alloy were examined after straining specified amounts at different test temperatures. In all cases the slip lines appeared straight, indicative of planar slip found in these alloys due to the presence of the ordered δ' precipitate. Slip lines were examined using Nomarski interference contrast on an optical microscope. The non-uniformity of slip from one grain to another makes it difficult to characterize the slip line spacing.

2.3.2. Transmission electron microscopy

Specimens were prepared by mechanically grinding to 0.25 mm (0.010 in) and punching 3 mm disks. Double jet electropolishing was conducted at -30°C in 3:1 mixture of methanol and nitric acid. The polishing conditions were 18-20 V and 0.16-0.2 A.

2.3.3. Fracture morphology

Primary fracture mode was characterized using scanning electron microscopy of the fracture surfaces and by optically examining the profile of specimens polished in cross section.

Secondary splits perpendicular to the crack plane were characterized by sectioning the fracture specimen within 2 mm of the fatigue precrack perpendicular to the crack plane and crack propagation direction. The resulting surface was then highly polished to reveal the fracture surface profile and the splits that extended into the specimen. The location of the beginning and end of each split was digitized from optical micrographs taken at 50x of the entire 12.5 mm (0.5 in.) thickness of the specimen using a digitizing tablet. This information was used to compute the depth and spacing of each split. After it was confirmed that reproducibility was reasonable, only a single specimen and fracture profile were digitized for each material, orientation and test temperature. When the two sides of the narrow "v" that delineates a split were not of the same height, their midpoint was selected as the beginning of the split. Mean split spacings and histograms of split spacing and depth were computed for each specimen. Since the splits varied significantly in depth, mean spacings and histograms of spacings were also computed for subsets of the splits whose depths were greater than specified cut-offs (generally 0.1, 0.2 and 0.4 mm).

3. RESULTS: MECHANICAL PROPERTIES

The strength and toughness combination of 2090-T81 and 2091-T8 plate was the primary focus of the mechanical testing. As has been mentioned, the strength-toughness relationship is generally improving as temperature decreases for these two alloys. This increase is often accompanied by an increase in tensile elongation. A second characteristic of these materials worth noting is that their mechanical properties are quite anisotropic and that this anisotropy varies with test temperature. The behavior of the Al-Li binary, 2090-T4 and the superplastic thermomechanically processed 2090-T6 provide useful comparisons to these results. Strain hardening rate behavior will be mentioned briefly, but most of the data and discussion on this subject will be deferred to Section 4. Since 2219, in either the -T87 or -T51 temper, is the incumbent cryogenic tank alloy its properties are included in a final section that compares the mechanical properties of these alloys to provide a point of reference. The properties of 2090-T81 at room temperature are similar to those of 7075-T6, so the properties of this alloy have been included as well.

3.1. 2090-T81

The mechanical properties of 2090-T81 plate are anisotropic with respect to the plate thickness as well as with respect to the rolling direction. The in-plane (L and LT) strengths measured at T/2 are uniformly about 15% higher than those measured at T/4. The tensile elongation and its response to temperature also vary through the thickness. The ST specimens test the through-thickness properties of the plate and hence represent minimum values for the section of the plate near T/2 contained in the gauge. The fracture toughness measurements test the entire thickness in parallel and represent average values. The variation in through-thickness properties significantly complicates interpreting the results, particularly in a quantitative sense since it makes even defining the strength-toughness combination ambiguous. The through-thickness anisotropy in this material arises primarily from textural rather than compositional variations through the plate thickness. It is accentuated by the distribution of T_1 precipitates [Vasudévan, et al., 1988]. As was mentioned previously, this variation has been significantly reduced in currently available material.

The mechanical properties of 2090-T81 at T/2 in the plane of the plate are summarized in Table 3.1 and Figures 3.1 and 3.2. The yield strength, ultimate tensile strength, elongation and fracture toughness all increase with decreasing temperature. Although little or no necking was observed in the tensile specimens, it is believed that they all failed at or slightly beyond the point at which uniform elongation is unstable (recall that the necking criterion is $d\sigma/d\varepsilon = \sigma$, where σ and ε are the true stress and strain, respectively).

Tensile tests were also performed at T/4. The results of these tests are tabulated in Table 3.2. As mentioned above, the yield strength at this location was approximately 15% lower than that measured at T/2. Another significant difference is that the LT elongation decreases, rather than increases, with decreasing temperature. Strain hardening rate

calculations show that the necking criterion is satisfied at all four test temperature in the L orientation. However, in the LT orientation, it was satisfied at 300 and 200 K, but not at 77 K. The results of Chu and Morris [1989] for 2090-T8 sheet are similar to the results for 2090-T81 plate at T/4. They found that tensile elongation increased with decreasing temperature in the L orientation, but decreased in the LT orientation in 2090-T8 sheet; in the LT orientation the necking criterion was not satisfied at low temperatures.

TABLE 3.1 - Mechanical Properties of 2090-T81 at Various Test Temperatures.
Specimens taken at T/2. Test directions are given as tensile / fracture toughness test orientations. (TYS = Tensile Yield Strength; UTS = Ultimate Tensile Strength)

Test Direction	Temp. (K)	E GPa (Msi)	TYS MPa (ksi)	UTS MPa (ksi)	% Elong. Unif.	% Elong. Total	KIc(J) MPa√m (ksi√in)
L / L-T	300	78.3 (11.4)	535 (77)	565 (82)	5.0	11.0	34 (31)
	77	86.9 (12.6)	600 (87)	715 (104)	7.0	13.5	57 (52)
	4	87.6 (12.7)	615 (89)	820 (119)	17.0	17.5	72 (65)
LT / T-L	300	78.3 (11.4)	535 (77)	565 (82)	4.0	5.5	25 (23)
	77	86.9 (12.6)	625 (91)	695 (101)	5.0	5.5	37 (34)
	4	87.6 (12.7)	705 (102)	815 (118)	6.5	6.5	43 (39)

Note 1. $K_{Ic}(J)$ have been calculated using the correct elastic modulus E at each test temperature. They differ slightly from values in Glazer, et al. [1986] computed using the modulus at 300 K for all calculations.
Note 2. Strengths given to nearest 5 MPa; elongations given to nearest 0.5%.

TABLE 3.2 - Tensile Properties of 2090-T81 at Various Test Temperatures.
Specimens taken at T/4

Test Direction	Test Temp. K	TYS MPa (ksi)	UTS MPa (ksi)	% Elongation Uniform	% Elongation Total
L	300	455 (66)	490 (71)	5.5	5.5
	200	475 (69)	525 (76)	5.5	6.0
	77	525 (76)	625 (91)	14.0	14.0
	4	540 (78)	655 (95)	17.0	18.0
LT	300	530 (77)	565 (82)	5.5	6.0
	200	550 (80)	585 (85)	2.0	2.0
	77	560 (81)	600 (87)	3.0	3.0

Note. Strengths given to nearest 5 MPa; elongations given to nearest 0.5%.

The tensile properties of 2090-T81 in the ST direction are given in Table 3.3 and illustrated in Figure 3.3. The yield strength and fracture strength in the ST direction increase with decreasing temperature. This result is perhaps surprising; Dew-Hughes et al. [1988] found that the ST fracture strength decreased with decreasing temperature for 8090. However, it may stem from differences in composition and precipitation. The strengths lie between those those measured at T/4 and T/2 in the longitudinal direction. (The short gauge length means that only the material near the center of the plate is tested.) The ultimate tensile strengths given in the table are fracture strengths; the stress-strain curve was still rising steeply at failure. Some plastic elongation was measured for all specimens, but the small size of the specimens precluded an accurate measurement. In all cases the elongation was less than 5%.

TABLE 3.3 - Tensile Properties of 2090-T81 at Various Test Temperatures.
ST orientation

Test Temp. K	TYS MPa (ksi)	UTS MPa (ksi)
300	475 (68)	500 (73)
77	525 (76)	595 (86)
4	545 (79)	705 (102)

Note. Strengths given to nearest 5 MPa.

The anisotropy of strength in this material varies significantly with test temperature (see Figure 3.4). At T/2, while there is no L/LT strength anisotropy at 300 K and little difference between the ultimate tensile strengths at any temperature, at low temperature the yield strength in the LT direction is significantly elevated over the value in the L orientation. The variation is different at T/4. At this test location, the yield strength is greater in the LT direction than in the L direction at all temperatures. The ultimate tensile strength is also higher, until premature failure at low temperatures in the LT orientation prevents it. The relative change in strength with test temperature also differs. Clearly the presence or lack of strength anisotropy at 300 K is not a useful predictor of low temperature anisotropy.

The temperature dependence of the apparent toughness of 2090-T81 in blunt notch toughness indicator tests was also determined. Results are given in Table 3.4. The marked increase in fracture toughness at low temperatures in sharp-notch tests is not observed in blunt notch tests. Verzasconi [1989] found that the tear/yield ratio measured in Kahn tear tests of specimens at T/2 was roughly the same at 77 K and 300 K; the UPE increased fairly substantially at 77 K over the 300 K value. Charpy tests of this material (L-T oriented specimen) yielded similar results; only a slight increase was observed. However, the notched tensile to yield ratio declined somewhat at 77 K. In all three tests some splitting is visible.

TABLE 3.4. Notched tensile and Charpy properties of 2090-T81. Specimens taken at T/2. (NTS = Notched tensile strength)

Orientation	Test Temp (K)	NTS MPa (ksi)	NTS/YS	Charpy energy CVKM (CVFP)
L	300	510 (74)	0.96	0.59 (4.3)
	200	-	-	0.68 (4.9)
	77	525 (76)	0.87	0.71 (5.1)
LT	300	525 (76)	0.98	-
	77	440 (64)	0.70	-

Note. Strengths given to nearest 5 MPa.

3.2. 2091-T8

The mechanical properties of 2091-T8 are summarized in Table 3.5 and Figures 3.5 and 3.6. The most important result is that while the yield and ultimate tensile strength increase monotonically with decreasing temperature, the elongation and toughness do not. In both orientations there is a peak in elongation between room temperature and 4 K. The L-T fracture toughness is roughly constant between 200 and 4 K. However, the T-L fracture toughness increases monotonically between 300 and 4 K. Comparison of the strain hardening rate to the true stress shows that the low elongations are the result of premature failures; in the L orientation, the 300 and 200 K specimens necked and the 77 K specimen failed at instability; in the LT orientation only the 200 K specimens clearly failed beyond instability. In general, the combination of mechanical properties achieved for 2091-T8 is substantially inferior to 2090-T81 at T/2. However, the strength levels are comparable to those measured for 2090-T81 at T/4 in the L orientation. In this condition, 2091 is more isotropic than 2090 and the LT yield strengths in particular are exceeded significantly by 2090, at both T/4 and T/2. The greater isotropy of 2091 may result partially from the fact that the tests were performed on specimens taken from thicker plate.

3.3. 2090-T4

The tensile properties of 2090-T4 are given in Table 3.6. Due to the low yield strength of this material at all test temperatures, no attempt was made to measure the fracture toughness. A number of the results are interesting. Unlike 2090-T81, there is little yield strength anisotropy. This observation may lend support to suggestions by Vasudévan et al. [1989] and Lee and Kim [1989] that the strengthening precipitates accentuate the influence of texture on mechanical anisotropy, presumably because their distribution and morphology is correlated with the texture. Lee and Kim note that a tensile stretch prior to aging introduces an oriented distribution of dislocations that act as sites for heterogeneous nucleation. The uniform tensile elongation is also the same in the L and LT orientations. It

does not vary monotonically with temperature; the lower values in the L orientation measured at 200 and 4 K were reproducible. The necking criterion was apparently satisfied in all cases; however, the strain hardening rate dropped abruptly shortly before failure, rather than declining smoothly.

TABLE 3.5 - Mechanical Properties of 2091-T8 at Various Test Temperatures.

Test Direction	Test Temp. K	TYS MPa (ksi)	UTS MPa (ksi)	% Elongation Unifor	Total	KIc(J) MPa√m
L / L-T	300	440 (64)	480 (70)	5.0	6.5	24
	200	460 (67)	495 (72)	7.5	11.5	32
	77	495 (72)	565 (82)	10.0	10.0	32
	4	550 (80)	630 (91)	7.0	7.0	32
LT / T-L	300	430 (62)	465 (67)	2.0	2.5	22
	200	445 (65)	495 (72)	4.0	4.5	28
	77	485 (70)	535 (78)	2.5	2.5	33
	4	510 (74)	585 (85)	3.0	3.0	38

Note. Strengths given to nearest 5 MPa; elongations given to nearest 0.5%.

TABLE 3.6 - Tensile properties of 2090-T4 at various test temperatures.
Specimens taken at T/4.

Test Direction	Test Temp. (K)	TYS (MPa)	UTS (MPa)	% Elongation Uniform	Total
L	300	125 (18)	270 (39)	19.0	19.0
	200	140 (20)	275 (40)	15.5	17.0
	77	165 (24)	350 (51)	29.0	29.0
	4	210 (30)	465 (67)	23.5	23.5
LT	300	115 (17)	230 (33)	18.5	24.0
	77	165 (24)	355 (51)	28.0	29.0

Note. Strengths given to nearest 5 MPa; elongations given to nearest 0.5%.

3.4. Superplastic thermomechanically-processed 2090-T6

The tensile properties of superplastic thermomechanically-processed 2090-T6 are given in Table 3.7. Properties for the unformed sheet are plotted in Figure 3.7. The behavior of formed and unformed material is compared in Figure 3.8.

TABLE 3.7 - Tensile properties of 2090 sheet before and after superplastic forming. Strain ε is true strain during superplastic forming.

Specimen	ε	Test Temp. (K)	σ_y MPa (ksi)	σ_{uts}¥ MPa (ksi)	uniform elong. %
Sheet	0	300	315 (46)	415 (60)	4.2
		77	350 (51)	510 (74)	11.3
		4	415 (60)	650 (94)	25.0
Flange	0	300	310 (45)	405 (58.5)	4.4
		77	345 (50)	510 (74)	13.4
		4	370 (54)	600 (87)	17.0
0.75 mm	-1.0	300	285 (41)	380 (55)	5.1
		77	315 (46)	480 (70)	10.5
		4	370 (54)	450 (65)	2.0
0.50 mm	-1.4	300	260 (38)	360 (52)	4.8
		77	275 (40)	>415 (60)†	>5.6†
		4	240 (35)	490 (71)	19.0

¥ Engineering stress computed from highest measured load.

† Specimen thickness along gauge length was uneven. Elongation was non-uniform.

TABLE 3.8 - Results of Kahn-type tear tests on unformed superplastic sheet aged to -T6 condition.

(1 in-lb/in^2 = 0.175 kJ/m^2)

Test Temperature (K)	Orientation	Tear strength (MPa)	Tear/yield ratio	Unit propagation energy (kJ/m^2)
300	L-T	335	1.05	60
	T-L	310	1.00	65
77	L-T	350	1.00	--*
	T-L	360	1.00	25

* Invalid test.

The material showed decreasing yield and ultimate tensile strengths with decreasing thickness (and increasing amount of superplastic deformation) at all temperatures. This decrease is at least partially attributable to increased cavitation in more severely formed regions which may effectively reduce the load-bearing cross section of the specimen by ten or more percent of its nominal value. The yield strengths increase about 15% between room temperature and 4 K, while the ultimate tensile strengths increase somewhat more rapidly. The improvement in elongation between room temperature and 4 K is particularly striking and is a factor of six in some cases. The uniform elongation varies considerably between specimens, but does not appear to be greatly affected by thickness. The majority of the specimens failed without necking. However, analysis of the strain hardening behavior indicated that the specimens failed at the tensile instability point. The increased elongation at low temperature seemed to be associated with increased strain hardening rates at low temperature that postponed tensile instability.

The results of the Kahn tear tests are given in Table 3.8. Because the recrystallized microstructure is relatively equiaxed, the L-T and T-L properties should be roughly equivalent. Kaufman and Holt [1965b] have established a correlation between K_c and UPE for a number of 2XXX and 7XXX alloys. Although the limited data set precludes firm conclusions, the K_c apparently decreases, although not catastrophically. It is difficult to make numerical comparisons because the UPE measured if the test is performed using an elastically hard testing machine (used by Kaufman and Holt) is higher than the apparent UPE measured using an elastically soft machine (used in this work). Applying the correlation of Kaufman and Holt to these data therefore underestimates the K_c, perhaps considerably. It is of course possible that this correlation does not extend to aluminum-lithium alloys; there are other engineering correlations used with older aerospace aluminum alloys that do not work well with aluminum-lithium alloys [James and Rioja, 1989]. With these caveats, the K_c values are estimated to be > 80 MPa$\sqrt{m}$ at room temperature and > 60 MPa$\sqrt{m}$ at 77 K. The tear/yield ratio is also an indicator of toughness and does not appear to be very sensitive to temperature for this material.

3.5. Al-Li binary alloy

Tensile properties of the peak-aged binary aluminum-lithium alloy are shown in Table 3.9. The slight decrease in yield strength between room temperature and 77 K may not be significant, but the fact that the yield strength does not increase with decreasing temperature is consistent with the results reported by Miura et al. [1987] and Tamura et al. [1973] for single crystal and Furukawa et al. [1985] for polycrystalline binary aluminum-lithium alloys. The "ultimate tensile strengths" correspond to fracture strengths since the stress-strain curves were still rising at failure. The large increase at 77 K is due to the very large increase in elongation to failure.

TABLE 3.9 - Longitudinal tensile properties of Al-2.4Li alloy.

Test Direction	Test Temp. (K)	TYS (MPa)	UTS (MPa)	% Elongation Uniform	Total
L	300	275	345	3	3
	77	270	420	11	11

3.6 Comparisons with other high-strength aluminum alloys

To provide a standard of comparison for the data given above, Table 3.10 lists the cryogenic mechanical properties of 2219-T87, currently used for the external tank of the space shuttle, and 7075-T6, the standard for room temperature property goals for 2090 alloy development. The design philosophies being promulgated for cryogenic tanks now in the planning stages differ greatly, so it is not possible to specify a single combination of properties that would be optimum. However, the lower density and higher stiffness of aluminum-lithium alloys will ensure that they will be seriously considered, even if their mechanical properties prove to be less than ideal.

At room temperature, the properties of 2090-T81 at T/2 are similar to those of 7075-T6; this rough match in basic mechanical properties was the original alloy design goal set by the aluminum companies. At lower test temperatures, the elongation and fracture toughness of 2090 increase while they decrease slightly or remain flat for 7075. At 4 K, 2090 has a lower yield strength, but a higher elongation, ultimate tensile strength and (presumably) fracture toughness. (Fracture toughness data for 7075 at 4 K were not located.) At T/4, 2090 is 15% lower in strength than at T/2 and therefore is substantially weaker than 7075-T6.

2090-T81 is a higher strength material than 2219-T87, the current standard for a weldable cryogenic alloy. Even at T/4 it exceeds the strength of 2219 markedly, especially at 300 and 77 K. The fracture toughness at room temperature is similar and values for both alloys increase with decreasing test temperature. However, in the L-T orientation it increases much more rapidly in 2090, so that at 4 K the strength-toughness combination of 2090-T81 is far superior to that of 2219-T87. 2219 is a less anisotropic alloy than the 2090 plate investigated in this study; consequently, its fracture toughness in the T-L orientation may be higher than that of 2090. However, the LT strengths of 2090-T81 are very high at low temperature, and 2090 almost certainly has a far higher strength-toughness characteristic than 2219 even for the LT/T-L combination. The weldability of 2090 is of course critical if it is to replace 2219 for cryogenic tankage applications. The cryogenic properties of 2090 weldments have been investigated [Sunwoo and Morris, 1989ab], and while further research is needed it seems likely that the properties will be acceptable, at least in some designs.

TABLE 3.10 - Cryogenic mechanical properties of 2219-T87 and 7075-T651. The data have been assembled from various sources since single complete data sets are not available in the literature. (Tensile properties L orientation, fracture toughness L-T orientation unless otherwise noted.)

Alloy	Test Temp. (K)	σ_y MPa (ksi)	σ_{uts} MPa (ksi)	Total elong. %	K_{Ic} MPa$\sqrt{m}$ (ksi$\sqrt{in}$)	
7075	300	505 (73)[1]	600 (87)[1]	11[1]		30 (27)[2], 36 (3
	200	545 (79)[1]	620 (90)[1]	11[1]	-	
	77	635 (92)[1]	705 (102)[1]	9[1]	30 (27)[3], 27 (25)[6]	
	4	770 (112)[4]	830 (120)[4]	8[4]	-	
2219	300	385 (56)[5]	465 (67)[5]	12[5]	36 (33)[6]	
	77	460 (67)[5]	575 (84)[5]	14[5]	43 (39)[6]	
	4	510 (74)[7]	675 (98)[8]	15[8]	48 (44)[7]	

[1] Aluminum standards and data, The Aluminum Association, Inc., 1984.

[2] Malcolm, et al., 1986.

[3] McHenry, 1983.

[4] Kaufman and Wanderer, 1971. Yield strengths at lower temperatures are about 10% higher than in ref. 1.

[5] Kaufman, Nelson and Johnson, 1963.

[6] Kaufman and Holt, 1965a.

[7] Fiftal, 1978; Shepic and Fiftal, 1979.

[8] Kaufman, Bogardus and Wanderer, 1971. For 2219-T851, LT orientation; yield strength is 511 MPa.

The superplastic version of 2090 has somewhat lower strength than 2090-T81 plate, primarily because it not stretched before peak-aging (i.e. T6 rather than T8 temper). The yield strengths are lower than those of 2219-T87 at all test temperatures; however, at 4 K the ultimate tensile strength approaches that of 2219. This increase in tensile strength is accompanied by a very large increase in elongation from a value lower than that of 2219 at room temperature to one that is quite a bit higher at 4 K. Thus the 4 K properties of this material are more promising than its room temperature properties.

4. RESULTS: TENSILE BEHAVIOR

This section is the first of two that describe the results of characterization of the mechanical test specimens for which data are quoted in Section 3. This section will discuss deformation behavior, including strain hardening behavior (Sections 4.1-4.3), strain anisotropy (Section 4.1) and slip line observations (Section 4.4), while section 5 will consider relevant fracture behavior such as the fracture mode and profile. The strain hardening rate is a macroscopic average of the effects of numerous unit interactions between dislocations whose glide causes strain and the solutes, precipitates, grain and subgrain boundaries and dislocations that resist this motion. As such, the strain hardening rate should provide important information about the deformation process. Slip line studies using both optical and transmission electron microscopy represent an attempt to look at the results of these interactions on a more local scale, for example to investigate the homogeneity (or lack of it) of the deformation process.

As future sections will discuss, deformation behavior, particularly strain hardening behavior, plays an important role in understanding fracture as well as being important in its own right as a basis for understanding plastic forming and working processes of all kinds. The strain hardening rate (or the related n-value) is a parameter in most theories of strain-controlled fracture. It takes on great importance because it may vary over a large range. In a tensile test of a material that strains readily, the strain hardening rate determines the necking point and thus the ultimate tensile strength and uniform elongation. Despite its importance, the strain hardening behavior of polycrystals, and especially polycrystals with significant solute or precipitation hardening, is poorly understood. For this reason, it is difficult to interpret strain hardening behavior in complex commercial and semi-commercial alloys of the sort studied here in terms of its microstructural causes. The influences of temperature are partially understood, but their consequences are not. For example, it is known that temperature influences the dislocation substructure that develops during deformation; however, despite the fact that the differences are readily observable, it is not clear that they influence future strain hardening. There is also a significant dependence on texture that is reflected in the tensile strain anisotropy.

In accordance with the belief that strain hardening behavior is of considerable importance, the strain hardening behavior of all the alloys studied here was analyzed. The data collected in this investigation, along with some accompanying slip line observations, are presented in some detail, in spite of the lack of a guiding theory and therefore of clear conclusions. It is hoped that these data will be useful to future investigators. An attempt will be made to relate the data to some of the existing theories, with particular emphasis on the influence of temperature, in the discussion (Section 7.3).

4.1. Average deformation parameters

Two parameters that are often used to roughly characterize the forming behavior of metals are the strain hardening rate exponent, n, and a strain anisotropy factor, r, both defined in Section 2.2.3. Although neither of these parameters is actually constant during

deformation, the averages represented by these values provide some of the same information included in representations of the strain hardening rate or incremental strain anisotropy as a function of stress or strain, but in a much compressed form. Furthermore, for an idealized material the n and r values may be used to define a relatively simple constitutive relation that can be used to investigate the effects of these parameters in theories of deformation and fracture.

Table 4.1 gives *n* and *r* values for the materials whose other tensile properties are reported in Section 3, notwithstanding the drawbacks of *n* values as a measure of strain hardening. In general, the *n* value increases as temperature decreases. It is highest in the solution-treated and quenched 2090-T4, which has the lowest strength and the greatest amount of solute in solution. With the exception of 2090-T81 LT at T/2, the *r* values are all less than one, indicating that deformation was easier in the thickness direction than in the plane of the plate or sheet. Values of *r* less than one are typical of wrought aluminum alloys; however, values in the 0.1 - 0.2 range are very low and probably reflect the severe texture of the 2090 material. It is noteworthy that the *r* values were much higher at T/2 than at T/4 and that the anisotropy is inverted between the L and LT orientations at T/2. These variations almost certainly arise from the strong texture of the material. At T/2, (111) and (200) pole figure show a strong asymmetry of texture with respect to the L and LT directions that is not present at T/4. The intensity of the texture was also stronger at T/2 [Bretz, 1985].

TABLE 4.1 *n* and *r* values from tensile tests.

Alloy	Orientation	Test temperature (K)							
		n value				*r value*			
		300	200	77	4	300	200	77	4
2090-T81 T/4	L	0.06	0.07	0.15	0.22	0.18	0.18	0.17	0.11
	LT	0.07	0.04	0.08	x	0.11	0.12	0.22	x
T/2	L	0.05	x	0.11	0.13	-	x	0.51	0.42
	LT	0.04	x	0.05	0.06	-	x	2.48	2.38
2090-T4	L	0.35	0.26	0.42	0.45	0.18	0.18	0.16	0.13
	LT	0.17	x	0.24	x	-	x	-	x
2091-T8	L	0.04	0.07	0.10	0.11	0.39	0.22	0.26	0.26
	LT	0.04	0.05	0.05	0.05	0.36	0.21	0.29	(0.56)
2090-T6	sheet, flange	0.14	x	0.19	0.30	0.28	x	0.24	0.24
spf	0.75 mm	0.14	x	0.19	(0.25)	0.43	x	0.36	0.46
Al-2.4Li	L	0.14	x	0.32	x	-	x	-	x

Uncertainty: n values ± 15%; r values ± 20%; values in parentheses may be spurious
(x) = Condition not tested; (-) = Value not determined due to experimental difficulties.

4.2. Strain hardening rate behavior

Even in polycrystalline metals, three stages of deformation can be distinguished in the stress-strain curves of annealed pure materials (see Figure 4.1). Stage I refers to easy glide on a single slip system during which most of the dislocations leave the crystal; it is rarely observed in polycrystals. Stage II refers to a linear hardening region in which the dislocation density and strain hardening rate rise rapidly. In Stage III, mechanically and thermally activated softening processes such as cross slip take on increased importance and the strain hardening rate begins to decline as the balance between hardening and softening shifts. In a torsional test where geometric instabilities do not intrude a fourth (steady-state) stage may also be observed. Room temperature is a relatively high homologous temperature for aluminum, about one-third the melting point. At this temperature thermally activated recovery processes can occur readily. As a consequence, at room temperature Stage II is not observed for aluminum, even in single crystals; Stage I lasts for a very small strain and is followed directly by Stage III. Dilute alloys are generally in Stage III immediately. At lower temperatures, where thermal activation is more difficult, Stage I is extended and Stage II accounts for a significant portion of the deformation in single crystals and polycrystals of pure aluminum [Honeycombe, 1984; Cottrell and Stokes, 1955]. In both 2090-T81 and 2091-T8, the presence of dislocations and precipitates in the initial microstructure means that all deformation is Stage III even at 4 K. In the binary alloy and in 2090-T6, Stage II behavior is observed at low temperature, but not at room temperature.

To determine whether a tensile specimen failed before or after the necking criterion was satisfied, the strain hardening rate and true stress are compared as a function of true strain. Although this determination can in theory be made directly from the engineering stress-strain curve by identifying a peak strength, in many of the tests the stress-strain curve was essentially flat over a considerable strain range and the specimen did not neck observably. In these cases a numerical method is required to check whether the specimen failed prior to or at the point of geometric instability. There are two reasons to describe tensile failures according to whether or not the necking criterion was satisfied. Checking for satisfaction of the necking criterion provides a way of understanding the determinants of the uniform and total elongation and provides some insight into strategies for improving elongation. Similarly, comparing strain hardening rates for different materials or for different test temperatures as a function of strain is a way of rationalizing differing elongations. Secondly, whether or not the necking criterion is satisfied also provides a clue as to the potential ductility of a material, for example in other stress states in which there is no geometric instability. While materials that fail after considerable necking in tension may fracture in a brittle manner when a sharp crack is introduced, the converse is rarely true. An archetypical example is a ceramic, whose stress-strain curve will generally show little if any plastic deformation.

Since strain is not a thermodynamic variable (thermodynamic quantities describing the material cannot be given in terms of strain since they depend on the strain path), it is common in the literature to compare strain hardening rates as a function of true stress rather than true strain. Two presentations are used [Mecking, 1975]; either strain hardening rate

($d\sigma/d\varepsilon$) or the product $\sigma(d\sigma/d\varepsilon)$ is plotted as a function of the true stress. In the first presentation the effect of temperature on yield strength is easily eliminated by shifting the curves on the stress axis. However, the parameters in the second presentation are intended to relate to microstructural parameters. A simple theory of strain hardening predicts that the true stress is proportional to the dislocation density, while the product $\sigma(d\sigma/d\varepsilon)$ is inversely proportional to the dislocation glide length (mean free path). In this type of plot, the strain hardening rate increases linearly in Stage II, and begins to rise more slowly at the onset of Stage III. Kocks [1976] has argued that in both types of curves the stress and strain hardening rate should be normalized by the shear modulus, which is temperature dependent. This argument is reasonable since the shear modulus appears in almost any relation between stress and dislocation parameters. This procedure has not been used in the following; however, it would have the effect of shifting low temperature curves toward lower stresses and strain hardening rates. The asymptotic nature of the temperature dependence of the modulus on temperature at low temperatures means that the relative shift will be greatest at higher temperatures. Plots of $\sigma(d\sigma/d\varepsilon)$ vs. σ are not presented in the following since the information is readily derivable from plots of $d\sigma/d\varepsilon$ vs. σ. The $\sigma(d\sigma/d\varepsilon)$ plots do not appear to provide any new insight at the current level of understanding of strain hardening processes in complex polycrystalline materials; their principal use is to distinguish the onset of Stage III, but in the materials investigated here the transition often remains ambiguous.

4.2.1 Satisfaction of necking criterion

It is well known that binary aluminum-lithium alloys are plagued by low tensile elongation and fracture toughness. It is generally believed that the low ductility is a result of the large slip steps and concomitant stresses caused by the intense planar slip that occurs in these alloys due to the presence of δ' precipitates [e.g. Sanders, 1981; Flower and Gregson, 1987]. This brittleness is reflected in plots of true stress and strain hardening rate as a function of true strain for the Al-2.4Li-0.1Zr alloy. Figure 4.2 indicates that fracture in the L orientation occurs well before the necking criterion is satisfied. However, the plots also provide an explanation for the increased tensile elongation observed for this alloy at 77 K and perhaps for improved low temperature toughness. The gap between the strain hardening rate and the true stress at failure is much less at 77 K than at 300 K. In addition, as illustrated in Figure 4.3, the strain hardening rate at 77 K decreases much more slowly with both stress and strain than at 300 K, indicating a slower rate of work softening that probably reflects decreased strain localization. The 77 K plot appears to contain a small region (in terms of ε) of Stage II behavior. These results suggest that maintaining a high strain hardening rate would have a positive influence on the tensile elongation of this material.

Although substantial necking (and concurrently a noticeable difference between the uniform and total tensile elongations) was observed in only a few specimens, Figures 4.4-4.8 show that most of the 2090 and 2091 specimens failed at or near the necking instability point. This result is somewhat surprising in view of the failure of the binary aluminum-lithium alloy to satisfy this criterion. However, it is consistent with the alloy design strategy employed in developing Al-Cu(-Mg)-Li alloys, which included homogenizing slip

(presumably reflected in an increased strain hardening rate) as a major objective. The plate-like precipitate phases in these alloys are expected to promote slip homogenization.

The most direct comparison to the binary alloy is the 2090-T4 alloy since it is also hardened primarily by δ' precipitates, although the precipitates are much smaller and the presence of copper either in solid solution or as GP zones may have a significant influence. In both the L and LT orientations the failures seemed to occur at or shortly before the instability point. However, the decrease in the strain hardening rate seems to accelerate rapidly shortly before failure. One consequence of this phenomenon is that even though the strain hardening rate at 4 K was higher than that at 77 K for strains up to ~ 15%, the elongation to failure at 77 K was greater. It is possible that the sudden rapid decline in strain hardening rate can be interpreted as a transition from Stage II to Stage III, since $\sigma(d\sigma/d\varepsilon)$ increased slightly with σ prior to the downturn. In the LT orientation, the necking criterion was not satisfied at 77 K. All of these observations suggest that stress may be a more revealing parameter than strain. When the strain hardening rates are compared at each temperature as a function of true stress (Figure 4.9) it can be seen that the strain hardening rates at 77 K are similar for L- and LT-oriented specimens. At 300 K the strain hardening rate is consistently higher for the L orientation, but the slopes are almost identical, suggesting that the operative softening processes are the same.

The 2090-T81 strain hardening rates were characterized in detail for specimens tested at T/4. In the L orientation the necking criterion was satisfied at all four test temperatures. At 4 K, Stage II pure hardening behavior occurred at low stresses. In the LT orientation it was met at 300 and 200 K, but at 77 K the specimens appeared to fail shortly before instability. There was little difference between the L and LT orientations in the strain hardening rates as a function of true strain. However, when they are compared at constant true stress (Figure 4.10) several differences become evident. The strain hardening rate is consistently higher in the LT orientation. The separation is greatest at 200 K and least at 77 K. The rate of decline of the strain hardening rate with stress is also higher, especially at low temperature.

A similar trend was observed in the superplastic 2090-T6. The necking criterion was satisfied at all three test temperatures, except perhaps at room temperature (Figure 4.11). Like the binary alloy, this material showed a small region of Stage II hardening behavior at low temperature, in this case 4 K. As shown in Figure 4.12, the strain hardening rates of formed (0.75 mm) and unformed materials (compared as a function of true strain) were almost identical. At 4 K, the single formed specimen failed almost immediately, making any comparison difficult, but the trend appears to hold.

For 2091-T8, low elongations were a result of premature tensile failures. In the L orientation, the 300 and 200 K specimens necked slightly, while the 4 K specimens failed short of instability; uniform elongation increased between 300 and 77 K, but decreased at 4 K. In the LT orientation, only the 200 K specimen clearly failed beyond instability. As for 2090-T81, comparison of the strain hardening rate as a function of strain did not reveal significant differences between L and LT specimens. However, in plots against true stress (Figure 4.13), the strain hardening rate in the L orientation was higher at all temperatures

except 200 K and the decline in strain hardening rate with stress tended to be less steep than for LT specimens.

4.2.2. Influence of temperature and microstructure on strain hardening.

Many factors besides test temperature determine the rate of strain hardening. Strain hardening is increased by fine grain size, low stacking fault energy and incoherent precipitates. It is also influenced strongly by texture. The following strain hardening rate comparisons will be rationalized briefly where possible with current understanding. The effect of temperature is of greatest importance to this study and will be discussed in more detail in section 7.3.

4.2.2.1. Effect of temperature.

It has been previously reported [Glazer, et al., 1986, 1987ab, 1989] that the strain hardening rate as a function of true strain increases with decreasing test temperature for 2090-T81, 2090-T4, superplastic 2090-T6, Al-2.4 Li and 2091-T8 in a more limited set of orientations and test temperatures. Data for the complete set of tests is shown in Figures 4.14 and 4.15. However, it was found that at 300 K the strain hardening rate was often close to that at 200 K or even slightly below it. When the data are plotted as a function of true stress, the strain hardening rate in Stage III increases with decreasing temperature in all cases (Figures 4.16 and 4.17). This result is consistent with other studies on a variety of materials [e.g. Kocks, 1976]; it is a consequence of the increasing stress required for thermally activated processes to be operative.

4.2.2.2. Effect of temper (2090-T4 vs. -T81 (T/4)).

The strain hardening rates are compared as a function of temper in Figure 4.18 for L-oriented 2090 tensile specimens. When the strain hardening rates are compared with respect to strain, the -T81 strain hardening rate drops off much more rapidly than the -T4 at 300 K. However, at lower temperature the strain hardening rates are more similar between the two tempers, and the slopes are nearly the same although the -T81 values remain smaller than the -T4 values. These results are consistent with the interpretation that the strain hardening rate at low temperature and moderate strain is controlled by dislocation-dislocation interactions that are only weakly affected by the precipitates present. In the LT orientation, the trends are similar to the L orientation, although the low -T81 elongations make comparison more difficult. However, if the strain hardening rates are compared as a function of true stress (Figure 4.19), a different picture emerges. Due to its much higher yield stress, the strain hardening rates for the -T81 temper are much higher than for the -T4 temper at a given stress. However, below 300 K the slopes at each temperature are similar. The more rapid decline in the strain hardening rate with stress of the -T81 temper at room temperature must be attributed to a softening process that is more sensitive to thermal activation than the processes operative at lower temperatures, perhaps non-conservative processes such as climb around impenetrable obstacles. These results are consistent with data reported by Kelly and Nicholson [1963] on the effect of aging on Al-1.6 Cu (at. %) alloys aged at 190°C. They found that the strain hardening rate (as a function of stress)

increased with aging. A steep change occurred at peak strength where there was a transition from the coherent θ" precipitate to the partially coherent θ' precipitate.

4.2.3. 2090-T81 vs. 2091-T8

Comparison of strain hardening rate as a function of strain for 2090-T81 and 2091-T8 in the L and LT orientations are shown in Figure 4.20 and 4.21, respectively. Both alloys showed an increase in strain hardening rate with decreasing temperature. The strain hardening rates are quite similar; the data for 2090 are perhaps slightly higher, especially in the LT orientation. If the strain hardening rates are plotted as a function of stress (Figures 4.22 and 4.23) they are similar in the L orientation, while those for 2090 are considerably higher in the LT orientation. Because the S' precipitate in 2091 is not shearable, it was expected that the strain hardening rate of 2091 would be higher than that of 2090. The fact that it is not is probably a reflection of the higher yield strength of 2090.

4.2.4. Further comments

There are a number of theories that attempt to explain strain hardening behavior in Stage III. Most of these theories were developed to explain the behavior of single crystals of pure metals or dilute solid solutions. None of the theories are entirely satisfactory for polycrystals of these relatively simple materials. There is very little work on the behavior of alloys that are extensively precipitation-hardened. However, Mecking [1976] states that in Stage III the data in a plot of strain hardening rate vs. true stress should fall on a straight line at high stresses. This type of behavior has been observed experimentally in polycrystalline Cu and Ag. The data can be extrapolated to zero strain hardening and define a saturation stress that is predicted to be logarithmically dependent on temperature. This dependence is rationalized on the basis that the softening processes are thermally activated and require a certain stress level to take place. The dependence of the saturation stress on temperature is believed to be closely related to the stacking fault energy. However, inspection of the plots included in this section, for materials that should have approximately the same stacking fault energy, shows that the situation is somewhat more complex in these materials. For example, when L and LT data are compared, it can be easily seen that the different slopes as well as displacements with respect to stress in a plot of strain hardening rate versus stress could not result in similar slopes in a plot of saturation stress versus stress (although strictly speaking the data should be corrected for the effect of temperature on flow stress at constant structure by using the Cottrell-Stokes ratio).

Kocks [1976] has developed a semi-empirical model for the effect of temperature on Stage III behavior. He has noted that in Stage III, the strain hardening rate data lies on a straight line when plotted as a function of stress; the slope of the line decreases with decreasing temperature (less negative). This behavior is rationalized by assuming that ease of cross slip, controlled by stress and temperature, determines the slope. For pure fcc polycrystals the lines extend back to a constant value of the initial strain hardening rate $(d\sigma/d\varepsilon)_0$ of $\tau/G \sim 0.06$; for a more complex alloy the intercepts were found empirically to lie between 0.05 and 0.08. The data obtained here shows the expected linear behavior and slope change with temperature, but extrapolate to values between 0.04 and 0.1 rather than to a constant

value. Thus these data are generally consistent with Kock's empirical work hardening law. Kocks has also observed that in tension the curves often flatten out shortly before the necking criterion is reached; this phenomenon is not well understood. Similar results were observed in some instances in this study.

4.4. Slip line observations

Surface slip lines provide a macroscopic view of the deformation process. Increased homogeneity of slip lines at low temperature has been observed previously in aluminum alloys [see Cottrell and Stokes, 1955]. Most of the observations in this study were performed on L-oriented 2090-T4 specimens because it was hoped that comparisons at large strains would make any differences due to test temperature more apparent.

2090. Examination of slip lines on tensile specimens (T/4) polished before deformation shows clearly the coarse planar slip found in 2090 (see Figure 4.24-4.26). As Figure 4.26 shows, slip lines may cross grain boundaries. In most regions, one or two slip variants are visible. In some grains there is considerable out-of-plane rotation, especially after large strains (see Figure 4.25).

Comparison of specimens deformed similar amounts at different temperatures does not reveal a striking change. However, as shown in Figure 4.27, the surfaces of the specimens deformed at low temperature seem rougher. This trend was observed after 2, 8 and 16% strain in 2090-T4 and after 2% strain in 2090-T81 (all L orientation). The roughest regions correspond to areas where subgrains or fine grains at grain boundaries deform independently (see Figure 4.25) Slip in these areas was much finer than in adjacent grains. In general, the surface after a given amount of strain was rougher for 2090-T81 than for 2090-T4. LT-oriented 2090-T81 specimens were considerably less roughened after straining than their L-oriented counterparts and showed a propensity for slip across boundaries. These results suggest that there may be a correlation between increased surface roughening and increased elongation at low temperature.

It is difficult to compare slip line spacings because the slip patterns differ much more from one grain to the next than between aging conditions, orientations and temperatures. Etch pits could potentially be used to overcome this difficulty by making it possible to identify the grain orientation with respect to the tensile axis. Slip line spacings were measured from enlargements of photographs of regions in which the slip lines were similarly oriented with respect to the tensile axis; these regions probably correspond to grains of similar orientation. Slip step height could also be important, but was not determined in this study. No consistent change in spacing with temperature was determined by this method. The average spacing of the coarse slip lines observable optically at magnifications of 1000X or less was 6-8 μm; the value tended to decrease with increasing strain. In a similar optical microscopy study of peak-aged binary Al-Li single crystals, Tamura, et al. [1973] did not observe a change in the slip line morphology or spacing with temperature. However, they did see an effect of temperature in an accompanying TEM study.

2091. Figure 4.28 shows the slip line pattern in a 2091-T8 specimen strained 5% at room temperature. Slip in this material is noticeably wavier than in 2090. This result has been reported by others [e.g. Miller, White and Lloyd, 1987] and is a consequence of the fact that the S' precipitate cannot be sheared even at very high stresses.

Transmission electron microscopy. A limited amount of transmission electron microscopy was performed on samples taken from 2090-T4 samples after straining. A diffuse cell structure was observed to form after 16% strain at room temperature. A 77 K, this structure was less well-defined, while at 4 K a cell structure had not formed after 20%, although some dislocation banding was observed. The suppression of cell formation at low temperature has been observed in other alloys (Keh and Weissmann, [1963]; Welpmann, Lee and Peters, [1989]). Distinct slip bands were not discerned. Jata and Starke [1986] found in investigation of an Al-3.6Cu-1.68Li-1.16Cd-0.16Zr alloy that few planar slip bands were visible in the as-quenched condition; slip bands became progressively more well-defined with aging toward peak strength.

5. RESULTS: FRACTURE BEHAVIOR

5.1. Fracture mode

The most important result of the fractographic observations was that the primary fracture mode in both tensile and fracture tests of in-plane orientations of 2090-T81 and 2091-T8 was largely unaffected by test temperature. The similarity of the microscopic fracture behavior at all temperatures means that the effect of temperature on fracture toughness cannot be interpreted directly in terms of the fracture behavior. However, the nature of the fracture process still provides important insights into the microstructural determinants of the strength-toughness relationship. Many specimens had intergranular cracks (delaminations) perpendicular to the primary crack plane and to the crack front. The discussion in this section will be limited to the primary fracture mode; secondary cracking will be discussed in section 5.2.

The constancy of the fracture mode in 2090-T81 has already been reported [Glazer, et al., 1986, Glazer, et al., 1987a; Dorward, 1986; Rao, et al., 1988]. Figure 5.1 shows the fracture surface appearance of 2090-T81 J_{Ic} specimens as a function of test temperature. The fracture mode consists of transgranular shear linking intergranular fractures in the plane of the plate. The fracture mode in tension, shown in Figure 5.2, is basically similar at both T/2 and T/4, although the primary fracture mode was somewhat masked by the extensive delamination that occurred in some specimens. The fracture mode in the notched tensile specimens (Figure 5.3) was also similar.

The fracture mode of 2091-T8 has a woody appearance similar to that seen for 2090-T81, especially in tension (Figures 5.4 - 5.6). The fracture mode again appears to be transgranular shear linking intergranular failures perpendicular to the main crack plane. No mode change was observed in either orientation in tension or in the L-T fracture specimens. However, the fracture mode in the T-L orientation did change with temperature; cleavage-like flat facets were observed at room temperature which were not present at low temperatures. In addition, ductile dimples are present in greater abundance at 77 and 4 K (see Figure 5.6). The source of this transition is not currently understood, but the facets appear similar to those reported by Fager, et al. [1986]. A possible mechanism responsible for these facets proposed by Fager, et al. will be discussed in section 6.1.2.

The fracture surface in tension in the ST orientation of 2090-T81 was compared and contrasted with the delaminated surface in tensile specimens broken at 200 and 77 K. The macroscopic 2090-T81 ST tensile failure mode (pictured in Figure 5.7) appears similar to that observed for 8090 by Dew-Hughes, et al [1988]; it is very flat and occasional large intermetallic particles are visible. The fracture surface appearance changes somewhat between 300 and 4 K; at 300 K the fracture appears to be transgranular, at 77 K the fracture appears to follow the grain boundaries, at 4 K it contains some regions of intersubgranular failure. Surfaces along which delamination occurred in 2090-T81 (L orientation, T/4) at 200 K and 77 K are shown in Figure 5.8. The failure surface is similar but not identical to the ST tensile failure appearance at 77 K. It is macroscopically much flatter, but shows

much more evidence of plastic deformation prior to fracture. Most of the features are on the order of the subgrain size.

A significant fracture mode transition was observed in the superplastic 2090 material. Figure 5.9 shows the variation in the tensile failure mode as a function of temperature. Although the tensile elongation increases six-fold between 300 and 4 K, the tensile failure mode changes dramatically for the worse. At 300 K final failure was by transgranular shear. At 4 K the fracture was intergranular. At 77 K, both modes were observed. The failure modes in the Kahn tear specimens at 300 and 77 K were similar to the modes observed in tension.

The fracture mode in 2090-T4 and in the binary alloy had a somewhat different appearance. Figure 5.10 shows the failure surface appearance of 2090-T4 longitudinally-oriented tensile specimens. At 300 K the surface appears smeared, whereas at 4 K there are large flat features where it appears that decohesion has occurred at grain boundaries. At intermediate temperatures, particularly 77 K, there are some intergranular splits and transgranular link-up similar to what occurs in 2090-T81. Figure 5.11 shows the appearance of the failure surfaces of longitudinally-oriented samples of the Al-2.4 Li material. Failure occurred by ductile dimple rupture at 77 K, without benefit of splitting. At room temperature, the failure occurred by a more complex shear mode and appeared to be intersubgranular in some places.

5.2. Intergranular splitting

Secondary cracking ("delamination") along short-transverse planes perpendicular to the fracture plane occurred in all L-T and T-L compact tension fracture toughness specimens. This splitting was examined in detail for 2090-T81 and 2091-T8, the two materials on which J_{Ic} tests were performed. In each specimen, the splits varied in depth and spacing along the fracture profile. There were a relatively small number of very deep splits with a much greater number of splits of lesser depth at varying intervals between them. Splitting was also visible in tensile failures of 2090-T81 and 2091-T8 and was very pronounced at some temperatures. A few shallow splits were visible in tensile failures of 2090-T4 at 200 K and below; the failure at room temperature was a smooth shear surface. Splits were also visible in tensile specimens of the binary alloy. No splits were observed in failures of the fine-grained superplastic 2090-T6 at any temperature in either tensile or Kahn tear specimens.

5.2.1. 2090-T81

Figures 5.12 and 5.13 illustrate the overall pattern of splitting in tensile and compact tension fracture toughness specimens of 2090-T81, respectively. Figure 5.14 shows that the splits are intergranular. The timing of splitting with respect to the main fracture was investigated for both types of specimens. Specimens tested at 77 K were selected since splitting was especially prevalent at this temperature. In tensile specimens, splitting seems to occur immediately before failure when a triaxial stress state is achieved as

necking begins. Figure 5.15 is a cross section of a specimen strained short of failure. No splits are visible at this stage although the final fracture shows many deep splits. This result is consonant with the fact that the r-ratio for this specimen is substantially less than one. A low r-value means that the specimen thins easily, making tensile stresses through the thickness that would drive splitting unlikely until the necking criterion is reached. Figure 5.16 is an optical micrograph of a section immediately above the crack plane in a compact tension specimen in which the crack has propagated only a short distance at 77 K. Several similar sections of this specimen ~0.4 mm apart were also studied to obtain a three-dimensional view of the splitting pattern. The splits are fairly regularly spaced and extend 0.5-1.0 mm away from the main crack plane. They extend beyond the tip of the primary crack for a distance of up to 5 mm, which is on the order of the plastic zone size. The splits corresponded to the region in which sufficient plasticity had occurred that the grain structure was noticeably distorted in a polished and etched cross section at the center of the specimen (taken along an L-LT plane). The split lengths in this specimen varied from 1-5 mm ahead of the crack. The deepest splits were generally the longest; many splits were about twice as long as deep. The significance of these observations will be considered in the next chapter.

The splitting behavior in the fracture toughness specimens was characterized as a function of test temperature. Figure 5.17 is a sample schematic profile of the fracture surface obtained by digitizing the locations of the splits for an L-T specimen tested at 77 K. Figure 5.18 is a histogram for splitting depth for the same profile. A depth histograms for the corresponding T-L specimen is shown for comparison. The splits in the T-L specimens were generally not as deep as in the L-T specimens. The most obvious reason for this behavior is that the grains are not as long in the splitting direction in the T-L specimens. A second reason may be that the fracture toughness, and therefore the applied stress intensity that provides the stress that causes splitting, is also lower. The low S-L/S-T fracture toughness of this material suggests that once an intergranular split is initiated it can propagate easily along the length of the grain boundary and will do so as long as the through-thickness stress (σ_z) is high enough. Even if σ_z remains high, since the main crack propagates transgranularly, one might expect that there would be few splits longer than the relevant grain dimension and that most splits would be about half of that value. Additional scatter would be introduced by the variability of the grain size. The mean grain size in this material is approximately 2 mm x 0.4 mm x 0.025 mm. The mean split depths are all much less than the grain dimensions. The deepest splits observed were 0.65 mm at 300 K, 0.9 at 77 K and 0.95 at 4 K in the L-T direction. In the T-L direction the deepest splits were .45, 0.8 and 0.95 mm, respectively. Thus although there was a difference in the frequency of the deepest splits (and in mean split depth), there was little difference in the maximum depth with respect to orientation. The values for L-T split depths were well within the long dimension of a typical grain. However, the similarity of the results in the T-L direction means that the splits extended for more than one grain. Since there is fairly good alignment between grains, this result may not be surprising. However, it does suggest that the depth of the splits is controlled by the drop-off in σ_z as the split propagates away from the main crack.

Figure 5.19 shows the variation of mean split spacing for various minimum split depths as a function of test temperature for L-T and T-L specimens. The measured mean split spacings are 1.5 - 2 times higher in the L-T direction than in the T-L direction for all minimum split depths (note the change in x-scale in the figure), indicating that the frequency of deep splits is greater for L-T specimens. The most important results illustrated in the figure are 1) that the mean split spacing varies with test temperature, 2) that the magnitude and direction of this variation depend on the minimum split depth considered and 3) that although the mean split spacings are greater for T-L than L-T specimens, the general trends are similar. Several authors [Dorward, 1986; Rao, et al., 1989] have stated that split spacing decreases as temperature decreases in this alloy. These results are based on tests performed at 300 and 77 K. However, the approximate average split spacings quoted by Rao, Yu and Ritchie [1989] agree closely with the mean split spacings determined here for splits of minimum depth of 0.4 mm. This agreement suggests that these authors considered only the deepest splits to be significant (perhaps a reasonable, although implicit, assumption since the deeper the split, the greater the expected effect on the stress state). However, for the deepest splits, the trend reverses and the mean spacing is greater at 4 K than at 77 K in both test orientations. When the shallower splits are included, either a slight decrease or a slight increase in spacing is observed depending on the minimum split depth considered.

The trends in the spacing of deep splits in the compact tension specimens are paralleled by the behavior of the tensile specimens. As illustrated by Figure 5.12 for 2090-T81 specimens tested at T/2, splitting was much more pronounced at 77 K than at either 300 or 4 K. The large "splinters" where the crack path followed a split for a large distance are particularly noteworthy. The same pattern was observed for specimens tested at T/4, with splitting being especially prevalent in specimens tested at 200 and 77 K. In both locations the difference in the amount of splitting was much greater for the tensile specimens than for the fracture toughness specimens.

Splitting was also observed in the fracture surfaces of the notched tensile specimens. There appeared to be more splitting at 77 K than at 300 K, though the difference was much less than in other types of tests. However, the fracture surface was macroscopically flatter at 77 K, particularly in the L orientation; the 300 K specimens had more regions where the crack path followed a split for a long distance.

5.2.2. 2091-T8

Like 2090-T81, 2091-T8 splits intergranularly under a through-thickness stress. Figure 5.20 illustrates the overall pattern of splitting in the 2091-T8 compact tension fracture toughness specimens. The splits in the T-L specimens were again shallower than in the L-T direction although the difference was not as great for 2091 as for 2090. In general the splits were deeper than those observed for 2090 in the same orientation and at the same test temperature. The tensile failures also showed splitting at all test temperatures. The trend in amount of splitting appeared to be the same as in the J_{Ic} specimens. However, the dramatic splitting and large delamination surfaces observed in 2090-T81 tensile specimens were not observed in this alloy.

The variation with test temperature of mean split spacing in the compact tension specimens with test temperature as a function of minimum split depth for 2091 is shown in figure 5.19. The split spacings generally decrease with decreasing temperature. In the T-L orientation and for large split depths in the L-T orientation, most of the decrease in split spacing occurs between 300 and 200 K. This observation remains true if splits deeper than 0.6 mm are considered. At 300 K the mean split spacing is more than twice as large for T-L specimens than for L-T specimens, except for the shallowest splits. However, unlike 2090-T81, at lower temperatures the split spacings are about the same.

5.2.3. Summary

The observed variation in mean split spacing with temperature discussed above provides a basis for a more detailed analysis of the potential effects of splitting on fracture toughness that will occur in the next chapter. For 2090-T81 in both the L-T and T-L orientations the fracture toughness increases with decreasing test temperature. The elongation increases as well in both the L and LT orientations at T/2 and in the L orientation at T/4. In all cases, the improvements are greatest in the longitudinal (L or L-T) orientation. For this alloy, when shallow splits are included, the split spacings are less than ~ 1 mm and do not vary much with temperature. The variation between 77 K and 4 K is especially small. Thus if splits have a significant effect it must come from the more significant variations in spacing observed for deeper splits (L-T: > 0.4 mm, T-L: > 0.2 mm, > 0.4 mm). For both orientations, the split spacing for splits of depth > 0.4 mm increased between 77 K and 4 K. While the small number of splits measured means that there is some uncertainty in these measurements, it seem safe to say that the split spacing did not decrease. Since the mechanical properties (E, K_{Ic}, σ_y, ε_f) vary monotonically with temperature, it appears that split spacing cannot explain the difference in fracture toughness between 77 K and 4 K.

Similarly, for 2091-T8 the variation in split spacing with temperature observed for these specimens does not appear to correlate with the measured fracture toughness. While the split spacing decreases monotonically with decreasing test temperature, the fracture toughness in the L-T orientation is flat between 200 and 4 K and tensile elongation peaks between 300 and 77 K. In the T-L orientation the decrease in split spacings with decreasing test temperature parallels a monotonic increase in the fracture toughness. However, the extent of the increase in fracture toughness is less than in 2090 although the decrease in split spacing is much greater.

The fracture path or profile between the splits is also of interest. If it is at 45° to the loading direction, the specimens are relatively near plane stress, whereas if it is relatively flat the stress state retains some triaxiality, although it is no longer plane strain. Rao and Ritchie [1989] have suggested that there is a transition in 2090-T81 between 300 and 77 K from flat to slant fracture. The micrographs shown in Figure 5.13 do not bear this out. In 2091-T8 in the L-T orientation (Figure 5.20) the longest shear facets occur at 300 K and the fracture at 4 K probably has the flattest profile between the splits. Other ways of viewing the effect of the fracture profile will be considered in the next section.

6. DISCUSSION: THE EFFECT OF (CRYOGENIC) TEMPERATURE ON FRACTURE TOUGHNESS

Several models have been proposed to account for the variations with test temperature of fracture toughness of aluminum-lithium alloys at ambient temperature and below. These models are not mutually exclusive; all probably play a role for at least some alloys and orientations in some temperature regimes. The debate has centered on the relative importance of each factor in determining the fracture toughness of aluminum-lithium alloys, especially 2090-T81. This discussion attempts to define and defend a hierarchy of factors that determine the variation in in-plane (L-T and T-L) fracture toughness with test temperature. Several perspectives are possible. The one chosen here is that of the alloy developer; to the extent possible the mechanisms are phrased in terms of microstructural variables that could potentially be manipulated to achieve improved strength and toughness at cryogenic temperatures. Consequently, the models described below are evaluated for their usefulness in understanding the effect of (low) temperature on the fracture toughness, a little studied topic for aluminum alloys, and not for their value in interpreting the mechanisms that affect the fracture toughness equally over a broad range of temperatures, a much more heavily studied topic.

The proposed determinants of the variation in fracture toughness at cryogenic temperatures can be grouped into four categories. The most obvious factor is the effect of a primary fracture mode transition. A second phenomenon of importance is the occurrence of secondary cracking or crack-dividing splitting. Here, useful comparisons can be drawn to studies of controlled-rolled steels. Thirdly, liquid metal embrittlement has been suggested as an explanation for some of the experimental observations. Finally, the effect of increased strain hardening, ductility and yield strength on strain-controlled fracture has also been postulated as an explanation for the observed behavior. Each of these models is discussed below as it applies to the data obtained in this and other studies of the cryogenic behavior of aluminum-lithium alloys. The effect of splitting on fracture toughness is the most controversial area and is accordingly devoted the greatest weight in the following discussion.

6.1. Primary fracture mode change

When a change in the primary fracture mode occurs in response to a change in test temperature, this mode change will dominate the fracture toughness response. This transition must be traceable to the effect of temperature on more fundamental microstructural processes. A dramatic mode change, for example the transition observed in some steels from ductile dimples to brittle intergranular cleavage, may occur over a very narrow temperature range and cause a drastic decrease in fracture toughness. In general, fcc materials do not exhibit a sharp ductile-brittle transition or an abrupt change in fracture mode. In the alloys investigated in this study, in most cases the primary fracture mode was not strongly affected by the test temperature. However, there were two cases in which a fracture mode transition was observed and in each case the variation in fracture toughness with test temperature was consistent with the expected effect of this mode change. The

materials in which these transitions occurred were superplastic 2090-T6 and 2091-T8, T-L orientation.

6.1.1. Superplastic 2090-T6

This equiaxed fine-grained material displayed a clear ductile-brittle fracture mode transition. Fracture at room temperature was by ductile transgranular shear. Failure at 4 K was intergranular. At 77 K the fracture was mixed mode. In apparent accordance with this unfavorable change in fracture mode, the toughness decreased substantially between room temperature and 77 K. The higher strength of the alloy at low temperature evidently was sufficient to cause a transition to intergranular fracture in spite of a marked increase in tensile elongation. This contrast underscores the importance of the primary fracture mode in determining the fracture toughness even when other sometimes indicators of toughness such as work to failure in a tension test apparently increase. These tests were performed on thin sheet, the fracture mode transition would probably occur at a higher temperature in thicker samples in which the maximum tensile stress would be elevated by the increased constraint.

6.1.2. 2091-T8 T-L

For alloy 2091-T8, T-L orientation, the fracture mode transition is to a relatively more ductile mode at low temperature. Cleavage-like facets were noted in 2091 T-L specimens at room temperature and the increase in fracture toughness at lower test temperatures is associated with their disappearance. Cleavage fracture is rare in aluminum alloys and f.c.c. materials in general. However, the fractographic observations are similar to observations reported by Fager, et al. [1986]. The cleavage facets they describe are almost identical in appearance to those observed in this study. Fager, et al. observed these facets in 2090 and in Al-Li-Cu-Mg alloys in as-quenched, underaged and peak-aged tempers in both tensile and bend specimens. The facets were found to be transgranular and to lie along {100} and {110} planes. They disappeared at low test temperatures and high strain rates. The temperature and strain rate sensitivity of the effect led Fager et al. to conclude that diffusion of an embrittling species was an important component of the effect. The embrittling species was not conclusively identified, but is probably either Na, K or Ti. In other systems, such cleavage has been associated with low melting point eutectics [Webster, 1986,1987].

6.1.3. Other studies

Other studies of aluminum-lithium alloys have shown that the toughness decreases when the fracture mode changes from a ductile to a brittle mode at low test temperatures. Rao et al. [1989] studied the trends in fracture toughness with test temperature in a large number of aluminum-lithium alloys. Alloys 2091-T8X, 8090-T8X and 8091-T8X all displayed a fracture mode transition between 300 and 77 K from ductile dimple rupture to the transgranular shear mode linking intergranular delaminations that is typical of 2090-T81. The fracture toughness decreased concurrently for all three alloys. The other alloys they tested did not show a primary fracture mode transition; the fracture toughness of these alloys increased with decreasing test temperature.

6.2. Crack-dividing splitting

The objective of this section is to attempt to elucidate the role of splitting in the observed changes in fracture toughness with test temperature. In particular one would like to know what trends would be expected in identical material that does not split, i.e. whether there is a trade-off between short-transverse and in-plane properties with respect to the influence of test temperature on fracture toughness. A separate question that is not the focus of this discussion is whether such a trade-off exists with respect to the fracture toughness at any given temperature. The discussion is divided into four sections: the possible consequences of splitting, the current view of the effect of splitting in other materials, especially controlled-rolled steels, the potential causes of splitting and an interpretation of the observations on aluminum-lithium alloys in the light of these comments are each considered in turn.

6.2.1. Possible consequences of splitting

Calculation of the fracture toughness of a compact-tension specimen with crack-dividing splits is an inherently three-dimensional problem. Since the secondary cracks (splits) intersect the main crack, there are discontinuities in two dimensions. In addition, the presence of internal free surfaces will affect the size and configuration of the plastic zone. Thus the effect of the splits and of the residual elastic constraint of the unsplit ligament cannot be solved exactly without a major computational effort, if at all. Consequently, it is not possible to quantitatively predict the difference in the fracture toughness of a laminate and a specimen that is monolithic everywhere except in a zone around the crack on the order of the plastic zone size.

Two related mechanisms have been proposed through which crack-dividing splitting could affect the measured fracture toughness. The most obvious is through the stress state in a manner analogous to the effect of specimen thickness on toughness. The second way is through the fracture morphology or profile, if splitting causes a transition from flat to slant fracture.

6.2.1.1 Effect of spacing via stress state

6.2.1.1.1 Qualitative arguments

The effect of splitting on measured fracture toughness is due to the local relaxation of the elastic constraint in a nominally plane strain specimen. In effect, crack-dividing splitting alters the effective thickness of the specimen locally by providing internal free surfaces that help to relieve the through-thickness stress. It is not known to what extent the through-thickness stresses are relieved, as the splits seem to extend only through the plastic zone and the elastic constraint outside that region remains. However, an upper limit on their impact can be obtained by considering the specimen to consist of lamina whose thickness corresponds to the major split spacing. The following discussion considers this upper limit and therefore probably somewhat overestimates the consequences of the

splitting. The possible consequences of splitting under this assumption on the measured fracture toughness will be considered in the first part of this section. The validity of the assumption and appropriate modifications will be considered afterward.

It is well-known that the Mode I K_c value is dependent on the thickness of the test specimen. Beyond a critical thickness, the fracture toughness is approximately constant; this region is referred to as plane strain and the value of the fracture toughness as K_{Ic}. As the specimen thickness decreases, the K_c value rises and eventually reaches a peak at a very small thickness, the maximum thickness at which plane stress is fully developed. Below this thickness, K_c may be constant, increase or decrease. This discussion will concern the estimation of K_c in the transition region between plane stress and plane strain and attempt to relate the variation to the effect of crack-dividing splitting.

The thicknesses that define the extent of the transition region are related to the plastic zone size. In plane strain, the plastic zone size is small with respect to all specimen dimensions including the thickness. Although the surfaces of the specimen remain in plane stress (σ_z = 0) and may develop shear lips, they perturb the measurement of the bulk plane strain properties of the material very little. The critical thickness that defines plane strain will be referred to as B_I. The maximum thickness at which plane stress is fully developed, B_O, is approximately twice the plane stress plastic zone size. The K_c curve for monolithic specimens of varying thickness B will be referred to as $K_c(B)$.

The driving force for splitting is the through-thickness stress σ_z. Presumably splits occur when this stress exceeds a critical value. The minimum split spacing B_S will occur when the specimen is nominally in plane strain since the potential value of σ_z will be maximized. The measured K_{Ic} will correspond to $K_c(B_S)$. For a specimen of total thickness less than B_I, the split spacing should increase since the through-thickness stresses will be lower. It seems likely that the peak σ_z in the specimens after splitting will be the same and that the fracture toughness will be approximately invariant with thickness in this regime. For specimens nominally in the transitional thickness regime, K_c would be measured as $K_c(B_S)$, the apparent K_{Ic} value. At thicknesses less than ~$2B_S$, one would expect no splitting (insufficient through-thickness stress) and an increasing value of K_c with further decreases in specimen thickness. Below ~$2B_S$ the curve for materials which splits should be the same as that for an otherwise identical material that does not split.

The key question in this analysis is how the $K_c(B)$ curve of a material that splits can be used to predict the fracture toughness of the same material with different split spacing and perhaps somewhat different tensile properties (in this case due to different test temperature). Under the assumption of independent lamina, if the material properties were identical it should be possible to obtain a particular K_c value corresponding to the split spacing from the $K_c(B)$ curve of the monolithic material or a material with a significantly larger split spacing. This K_c value is the predicted apparent K_{Ic} value for the split spacing in question. However, any change in material properties that alters the fracture behavior will affect this identification of the fracture toughness of the more finely split material with a point on the $K_c(B)$ curve of the widely split or unsplit material. The influence of the yield strength and stress intensity through the plastic zone size on the stress state is obvious.

However, any changes in elastic modulus E and elongation to failure ε_f will also have an effect. Therefore, in order to obtain the expected fracture toughness of a new, lower split spacing from the $K_c(B)$ curve for $B<B_s$, the curve must be parametrized according to the stress state and materials compared when they are in the same stress state rather than at the same thickness.

Because of the change in stress state possible due to a change in test temperature, it is possible for an observed decrease in split spacing between 300 and 77 K to correspond to an increase or decrease in the true K_{Ic} of the material or to no change at all (see figure 6.1). This highly schematic argument has little theoretical justification, but it can be phrased in a more quantitative way using one of several models for $K_c(B)$ in the transition region. The predictions of these approaches will be examined in the next section.

For 2090-T81 the difference in properties between 77 K and 300 K is fairly substantial and has significant consequences in interpreting the effect of splitting. The usual way of parameterizing the stress state with thickness is to use the ratio $(K_{Ic}/\sigma_y)^2 \propto r_p$ as in the ASTM standard. In this case the true K_{Ic} for material that does not split is an unknown. As a result it is difficult to compare the stress states at the two temperatures even in an average sense. In addition there must be some effect of the splits on the local plastic zone size. These uncertainties make it difficult to qualitatively predict the effect of the number or depth of splits on the measured fracture toughness.

6.2.1.1.2 Quantitative models of fracture toughness in intermediate stress states

Since the implications of a change in split spacing are not qualitatively obvious, several models were investigated that predict the elevation of K_c (Mode I) over K_{Ic} with decreasing specimen thickness. Of these, the model by Broek and Vlieger [1974] lends itself best to evaluating this problem and will be discussed in more detail below. Sih and Hartranft [1973] have attempted to evaluate the effect of thickness by allowing the stress intensity factor to vary through the thickness along the crack front. Anderson [1969] suggested that the decrease with thickness of K between plane stress and plane strain is linear; the toughness values predicted by this model lie above those of the other models everywhere. All of these models are applicable only under the assumption that the regions between splits act as independent specimens of the same thickness and therefore must overestimate the effect of splitting.

Broek and Vlieger [1974] developed a relation between K_c and K_{Ic} in the transitional regime between plane stress and plane strain (see Appendix 2 for derivation). The formula applies only to thicknesses greater than the maximum thickness for which full plane stress is developed, B_o. The relation is:

$$\frac{K_c}{K_{Ic}} = \sqrt{1+\frac{B_o}{B}\left(\frac{\varepsilon_f E}{24\sigma_y}\right)} \qquad (6.1)$$

where

ε_f is the true strain-to-failure in uniaxial tension
E is the elastic modulus
σ_y is the yield strength
B_o is the maximum thickness at which full plane stress is developed
B is the (effective) specimen thickness
K_c is the fracture toughness for a specimen of thickness B
K_{Ic} is the plane strain fracture toughness.

This model suggests that not only does the shape of the $K_c(B)$ curve depend on the yield strength and K_{Ic}, it also depends on other material properties such E and ε_f that vary with temperature as well. The value of B_o also depends on the test temperature.

The remaining difficulty in applying the model is determining an appropriate value for ε_f, which depends on stress state. Some of the problems involved in determining ε_f are discussed in Appendix 3. In their study of aluminum-lithium alloys, Rao, et al. [1989] suggest using ε_f measured in uniaxial tension ($\sigma/\bar{\sigma} = 0.3$) although their calculation appears to use ε_f for $\sigma/\bar{\sigma} = 0.8$. However, it is unclear what the correct choice of ε_f really is since it depends on the complex stress state at the crack tip and perhaps also on the fracture mechanism. Ideally, it should probably be adjusted with B to account for these changes. The split spacing is assigned to the value of B. Furthermore, the values of B_o and the other material parameters will be functions of the test temperature.

6.2.1.1.3 Maximum effect of splitting

Recently Chan [1989] has attempted to predict the maximum influence of crack-dividing splitting on toughness. The model considers only the effect of splitting on the stress state. His model of "thin sheet toughening" assumes that delamination throughout the fracture process zone is equivalent to full delamination (as has been assumed in the last two sections). He does not consider the effect of split spacing since he attempted to find an upper limit only. He begins from a relation between K_{Ic} and the crack tip opening displacement (CTOD) δ_c similar to that given by Isherwood and Williams [1970] (see Appendix 1, eqn A1.8) and by relating the CTOD to the effective strain to failure and the size of the process zone arrives at the relation:

$$K_{Ic} = \sqrt{\frac{E\sigma_y\bar{\varepsilon}_f n^2}{\alpha(1-\nu^2)}} \tag{6.2}$$

where α is a constant of order 1 and $\bar{\varepsilon}_f$ is the effective strain that corresponds to the true strain-to-failure in the applicable stress state. Failure is postulated to occur at a critical effective strain.

In many materials the effective fracture strain under plane strain deformation is approximately one-third the value obtained in uniaxial tension, so this analysis predicts that the maximum increase in K_{Ic} due to delamination is $\sqrt{3}$ or about a factor of 1.7. This effect is slightly larger than the prediction of equation 6.1 for values of the material properties reasonable for 2090-T81 at room temperature. The experimental effects Chan

interprets as due to splitting are about half of what he predicts; he attributes the difference to the fact that the entire specimen is not split.

It should be noted Chan's relation also predicts that increasing elastic modulus, yield strength and strain to failure will increase the fracture toughness. If the n value doubles while the modulus and yield increase 7-10%, the effects of these parameters would outweigh the effect of splitting, although the two effects would still be of the same order of magnitude.

6.2.1.2 Effect of spacing via change of fracture profile

An alternative approach to the effect of splitting on fracture is to consider the influence of the transition from flat to shear fracture that occurs with decreasing thickness in sheet specimens. This transition is a macroscopic consequence of the influence of thickness on stress state discussed above. Rao and Ritchie [1989] proposed recently that the effect of splitting in aluminum-lithium alloys was to change the fracture profile in the ligaments from flat at room temperature to 45° shear at 77 K and below. They argue that this change in gross fracture morphology is responsible for the change in fracture toughness and that the amount and depth of splitting are important only to the extent that they determine the fracture morphology. As will be discussed in section 6.4, in the shear mode the toughness is expected to depend on the yield strength and therefore would be expected to increase between 77 K and 4 K.

The transition to the shear mode of fracture does not require that the splits are deep. In a continuum sense shear can occur if the depth of the splits is comparable to their spacing (the requirement for full plane stress). This statement would imply that if splits occurred at every grain boundary, they would only need to be 20 μm deep for the entire specimen to be effectively in plane stress. This example is obviously exaggerated since a continuum analysis does not apply at the level of individual grains, but it suggests examining the fracture profiles to see what proportion of the surface could be viewed as being potentially in plane stress. There does not appear to be a consistent change in the proportion of long 45° facets; however, since a macroscopically flat fracture can be made of small slanted segments, this observation does not necessarily preclude an effect. Examination of the digitized fracture profiles (e.g. Figure 5.17) suggests that at least for 2090-T81, L-T, this suggestion may have some merit. At room temperature there are regions where the splits are too shallow and widely spaced for shear to occur. At 77 and 4 K, the potential for shear between splits of varying depth and spacing seems to occur essentially everywhere in the specimen.

If it is postulated that the low temperature fractures occur under essentially plane stress conditions (i.e. at effective thicknesses less than B_0, the maximum thickness at which full plane stress occurs) then the fracture toughness should be insensitive to the amount of splitting in this regime. In plane stress the strain energy release rate is proportional to the ligament thickness. Since the total thickness of the specimen is unchanged by the ligament thickness, the fracture toughness should also be unchanged. Any change of temperature that affects the split spacing will affect the fracture toughness only through the variation of

other material properties, specifically E and σ_y. Within this regime where the amount of splitting is sufficient to cause plane stress, altering the material in ways that affect its propensity to split should not affect its toughness to first order. Future studies of materials with altered short-transverse properties will shed light on the validity of this hypothesis.

6.2.2. Results for controlled-rolled steels and comparison

The effect of splitting on low temperature fracture toughness has been investigated in some detail for controlled-rolled steels, for which splitting is associated with an elongated grain structure. In these materials a decrease in upper shelf toughness is often observed relative to alloys that do not split. On the other hand, the steel literature identifies an important role of transverse splitting that is independent of its numerical influence on toughness; because a fully triaxial stress state is not achieved in a split specimen, the ductile-brittle transition is often suppressed. The literature in this area is summarized below.

6.2.2.1. Conditions for occurrence of splitting

It is somewhat difficult to define the conditions necessary for splitting as no one material characteristic can be manipulated independently. However, the steel results point to several conditions that must be met in order for splitting to occur in a nominally homogeneous material [Inagaki, 1988; Mintz and Morrison, 1988; Bourell, 1983; Bramfitt and Marder, 1977; Tanaka, 1988; Dabkowski, 1976]. First, the fracture stress on the rolling (S-T) plane must be significantly lower than the fracture stress on the planes normal to it. In general a sufficiently low value will be achieved only when the grains are highly elongated (~ 10 times their thickness) and aligned. The split region is limited to the plastic zone where severe plastic deformation has taken place. The splits seem to be caused by intense slip at the grain boundaries. Some authors have argued that crystallographic texture contributes to this localization; the source of this effect is the mechanical incompatibility due to strain anisotropy of colonies of {100} and {111} grains. Other causes of short-transverse embrittlement including mechanical fibering and microstructural banding have also been suggested. Increased strain hardening seems to contribute by raising the maximum stress. Whatever the exact cause of splitting, the presence of large planar grain boundaries found in alloys with a highly elongated grain structure is a precondition.

The amount of splitting varies with the test temperature in these alloys. Splitting does not occur in the brittle lower shelf regime, presumably because the critical stress for brittle propagation of the main crack is reached before the stress for splitting is achieved [Bourell]. In the upper shelf regime, the amount of splitting increases with decreasing test temperature to a maximum at the upper end of the ductile-brittle transition [Dabkowski, Mintz and Morrison, Tanaka].

6.2.2.2. Influence of splitting on properties

All of the steel studies discussed here measured fracture toughness using blunt-notched Charpy impact specimens. If the material is processed to induce greater amounts

of splitting, the ductile-brittle transition temperature decreases because the splits relieve the stress triaxiality needed to drive intergranular cleavage. However, as illustrated in Figure 6.4, the upper shelf toughness often decreases as well [Dabkowski, Bramfitt and Marder]. Bramfitt and Marder note that the same effect is observed when the Charpy specimen thickness is decreased. An explanation for this phenomenon is that the total volume of deformed material is also decreased, lowering the energy required for fracture. This explanation makes sense in plane stress where the size of the plastic zone corresponds roughly to the thickness of the material. Micrographs shown by Morrison [1975] suggest that the ligaments between the splits are nearly in plane stress; each exhibits the classic slant fracture typical of plane stress conditions. However, despite the fact that plane stress toughness is generally higher than plane strain toughness, the upper shelf toughness in the alloys they studied generally decreases as splitting becomes more prevalent.

Similar results have been reported in studies of conventional aluminum alloys in which splitting has been observed. Niinomi, et al. note that in previous work on 7N01 (and 5083, laminar cracking was associated with a decrease in toughness with decreasing temperature. Saji, et al. [1987] did a detailed study of the tensile behavior of 7075 in several tempers between 6.5 K and 300 K. They report increasing toughness as estimated by work-to-fracture and elongation with decreasing temperature until a peak at 30 K and decreasing values from there to 4 K. The peak in apparent toughness and elongation is associated with a maximum amount of laminar splitting, and a minimum in the localized (post-uniform) strain. However, previous direct measurements of the toughness of 7075-T6 have shown that it is roughly unchanged between 300 K and 77 K [McHenry, 1983]. Thus, while there is considerable evidence for increased laminar cracking at low temperatures in aluminum alloys, it is not clear that its presence is responsible for increased low temperature toughness.

6.2.2.3. Preservation of ductile fracture mode

As mentioned above, an important consequence of crack-dividing splitting is that by relieving somewhat the triaxial stresses that drive intergranular cleavage it promotes ductile fracture over cleavage. In steels, this is easily observed as a lowering of the ductile-brittle transition temperature. It follows from this observation that in a certain temperature regime splitting vastly improves the fracture toughness, even though it may decrease the fracture toughness at higher temperatures.

6.2.3. Comparisons with experimental data on aluminum-lithium alloys

Three approaches to evaluating the influence of splitting on fracture toughness have been described. The first model considers splitting as being roughly equivalent to testing a specimen of the thickness of the major split spacings and predicts that toughness will be elevated to the corresponding value on the $K_c(B)$ curve. The second approach considers the effects of all splits, shallow or deep, in promoting a shear type failure, such as that which occurs in plane stress. The third view considers the potential of postponing a harmful fracture mode transition, the apparent mechanism in control-rolled steels, where the principal influence of splitting seems to be to lower the ductile-brittle transition, while

slightly lowering the Charpy impact energy in the ductile regime. These models will be evaluated for the available experimental data on the cryogenic fracture toughness of commercial aluminum-lithium alloys reported in this work and in the literature.

6.2.2.1. Spacing and depth vs. temperature

The first model, that predicts an increase in fracture toughness with decreasing major split spacing due to a change in the stress state was proposed by Dorward and extended by Rao et al. [1988]. This model would appear to be ruled out by the fact that there is no consistent experimental correlation between the split spacing and the fracture toughness. In three of the four cases studied here the correlation is reversed for at least part of the temperature range; a decrease in the amount of splitting and consequent increase in split spacing is associated with increased toughness. The fracture toughness of 2090-T81 L-T and T-L increases between 77 and 4 K, but the spacing between deep splits increases. The fracture toughness of 2091-T8 L-T does not increase between 200 and 4 K, but the split spacing decreases monotonically with temperature. In 2091-T8 T-L, the decrease in split spacing with temperature is monotonic and greater than that observed for 2090. However, while the toughness does increase, the increase is considerably less than in 2090 despite a beneficial change in the microscopic fracture mode. The lack of a consistent correlation between the amount of splitting and toughness has also been noted by Webster [1987].

A quantitative assessment of the influence of splitting on toughness using a model of the sort described in section 6.2.1.1 is at best speculative because not all of the relevant material parameters are known. Rao, et al. [1989] attempted to show that the improvement in fracture toughness of 2090-T81, L-T between room temperature and 77 K could be explained using the model of Broek and Vlieger. However, their calculation contains several errors. The most important of these are that they have set the effective thickness B to a value less than B_0 in a relation valid only for $B > B_0$ and that the significant effect of temperature on the value of B_0, the maximum thickness at which full plane stress is achieved, is not considered. Data obtained by Rao and Ritchie [1989] for 1.6 mm 2090-T83 sheet shows clearly that the value of B_0 at 77 K is substantially smaller than at 300 K; for this thickness, full plane stress is achieved at 300 K, but at 77 K about half the fracture is macroscopically flat. The maximum effect of splitting at 300 K for this alloy can be estimated by using their value for B_0 of 2 mm and setting ε_f to the value measured in uniaxial tension; on this basis the maximum increase in toughness due to splitting is predicted to be less than 20%, a much smaller increase than that which is obtained by decreasing the test temperature to 77 K.

6.2.2.2. Fracture profile vs. temperature

The second model, which predicts an increase in fracture toughness due to a change in the overall fracture morphology, also does not appear to be consistent with the fracture profiles determined in this study. Low magnification profiles (Figures 5.12 and 5.20) showing the fracture morphology across the entire thickness of the compact tension specimen (12.7 mm) indicate that specimens at all test temperatures have regions of slant

fracture in both 2090 and 2091 alloys and in both test orientations. As mentioned previously, it is difficult to describe the proportion of slant fracture quantitatively, because it depends on the scale at which the fracture is examined or, equivalently, on the facet length that is considered significant. Furthermore, it is difficult to see how a change of morphology of sufficient magnitude to increase the fracture toughness significantly could be accomplished without a change in the primary fracture mode. Thus, it seems that a fracture morphology transition probably cannot account for the observed variation in fracture toughness.

The results of Niinomi et al. [1988] also support the view that increased low temperature toughness cannot be explained by a change in fracture morphology. Niinomi et al. studied the strength-toughness relationship of an Al-Cu-Li-Mg-Zr using tensile and instrumented Charpy tests. In the T6 temper, both the strength and toughness increased between 295 K and 77 K. The micrographs in Figure 10 of their paper again show the typical fracture mode of high strength aluminum-lithium alloys — intergranular splits (more pronounced at 77 K) linked by regions of transgranular shear. The local crack path appears to be at 45° to the macroscopic crack path at both test temperatures.

6.2.2.3. Preservation of fracture mode

None of the specimens that displayed significant splitting at room temperature displayed a transition to a more brittle fracture mode at low temperature. Similar observations have been made by Rao, et al. [1989] for 2090-T81, 2091-T351, 8090-T8X and 8091-T8X and Dew-Hughes for 8090-T651 as well as by Niinomi. The low temperature behavior of the fine-grained superplastic 2090-T6 indicates that it is possible for such a transition to occur, in that case to intergranular fracture. This transition is similar to what is observed in controlled-rolled steels. Thus it is fully possible that as in the steel case the splitting plays an important role in aluminum-lithium alloys with an elongated grain structure in preserving a fracture mode that involves transgranular shear.

6.2.4. Causes of splitting and interpretation of observations

6.2.4.1. Driving force for splitting

The driving force for splitting is the through-thickness stress σ_z that exists in a thick specimen in which through-thickness plastic deformation is constrained by the elastic material surrounding the plastic zone. The value of σ_z has a well-defined relationship to the applied stress intensity in plane strain, and must be proportional to the applied stress intensity for any stress state. Splits are expected to occur when σ_z exceeds a critical fracture stress σ_{zs}. The value of σ_{zs} is the fracture stress along the grain boundaries that split. Due to the three-dimensional nature of the problem, the local values of σ_z after the first split occurs are unknown and the variation in split spacing with stress intensity and σ_{zs} is therefore unknown. It is not known *a priori* whether σ_{zs} varies with test temperature. However, if the split spacing changes with test temperature, it must result from a change in either the applied stress intensity, or the value of σ_{zs}, or both.

6.2.4.2. Effect of stress intensity on splitting

This section considers the cause of the variation in split spacing with test temperature rather than its consequences and attempts to infer the way in which the inherent fracture toughness of the material is changing. The effect of the stress intensity is examined by reconsidering the concept that splitting affects the fracture toughness through its effect on the stress state. If σ_{zs} is a function of test temperature, split spacing will be affected even if all other material properties remain the same. If the K_{Ic} remains constant and σ_{zs} decreases then the measured fracture toughness will increase due to more splitting and further loss of constraint. Conversely, if σ_{zs} increases then the measured fracture toughness will decrease, again for constant "true" K_{Ic}. However, since σ_z is related to the stress intensity K, if K_{Ic} increases, then, for a constant value of σ_{zs}, the number of splits will increase to maintain the maximum σ_z at σ_{zs}. Thus an increase in the number of splits can mean either that resistance to splitting has increased, with no concurrent change in K_{Ic}, or that the value of K_{Ic} has increased. It is consistent with this view that for 2090-T81, the fracture toughness in the L-T orientation is significantly higher than in the T-L orientation at all test temperatures, while the split spacings for L-T specimens are about half of those for T-L oriented specimens. Conversely, the fracture toughness of 2091-T8 is much less anisotropic and the split spacings in the L-T and T-L orientations are relatively similar except at 300 K. However, the amount of splitting associated with a given stress intensity will depend on the relative values of σ_z and σ_{zs}, a question that will be discussed in the next section.

6.2.4.3. Effect of temperature variation of ST strength and S-T toughness

In order to discuss the causes and consequences of splitting, a mechanical criterion for the occurrence of splitting must be hypothesized. Although low S-T and S-L fracture toughness is to be expected in a material that delaminates, it must be recognized that in an L-T or T-L compact tension specimen there are no introduced sharp crack along the S-T fracture planes. Short-transverse cracks must nucleate as well as propagate in response to the through-thickness stress caused by the triaxial nature of the stress state introduced by a sharp crack in a thick L-T or T-L specimen. This situation is in many ways similar to fracture in tension (although the stress state suggests plane strain tension rather than axisymmetric tension). Thus the mechanical criterion for splitting will arise from the competition between failure when the ST tensile fracture stress is exceeded and failure when the stress required to cause fracture at an inclusion or other flaw is exceeded.

Both the ST tensile fracture strength and the S-T fracture toughness have been measured for 2090-T81. In this study it was found that the ST yield and fracture strengths were relatively high compared to the strength in other orientations and increased as temperature decreased. Rao, et al. [1988] found that the S-T fracture toughness was relatively low and decreased as temperature decreased. This inverse relationship is the conventional one predicted for stress-controlled fracture brittle fracture. The S-L fracture toughness, which involves cracking on the same plane, is also low and decreases with decreasing temperature as well [Dorward, 1986; Rao, et al., 1989].

In conjunction with the S-T and S-L K_{Ic} values, the ST tensile fracture stresses can be used to estimate the minimum flaw size that will propagate under the applied stress. The required stress for a reasonable flaw size may provide a way of determining if splitting is controlled by the tensile fracture stress in the short-transverse direction, σ_f(ST), over the net section of the plastic zone rather than K_{Ic}(S-T). This question is of considerable importance since the variations with temperature of the ST yield strength and the S-T fracture toughness are opposite. To determine the minimum flaw size, the stress that drives splitting must be estimated. Since the stress state is triaxial and the loading non-uniform any calculation must be quite approximate. The peak through-thickness stress may be equated with σ_f(ST), but certainly cannot exceed $2\sigma_y$(L or LT), the value achieved for plane strain. If we assume an internal penny-shaped crack or radius *a* with uniform loading then

$$K_I = \frac{2}{\pi}\sigma^{\infty}\sqrt{\pi a}. \tag{6.3}$$

Using K_{Ic}(S-T) = 16 MPa$\sqrt{m}$ at room temperature, and assuming a maximum stress of σ_y(LT) = 535 MPa and letting $\sigma^{\infty} = 2\sigma_y$, then *a* must be greater than or equal to about 175 μm (0.007 in) if the split is to propagate before the material pulls apart under the tensile load. Since this is a half-length, the internal flaw would have to be quite large. Even if the geometric factor $2/\pi$ were increased to 1 for the actual crack shape and loading geometry, the flaw would would still have to 70 μm in total length. The only flaws in the material of this size are occasional aligned groups of inclusions and the grain boundaries themselves. To cause crack propagation at defects found on the boundaries, such as intermetallics, the applied stress would have to be increased further to cause fracture. However, since σ_f(ST) would be exceeded over the entire plastic zone by a significant amount, splitting is likely to occur before the stress required to cause a crack to propagate from an existing flaw is reached. Thus assuming that the value of σ_f controls splitting is not an unreasonable assumption.

Dew-Hughes et al. [1988] have calculated that inclusions of 1 μm in size or less are sufficient to cause brittle fracture using a Griffith criterion under the assumption that the work of fracture is dominated by the surface energy of the free surfaces generated by the crack (estimated at 1 J/m^2). Although the ST failure surface in tension appears extremely brittle and shows little evidence of plastic deformation (Figure 5.7 and 5.8), this assumption is inconsistent with the measured S-T fracture toughness in 2090-T81 and other aluminum-lithium alloys [Rao, et al., 1989], as is evident by the much larger critical crack size calculated using the stress intensity factor given in equation 6.3.

In view of these considerations, one way of measuring the value of σ_{zs} is to use the peak tensile stress prior to failure, σ_f, measured in a tensile test in the z-direction, the ST direction for L-T and T-L fracture toughness specimens, although this idealization is admittedly complicated somewhat by the fact that σ_f probably varies through the thickness of the plate, as other tensile properties do. Many investigators of splitting in controlled-rolled steels have concluded that splitting in those materials is controlled by σ_f(ST). If the tensile fracture stress does control delamination crack initiation, then delamination becomes more difficult at low temperature since the tensile fracture stress in the ST direction

increases. Thus, the increased number of splits at low temperature compared to room temperature indicates that the stress intensity is higher.

Under the hypothesis that splitting is indeed controlled by $\sigma_f(ST)$, the region over which splitting would be expected to occur can be estimated. Since splitting does occur in these materials, if the fracture stress σ_f corresponds to σ_{zs}, then it must be considerably less than the σ_z stress developed near the crack. Under the assumption of linear elastic fracture mechanics, the value of σ_z under plane strain conditions can be estimated as a function of θ and r (origin at crack tip). Figure 6.3 shows values of σ_z as a function of θ for a room temperature 2090-T81 L-T orientation specimen (K=34 MPa$\sqrt{m}$, σ_y = 535 MPa, ν = 0.35) using $r \geq r_p$ as a parameter. The relevant equations are:

$$\sigma_z = \frac{2\nu K}{\sqrt{2\pi r}} \cos\frac{\theta}{2} \qquad r > r_p \tag{6.4}$$

$$r_p(\theta) \cong \frac{K^2}{4\pi\sigma_y^2}\left[\frac{3}{2}\sin^2\theta + (1-2\nu)^2(1+\cos\theta)\right] \tag{6.5}$$

where r_p is determined by applying the Von Mises' yield criterion. The top figure shows the shape of the equivalent Von Mises' stress contours, r_p and multiples of r_p along which the values of σ_z are calculated. For 2090-T81 L-T the calculations show that σ_z is greater than the measured value of σ_f in ST tension of 500 MPa between θ=0 and $\pi/4$ at the edge of the (plane strain) plastic zone. Along a contour 4 times the size of the plastic zone, the stress is greater than σ_f over a much smaller angle. Figure 6.4 shows the region over which splitting is predicted; the results of similar calculations at 77 K and 4 K are also shown. These results compare favorably with the experimental observation that the splits extend over a region whose size is on the order of the size of the plastic zone; however, this calculation is rather approximate and cannot provide the basis for a detailed discussion of the expected extent of splitting. The value of K used in the calculation is that measured from a specimen that has split; it is not the "true" K_{Ic} of the unsplit material. As the material splits, the stress state of the ligaments moves in the direction of plane stress; consequently, the measured value K_c rises, σ_z decreases and the plastic zone size r_p increases.

6.2.5. Summary

The arguments of the preceding pages regarding the importance of crack-dividing splitting in determining low temperature fracture toughness may be summarized as follows. It is well known that intergranular splits that divide a thick specimen into thin laminates can raise the apparent fracture toughness by relieving some of the stress triaxiality present in a nominally plane strain fracture toughness specimen. Conversely, if a material is relatively weak in the short-transverse direction a high fracture toughness will induce splitting because of the large through-thickness stress at the crack tip. Hence transverse splitting may be either a cause of high fracture toughness or a consequence of it, and detailed studies are necessary to elucidate its role. Several investigators have suggested that increased splitting can explain the observed improvement in low temperature fracture toughness in

2090-T81. The results of this investigation seem to establish that transverse splitting is not the dominant cause of the toughness increase at low temperature.

This conclusion is supported by three main considerations:
1) There is no theoretical basis from which to conclude that increased splitting must cause an increase in fracture toughness.
2) There is no correlation between amount of splitting or the fracture profile and the fracture toughness.
3) The splitting pattern can be roughly explained on the basis of an alternative viewpoint.

It remains possible that transverse splitting is necessary to preserve a ductile fracture mode of Al-Li alloys, and is hence an essential element in the design of cryogenic aluminum-lithium alloys. It is also probable that the splitting has a beneficial effect on the fracture toughness at all temperatures. Studies of the effect of splitting on other aluminum alloys are conflicting.

6.3. Liquid metal embrittlement

Webster has proposed that low melting point phases formed by impurities that segregate to the grain boundaries cause embrittlement because they are present as liquid even at temperatures well below room temperature. Intergranular embrittlement above the melting point of a second phase present in very small volume fraction has been observed in Be alloys [Webster, 1975] and in Al alloyed with Pb, Bi and Cd [Roth, et al., 1980]. Impurities such as Na, K and Cs have been detected on the grain boundaries of fractured Al-Li specimens. Existing phase diagrams indicate that there are phases containing these elements that solidify at temperatures as low as 195 K. Apparently, the presence of a liquid phase at grain boundaries and grain boundary triple points results in liquid metal embrittlement. Webster predicts that the toughness will increase over the freezing range of the phase. Niinomi, et al. support this interpretation based on their observation that there is evidence of Na and K segregation on the fracture surfaces of specimens broken at 300 K and 123 K, but not at 77 K. They compare the expected temperature at the crack tip after accounting for adiabatic heating to Webster's phase diagrams and find good agreement between these temperatures.

A major flaw of this model is that it does not explain the continued improvement in fracture toughness between 77 and 4 K. No phases have yet been identified that would solidify in that temperature range. An additional model would have to be invoked to explain the low temperature behavior. A second problem is that the improvement of toughness at low temperature does not appear to be significantly diminished in alloys prepared from extremely pure starting materials.

Nonetheless, this model may provide insight into the behavior of some materials in some temperature regimes. For example, it might provide an explanation for the unusual cleavage-like failures discussed in section 6.1.2 observed by Fager et al. and in this work for 2091-T8 in the L-T orientation. The embrittling agent responsible for the cleavage

facets has not been identified, but preliminary experiments by Fager, et al. show that a K-Na eutectic can promote cleavage fracture. The cleavage facets are transgranular fractures on {110} and {100} planes. Cleavage did not occur at low temperature or at high strain rates, leading the authors to speculate that the cleavage depends on the mobility of the embrittling agent.

6.4. Theories of strain-controlled fracture

The final approach to understanding the effect of temperature on fracture toughness that will be considered here concerns the influence of the elastic and plastic properties of the material on fracture. For both 2090-T81 and 2091-T8 in the in-plane orientations, the elastic modulus, yield and ultimate tensile strengths and strain hardening rate all increase with decreasing test temperature. The tensile elongation also increases in most cases as well.

6.4.1. Models of strain-controlled fracture

Analytic theories of elastic-plastic fracture predict that if the fracture mode is unchanged, increases in yield strength, ultimate tensile strength, elongation and strain hardening rate should result in an increased value of K_{Ic} or J_{Ic}. These models are applicable to strain-controlled ductile fracture. While it has not been rigorously proved that the fracture mode is strain-controlled for aluminum-lithium alloys with elongated grain structures in general, or for 2090 or 2091 in specific, it seems likely that it is, since the final separation appears to occur by transgranular shear.

Numerous models for strain-controlled fracture exist. Each predicts a different dependence of the fracture toughness on the deformation properties of the material mentioned above. It does not appear that any of the models describe the data obtained in this study in a satisfactory quantitative fashion. This indicates either that the models are inadequate or, more likely, that several factors contribute to the variation of the measured fracture toughness with temperature. It is beyond the scope of this work to determine which of these models is most suitable for quantitatively predicting the fracture behavior of aluminum-lithium alloys or how they should be modified; all predict similar trends. To illustrate the qualitative predictions of these models, several will be presented in the following section. The most important difference between these models is that different fracture criteria are used. Other models that lead to similar consequences could also be cited. Quantitative results will be mentioned only to check the order of magnitude of the expected variation in fracture toughness with material properties. It should be noted that these models do not contradict the usual concept that toughness decreases with increasing yield strength, since strain-to-failure and strain hardening rate often decrease concurrently [Embury and Nes, 1973].

One of the oldest discussions of the effect of strain hardening on fracture is due to Krafft [1964] who found an empirical correlation between the n-value and K_{Ic}. Krafft hypothesized that plane strain cracking occurs when the crack tip stress field causes a tensile strain equal to that for plastic flow instability in the material a small fixed distance

ahead of the crack tip. The strain hardening rate employed by Krafft was modified to account for the adiabatic heating and increased strain rate at the crack tip. Because specific heat goes to zero as temperature goes to absolute zero, the correction to the n-value for adiabatic heating may be very large at low temperatures.

Another, older, technique for modeling fracture is to model the plastic relaxation around the crack tip and the growth of the crack using dislocations. The fracture criterion is the achievement of a critical displacement. This approach is termed the "dislocation relaxed-crack model" by Smith (1985) and was originated by Bilby, Cottrell and Swinden [1963]. The model describes both the plastic relaxation and the discontinuity associated with the crack by edge dislocations with Burgers vectors parallel to the loading axis. The relaxation is artificially restricted to the plane of the crack. For small values relative to the crack length of the plastic zone size and critical displacement for fracture the model reduces to

$$K=\sigma\sqrt{\pi a}=\left[\frac{3E\sigma_y\delta_c}{4(1-\nu)}\right]^{1/2} \tag{6.6}$$

where δ_c is the critical displacement for fracture. This relation predicts that the fracture toughness will increase with increasing yield strength for a constant value of δ_c. A later paper [Bilby and Swinden, 1965] considers deformation on the planes of maximum shear at 45° to the loading axis and allows for strain hardening; the results are qualitatively similar.

For thin sheets that fail at 45° to the crack plane this model predicts that the critical strain energy release rate G is proportional to the product of the yield strength and the strain, so that if strain hardening is ignored

$$K \propto \sqrt{2E\sigma_y B} \tag{6.7}$$

in this regime. This model is probably only applicable if it is assumed that splitting causes the specimens to act as parallel thin sheets.

Thomason [1971] has developed a model of ductile fracture based on link-up by plastic shear instability of voids. For small values of ε_f, the model predicts

$$K_{Ic} \propto n\sqrt{E\sigma_y}. \tag{6.8}$$

The model used by Chan (section 6.2.1.1.3) assumes that failure occurs when a critical value of the crack tip opening displacement is achieved. This critical displacement is then assumed to be related to a critical effective strain. The model predicts that the fracture toughness is

$$K_{Ic}=\sqrt{\frac{E\sigma_y\bar{\varepsilon}_f n^2}{\alpha(1-\nu^2)}}. \tag{6.2}$$

Similar models that use a critical strain fracture criterion give an almost identical result, although the proportionality constant is different [Hahn and Rosenfield, 1968; Garrett and Knott, 1978]. These authors of these models suggest that the value of ε_f should be appropriate to the stress state.

Yet another fracture criterion is that a critical stress be achieved over a critical microstructural distance. The strain a distance r ahead of the crack tip can be written:

$$\frac{\varepsilon_{ij}}{\varepsilon_o} = \alpha\left[\frac{J}{\alpha\sigma_y\varepsilon_y I_N r}\right]^{\frac{N}{N+1}} \tilde{\varepsilon}_{ij}(N,\theta) \tag{6.9}$$

for the constitutive relation $$\left(\frac{\varepsilon_{ij}}{\varepsilon_y}\right) = \alpha\left(\frac{\sigma}{\sigma_y}\right)^N \tag{6.10}$$

where σ_y and ε_y are the stress and strain at yielding respectively, I_N is an integration constant weakly dependent on N, $\tilde{\varepsilon}_{ij}(N,\theta)$ is a dimensionless angular function of N and θ and J is the path independent integral around the crack tip [Pendse and Ritchie, 1985]. In terms of these variables the fracture criterion can be phrased as $J = J_{Ic}$ when $\varepsilon_{ij} = \bar{\varepsilon}_f$ over a characteristic microstructural distance l_o. If l_o is assumed to be constant for a given fracture mode and the variations in $\tilde{\varepsilon}_{ij}$, α and I_N are neglected this model becomes

$$J_{Ic} \propto (\varepsilon_f)^{n+1}\sigma_y \rightarrow K_{Ic} \propto \sqrt{\frac{E\sigma_y\varepsilon_f^{n+1}}{(1-\nu^2)}} \tag{6.11}$$

where ε_f is the true strain-to-failure and n is the strain hardening rate in the constitutive relation $\sigma=k\varepsilon^n$ used herein. This relation is more weakly dependent on the strain hardening rate than equation 6.2, but has a stronger dependence on the yield strength and strain-to-failure.

Many of the models described above have been specialized to predict the dependence of the toughness on particular microstructural features, such as the slip band width and spacing, the spacing between inclusions (for ductile dimple failure) and so on. An example of this type of model is the one proposed by Jata and Starke [1986] that uses the same critical stress over a critical distance fracture criterion used to arrive at equation 6.11. The critical shear strain is taken as one-half (plane strain) or one-third (plane stress) of the fracture strain in uniaxial tension and it is assumed that only dislocations in a set of symmetric slip bands at the crack tip contribute to achieving this critical strain. Jata and Starke make some simple further assumptions to relate the remaining values to microstructural parameters and arrive at

$$K_{Ic} = \left[8(\sin\alpha)E\sigma_{ys}r_p\left(\frac{W}{d}\right)\gamma_{SB}\right]^{1/2} \tag{6.12}$$

where α is the angle between the slip band and the crack plane, W is the slip band width, d is the slip band spacing and γ_{SB} is the shear strain in the slip band.

Although the quantitative results of these models differ, when all four parameters, E, σ_y, ε_f and n, increase together, the prediction of increased toughness if the fracture mode remains unchanged is the same. Only when ε_f decreases do the exact dependences come into play. The choice of a suitable value for ε_f does not affect the qualitative results as long as the proportionality between the value in uniaxial tension and the value in the actual stress state does not change (e.g. ε_f equal to one-third the value in uniaxial tension).

Finally, even fracture models that assume a critical stress criterion for fracture lead to similar predictions for the dependence of the fracture toughness on E, σ_y and n. One such model proposed by Chen and Knott [1981] leads to

$$K \propto \sqrt{E\sigma_c\sigma_y n^2 \frac{\lambda}{d}} \tag{6.13}$$

where σ_c is the critical stress and λ and d are the average spacing and diameter of the particles at which fracture initiates. If σ_c, λ and d are assumed constant with temperature, the proportionality is the same as in the Thomason critical strain model.

6.4.2. Application to aluminum-lithium alloys

Assuming that the fractures are strain-controlled, the models described above should apply to 2090-T81 in both orientations and 2091-T8 in the L-T orientation since no primary fracture mode change is observed in these cases. They should underestimate the increase in fracture toughness of 2091-T8 in the T-L orientation, since this condition exhibited cleavage facets at room temperature.

Reviewing the mechanical properties briefly, for 2090-T81 in the L orientation, all of the relevant tensile properties increase with decreasing temperature and so does the L-T toughness. In the LT orientation, the T/2 tensile specimens indicate that all properties are again increasing, although to a lesser degree; in keeping with this result, the T-L toughness also increases with decreasing temperature, but to a lesser extent than in the L-T orientation. The tensile data measured at T/4 show a smaller increase in yield strength at low temperature as well as a sharp decrease in tensile elongation below room temperature that is associated with a failure to meet the necking criterion. It is difficult to assess how this through-thickness variability in mechanical properties should be accounted for. For consistency T/2 tensile properties were selected for the calculations described below.

In the L-T orientation the fracture toughness of 2091-T8 increases only between 300 and 200 K and is approximately constant between 200 and 4 K. The tensile elongation in the L direction increases between 300 and 200 K, but decreases at 4 K due premature failure. The strain hardening rate increases monotonically if it is compared on the basis of true stress (but not true strain or *n* values). Only the yield strength and, presumably, the elastic modulus increase monotonically with decreasing temperature. Apparently these factors

roughly balance to produce the approximately constant fracture toughness with test temperature. However, it is difficult to explain the large increase in fracture toughness between 300 and 200 K on the basis of this model or the other models that have been discussed.

Figure 6.5 compares the experimental results to predictions for the relative change in fracture toughness of each alloy and orientation with respect to its value at room temperature. Four of the models described above were considered: Pendse and Ritchie, eqn 6.11; Chan, eqn. 6.2; Thomason, eqn 6.8; and Bilby, et al., eqn 6.7 for constant total thickness B. Only the predicted influence of the changing material properties is considered; no attempt was made to determine the absolute values of the fracture toughness which depend on various unknown proportionality constants. Both the uniform and total elongation were considered. The total elongation represents the strain-to-failure and is therefore the obvious choice. However, it is more variable between specimens than the uniform elongation. Furthermore, in flat specimens the actual true strain at failure cannot be determined and the value determined from the engineering total strain must be used. The uniform elongation can be determined consistently. Of the various models, the model of Pendse and Ritchie gives the best correlation to the measured values. The models of Chan and Thomason both significantly overestimate the increase in fracture toughness that should be expected, especially at 4 K. The Bilby model underestimates the increase in fracture toughness, but does lead to a linear relationship between the predicted and experimental values. Since the Chan and Thomason models overestimate the effect of temperature on fracture toughness, any additional increment due to splitting would further skew their predictions. The Bilby model already assumes splitting, so yet another contribution to the fracture toughness is required if it is to explain the low temperature fracture toughness values. Suresh, et al. [1987] have considered the applicability of some of these models in an extensive study of fracture toughness of various aluminum-lithium alloys over a range of aging condition. They find models that predict that toughness increases with increasing σ_y and n appealing, because σ_y and n vary in opposite directions in response to aging. However, it was difficult to apply these models to many of the materials they tested because of marked crack deflection and bifurcation that create mixed mode loading and alter the local stress state at the crack. This problem exists to a much lesser extent in this study, but it cannot be totally ignored.

As was alluded to in the previous section, the prediction that the fracture toughness increases greatly at low temperature depends heavily on the increase in uniaxial tensile elongation in this alloy at low temperature. It should be noted that Rao, et al. [1989] have published data measured using circumferentially notched tensile specimens that indicate that in triaxial stress states the value of ε_f is higher at 300 K than at 77 K. It is difficult to know how to apply this data. Values of ε_f in triaxial stress states obtained by this method may not be reliable; this point is discussed in more detail in Appendix 3. Furthermore, if these data are correct and the relative values of ε_f interchange, there is no reason to believe that the entire constitutive relation, and consequently, the n-value, do not change as well. Use of the Von Mises' equivalent stress and strain depends on an implicit assumption that the material is macroscopically isotropic; this assumption is obviously violated for the alloys studied here.

Jata and Starke [1988] have suggested that the improved low temperature toughness in 2090 and 8090 can be correlated with a decreased slip band spacing and increased slip band width, as well as with increased E and σ_y. This observation is consistent with the data described here since it implies improved strain hardening at low temperatures. The slip band decohesion failure mechanism postulated by Jata and Starke [1988] also implies that the 45° facets on the fracture surface will be longer. This increase in crack roughness has been observed [Rao, et al., 1988; Jata and Starke, 1988] and may also contribute to the improvement in toughness.

6.5 Consequences for alloy design

This section attempts to summarize the discussion of the influence(s) of temperature on the strength-toughness relationship of aluminum-lithium alloys at cryogenic temperatures and to phrase recommendations for potential directions in alloy design.

The results of this and other studies of cryogenic fracture toughness of aluminum-lithium alloys reinforce the old maxim that preserving a high-energy fracture mode is of primary importance. In alloys in which there is a fracture mode transition at low temperature from void coalescence to intergranular splits linked by transgranular shear or from shear to intergranular cleavage, the fracture toughness decreases. In those alloys in which the mode operative at room temperature is preserved, the fracture toughness increases with decreasing temperature and increasing strength, stiffness, elongation and strain hardening rate.

The occurrence of intergranular crack-dividing splitting does not seem to increase fracture toughness at low temperatures in and of itself. However, it may play an important role by inhibiting a transition to a lower energy fracture mode. It is possible that if the tendency to split were eliminated the fracture toughness would decrease. However, the decrease in fracture toughness measured by Rao et al. [1989] that accompanied the transition at low temperature from void coalescence to transgranular shear in some of the alloys they studied suggests that splitting might also be viewed as making the shear mode possible at a higher temperature and thus lowering the fracture toughness rather than elevating it.

Finally, fracture theory suggests that any increases in strength, stiffness, strain hardening and elongation consistent with maintaining a constant fracture mode will result in improved fracture toughness.

7. OUTSTANDING ISSUES

This discussion will consider some outstanding issues suggested by the results that bear peripherally on the main theme of the effect of temperature on the strength-toughness relationship at cryogenic temperatures. Four topics will be considered: 1) the variation with temperature of the strain hardening rate, 2) the effect of temperature on mechanical anisotropy, 3) the influence of grain shape on mechanical properties, and 4) the effect of temperature on sharp and blunt notch measures of toughness. The discussion attempts to clarify the importance of these issues and to set out what can be said on the basis of currently available literature and data.

7.1. Influence of Temperature on strain hardening rate

The strain hardening rate is of great importance in determining the fracture toughness in any strain-controlled fracture model since it enters directly and through the strain-to-failure, to which it is closely related. Promoting slip homogenization has been one of the guiding principles in aluminum-lithium alloy development. In general, increased slip homogeneity is associated with an increased strain hardening rate, although Keh and Weissmann [1963] have argued that since the peak local dislocation density is lower, the strain hardening rate should be decreased. Since the strain hardening rate also usually increases with decreasing temperature in the low temperature regime, increased strain hardening at low temperature is often assumed to be tied to increased slip homogeneity. Since the mechanisms behind increased strain hardening at low temperatures may be closely related to those that homogenize slip, the microstructural features associated with the latter will be discussed first. The effect of temperature on the strain hardening rate will then be considered. These two aspects are closely related since the dislocation substructure that develops during deformation is affected by the temperature.

Cross slip plays an important role in determining the dislocation structure. Because it is a thermally activated process it is sensitive to temperature and to solute atoms that interact with dislocations. Cross slip is difficult at low temperatures, when the stacking fault energy is low so that partial dislocations must recombine before cross slip, and when there are strong dislocation-solute interactions. The increased shear modulus also contributes. When cross slip is difficult strain hardening should increase due to the decreased ability of a dislocation to bypass an impenetrable obstacle. Incoherent precipitates have a much greater effect on the flow stress at low temperature than at higher temperatures because they are bypassed by a cross slip mechanism [Kelly and Nicholson, 1963]. Since slip planes are more easily blocked at low temperature, deformation should become more diffuse. On the other hand, slip might also be expected to become more planar since a dislocation cannot leave its original glide plane except by cross slip or climb. Keh and Weissmann [1963] have shown that in many BCC metals the formation of dislocation cells and tangles is inhibited at low temperature; this sometimes dramatic change in the microstructure of the deformed material is ascribed to the increasing difficulty of cross slip at low temperatures. Solute atoms have a similar effect, tending to inhibit the formation of tangles and cells

[Chandra-Holm and Embury, 1983], although work on alloyed aluminum single crystals suggests that the effect of solute on the strain hardening rate is most important above 77 K [Kelly and Nicholson, 1964]. However, it is unclear what the effect of the dislocation substructure is on the strain hardening process or indeed whether there is an effect. Recent work by Vincent [1988] and Johnson, Schmitt and Morris [1989] has shown that, at least under some conditions, subsequent deformation and strain hardening behavior at one temperature are not affected by a prestrain at another, even though the equilibrium dislocation substructure is different. It is possible that the dislocation arrangement is merely a by-product of the deformation whose form changes with the deformation temperature.

It is often suggested that slip homogeneity is associated with a high strain hardening rate, especially systems such as aluminum-lithium alloys in which planar slip is associated with work softening. However, the influences of various microstructural features on slip homogeneity are still being debated; sensitivity to precipitate morphology and the nature of precipitate-dislocation interactions is obviously high. Heterogeneous slip is favored by shearable second phase particles (local work softening), by large grain size and when only a few slip systems are operating [Hornbogen and Zum Gahr, 1975]. Heterogeneous slip is probably also favored by difficult cross-slip as suggested by Zum Gahr and Hornbogen, although the work of Keh and Weissmann [1963], Vincent [1988] and Johnson, Schmitt and Morris [1989] shows that the resulting dislocation distribution may appear more homogeneous, for example when dislocation tangles replace cells at low temperature. Computer simulations of yielding behavior that do not consider the effect of cross slip also suggest that initial deformation would be more heterogeneous at low temperature because of the increased difficulty of thermal activation past obstacles in general [Altintas, Hanson and Morris, 1976]. Richert [1987] has also considered the conditions favoring the occurrence of coarse slip bands in single crystals of f.c.c. metals with a high stacking fault energy. Richert concludes that weak interaction of slip dislocations with forest dislocations encourages strain concentration in slip bands and a low strain hardening rate. The strength of the interaction depends on which slip systems are active and whether jogs or Lomer-Cottrell locks are formed when glissile and forest dislocations interact. Presumably, this means that in a polycrystal the extent of slip localization will be strongly affected by the texture of the material as well as by its microstructure.

The effect of coarsening small shearable precipitates on slip heterogeneity is unclear and probably depends on volume fraction. Zum-Gahr and Hornbogen predict that slip will be coarser for small shearable particles than for larger ones on grounds that the passage of a relatively small number of dislocations will completely eliminate the precipitates as obstacles. Tamura, et al. [1973] found that slip lines were finer and more closely spaced after aging in single crystals of a binary aluminum-lithium alloy. However, Duva et al. [1988] have disputed this on both experimental and theoretical grounds, arguing that it is large shearable particles that promote the greatest degree of slip localization. They adduce two ideas to support their position. First, in the limit of infinitely small particles there will be no localization. Second, localization depends on a balance between softening and hardening; slip will continue on a plane with large shearable precipitates longer because the

softening process will continue for longer. Experimental results of Jata and Starke [1986] support this conclusion; slip bands became more well-defined after artificial aging.

All of the mechanisms that encourage slip heterogeneity are operative in commercial aluminum-lithium alloys. The presence of the δ' precipitate is not the only factor that encourages planar slip, although the effect of precipitates on deformation is in general relatively greater in f.c.c. alloys than in b.c.c. alloys because the matrix makes a much lower contribution to the shear stress. Most of the alloys studied were peak-aged, so the precipitates were of moderate size. The distribution of the plate-like phases is relatively inhomogeneous as is their distribution over the possible variants. In addition, in alloys with an elongated grain structure, it may be that relatively fewer slip systems will operate in a single grain because some shear strain can be accommodated at the large planar boundaries. Finally, with the exception of the superplastic modifications, the grain size of commercial aluminum-lithium alloys is relatively large.

Just as the effect of microstructure and deformation substructure (and even whether there is an effect of substructure) is in question, so the mechanisms through which temperature influences the strain hardening rate are in doubt. In part this is due to the fact that there is no single agreed upon model for Stage III behavior.

The strain hardening rate in Stage III is a balance between hardening and softening mechanisms that occur in response to the enforced deformation. The variation in the strain hardening rate with temperature is controlled by the relative changes in dislocation multiplication (hardening) and recovery (softening). The theories divide into two general categories, according to whether short range or long range dislocation interactions are emphasized. Long range theories consider that the flow stress is determined by the maximum amplitude of the internal stress field due to the large dislocation density developed during deformation. Short range theories focus on the interaction of gliding dislocations with dislocations and debris on intersecting slip planes. As discussed in Section 4.2, recovery processes are important even in the low temperature deformation of aluminum alloys, since room temperature is greater than one-third the melting point. The most obvious source of the temperature dependence of the strain hardening rate is through the increased difficulty at low temperatures of activating these recovery processes, most of which require cross slip, a thermally activated process. However, other non-conservative processes such as the generation and climb of jogs, vacancies and interstitials may also play a role. The trend observed in this work that the strain hardening rate increases with decreasing temperature for a given stress is consistent with this idea. The rapid drop in strain hardening rate that occurs at room temperature, especially in the binary alloy, may be explained by a different mechanism, the dissolution of δ' precipitates as a result of planar deformation [Brechet, 1987].

Several investigations of the initial strain hardening rate as a function of temperature have shown that it is always highest at very low temperatures and lowest at very high temperatures. However, in this comparison of strain hardening rates at a particular small strain, depending on the temperature sensitivity of the mechanisms involved, the strain hardening rate may decrease uniformly with increasing temperature, plateau at intermediate

temperatures or display a peak at an intermediate temperature [Schmidt and Miller, 1982]. A peak near room temperature (about $0.2T_m$) has been observed in polycrystalline iron by Keh and Weissmann, who argue that the strain hardening rate ought to decline with decreasing temperature because regions of very high dislocation density are no longer created by recovery processes and should not begin to increase again until the temperature is sufficiently low that the process of cutting dislocations and creating jogs acquires a dominant effect. In an Al-Mg alloy, a peak in the initial strain hardening rate has been observed at about $0.3T_m$ (slightly below room temperature). The exact location of the peak depends on the precipitates formed and the interaction of the remaining solutes with the matrix, vacancies and dislocations. Al-Haidary et al. [1983] compared hardening in a similar alloy with pure aluminum. They concluded that there is a greater tendency in the alloy for dislocations to remain on their original slip planes and pile-up against grain boundaries. The long-range stress from these pile-ups contributes to hardening. The planarity of slip also slows the generation of new unlocked dislocation sources by interaction of dislocations. At room temperature, annihilation of dislocations during deformation is an important process in both pure and alloyed aluminum. Annihilation and dynamic recovery are significantly less important at 77 K [see also Hansen, 1983].

For many of the alloys and conditions investigated in this study, the strain hardening rate at 200 K was depressed below values measured at room temperature when strain hardening rates at different temperatures were compared as a function of strain. However, when they are compared as a function of stress the variation in strain hardening rate with temperature is monotonic. The peaks observed by the investigators mentioned above in the initial strain hardening rate may similarly be a result of comparing the strain hardening rate as a function of strain rather than stress. This result suggests that the minimum in the strain hardening rate observed at an intermediate temperature may come from the yield strength having a stronger dependence on temperature than the initial strain hardening rate. Thus the strain hardening rate appears depressed in this regime when plotted against true strain, but is elevated over higher temperatures when compared at constant true stress.

Ideally strain hardening rates at different temperatures should be compared at equivalent flow stresses, i.e. at the flow stress at some reference temperature for the same microstructure. Since strain hardening is determined both by the original microstructure (precipitate distribution, etc.) and by the dislocation density, comparing at true stress is imperfect, although it is an improvement over true strain. The problem arises because the same stress at two different temperatures is associated with significantly different strains and therefore, more importantly, dislocation densities. However, the results of this work indicate that important trends in strain hardening behavior with temperature, and probably also with other microstructural features, are much clearer if the comparisons are made with respect to true stress.

The effect of temperature on the tensile properties and deformation substructure in aluminum-lithium alloys has been studied by several other investigators. Welpmann, et al. [1989] have investigated the low temperature deformation behavior between 77 and 300 K of 8090-T4. There is a minimum in the ultimate tensile strength and a maximum in the reduction in area between 170 and 190 K. The uniform elongation and total elongation

both increase monotonically, the uniform elongation from about 23% at 300 K to greater than 40% at 77 K. Transmission electron microscopy indicates that lower deformation temperatures inhibit planar slip and cell formation. At 173 K, the deformation substructure is discontinuous at grain boundaries, whereas at 300 K slip bands continue through the grain boundaries uninterrupted. Welpmann et al. interpret the peak in the reduction in area at 173 K as being due to the lower dislocation density in the cell interiors, which gives the material a greater capacity for deformation along the alternate loading path that applies when necking begins. Jata and Starke [1988] have observed that slip bands are closer together and wider at low temperature in 2090 in -T6 and -T8 conditions. These observations indicate a more uniform deformation mode at low temperature which may result in increased strain hardening.

7.2. Variation with temperature of anisotropy

The results of this work show that the mechanical anisotropy of these alloys varies significantly with temperature. The presence of precipitates in the microstructure may influence the anisotropy of yield and ultimate tensile strengths in two ways. Firstly, since the plate-like phases (T_1 and T_2) nucleate heterogeneously on dislocations introduced during the stretch, their distribution is probably not random. The stretch is performed in uniaxial tension along the rolling direction and the dislocations are distributed along favorably oriented slip planes [Lee and Kim, 1989]. Since the precipitates have a specific relation to the dislocation [Cassada, Shiflet and Starke, 1987] it follows that their distribution is not random either and will contribute to anisotropies in the stress and strain response of the material. Thomas, et al. [1988] found that only some of the possible variants exist in these alloys. A second influence on anisotropy comes from the habit planes of the precipitates themselves [Bate, Roberts and Wilson, 1981]. Bates et al. found that plate-like precipitates could induce significant deviations from the r-ratio (plastic strain ratio) predicted on the basis of textural analysis. In particular, {100} platelets reduced the plastic anisotropy significantly, while precipitation of {111} platelets had little effect. The significantly greater yield strength anisotropy observed for 2090-T81 than for 2091-T81 may be consistent with these results, since the fraction of {111} platelets (T_1) is much higher in 2090 than in 2091. In addition, Vasudévan et al. showed by reversion experiments that the yield strength gradient in 2090 persisted in the absence of δ' and θ' precipitates if T_1 remained.

7.3. Influence of grain shape

The thin, elongated grains found in these alloys are likely to have a marked effect on both the deformation and fracture behavior of these alloys. The grains in the alloys investigated here are highly elongated, with aspect ratios as high as 100:1. In controlled-rolled steels, grain aspect ratios of 10:1 are considered be high enough to have a major influence on properties. The influence of the grain shape on fracture behavior has already been discussed; the large planar boundaries fail easily, resulting in the crack-dividing

intergranular splitting observed in in-plane fracture toughness specimens and high toughnesses in orientations in which failure at these boundaries blunts, or arrests, the crack [Rao, et al., 1989]. However, grain shape also has an influence on the deformation behavior, including the development of texture. Grain shape effects on deformation would be expected to arise from three effects. At low strains, the grain boundaries act as barriers to dislocations; therefore the grain shape will have a strong effect on the internal stress distribution during the early stages of plastic deformation. Secondly, the size and shape of the grains may influence the number of slip systems required for an arbitrary deformation. Thirdly, as a consequence of the first two factors and geometrical restrictions, the grain shape will influence dislocation transmission from grain-to-grain and the development of texture.

The second and third points can potentially be addresses using the concept of "relaxed constraint." This model has been relatively successful at predicting the evolution of texture in rolling and in other geometries in which the grains become highly elongated [e.g. Kocks and Chandra, 1982; Fortunier and Driver, 1987]. The "relaxed constraint" model is a modification of the Taylor model for plastic deformation. The Taylor model is based on the assumption that the strain in each grain is the same as the strain of the aggregate. The relaxed constraint model drops the restrictions on the shear strains that cross the grain in the short direction since the total displacement across one grain must be small and could easily be taken up at the grain boundary. While the Taylor model predicts that five independent slip systems are required to produce an arbitrary deformation, the relaxed constraint model predicts that three slip systems should be sufficient. Thus the overall deformation pattern (and almost certainly the strain hardening rate) are markedly affected by the elongated grain shape. Decreasing the aspect ratio of the grains would almost certainly affect the mechanical properties of the material by changing its deformation pattern as well as its tendency to split along the planar boundaries.

In the available literature, relaxed constraint theory has not been used to address the question of the influence of grain shape for a given texture. However, one can speculate that shear across the thin dimension is easier in elongated grains. Since elongated grains promote splitting, shear at 45° to the planar boundaries is further eased because plane stress conditions can develop. Decreasing the grain aspect ratio might reduce the likelihood of shear by decreasing the size of the large planar grain boundaries and by making through-thickness shear more difficult. Of course, the texture will also play an important role.

The first point, the potential influence of grain shape on the distribution of internal stresses, could potentially be of considerable importance in understanding both deformation and fracture. However, the author is not aware of any work to date that addresses this question.

7.4. Comparison of sharp notch vs. blunt notch behavior vs. temperature

Fracture toughness rankings obtained from blunt (machined) notch tests such Charpy impact energy measurements do not always match the results of precracked fracture mechanics measurements of toughness such as K_{Ic} and J_{Ic} that use sharp notches (fatigue precracks) (e.g. Ritchie, Francis and Server [1976]). For K_c panels, many aluminum alloys display little difference in measured fracture toughness between specimens with a machined notch of small root radius and those with a fatigue precrack. However, relatively large differences have been observed for aluminum-lithium alloys [James and Rioja, 1989]. An example of this phenomenon exists in the current study; the large increase in toughness at low temperature observed for 2090-T81 L-T is not seen in the corresponding Charpy impact specimens. Verzasconi [1989] found that the tear/yield ratio measured in a Kahn tear test did not change significantly from 300 to 77 K, although the UPE did increase somewhat. The discrepancy between the results of sharp notch and blunt notch tests is not limited to 2090. Verzasconi also measured the tear/yield ratio in Kahn tear specimens of 2219-T87 and found that it was much higher than 2090-T81 at all temperatures, but decreased between 300 and 77 K, while the UPE increased slightly. In this case, the relative toughness ranking for 2090 and 2219 as well as the influence of temperature on toughness are reversed between the sharp and blunt notch test. Kaufman and Holt [1965b] also found that Charpy impact values were unaffected by test temperature between 77 and 300 K for several wrought aluminum alloys; several of these alloys showed improved properties at low temperature in Kahn tear tests.

Differences in splitting behavior do not appear to be the source of the differing predictions of these measures of toughness. Verzasconi observed splitting at both 300 and 77 K in Kahn tear samples of 2090-T81. As in the J_{Ic} samples, there was more splitting at 77 K. The fractures were flat, indicating a relatively low toughness to strength ratio. The 2219-T87 specimens do not show any splitting.

The differences between Charpy and K_{Ic} results have been attributed to two main differences: the need to initiate the crack in a blunt-notched specimen and the consequent large increase (sometimes an order of magnitude) in the size of the plastic zone and/or process zone [Ritchie, et al., 1976]. The very large plastic zone of a blunt-notched specimen means that a much greater volume of material is sampled, increasing the likelihood of crack at unusually weak points. On the other hand, the peak stress is higher in a sharp-notched specimen. The measurement technique that predicts the higher toughness depends on the microstructural determinant of fracture.

It is possible that the differing results for 2090 in these two classes of tests can shed some light on the mechanisms controlling the effect of temperature on toughness. Although the insensitivity of the Kahn tear toughness to temperature could be ascribed to the fact that thin sheet is tested and splitting is correspondingly less important, the results of the Charpy tests, in which considerable splitting is also observed, cannot. It should be recalled that the work on the effect of splitting on the toughness of controlled-rolled steels was all

performed using Charpy tests. A possible interpretation is that the critical distance over which fracture occurs is on the order of the plastic zone size in the sharp-notched specimens so that the fracture is sensitive to variations in mechanical properties that affect the plastic zone size. The much larger plastic zone present in a blunt-notched specimen at all temperatures would eliminate this sensitivity. In a sharp-notched specimen the plastic zone size is on the order of 1 mm which spans 2-3 grains in the L-T orientation. However, in the T-L orientation in 2090, the plastic zone size extends perhaps only one grain ahead of the crack, but the toughness increase with decreasing temperature is less.

8. SUMMARY AND CONCLUSIONS

The cryogenic mechanical properties of 2090 in various conditions and 2091-T8 were investigated. In in-plane orientations, 2090-T81 displays generally increasing elastic modulus, yield strength, ultimate tensile strength, strain hardening rate and fracture toughness with decreasing test temperature. The tensile properties are sensitive to the location of the test specimen in the plate thickness and probably are controlled by textural variations. 2091-T8 has a more complex behavior, but there is a temperature regime (300 to ~ 77 K) in which all the mechanical properties increase with decreasing temperature. Except in the T-L orientation for 2091-T8, no change in primary fracture mode with temperature was noted for either 2090-T81 or 2091-T8.

Fracture behavior and probably also deformation behavior are strongly influenced by the highly elongated grain shape in unrecrystallized alloys. In both 2090-T81 and 2091-T8 crack-dividing splitting occurs in L-T and T-L fracture toughness tests and in tensile failures. This splitting is more prevalent at 77 K than at 300 K in both alloys. In 2091, there are even more splits at 4 K than at 77 K; however, in 2090 there are fewer splits at 4 K than at 300 K.

Four mechanisms that might contribute to the observed variation in the strength-toughness combination with temperature were considered.

It was concluded that the primary fracture mode dominates the behavior when there is a transition. Examples are the transition from ductile shear to intergranular cleavage in superplastic 2090-T6, which was associated with a decrease in toughness at low temperature, and the increase in fracture toughness for 2091-T8 in the T-L orientation in spite of decreasing tensile ductility at low temperatures. When the primary fracture mode is unchanged, other mechanisms determine the effect of test temperature on fracture toughness.

Freezing of low melting point phases could be responsible for the disappearance at low temperatures of the cleavage facets observed in 2091-T8 T-L fracture specimens broken at room temperature. However, this hypothesis cannot explain the continued increase in fracture toughness between 77 K and 4 K observed in these alloys; no phases that solidify below 77 K have been suggested.

Crack-dividing splitting may play some role in determining the overall level of toughness and in preserving the shear fracture mode at low temperatures. However, the results of this study do not support the contention that splitting is largely responsible for the increase in toughness at low temperatures. The trends in amount of splitting are not consistent with the fracture toughness trends, and can be interpreted as a consequence rather than a cause of the change in fracture toughness.

The most persuasive explanation relies on the fact that almost any theory of ductile fracture predicts that the fracture toughness will scale with the elastic modulus, yield strength and

elongation and/or strain hardening ability of the material. When the fracture mode is unchanged, these models predict an increase in fracture toughness of the alloys studied here due to the increase in these other mechanical properties at low temperature. While the quantitative agreement with existing models is only fair, it seems highly likely that the answer lies with this type of approach.

The fracture models suggest that strain hardening behavior and elongation, which are closely related in a ductile material, are key to improving the fracture toughness. Some initial studies of the strain hardening rate behavior were performed. It was found that it is important to compare strain hardening rates on the basis of true stress rather than strain. If the data are analyzed in this manner, then the strain hardening rate increases monotonically with decreasing temperature for all of the alloys investigated here. The grain shape may also be of importance in determining the deformation pattern and distribution of internal stresses and consequent strain hardening behavior.

9. ACKNOWLEDGMENTS

Many people have contributed to this work. Stephanie Verzasconi worked closely with me during much of the project. Most of the work on the binary aluminum-lithium alloy and some of the micrographs of 2090-T81 are hers. Ralph Sawtell collaborated on another portion of the work while at Berkeley. Roger Emigh helped analyze some of the J_{Ic} tests. Programs by David Chu, Jin Chan and Tom McKnelly provided the basis for some of the Fortran codes used to analyze the data. Shelly Miyasato performed the transmission electron microscopy on 2091. Jin Chan in many ways, large and small. Numerous others provided assistance at one time or another. Don Hoffman, Lawrence Livermore National Laboratory, made the electron beam welds for the 2090 ST tensile specimens. There were many helpful discussions with most of the aforementioned and with Prof. Morris. Thanks are also due to K.T. Rao and Prof. R.O. Ritchie for stimulating discussion. I would also like to express my appreciation to Profs. G. Thomas and R.O. Littlejohn who read this dissertation and provided some perceptive comments.

Portions of this work were sponsored by grants from the Aluminum Company of America (mechanisms of cryogenic mechanical properties) and Lockheed Palo Alto Research Laboratory, Lockheed Missiles and Space Company (superplastic 2090). I was supported by an AT&T Bell Laboratories PhD Scholarship for the majority of the period over which the work was performed. The remainder of the research was funded by the Director, Office of Energy Research, Office of Basic Energy Science, Material Sciences Division of the U.S. Department of Energy under Contract No. DE-AC03-76SF00098. Thanks are also due to numerous industrial researchers who lent their time, expertise and data including Phil Bretz, Roberto Rioja, Ralph Sawtell and Warren Hunt of Alcoa, Jeff Wadsworth and T.G. Nieh of Lockheed, Bill Quist of Boeing Commercial Airplane Company and Joe Hackett of Martin Marietta.

Lastly, but perhaps most importantly, I would like to thank all of those who contributed through their friendship, encouragement and good cheer - and sometimes just by being there. I can't thank the entire Morris Group, past and present, enough for providing a warm and productive environment in which to work. To all these friends I hope that I have given as much as I have received. Special thanks are due to Dan Dietderich for getting me started, to the Al-Li group for keeping me going, and to Bill Morris for making it all possible at every step by creating and maintaining the caring attitude that typifies our group.

Although this thesis seemed at every turn to pose more questions than it answered, I have learned much that does not appear on its pages.

"Never mistake knowledge for wisdom.
One helps you to make a living,
the other to make a life."
-- Sandra Carey

My deepest gratitude to Bill, Stephanie and Ralph, who helped with the wisdom part.

10. REFERENCES

General references

Aluminum, ed. J.E. Hatch, American Society for Metals, 1984.

Aluminum-Lithium Alloys I, eds. T.H. Sanders, Jr. and E.A. Starke, Jr., TMS-AIME, Warrendale, PA, 1981.

Aluminum-Lithium Alloys II, eds. T.H. Sanders, Jr. and E.A. Starke, Jr., TMS-AIME, Warrendale, PA, 1984.

Aluminium-Lithium Alloys III, eds. C. Baker, P.J. Gregson, S.J. Harris and C.J. Peel, The Institute of Metals, London 1986.

Aluminum-Lithium Alloys IV, *Journal de Physique,* Colloque C3, supplément au n°9, Tome 48, September, 1987.

Aluminum-Lithium Alloys V, Proceedings of conference, Williamsburg, VA, March 1989, to be published.

Citations

Al-Haidary, J.T., N.J. Petch and E. de los Rios, "The plastic deformation of polycrystalline aluminium," in: *Yield, flow and fracture of polycrystals,* ed. T.N. Baker, Applied Science Publishers, London, 1983.

Altintas, S., K. Hanson and J.W. Morris, Jr., "Computer simulation of plastic deformation through planar glide in an idealized crystal," *J. Eng. Mat. Tech.*, 98, pp. 86-91, 1976.

Anderson, W. E., "Some designer-oriented views on brittle fracture," *Battelle Northwest Rept.* SA-2290, 1969.

Ashton, R. F., D.S. Thompson, E.A. Starke, Jr and F.S. Lin, "Processing Al-Li-Cu-(Mg) alloys," Aluminum-Lithium Alloys III, *ibid.*, pp. 66-77.

Bate, P., W.T. Roberts and D.V. Wilson, "The plastic anisotropy of two-phase aluminum alloys -- I. Anisotropy in unidirectional deformation," *Acta Metall.*, 29, pp. 1797-1814, 1981.

Bilby, B. A. and K. H. Swinden, "Representation of plasticity at notches by linear dislocation arrays," *Proc. Roy. Soc. A*, 285, pp. 22-33, 1965.

Bilby, B.A., A.H. Cottrell and K.H. Swinden, "The spread of plastic yield from a notch," *Proc. Roy. Soc. A,* 272, pp. 304-310, 1963.

Bourell, D., "Cleavage delamination in impact tested warm-rolled steel," *Metall. trans.,* 14A, pp. 2487-2496, 1983.

Bramfitt, B.L. and A.R. Marder, "A study of the delamination behavior of a very low-carbon steel," *Metall. Trans.*, 8A, pp. 1263-1273, 1977.

Brechet, Y., F. Louchet, C. Marchionni and J.L. Verger-Gaugry, "Experimental (TEM and STEM) investigation and theoretical approach to the fatigue-induced dissolution of δ' precipitates in a 2.5 wt % Al-Li alloy," *Phil. Mag. A*, 56, pp. 353-366, 1987.

Bretz, P.E., Alcoa Laboratories, private communication, 1985.

Broek, D. and H. Vlieger, "The thickness effect in plane stress fracture toughness," *Nat. Aerospace Inst.*, Amsterdam, 1974.

Broek, D., *Elementary engineering fracture mechanics,* 4th edition, Martinus Nijhoff Publishers, 1986.

Cassada, W.A., G.J. Shiflet and E.A. Starke, Jr., "The effect of plastic deformation on T_1 precipitation," Aluminum-Lithium Alloys IV, *ibid.*, pp. 397-406.

Chan, J.W. and J.W. Morris, Jr., Center for Advanced Materials, Lawrence Berkeley Laboratory, unpublished research, 1987.

Chan, K.S., "Evidence of a thin sheet toughening mechanism in Al-Fe-X alloys," *Met. Trans.*, 20A, pp. 155-164, 1989.

Chandra-Holm, H., and J.D. Embury, "The development of substructure in aluminum and aluminium alloys," in: *Yield, flow and fracture of polycrystals*, ed. T.N. Baker, Applied Science Publishers, London, 1983.

Chen, C.Q. and J.F. Knott, "Effect of dispersoid particles on toughness of high-strength aluminium alloys," *Metal Sci.*, 15, pp. 357-364, 1981.

Chin, G.Y., W.F. Hosford, Jr. and W.A. Backofen, "Ductile fracture of aluminum," *Trans. AIME*, 230, pp. 437-449, 1964.

Chu, D. and J.W. Morris, Jr., Lawrence Berkeley Laboratory, unpublished research, 1989.

Cottrell, A.H. and R.J. Stokes, "Effects of temperature on the plastic properties of aluminium crystals," *Proc. Roy. Soc. A*, 233, pp. 17-34, 1955.

Dabkowski, D.S., P.J. Konkol and M.F. Baldy, "Splitting-type fractures in high-strength line-pipe steels," *Met. Eng. Q.*, 16, pp. 22-32, 1976.

Dew-Hughes, D., E. Creed and W.S. Miller, "Grain boundary failure in an Al-Li alloy," *Matls. Sci.Tech.*, 4, pp. 106-112, 1988.

Dorward, R.C., "Fracture behavior of commercial Al-Li alloys," 7th International Conference on Fracture, Houston, Texas, 1989.

Dorward, R.C., "Cryogenic toughness of Al-Cu-Li alloy AA 2090," *Scripta Met.*, 20, pp. 1379-1383, 1986.

Duva, J.M., M.A. Daëubler, E.A. Starke, Jr. and G. Luetjering, " Larger shearable particles lead to coarse slip in particle reinforced alloys," *Acta Metall.*, 36, pp. 585-589, 1988.

Embury, J.D. and E. Nes, "The fracture behavior of a medium strength Al-Zn-Mg alloy," *Z. Metallkde*, 64, pp. 805-812, 1973.

Fager, D.N., M.V. Hyatt and H.T. Diep, "A preliminary report on cleavage fracture in Al-Li alloys, " *Scripta Met.*, 20, pp. 1159-1164, 1986.

Fiftal, C., NBS/DOE report on Cryogenic Structural Materials for Superconducting Magnets, 1, 1978.

Flower, H.M. and P.J. Gregson, "Solid state phase transformations in aluminium alloys containing lithium," *Matls. Sci. Tech.*, 3, pp. 81-90, 1987.

Fortunier, R. and J.H. Driver, "A continuous constraint model for large strain grain deformations," *Acta Metall.*, 35, pp. 509-517, 1987.

Furukawa, M., Y. Miura and M. Nemoto, "The effect of temperature on the yield stress of Al-Li alloys," *Trans. JIM*, 26, pp. 414-422, 1985.

Garrett, G.G. and J.F. Knott, "The influence of compositional and microstructural variations on the mechanism of static fracture in aluminum alloys," *Met. Trans.*, 9A, pp. 1187-1201, 1978

Glazer, J., S.L. Verzasconi, E.N.C. Dalder, W. Yu, R.A. Emigh, R.O. Ritchie and J.W. Morris, Jr., "Cryogenic mechanical properties of Al-Cu-Li-Zr alloy 2090," *Adv. Cryo. Eng.*, 32, pp. 397-404, 1986.

Glazer, J., S. L. Verzasconi, R. R. Sawtell and J. W. Morris, Jr., "Mechanical behavior of aluminum-lithium alloys at cryogenic temperatures," *Metall. Trans.*, 18A, pp. 1695-1701, 1987a.

Glazer, J., J.W. Morris, Jr. and T.G. Nieh, "Tensile behavior of superplastic Al-Cu-Li-Zr alloy 2090 at cryogenic temperatures," Adv. Cryo. Eng., 34, pp. 291-298, 1987b.

Glazer, J., J.W. Morris, Jr., S.A. Kim, M. W. Austin and H. M. Ledbetter, "Temperature variation of the elastic constants of aluminum alloy 2090-T81," *AIAA Journal*, 25, pp. 1271-1272, 1987c.

Glazer, J., Nieh, T.G., Wadsworth, J. and Morris, J.W., Jr., "Mechanical behavior of superplastically-formed Al-Cu-Li-Zr alloy," MRS Superplasticity symposium, 1988; proceedings to be published.

Glazer, J. and J.W. Morris, Jr., "The strength-toughness relationship at cryogenic temperatures in aluminum-lithium alloy plate, Aluminum-Lithium Alloys V, *ibid*, 1989.

Gregson, P.J. and H.M. Flower, "Microstructural control of toughness in aluminum-lithium alloys," *Acta Metall.*, 33, pp. 527-537, 1985.

Gwynne, P., "Space plane," Air&Space, Aug/Sept, 1986 pp.26-33.

Hahn, G.T. and A.R. Rosenfield, "Sources of fracture toughness: the relation between K_{Ic} and the ordinary tensile properties of metals," ASTM STP 432, pp. 5-32, 1968.

Hansen, N., "Flow stress and grain size dependence of non-ferrous metals and alloys," in: *Yield, flow and fracture of polycrystals*, ed. T.N. Baker, Applied Science Publishers, London, 1983.

Henshall, C.A., J. Wadsworth, M.J. Reynolds and A.J. Barnes, "Design and manufacture of a superplastic-formed aluminum-lithium component," Materials and Design, 8, p. 324 1987.

Hirose, Y., M. Aoki, Y. Miyagi and M. Hino, "Properties of thick 5083-O aluminum alloy plates for the equatorial ring of spherical LNG cargo tanks," in Proceedings, International Cryogenic Materials Conference, Kobe City, Japan, 1982.

Honeycombe, R.W.K., *The plastic deformation of metals*, 2nd ed., Edward Arnold, London, 1984.

Hornbogen, E. and K.-H. Zum Gahr, "Distribution of plastic strain in alloys containing small particles," *Metallography*, 8, pp. 181-202, 1975.

Huang, J. and A.J. Ardell, "Microstructural evolution in two Al-Li-Cu alloys," Aluminum-Lithium Alloys III, *ibid.*, pp. 455-470

Inagaki, H., "Fractographic study of the formation of the separation in a control-rolled, low carbon Nb steel," *Z. Metallkde.*, 79, pp. 364-374, 1988.

Isherwood, D.P. and J.G. Williams, "The effects of stress-strain properties on notched tensile failure in plane stress," *Eng. Fract. Mech.*, 2, pp. 19-35, 1970.

James, R. S. and R.J. Rioja, "Lessons learned - Al-Li alloy development," Aluminum-Lithium Alloys V, *ibid.*, 1989.

Jata, K. and E. A. Starke, Jr., "Fatigue crack growth and fracture toughness behavior of an Al-Li-Cu alloy," *Met. Trans.*, 17A, pp. 1011-1026, 1986.

Jata, K. and E.A. Starke, Jr., "Fracture toughness of Al-Li-X alloys at ambient and cryogenic temperatures," *Scripta Met.*, pp. 1553-1556, 1988.

Johnson, P., J.H. Schmitt and J.W. Morris, Jr., Lawrence Berkeley Laboratory, unpublished work.

Kaufman, J.G., K.O. Bogardus and E.T. Wanderer, "Tensile properties and notch toughness of aluminum alloys at -452°F in liquid helium," *Adv. Cryo. Eng.*, 13, pp. 294-308, 1968.

Kaufman, J.G. and M. Holt, "Evaluation of fracture characteristics of aluminum alloys at cryogenic temperatures," *Adv. Cryo. Eng.*, 10, pp. 77-85, 1965b.

Kaufman, J.G. and M. Holt, "Fracture Characteristics of Aluminum Alloys," Alcoa Research Laboratories Technical Paper No. 18, Aluminum Company of America, Pittsburgh, PA, 1965a.

Kaufman, J.G., F.G. Nelson and E.W. Johnson, "The properties of aluminum alloy 2219 sheet, plate, and welded joints at low temperatures," *Adv. Cryo. Eng.*, 8, pp. 661-670, 1963.

Kaufman, J.G. and E.T. Wanderer, "Tensile properties and notch toughness of some 7XXX alloys at -452°F," *Adv. Cryo. Eng.*, 16, pp. 27-36, 1971.

Keh, A. S. and S. Weissmann, "Deformation substructure in body-centered cubic metals," in *Electron microscopy and strength of crystals*, eds. G. Thomas and J. Washburn, Interscience, New York, 1963.

Kelly, A. and R.B. Nicholson, "Precipitation hardening," *Prog. Matls. Sci.*, 10, pp. 149-391, 1963.

Kelsey, R. A., R.H. Wygonik and Per Tenge, "Crack growth and fracture of thick 5083-O plate under liquefied natural gas ship spectrum loading," ASTM STP 579, pp. 44-79, 1975.

Kocks, U.F., "Laws for work-hardening and low-temperature creep," *Trans. ASME: J. Eng. Matls. Tech.*, Jan. 1976, pp. 76-85.

Kocks, U.F. and H. Chandra, "Slip geometry in partially constrained deformation," *Acta Metall.*, 30, pp. 695-709, 1982.

Krafft, J.M., "Correlation of plane strain crack toughness with strain hardening characteristics of a low, a medium and a high strength steel," *Applied Materials Research*, pp. 88-101, April 1964.

Lebrun, Ph., CERN, Geneva, Switzerland, private communication, 1987.

Lebrun, Ph., S. Pichler, T.M. Taylor, T. Tortschanoff and L. Walckiers, "Design, test and performance of the prototype superconducting quadrupole for the LEP low-beta insertions," International Conference on Magnet Technology, Boston, Sept. 1987.

Ledbetter, H.M., "Temperature behavior of Young's modulus of forty engineering alloys," in Materials Studies for Magnetic Fusion Energy Applications at Low Temperatures - IV, NBSIR 81-1645, R.P. Reed, ed., National Bureau of Standards, Boulder, Colorado (April 1981) pp. 257-269.

Ledbetter, H.M., N.V. Frederick and M.W. Austin, "Elastic-constant variability in stainless-steel 304," *J. Appl. Phys.*, 51, pp. 305-309, 1980.

Lee, E. W. and N.J. Kim, "Microstructural effects on anisotropy of Al-Li alloy 2090," Aluminum-Lithium Alloys V, *ibid.*, 1989.

Lipinski, P., M. Berveiller, A. Hihi, P. Sainfort and P. Meyer, "Effect of crystallographic and morphologic textures on the anisotropy of mechanical properties of Al-Li alloys," Aluminium-Lithium Alloys III, *ibid.*, pp. 613- 619.

Marinaro, D.E., Alcoa Technical Center, Pittsburgh, Pennsylvania, private communication, 1989.

Malcolm, R.C., F.J. Cordier and R.J. Bucci, "The effect of various thermal conditions on the tensile properties of aluminum alloy 2090-T8E41 plate (0.500-inch thick)," Alcoa Laboratories Alloy Technology Division, Report 56-86-AH429, 1986.

Martukanitz, R.P., C.A. Natalie and J.O. Knoefel, Alcoa Laboratory PREN Division Report 52-87-20, 1987.

McHenry, H.I., in *Materials at Low Temperatures*, R.P. Reed and A.F. Clark, eds., ASM, Warrendale, PA 1983.

Mecking, H., "Description of Hardening Curves of FCC Single and Polycrystals," in: "Work Hardening in Tension and Fatigue," ed. A.W. Thompson, TMS-AIME, New York, NY, pp. 67-88, 1975.

Meister, R.P. and D.C. Martin, "Welding of aluminum and aluminum alloys," DMIC Report 236, Defense Metals Information Center, Battelle Memorial Institute, Columbus, Ohio, 1967.

Meyer, P., Y. Cans, D. Ferton and M. Reboul, "The metallurgy of industrial Al-Li alloys," Aluminium-Lithium Alloys III, *ibid,*. pp 131-138, 1987.

Miller, W.S., J. White and D.J. Lloyd, "The physical metallurgy of aluminum-lithium-copper-magnesium-zirconium alloys - 8090 and 8091," Al-Li IV, *J. Physique,* 48, no.9, 1987, C3:139-149.

Mintz, B. and W.B. Morrison, "Influence of warm working and tempering on fissure formation," *Matls. Sci. Tech.*, 4, pp. 719-731, 1988.

Mintz, B., W.B. Morrison, P.P. Morris and G.J. Davies, "The influence of texture on the tensile and impact properties of controlled-rolled steels," in *Texture and properties of materials,* (ed. G.J. Davies), pp. 224-234, London, The Metals Society, 1976.

Miura, Y., K. Yusu, M. Furukawa and N. Nemoto, "Temperature dependence of yield strength of Al-Li singles crystals," Aluminum-Lithium Alloys IV, *ibid.*, pp. 549-555.

Morris, J.W., Jr. and J. Glazer, "Mechanical properties of high-strength aluminum alloys at cryogenic temperatures," *International Cryogenic Materials Conference,* Shenyang, China, pp. 713-726, 1988.

Morrison, W.B., "Influence of testing direction on the mechanical properties of wrought steel," *Metals Tech.*, 22, pp. 33-41, 1975.

Naimon, E.R., H.M. Ledbetter and W.F. Weston, "Low-temperature elastic properties of four wrought and annealed aluminum alloys," *J. Matls. Sci.*, 10, pp. 1309-1316, 1975.

Niinomi, M., K. Degawa and T. Kobayashi, "Effect of thermomechanical treatment on toughening of Al-Li-Cu-Mg-Zr alloy and its toughness," Aluminum-Lithium Alloys IV, *ibid,* 1988.

Peel, C.J., B. Evans, C.A. Baker, D.A. Bennett, P.J. Gregson and H.M. Flower, "The development and application of improved aluminium-lithium alloys," Aluminum-Lithium Alloys II, *ibid.*, pp.363-392, 1984.

Pendse, R.D. and R.O. Ritchie, "Influence of high pressure hydrogen pre-exposure on crack growth under monotonic and cyclic loading," in: *Modeling Environmental Effects on Crack Growth Processes,* TMS-AIME, Warrendale, PA, 1985.

Rao, K.T.V., H. Hayashigatani and R.O. Ritchie, "On the fracture toughness of aluminum-lithium alloys at ambient and cryogenic temperatures," *Scripta Met.*, 22, pp. 93-96, 1988.

Rao, K.T.V., W. Yu and R.O. Ritchie, "Cryogenic toughness of commercial aluminum-lithium alloys: role of delamination toughening," *Met. Trans.*, 20A, pp. 485-497, 1989.

Rao, K.T.V. and Ritchie, "Influence of extrinsic crack deflection and delamination mechanisms on the cryogenic fracture-toughness of commercial Al-Li alloys", Aluminum-Lithium Alloys V, *ibid.*, 1989.

Reed, R.P., "Aluminium: 2. A review of deformation properties of high purity aluminium and dilute aluminium alloys," *Cryogenics,* pp. 259-291, August, 1972.

Richert, M. "Localization of deformation in rolled aluminum," *Z. Metallkde,* 78, pp. 862-870, 1987.

Rioja, R.J. and E.A. Ludwiczak, "Identification of metastable phases in Al-Cu-Li alloy (2090)," Aluminum-Lithium Alloys III, *ibid.*, pp. 471-482.

Ritchie, R.O., B. Francis and W.L. Server, "Evaluation of toughness in AISI 4340 alloy steel austenitized at low and high temperatures," *Met. Trans.*, 7A, pp. 831-838, 1976.

Ritchie, R.O., W.L. Server and R.A. Wullaert, "Critical fracture stress and fracture strain models for the prediction of lower and upper shelf toughness in nuclear pressure vessel steels," *Metall. Trans.*, 10A, pp. 1557-1570, 1979.

Robinson, J., "Getting the space plane off the ground," J. Metals, July, 1987 pp.8-9.

Roth, M.C., G.C. Weatherly and W.A. Miller, "The temperature dependence of the mechanical properties of aluminum alloys containing low-melting-point inclusions," *Acta Metall.*, 28, pp. 841-853, 1980.

Saji, S., K. Yasuhara and S. Hori, "Mechanical properties of 7075 aluminum alloy at 6-130 K," *Trans. JIM*, 28, pp. 773-780, 1987.

Sanders, T.H. Jr., " Al-Li-X alloys --an overview," Aluminum-Lithium Alloys, *ibid.*, pp. 63-67, 1981.

Schmidt, C.G. and A.K. Miller, "The effect of solutes on the strength and strain hardening behavior of alloys, *Acta Metall.*, 30, pp. 615-625, 1982.

Shepic, J.A. and C. Fiftal, "Testing of 2219-T87 aluminum alloy at 4 K," in: *Materials studies for magnetic fusion energy applications at low temperatures - II.*, NBSIR 79-1609, National Bureau of Standards, Boulder, Colorado, pp. 17-31, 1979.

Sih, G.C. and R.J. Hartranft, "Variation of strain energy release rate with plate thickness," *Int. J. Fract. Mech.*, 9, pp. 75-82, 1973.

Smith, E., "Dislocations and fracture" in: Dislocations and Properties of Real Materials, Proceedings of the conference to celebrate the fiftieth anniversary of the concept of dislocations in crystals, December 1984; The Institute of Metals, 1985, pp. 205-220.

Starke, E.A., Jr. and T.H. Sanders, Jr., "New approaches to alloy development in the Al-Li system," *J. Metals.*, August. 1981, pp. 24-32.

Sunwoo, A.J. and J.W. Morris, Jr., "Weldability of 2090 Al-Cu-Li alloy," to be published in American Welding Society Journal.

Sunwoo, A.J. and J.W. Morris, Jr., "Cryogenic tensile properties of AA 2090 weldments," Aluminum-Lithium Alloys V, *ibid.*, 1989.

Suresh, S., A.K. Vasudévan, M. Tosten and P.R. Howell, "Microscopic and macroscopic aspects of fracture in lithium-containing aluminum alloys," *Acta Metall.*, 35, pp. 25-46, 1987.

Tamura, M., T. Mori and T. Nakamura, "Plastic deformation of Al-Li single crystals containing Al_3Li particles," *Trans. JIM*, 14, pp. 355-363, 1973.

Tanaka, T., "Deformation in the (austenite plus ferrite) two-phase region" in: *Thermomechanical processing of high-strength low alloy steels,* by I. Tamura, C. Ouchi, T. Tanaka and H. Sekine, Butterworths, London, 1988, pp. 101-116.

Thomas, G., S. Miyasoto and V. Radmilovic, Center for Advanced Materials, Lawrence Berkeley Laboratory, presentation at WESTEC Aluminum-Lithium conference, 1988.

Thomason, P.F., "A theoretical relation between K_{Ic} and basic material properties in ductile metals," *Int. J. Fract. Mech.*, 7, pp. 409-419, 1971.

Thornton, P.H., R.G. Davies and T.L. Johnston, "The temperature dependence of the flow stress of the γ' phase based on Ni_3Al," *Met. Trans.*, 1, pp. 207-218, 1970.

Tobler, R.L. and R.P. Reed, "Fracture mechanics parameters for a 5083-O aluminum alloy at low temperatures," *Trans. ASME*, 99, pp. 306-312, 1977.

Tosten, M.H., A.K. Vasudévan and P.R. Howell, "Microstructural development in Al-2%Li-3%Cu alloy," Aluminum-Lithium Alloys III, *ibid.*, pp. 483-489.

Tosten, M.H., A.K. Vasudévan and P.R. Howell, "The aging characteristics of an Al-2 pct Li-3 pct Cu-0.12 pct Zr alloy at 190°C," *Met. Trans.*, 19A, p. 51-66, 1988.

Vasudévan, A.K., W.G. Fricke, Jr., R.C. Malcolm, R.J. Bucci, M.A. Przystupa and F. Barlat, "On through thickness crystallographic texture gradient in Al-Li-Cu-Zr alloy," *Met. Trans*, 19A, pp. 731-732, 1988.

Verzasconi, S.L., "Cryogenic mechanical properties of low density superplastic aluminum alloys," M.S. Thesis, University of California, Berkeley, 1989.

Vincent, S.A., "An investigation of the influence of dislocation substructure on the deformation behavior of AK, DQ steel sheets," M.S. Thesis, University of California, Berkeley, 1987.

Wadsworth, J., C.A. Henshall, A.R. Pelton and B. Ward, "Superplastic properties of an Al-Cu-Li-Zr alloy," *J. Mater. Sci. Lett.*, 4, p. 674, 1985.

Webster, D., "Aluminum lithium alloys," *J. Metals*, pp. 33-37, 1984.

Webster, D., "Temperature dependence of toughness in various aluminum-lithium alloys," Aluminum-Lithium Alloys III, *ibid.*, pp. 602-609, 1986.

Webster, D., "The effect of low melting point impurities on the properties of aluminum-lithium alloys," *Metall. Trans*, 18A, pp.2181-2193, 1987.

Webster, D., "The effect of low melting point phases on the elevated temperature microstructural stability of hot pressed beryllium," *Met. Trans.*, 6A, pp. 803-808, 1975.

Welpmann, K.H., Y.T. Lee and M. Peters, "Low temperature deformation behaviour of 8090," Al-Li V, *ibid*, 1989.

Westinghouse Electric Corporation, Pittsburgh, PA, "Superconducting magnet coils for Large Coil program, Phase 2," Final Report to Union Carbide Corp., Oak Ridge, Tennessee, on contract no. 22X-31747C (March 31, 1980)

Yoshimura, H., H. Matsumoto and T. Inoue, *Adv. Cryo. Eng.*, 28, pp. 115-125, 1982.

APPENDIX 1. MATERIAL CONDITION AND ORIENTATION DESIGNATION CODES.

Thermal and mechanical processing codes. There are standard designations in the aluminum industry that describe concisely common sequences of thermal and mechanical processing. Although the processing of the alloys investigated in this study is described in detail, data are referred to for a number of other aluminum alloys whose metallurgical condition is described only by these codes. Accordingly, a partial list of these temper designations, abstracted from Aluminum [J.E. Hatch, ed., ASM, 1984], is provided below:

F As-fabricated: Products of shaping processes in which no special control is exercised over temperature or strain-hardening.

O Annealed: For wrought products, annealed to provide the lowest strength temper.

H Strain-hardened

T Thermally treated to produce stable tempers other than F, O or H: Product thermally treated with or without strain hardening to produce a substantially stable condition.

T tempers are always further specified. Natural aging refers to precipitate hardening at room temperature; artificial hardening to aging at an elevated temperature. Some of the possible treatments are:

T3 Solution heat treated, cold worked and naturally aged
T4 Solution heat treated and naturally aged
T6 Solution heat treated and artificially aged (usually to peak strength)
T8 Solution heat treated, cold worked and artificially aged

A second digit indicates a particular processing sequence. For example, 2090-T81 refers to a particular -T8 processing: solution heat treatment, followed by a 6% stretch and aging for 24 hours at 163°C. The combination -T8X refers to a specific experimental -T8 treatment.

Occasionally, an additional suffix is used in combination with one of the temper designations given above, for example (for sheet and plate)

T—51 Stress relieved by stretching $1\frac{1}{2}$ to 3% permanent set

Thus -T651 means solution treated, stress relieved by stretching and aged at elevated temperature.

Orientation codes. The properties of wrought material such as sheet and plate are anisotropic with respect to the primary working, or rolling, direction. The rolling direction is termed the longitudinal, or L, direction. The perpendicular direction in the plane of the plate is referred to as the transverse (T) or long-transverse (LT) direction to distinguish it from the through-thickness direction, the short (S) or short-transverse (ST) direction. The directions in the plate and the designations for tensile and fracture toughness specimens with standard orientations with respect to these directions are given in Figure A1.

APPENDIX 2. DERIVATION OF RELATION BETWEEN K_C AND K_{IC} FOR SPECIMEN THICKNESSES IN THE TRANSITIONAL THICKNESS REGION.

There are several models that predict fracture toughness for thicknesses below that required for plane strain. The results have been summarized by Broek [1986]. Derivations of two of these relations are given here to illustrate the assumptions of these theories and the regimes of their applicability.

Bluhm [1961] estimates the total energy to propagate a crack in a sheet in the transitional thickness range by dividing the thickness into plane stress and plane strain regions. He then assumes that the energy for plane stress shear is volumetric while the energy required for flat fracture in plane strain is dominated by surface terms. Then the energy dW absorbed in extending the crack by an amount da is:

$$dW = \tfrac{1}{2}\theta B^2 da \qquad B<B_o \qquad \text{(A2.1a)}$$

$$dW = [\tfrac{1}{2}\theta B_o^2 + \kappa(B-B_o)]\, da \qquad B>B_o \qquad \text{(A2.1b)}$$

where θ and K are material constants and B_o is the maximum thickness at which full plane stress is developed. Since

$$G_c = \frac{1}{B}\frac{dW}{da} \qquad \text{(A2.2)}$$

when $B < B_o$ (the plane stress regime)

$$G_c = \frac{K_{1c}^2}{E} = \frac{1}{2}\theta B \qquad \text{(A2.3)}$$

and

$$\frac{K_c}{K_c^{max}} = \sqrt{\frac{B}{B_o}} \qquad \text{(A2.4)}$$

When $B \to \infty$ (plane strain)

$$G_{Ic} = \frac{K_{Ic}^2}{E} = \kappa. \qquad \text{(A2.5)}$$

Strictly, for plane strain, E should be replaced by $E(1-\nu^2)$.

Combining relations A2.1a and A2.5 gives

$$\frac{K_c}{K_{Ic}} = \sqrt{1 + (\frac{1}{2}\theta B_o \frac{E}{K_{Ic}^2} - 1)\frac{B_o}{B}} \qquad B > B_o. \qquad \text{(A2.6)}$$

Equating B_o to the plastic zone size in plane strain

$$B_o \sim \frac{K_{Ic}^2}{3\pi\sigma_y^2}$$

gives

$$\frac{K_c}{K_{Ic}} = \sqrt{1 + \left(\frac{E\theta}{6\pi\sigma_y^2} - 1\right)\frac{B_o}{B}} \qquad B > B_o \qquad \text{(A2.7)}$$

which is equation 8.23 in Broek. Isherwood and Williams [1970] find that for a non-work-hardening material,

$$K_c^2 = E\sigma_y\delta \qquad B < B_o \qquad \text{(A2.8)}$$

where δ is the crack opening displacement. By further assuming that $\delta/B \sim \frac{1}{2}\varepsilon_f$ where ε_f is the strain-to-failure in uniaxial tension, $\theta = \sigma_y\varepsilon_f$ may be obtained from equation A2.1a. There is an implicit assumption here that the value of ε_f in a triaxial stress state is about one-half the value in uniaxial tension. Using $\delta/B \sim \frac{\pi}{8}\varepsilon_f$ (which is numerically similar) leads to the equation given by Broek and Vlieger [1974]

$$\frac{K_c}{K_{Ic}} = \sqrt{1 + \left(\frac{\varepsilon_f E}{24\sigma_y} - 1\right)\frac{B_o}{B}} \qquad B > B_o. \qquad \text{(A2.9)}$$

These equations provide a method of predicting K_c in terms of K_{Ic} at any thickness since equations A2.7 and A2.9 can be used to predict the value of K_c^{max} in equation A2.4.

References:

Bluhm, J.I., "A model for the effect of thickness on fracture toughness," *ASTM Proc. 61.*, pp. 1324-1331, 1961.

Broek, D., *Elementary engineering fracture mechanics,* 4th edition, Martinus Nijhoff Publishers, 1986.

Broek, D. and H. Vlieger, "The thickness effect in plane stress fracture toughness," Natl. Aerospace Inst. Amsterdam, Rept. 74032, 1974

Isherwood, D.P. and J.G. Williams, "The effects of stress-strain properties on notched tensile failure in plane stress," *Eng. Fract. Mech.*, 2, pp. 19-35, 1970.

APPENDIX 3. USE OF CIRCUMFERENTIALLY NOTCHED TENSILE SPECIMENS TO OBTAIN ELONGATIONS IN TRIAXIAL STRESS STATES

Strain-controlled theories of fracture lead to a dependence of the fracture toughness on some measure of the ductility of the material. The evaluation of this parameter is a major problem in the quantitative application of these theories. The strain-to-failure, ε_f, is sometimes taken for simplicity as either the uniform or total elongation in tension, but is often identified as the strain-to-failure in the stress state under which the toughness test is being conducted. It is generally assumed that the value of ε_f in triaxial stress states is simply proportional to its value in uniaxial tension. A common rule of thumb (used by Chan) is that the value of ε_f in plane strain is one-third of its value in uniaxial tension. This assumption is based on the use of the Von Mises' equivalent strain. It depends on the macroscopic isotropy of the material. Aluminum-lithium alloys can deviate significantly from this idealization.

There are two difficulties that must be resolved in order to determine the value of ε_f. The first is selecting the stress state at the point in the fracture process in which the ductility is relevant; although it is of great importance to a quantitative theory, this question is beyond the scope of this work. The second problem is measuring ε_f in stress states other than uniaxial tension. It is desirable to know the value of ε_f in various stress states both to limit the possible range of values relevant to theory and to check whether the relative values in different stress states remain the same when other conditions such as test temperature are varied. A single point can be obtained by using a plane strain tension specimen of the sort described by Clausing [1970]. Another possible specimen that allows a variety of stress states to be examined is a round tensile specimen with a machined circumferential notch of circular profile. The advantages and disadvantages of this specimen are discussed in the following.

Bridgman [1956] has performed an analysis of tensile necking that allows the true stress and strain distribution in the neck to be determined from its minimum diameter. On the basis of experimental observations, Bridgman assumed that the strain is uniform across the neck of the tensile specimen and that the surfaces of constant principal stress in the region of the neck have uniform curvature. He further assumes that the strain hardening rate is zero once necking begins; this assumption is reasonable since the necking criterion is satisfied only when the strain hardening rate has decreased to a value far below its initial one. These assumptions lead to the relations

$$\varepsilon_{zz} = -2\varepsilon_{rr} = -2\varepsilon_{\theta\theta} = -2 \ln d/d_o \qquad \text{A3.1}$$

and

$$\frac{\sigma_m}{\bar{\sigma}} = \frac{1}{3} + \frac{\sigma_{rr}}{\bar{\sigma}} = \frac{1}{3} + \ln(1 + a/2R) \qquad \text{A3.2}$$

where ε_{zz}, ε_{rr} and $\varepsilon_{\theta\theta}$ are the longitudinal, radial and hoop strains respectively, d and d_o are the current and original diameters of the specimen at the neck, a is the cross-section radius and R is the profile radius of curvature of the neck. The ratio of σ_m, the mean

normal stress and $\bar{\sigma}$, the Von Mises' equivalent stress, defines the triaxiality of the stress state. Relation A3.1 is exact before necking and is assumed to apply in the neck, where d = 2a. Relation A3.2 applies only at the center of the specimen where the stresses σ_{rr} and $\sigma_{\theta\theta}$ are highest. These relations appear to work fairly well experimentally for necking of initially smooth tensile specimens. It has been shown that failures do initiate in the center of the specimen where the stresses are the highest. The analysis has also been extended to provide the stresses along the central axis of the specimen away from the minimum diameter of the neck [Argon, Im and Needleman, 1975].

A number of investigators have used the Bridgman analysis to derive the stress and strain distribution in specimens in which a circumferential notch has been machined [e.g. Mackenzie, Hancock and Brown, 1977; Ritchie, Server and Wullaert, 1979; Rao, Yu and Ritchie, 1989]. The objective of these studies is generally to determine ε_f in stress states of varying degrees of triaxiality. However, the Bridgman analysis does not apply exactly to this case. Qualitatively, the accuracy of the solution must decrease as the ratio a/R becomes large; when this ratio becomes very large, the specimen approaches the geometry of a conventional notched tensile specimen and the stresses and strains are maximum near the notch rather than in the center of the specimen.

McClintock [1971] has summarized the results of Clausing [1966] and Norris [1967] for specimens with an initial machined notch profile. In these specimens the value of ε_{zz} need not be constant at every point on the plane of the neck. Clausing has found an approximate strain distribution for a specimen with an initial neck. The relations are of the form

$$d\varepsilon_{zz} = -2(1 + 2Cr^2/a^2)\, d \ln d/d_0 \qquad \text{A3.3}$$

where r is the radial distance from the center of the specimen and C is a constant related to the strain increment ratio $d\varepsilon_{zz}/d\varepsilon_{\theta\theta}$. The coefficient C is about 2/3 for specimens with an initial a/R ratio of 1.5, but decreases toward zero with strain. Prompted by this result, Argon et al. [1975] showed experimentally that the Bridgman analysis could be made to apply at all strains if the specimen was machined with a "natural neck" profile rather than a circular one.

If the material is allowed to strain harden, the analytic results differ significantly from the Bridgman analysis. Argon et al. point out that for a linearly hardening material the triaxiality is maximum at the outer surface of the neck and decreases toward the specimen center and away from the neck. The non-hardening bound (Bridgman analysis) will be a better approximation if the material is ductile and the strain hardening rate decreases significantly before failure; however, if the specimen breaks at low strains when the strain hardening rate is still high, the linear material may be more representative.

Beremin [1980] has done a finite element analysis of circumferentially notched specimens of varying notch severity using the stress-strain curve of a mild steel as a constitutive relation. The necking strain of this alloy in simple tension was about 11%. Beremin showed that the initial plasticity occurred near the notch and then spread out until a distribution of plastic strain like the Bridgman distribution was achieved. The evolution to

a uniform strain distribution was much more rapid when the notch was shallow. Even when a/R = 0.5, a relatively small value, the deviation of the exact solution from the Bridgman solution is substantial; the triaxiality $\sigma_m/\bar{\sigma}$ at the center of the specimen is 0.56 rather than 0.72; however, in this case the deformation is relatively homogeneous in the cross section. In the specimens with sharper notches - in their study, a/R = 1.2 and 2.5 - the Bridgman solution is not just quantitatively, but qualitatively, different from the exact solution; the triaxiality remains maximum at the center of the specimen, but the strain is much greater at the periphery of the specimen. For a/R = 2.5, the strain ratio $\bar{\varepsilon}/\varepsilon_{zz}$ is 1.8 at the periphery as opposed to the Bridgman value of 1.

These results suggest that the Bridgman analysis must be applied to circumferentially notched specimens with caution. It will work passably under a particular set of conditions: a) a relatively large failure strain even in triaxial stress states that allows evolution toward uniform plastic strain in the neck [e.g. Mackenzie's study in which $\varepsilon_f = -0.2$ even for $\sigma_m/\bar{\sigma} = -1.3$], b) a relatively low strain hardening rate (usually achieved if there is significant strain before failure), and c) a relatively small value of a/R. When none of these requirements are met use of the Bridgman analysis can result in significant misinterpretation of the experimental data in addition to incorrect values of the stress triaxiality and strain. In particular, at large values of a/R and low failure strains, the specimen may fail near the notch where the strains are high, rather than in the region of maximum triaxiality where the strains are low. In addition, any plastic strain anisotropy will distort the results further since a specimen of initially circular cross section becomes elliptical.

Most of the conditions that can make the Bridgman analysis of dubious applicability in circumferentially notched specimens exist for aluminum-lithium alloys. The average triaxial strains appear to be low [Rao et al., 1989] so that the strain hardening rate at failure in triaxial stress states will be relatively high. While at room temperature the strain hardening rate is relatively low after a few percent deformation, at low temperatures it is substantially increased at all strains. Furthermore, the plastic strain ratio is always less than 0.5 in wrought aluminum-lithium alloys, so that a round specimen becomes elliptical with deformation.

McClintock, F.A., "Plasticity aspects of fracture," in *Fracture: An advanced treatise*, ed. H. Liebowitz, Vol. 3, pp. 47-225.

Argon, A.S., J. Im and A. Needleman, "Distribution of plastic strain and negative pressure in necked steel and copper bars," *Met. Trans.*, 6A, pp. 815-824, 1975.

Mackenzie, A.C., J.W. Hancock and D.K. Brown, "On the influence of state of stress on ductile failure initiation in high strength steels," *Eng. Fract. Mech.*, 9, pp 167-188, 1977.

Clausing, D.P., "Tensile fracture of steel," PhD thesis, California Institute of Technology, Pasadena, CA, 1966.

Clausing, D.P., "Effect of plastic strain state on ductility and toughness," *Int. J. Fract. Mech.*, 6, pp. 71-85, 1970.

Norris, K.C., "Strain in the neck of a tensile specimen," M.S. Thesis, Massachusetts Institute of Technology, 1967.

Beremin, F.M., "Calculs élastoplastiques par la méthode des éléments finis d'éprouvettes axisymétriques entaillées circulairement," *J. Mec. Appl.*, 4, pp. 307-325.

APPENDIX 4. ESTIMATION OF STACKING FAULT ENERGY USING PSEUDOPOTENTIAL THEORY

The pseudopotential theory of metallic bonding provides a simple method of comparing the energies of potential metallic crystal structures for simple metals. The ranges of stability for common metallic crystal structures can be predicted under various stability criteria as a function of Z, the electron to atom ratio. The properties of uniform random solid solutions of simple metals can also be studied through use of the virtual crystal model; the alloy is treated as a one-component simple metal of pseudoatoms of averaged properties. The energies associated with faults in these structures, such as stacking faults and twins, can also be estimated [Blandin et al., 1966; Krause, 1974]. The structure-dependent part of the cohesive energy of the crystal is calculated by applying second-order perturbation theory to the interaction between the electron gas and the ionic pseudopotentials. The potential used in the models described here is for well separated ions whose electrostatic interaction is screened by an electron gas. This potential was first proposed by Friedel and is

$$V(r) = V_o \frac{\cos 2k_f r}{(2k_f r)^3} \qquad \text{(A4.1)}$$

where k_f is the Fermi wave-vector and V_o is a structure independent constant. The value of V_o depends on the parameters of the pseudopotential; the choice of V_o is the main difference between the approaches of Krause and Blandin, et al. The interaction between planes can be obtained from partial sums of the Friedel potential. The interplanar interaction energies make it relatively easy to calculate energies of stacking faults.

To summarize, the major assumptions of this model beyond those of pseudopotential theory are:

1) the effective interatomic potential is replaced by the Friedel potential which is its asymptotic form;

2) the variation in equilibrium atomic volume between crystal structures is ignored;

3) solid solutions are treated using pseudoatoms of average properties.

In spite of these assumptions, the model has been found to predict equilibrium crystal structures with reasonable success.

It was hoped that this model could be used to predict the relative effects of various alloying elements on the intrinsic stacking fault energy of aluminum. The required equations are sketched below.

For a face centered cubic crystal, the energy of an intrinsic stacking fault is given by

$$\Delta E = \frac{V_o}{(\sqrt{3}a^2/2)} \sum_{n=1}^{\infty} [3n\,\Delta\phi(3nd) - (3n-1)\,\Delta\phi((3n-1)d)] \qquad \text{(A4.2)}$$

where a is the nearest neighbor distance in the plane, n is the number of atomic planes separating each pair of planes whose interaction is being summed, d is the interplanar distance and $\Delta\phi$ is the energy per unit area. For a face centered cubic crystal, the atomic volume Ω is given by $a^3/\sqrt{2}$.

The equation for $\Delta\phi$ depends on whether or not the electron-atom ratio Z is greater than the valence Z_c at which the first non-zero reciprocal lattice vector equals $2k_f$. This value is 1.14 when the structure is ideally close-packed, so for aluminum $Z > Z_c$. The expression obtained by Blandin et al. for $Z > Z_c$ for $\Delta\phi$ is:

$$\Delta\phi(nd) = A\frac{\sin n\theta}{n^2} \tag{A4.3}$$

where

$$A = \frac{V_o k_f^2 (1-(Z_c/Z)^{2/3})^{1/2}}{(2\pi)^3 Z^2}. \tag{A4.4}$$

$$k_f = \left(\frac{3\pi^2 Z}{\Omega}\right)^{1/3} \tag{A4.5}$$

and $$\theta = 5.67(Z^{2/3} - Z_c^{2/3}) \tag{A4.6}$$

This potential goes to zero as Z approaches Z_c, so that region cannot be treated accurately by this model. The required infinite sums of the sine term in $\Delta\phi(nd)$ have been evaluated by Blandin et al. The intrinsic stacking fault energy is given by

$$A\left[\frac{V_o}{(\sqrt{3}a^2/2)}\right] x \frac{\sqrt{3}}{6}\left[\beta\left(\theta+\frac{4\pi}{3}\right) - \beta\left(\theta+\frac{2\pi}{3}\right)\right] + \frac{1}{2}f(\theta) \tag{A4.7}$$

where $$\beta(\theta) = \sum_{n=1}^{\infty}\frac{\cos n\theta}{n} = -\ln\left(2\left|\sin\frac{\theta}{2}\right|\right) \tag{A4.8}$$

and $$f(\theta) = 2\pi - \theta \text{ for } \frac{4\pi}{3} < \theta < 2\pi. \tag{A4.9}$$

These formula allow the stacking fault energy to be evaluated in terms of three parameters, the values of a, Z and V_o appropriate to the alloy or solid solution under consideration. A similar set of formulae exist for hexagonal close-packed metals. Both Krause and Blandin, et al give values for V_o. These values depend on the exact pseudopotential used to calculate them and they differ, significantly in some cases. These differences were not considered by Krause since while they affect the magnitude of the stacking fault energy and the

influence of alloying elements on the stacking fault energy, they do not affect the criteria for phase stability, which depend solely on Z.

The stacking fault energy of aluminum is very high and is generally believed to be between about 150 and 200 ergs/cm^2. Blandin, et al predict a value of about 150 ergs/cm^2, which is reasonable, but if the value of V_0 given by Krause, et al. is used instead, the predicted value is only 90. However, neither model seems to do a good job of predicting the accepted belief that the addition of most solutes will lower the stacking fault energy of aluminum. In the model, the Z value of 3 for aluminum places it squarely within an fcc stability range than extends from Z = 2.2 to Z = 3.5. For this reason relatively small additions of solute atoms would not be expected to change the stacking fault energy greatly. Lowering the Z value slightly by the addition of monovalent (Li) or divalent (Mg) species might even be expected to raise the stacking fault energy on this basis, although both elements have lower values of V_0 that would counterbalance this effect. Calculations performed using the equations given above for additions of 5 atomic percent or less of Li and Mg bear this out. In both cases the stacking fault energy increases slightly. Large additions of Zn are also predicted to increase the stacking fault energy.

The stacking fault energy cannot be measured directly, but as was alluded to above, the available experimental results to do not seem to agree with the predictions of this theory. Both Mg [Kannan and Thomas, 1966] and Zn [Lee, Kranzlein and Underwood, 1971] have been reported to decrease the stacking fault energy of aluminum significantly, which would not be surprising since both crystallize in a hexagonal structure as pure metals. Most of the other cases in which alloying has been found to significantly affect the stacking fault energy involve Cu, Ag or Au [see Gallagher, 1970 for a review]. None of these elements have the crystal structure predicted by this model for their generally accepted values of Z; the model is unlikely to predict the influence of these elements on stacking fault energy either. The discrepancy between the experimental and predicted results suggests one of three things. One possibility is that the pseudoatom approach to alloys fails rather badly, particularly in concentrated alloys; Lee et al. found significantly elevated Zn concentrations at the stacking faults in an Al-21Zn alloy. A second possibility is that the solute atoms interact with the partial dislocations bounding the faults causing the effective stacking fault energy measured experimentally to decrease [Gallagher, 1970]. These interactions may have a much greater effect on the deformation behavior and consequent mechanical properties than the change in equilibrium dislocation pair spacing that would result from the influence of the solute addition on the energy of the structure alone. A third possibility applies to aluminum in particular. Gallium crystallizes in a distorted fcc structure not considered in this type of model. Aluminum, next to gallium on the periodic table, is only marginally stable with respect to this structure. An investigation of the effectiveness of various solutes in hardening aluminum concluded that the data could be most easily interpreted by assuming that aluminum is nearly divalent [Dorn, et al., 1950]. Thus the variation in the stacking fault energy of Al may reflect instabilities of the crystal structure not considered in the model or differences in the effective valence.

References:

Blandin, A., J. Friedel and G. Saada, "Les energies de fautes d'empilement et de macles dans les metaux normaux," *J. de Physique,* Colloque C3, 27, pp. 128-136, 1966.

Dorn, J. E., P. Pietrokowsky and T. E. Tietz, "Effect of alloying elements on the plastic properties of Al alloys," *Trans. AIME,* 188, pp. 933-943, 1950.

Gallagher, P. C. J., "The influence of alloying, temperature, and related effects on the stacking fault energy," *Met. Trans.*, 1, pp. 2429-2461, 1970.

Kannan, V. C. and G. Thomas, "Dislocation climb and determination of stacking-fault energies in Al and Al-1%Mg, " *J. Appl. Phys.*, 37, pp. 2363-2370, 1966.

Krause, C. W., "The effect of a long range interatomic potential on the stability of crystal lattices, " Ph.D. thesis, University of California, Berkeley, 1974.

Krause, C. W. and J. W. Morris, Jr., "On the relative energies of simple metallic structures," *Acta Metall.*, 22, pp. 767-777, 1974.

Lee, E. U., H. H. Kranzlein and E. E. Underwood, "Stacking-fault energy of Al-21% Zn alloy," *Mater. Sci. Eng.*, 8, pp. 336-339, 1971.

FIGURE CAPTIONS

Figure 1.1 Variation of yield strength with temperature for a selection of fcc alloys. (Dashed lines denote aluminum alloys; solid lines denote steel alloys).

Figure 1.2 The strength-toughness-temperature relation of the aluminum alloys 2090-T81 and 2219-T87. The strength-toughness trend line for advanced aerospace aluminum alloys at room temperature (hatched band) is shown for comparison.

Figure 1.3 Fracture toughness relative to toughness at room temperature plotted as a function of temperature for selected fcc alloys. All specimens were in the L-T orientation unless specified otherwise. (Dashed lines denote aluminum alloys, dotted lines nickel alloys, and solid lines steel alloys.)

Figure 1.4 Tensile total elongation relative to elongation at room temperature plotted as a function of temperature for selected fcc alloys. All specimens were in the L orientation unless specified otherwise. (Dashed lines denote aluminum alloys, dotted lines nickel alloys, and solid lines steel alloys.)

Figure 1.5 Al-Cu-Mg section of the Al-Cu-Li-Mg phase diagram at 2-3 wt% Li. Compositions of commercial alloys and precipitate phases observed at various compositions are shown. (From Flower and Gregson, 1988.)

Figure 2.1 Composite optical micrograph showing grain structure of 2090-T81.

Figure 2.2 Composite optical micrograph showing grain structure of 2091-T8.

Figure 2.3 Bright-field, dark-field pair of transmission electron micrographs illustrating the microstructure of 2091-T8. The diffraction beam $g=\frac{2}{3}g_{220}$ corresponds to one variant each of the T_1 and S' precipitates. In the dark-field micrograph, T_1 plates are viewed edge-on as streaks, while S' rods are viewed end-on as dots. The δ' precipitate is also present.

Figure 2.4 Composite optical micrographs showing grain structure of superplastically formable modification of 2090.

Figure 2.5 Variation in elastic properties of 2090-T81 with temperature relative to the room temperature values given in Table 2.2.

Figure 2.6 Tensile specimen designs used in this study. Scale ~1:1 except d).

Figure 2.7 Design for short-transverse tensile specimen. Grip sections are attached by electron-beam welds.

Figure 5.14 Optical micrograph of polished and etched cross section perpendicular to crack path of 2090-T81 J_{Ic} specimen broken at 4 K. Splits appear to follow grain boundaries.

Figure 5.15 Optical micrographs of polished (all) and etched (top and bottom, only) cross section of 2090-T81 tensile specimen centered at T/4. Specimen was strained at 77 K to an engineering strain of 8%. Although there is extensive splitting in specimens broken at this temperature, no splits are observed in this strained but unbroken specimen.

Figure 5.16 Optical micrograph of polished cross section of 2090-T81 J_{Ic} specimen tested at 77 K. After crack had propagated a few millimeters, the specimen was sectioned about one millimeter from the crack plane and parallel to it. White lines are splits. The crack tip location is marked.

Figure 5.17 Schematic split profile obtained after digitizing splits in optical micrographs of polished cross section of J_{Ic} specimen. Data shown are for a 2090-T81 specimen tested at 77 K in the L-T orientation.

Figure 5.18 Histograms of split spacing for 2090-T81 specimens tested at 77 K in L-T and T-L orientations. Separate histograms were computed for splits deeper than the specified values.

Figure 5.19 Variation in mean split spacing with test temperature and minimum split depth for 2090-T81 and 2091-T8 J_{Ic} specimens in the L-T and T-L orientations. Note the change in the horizontal scale for L-T and T-L orientations.

Figure 5.20 Optical micrographs showing fracture profile and splitting in 2091-T8 J_{Ic} specimens. Specimens were sectioned perpendicular to crack path near the crack initiation point. Cross section shown is the entire thickness of specimen.

Figure 6.1 Schematic illustration of possible effects of temperature on apparent K_{Ic} in specimens that split. Possible effects on the K_c vs. specimen thickness curve and predicted toughness for various split spacings are shown. It is experimentally observed that the split spacing at 77 K is lower than at 300 K for both 2090-T81 and 2091-T8 in both test orientations.

Figure 6.2 Effect of intergranular delamination in crack-divider orientation on Charpy impact energy in an Fe-1Mn steel. Both the ductile-brittle transition temperature and the upper shelf toughness decrease with increasing amounts of splitting. (From Bramfitt and Marder, 1977.)

Figure 6.3 Calculated stresses under linear elastic fracture mechanics for 2090-T81, L-T tested at 300 K when the stress intensity is equal to K_{Ic}. It is assumed that plane strain conditions prevail. The origin is the crack tip. Top: Equivalent von Mises' stress contours parameterized by the plastic zone size R_p. Bottom: Calculated values of through-thickness stress σ_z along equivalent von Mises' stress contours shown above.

Figure 6.4 Calculated regions in which the through-thickness stress σ_z due to the applied stress intensity K_{Ic} exceeds the ST tensile fracture stress σ_f of 2090-T81 tested in the L-T orientation. The origin is the crack tip. The calculation assumes that plane strain linear elastic fracture mechanics apply.

Figure 6.5 Comparison of experimental results and predictions of various fracture theories for relative variation in fracture toughness K_{Ic} below room temperature due to changes in other material properties. Data are for 2090-T81 and 2091-T8 in the L-T and T-L orientations. Top: ε_f taken as uniform elongation; bottom: ε_f taken as total elongation. Equations are given in the text.

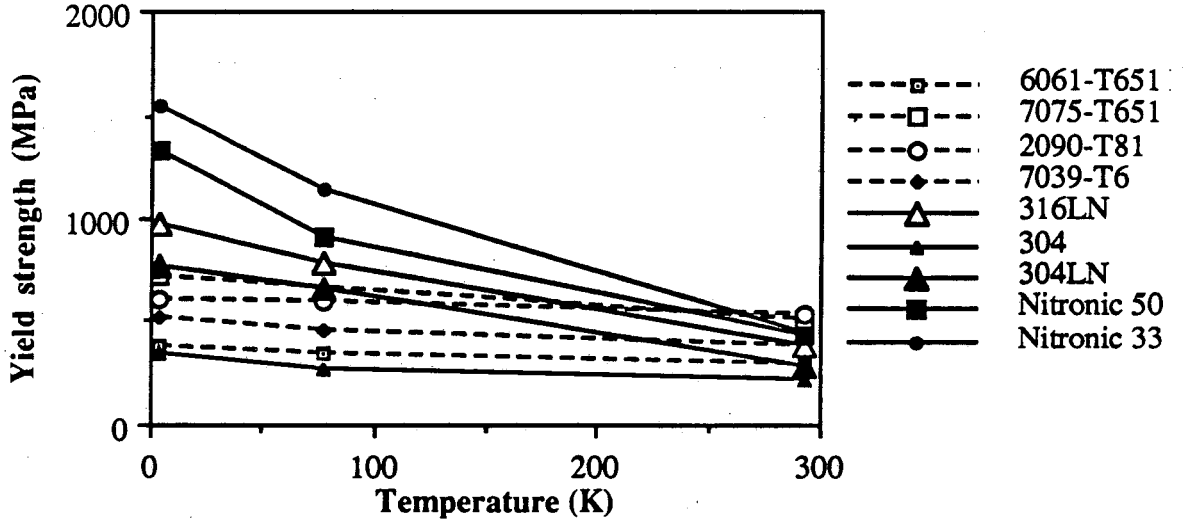

Figure 1.1 Variation of yield strength with temperature for a selection of fcc alloys. (Dashed lines denote aluminum alloys; solid lines denote steel alloys).

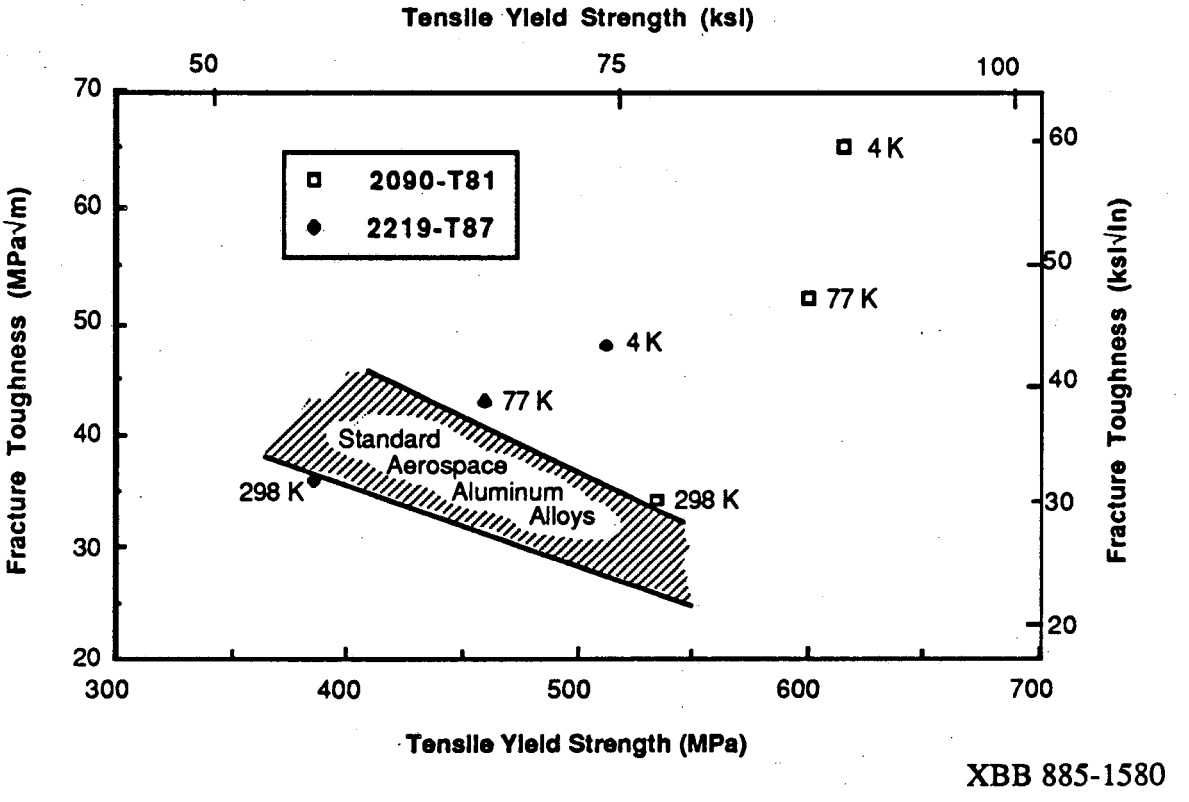

Figure 1.2 The strength-toughness-temperature relation of the aluminum alloys 2090-T81 and 2219-T87. The strength-toughness trend line for advanced aerospace aluminum alloys at room temperature (hatched band) is shown for comparison.

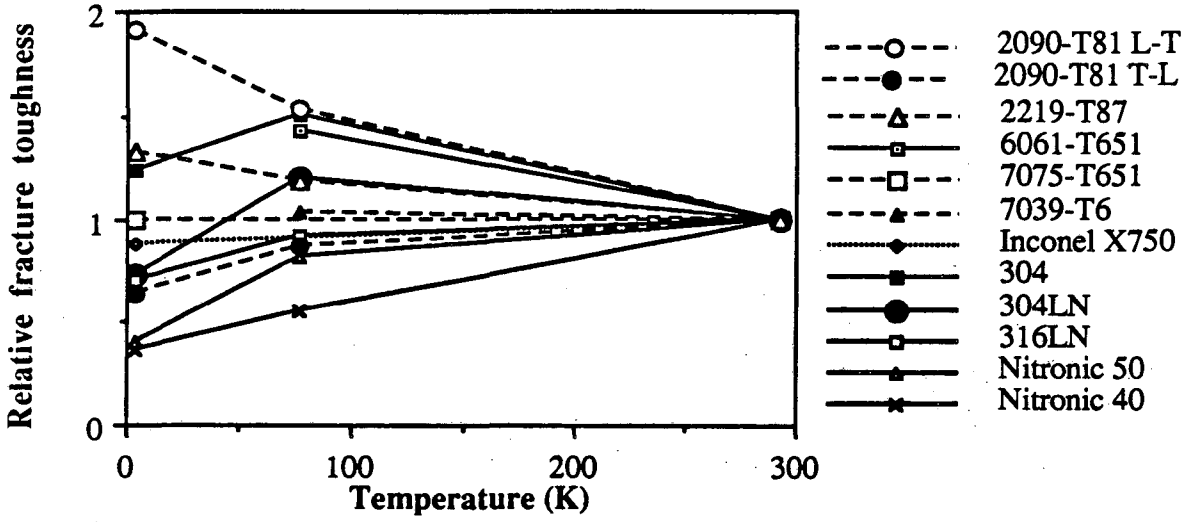

Figure 1.3 Fracture toughness relative to toughness at room temperature plotted as a function of temperature for selected fcc alloys. All specimens were in the L-T orientation unless specified otherwise. (Dashed lines denote aluminum alloys, dotted lines nickel alloys, and solid lines steel alloys.)

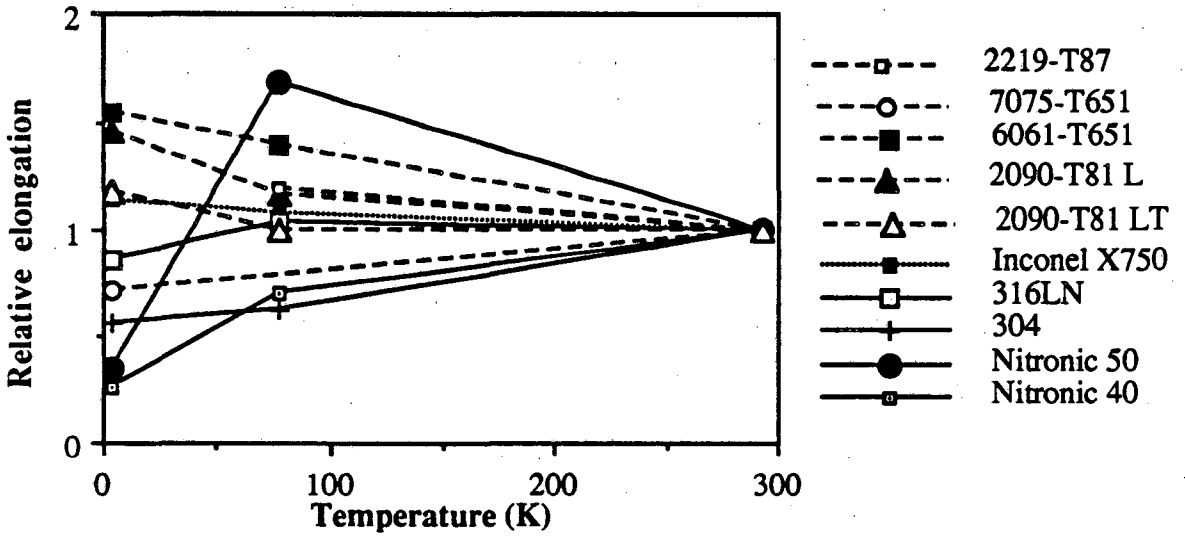

Figure 1.4 Tensile total elongation relative to elongation at room temperature plotted as a function of temperature for selected fcc alloys. All specimens were in the L orientation unless specified otherwise. (Dashed lines denote aluminum alloys, dotted lines nickel alloys, and solid lines steel alloys.)

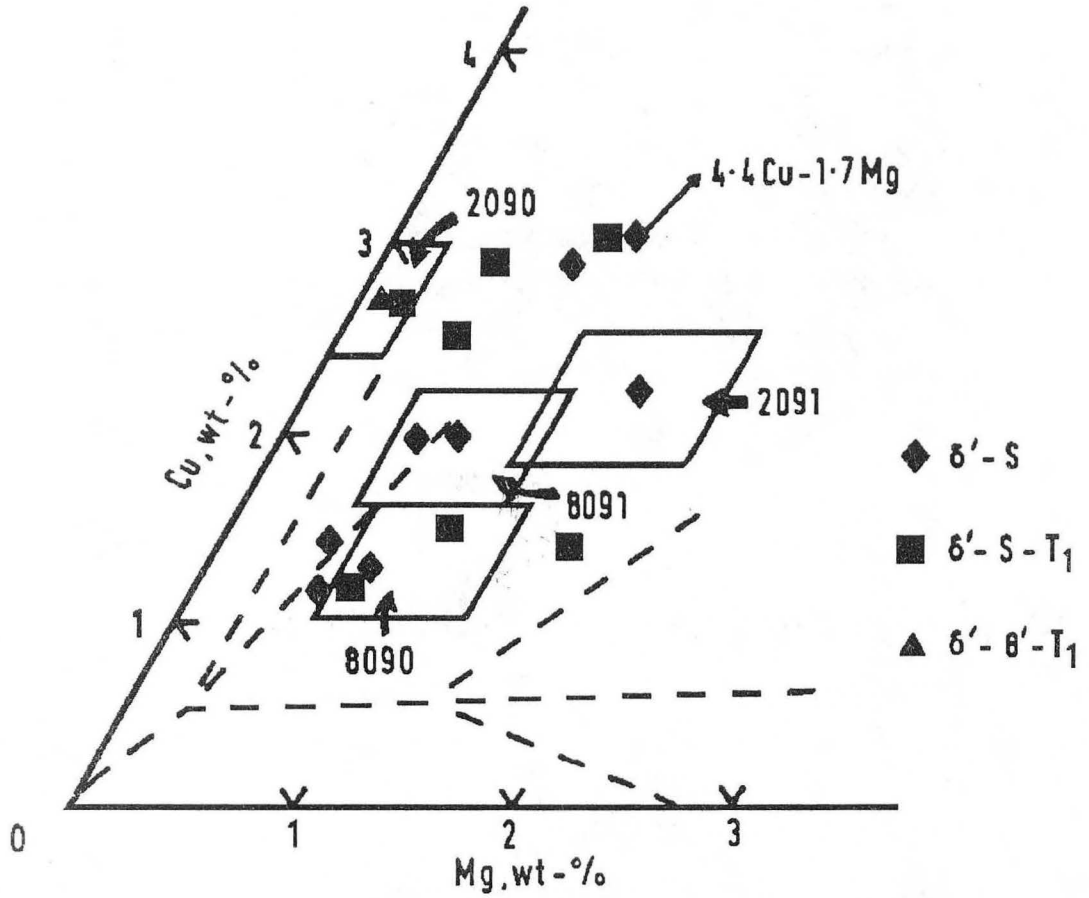

Figure 1.5 Al-Cu-Mg section of the Al-Cu-Li-Mg phase diagram at 2-3 wt% Li. Compositions of commercial alloys and precipitate phases observed at various compositions are shown. (From Flower and Gregson, 1988.)

XBB 857-5875

Figure 2.1 Composite optical micrograph showing grain structure of 2090-T81.

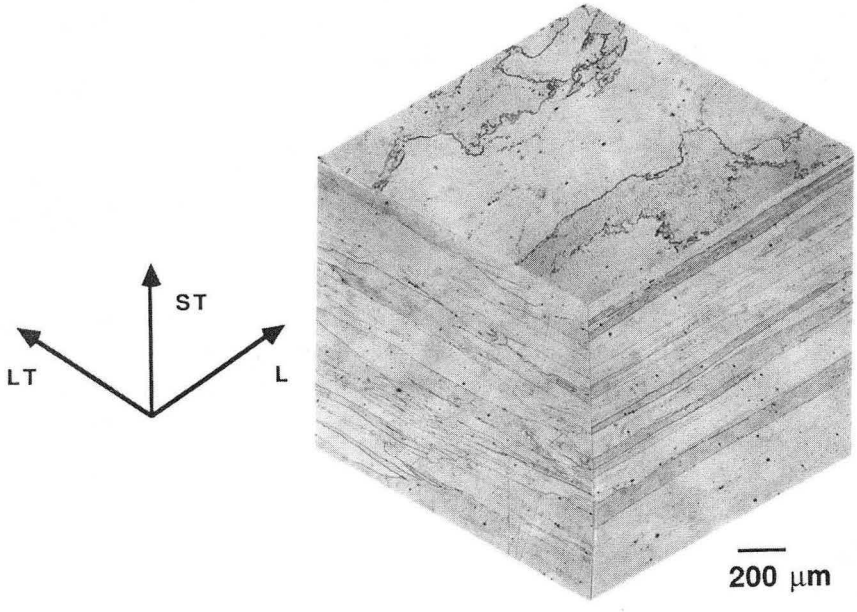

XBB 882-1499

Figure 2.2 Composite optical micrograph showing grain structure of 2091-T8.

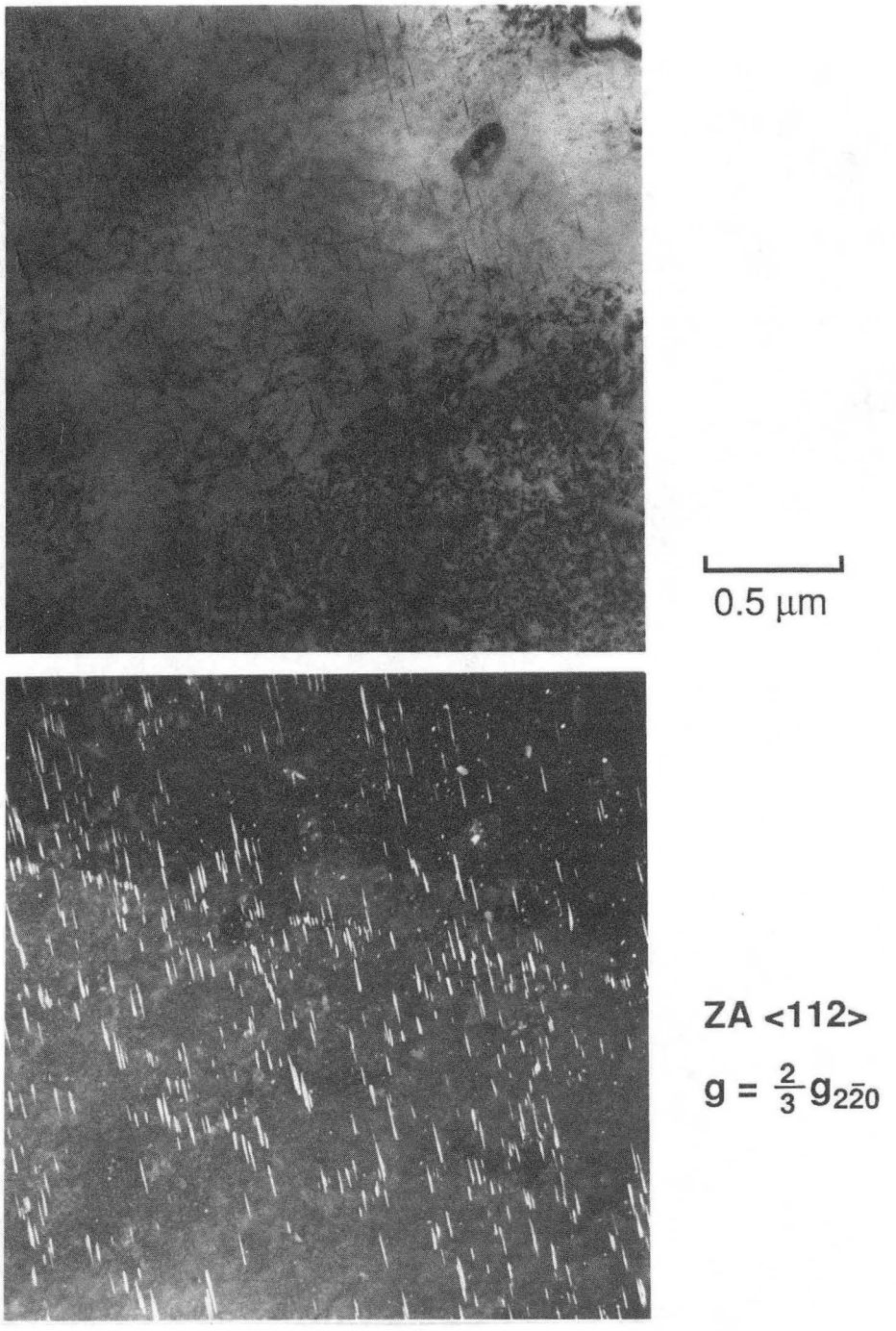

Figure 2.3 Bright-field, dark-field pair of transmission electron micrographs illustrating the microstructure of 2091-T8. The diffraction beam $g = \frac{2}{3}g_{220}$ corresponds to one variant each of the T_1 and S' precipitates. In the dark-field micrograph, T_1 plates are viewed edge-on as streaks, while S' rods are viewed end-on as dots. The δ' precipitate is also present.

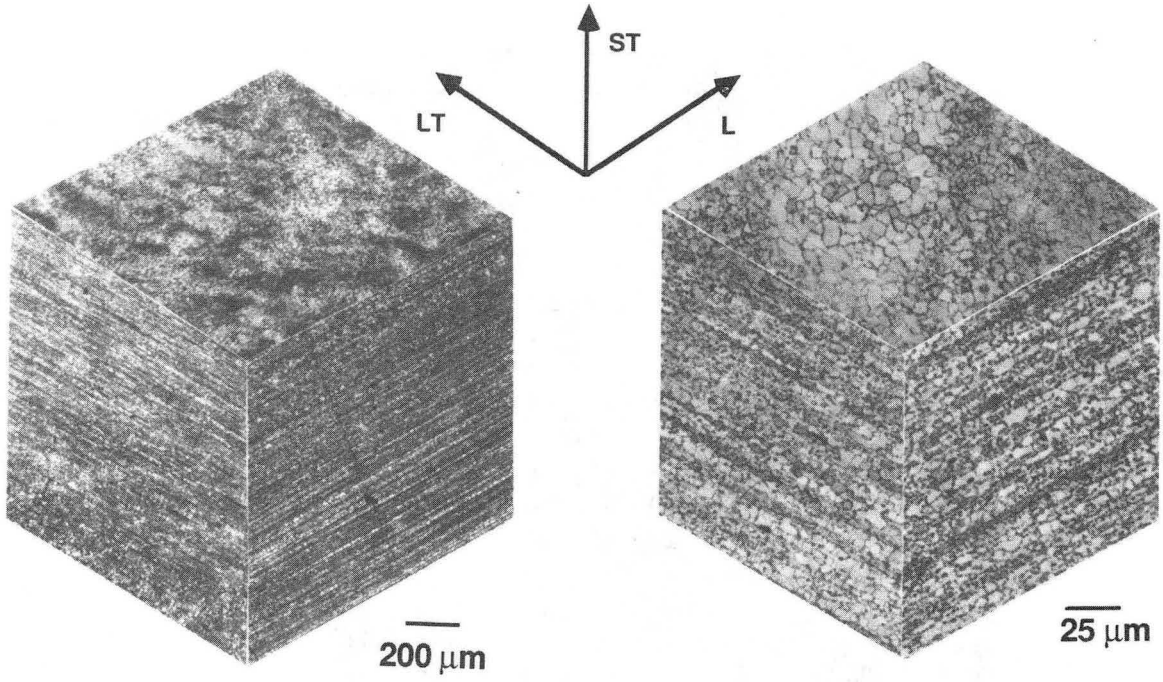

Figure 2.4 Composite optical micrographs showing grain structure of superplastically formable modification of 2090.

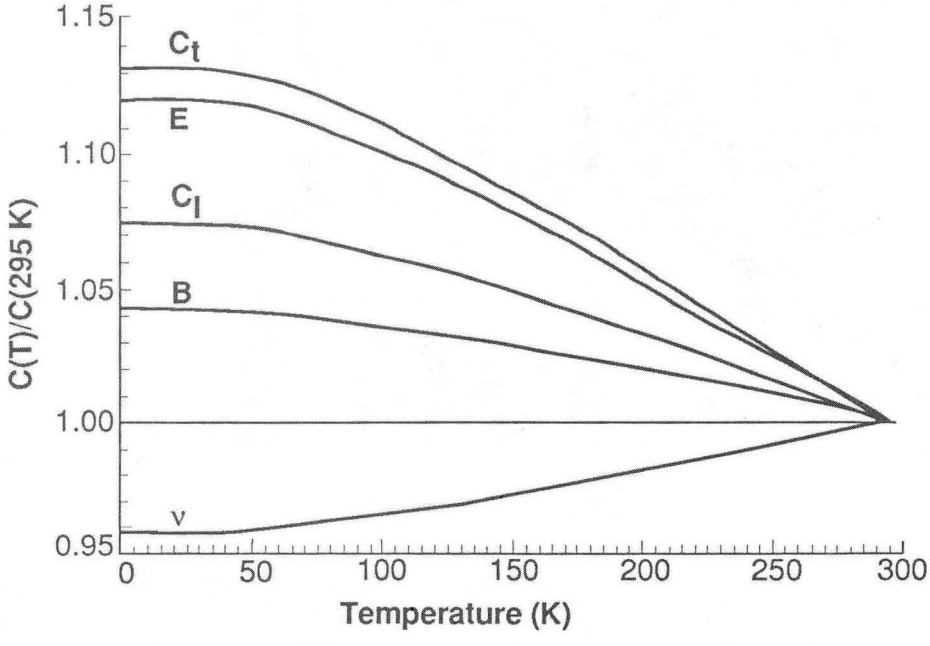

Figure 2.5 Variation in elastic properties of 2090-T81 with temperature relative to the room temperature values given in Table 2.2.

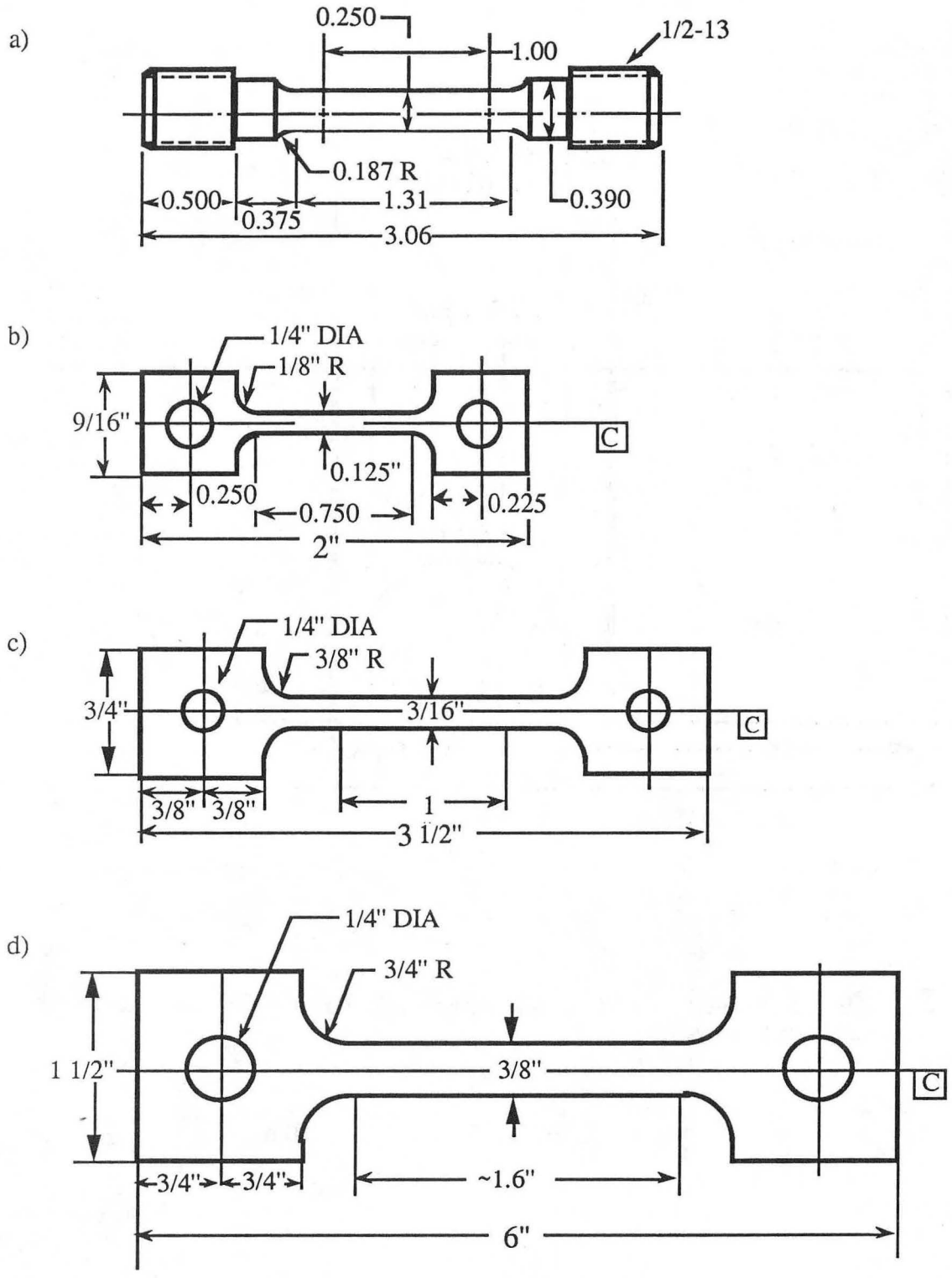

Figure 2.6 Tensile specimen designs used in this study. Scale ~1:1 except d).

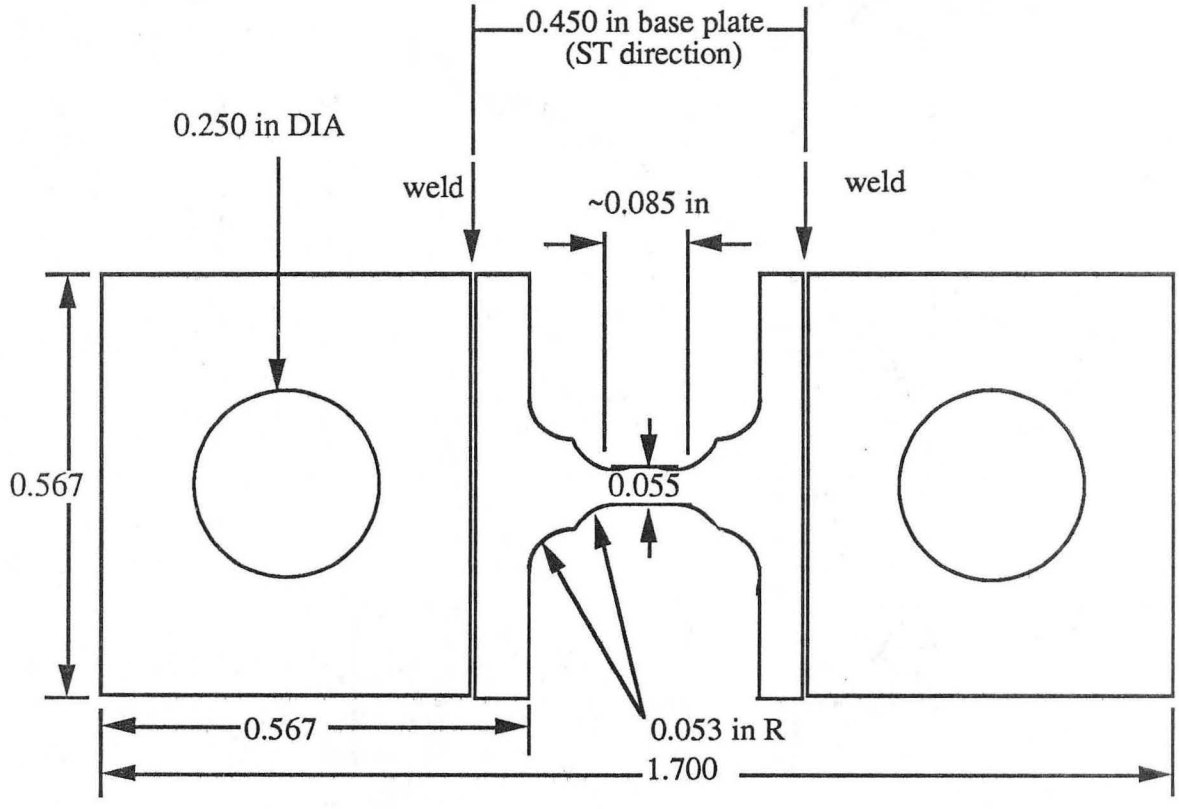

Figure 2.7 Design for short-transverse tensile specimen. Grip sections are attached by electron-beam welds.

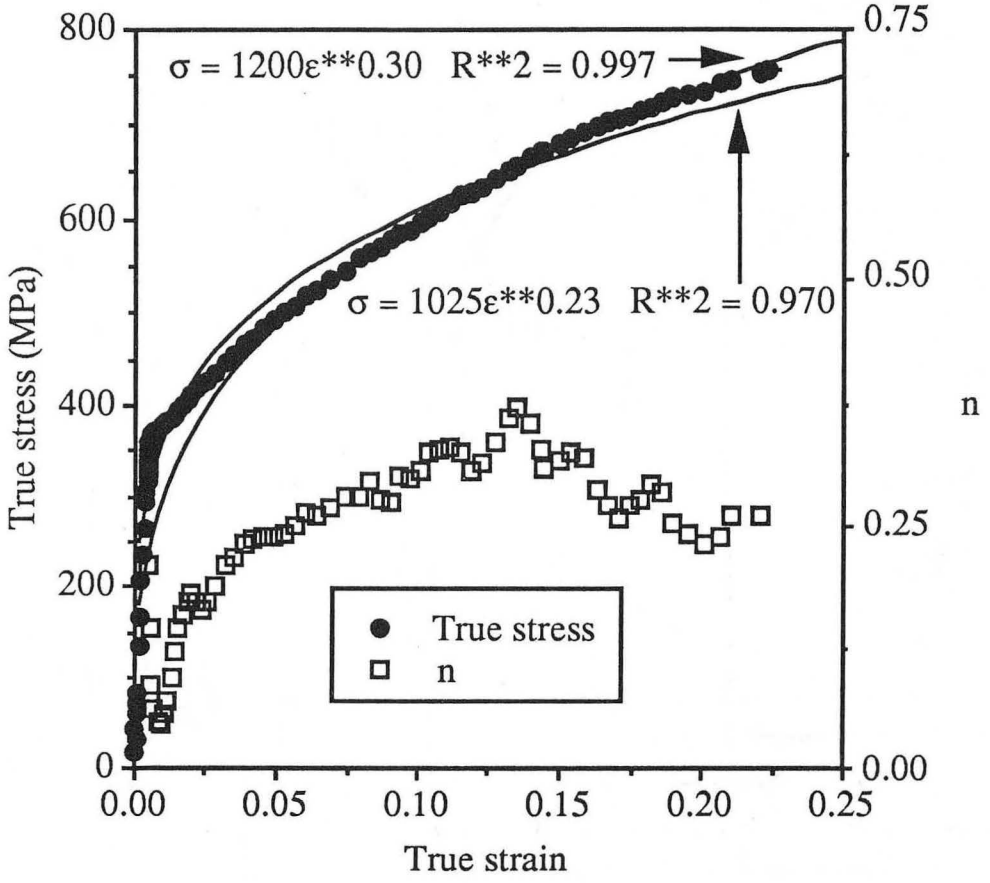

Figure 2.8 Illustration of the deviation of the Hollomon equation for tensile stress-strain behavior ($\sigma = k\varepsilon^n$) from actual behavior of aluminum-lithium alloys. Lower equation is for entire plastic region; upper equation is for stresses greater than half the sum of the yield and ultimate tensile stresses. Data shown are for unformed superplastic 2090-T6 sheet tested at 4 K. The n-value computed using a sliding 5-point fit is also shown to illustrate its variation with strain.

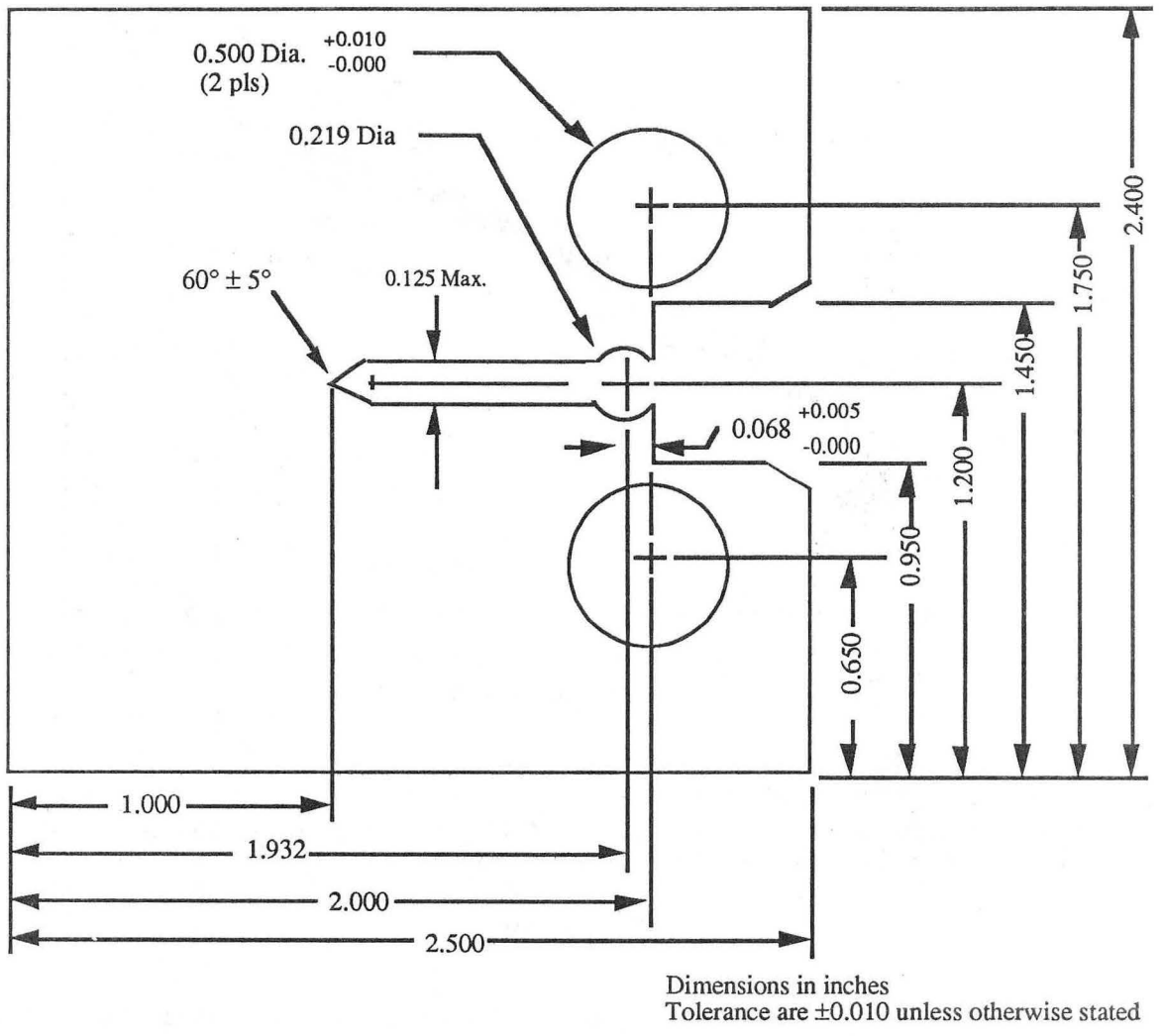

Figure 2.9 Design for J_{Ic} specimen.

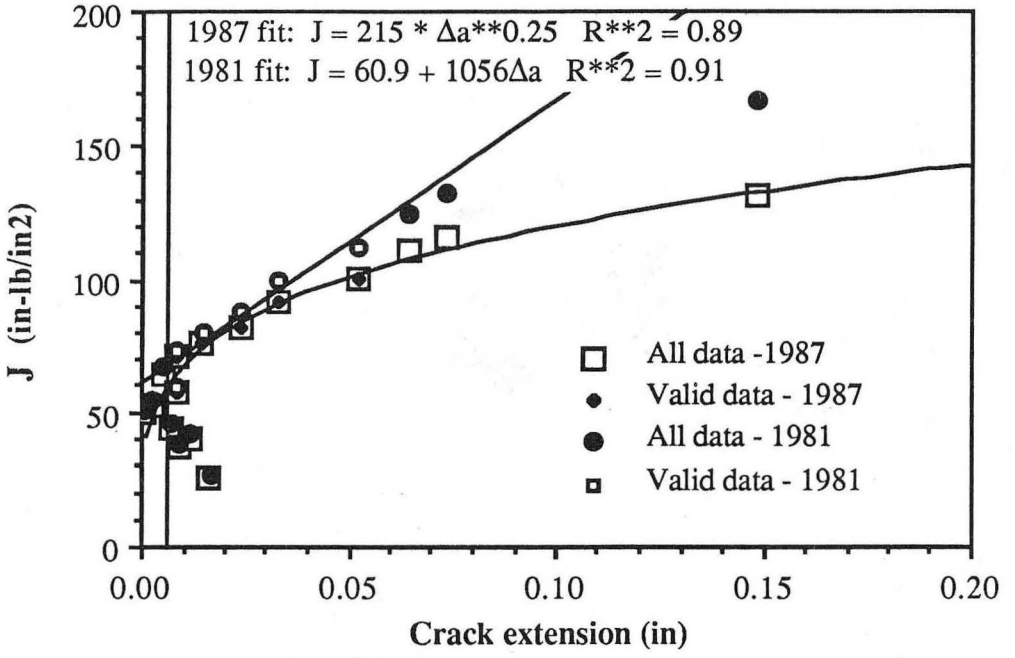

Figure 2.10 Sample curve illustrating the variation of J with crack extension Δa and determination of J_{Ic} under the 1981 and 1987 ASTM standards. Data shown are for 2091-T8 T-L oriented sample tested at 200 K.

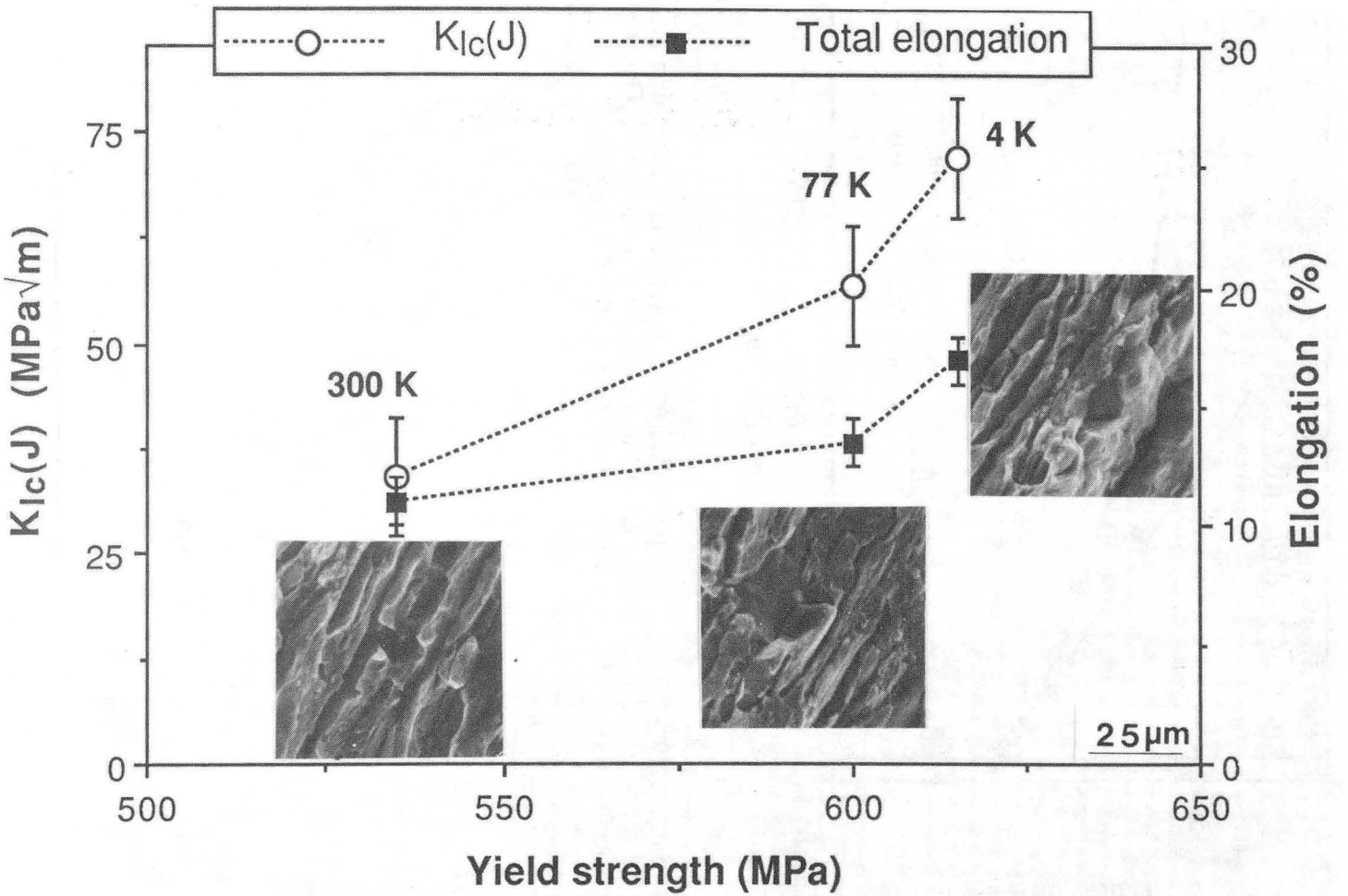

XBB 894-3137

Figure 3.1 Summary of 2090-T81 L strength and L-T toughness combination as a function of temperature. Tensile data were obtained at T/2. Error bars represent scatter in data. Insets are scanning electron micrographs of fracture surfaces of J_{Ic} specimens used to determine fracture toughness.

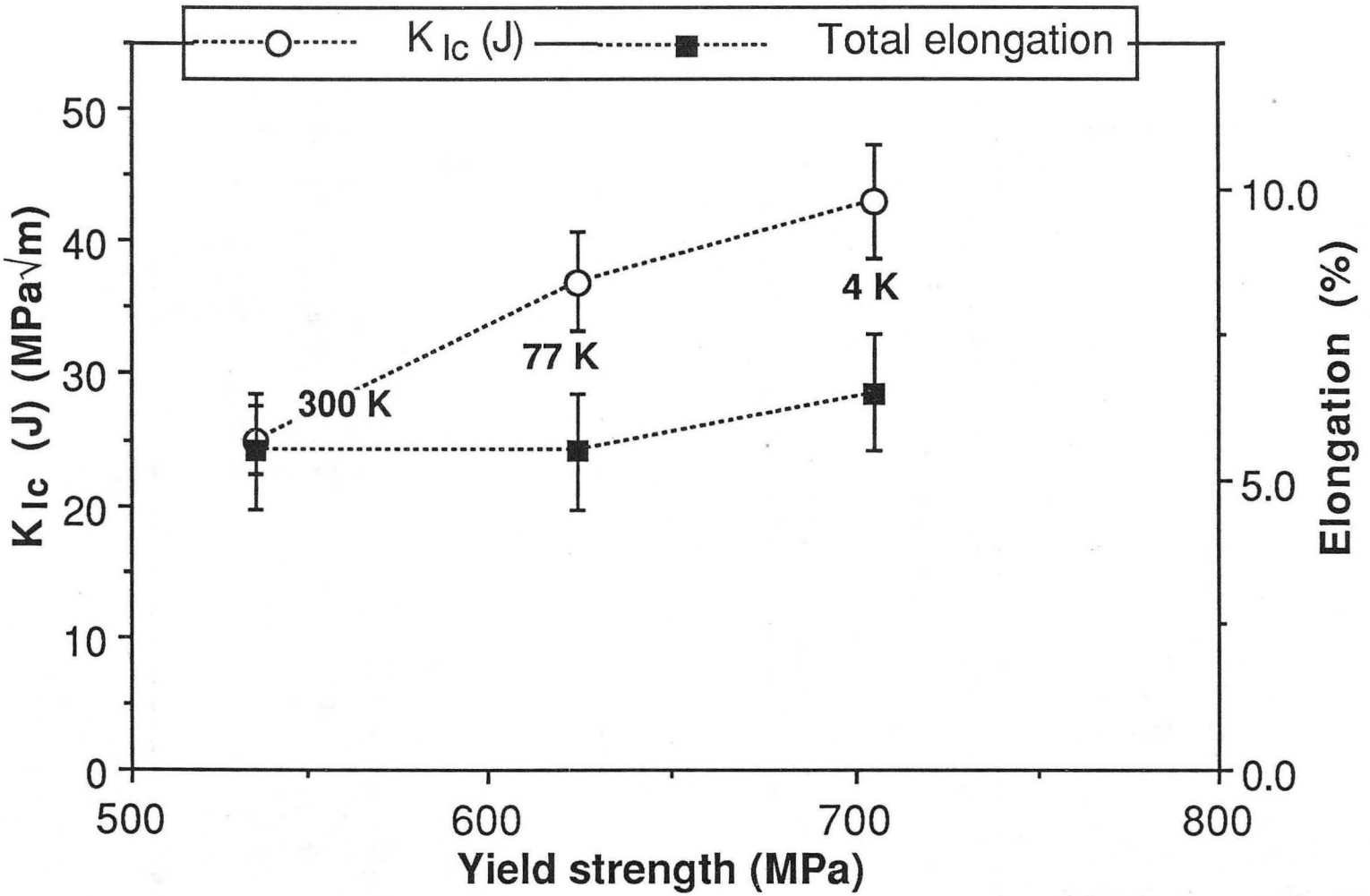

Figure 3.2 Summary of 2090-T81 LT strength and T-L toughness combination as a function of temperature. Tensile data were obtained at T/2. Error bars represent scatter in data.

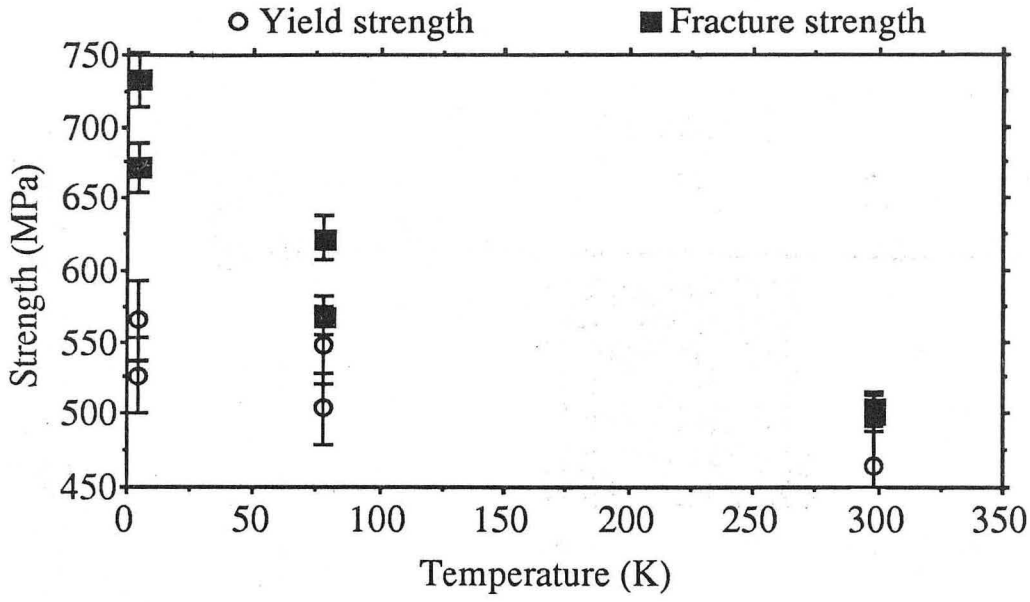

Figure 3.3 Yield and fracture strengths of 2090-T81 in the ST direction as a function of temperature. Error bars indicate estimated measurement error.

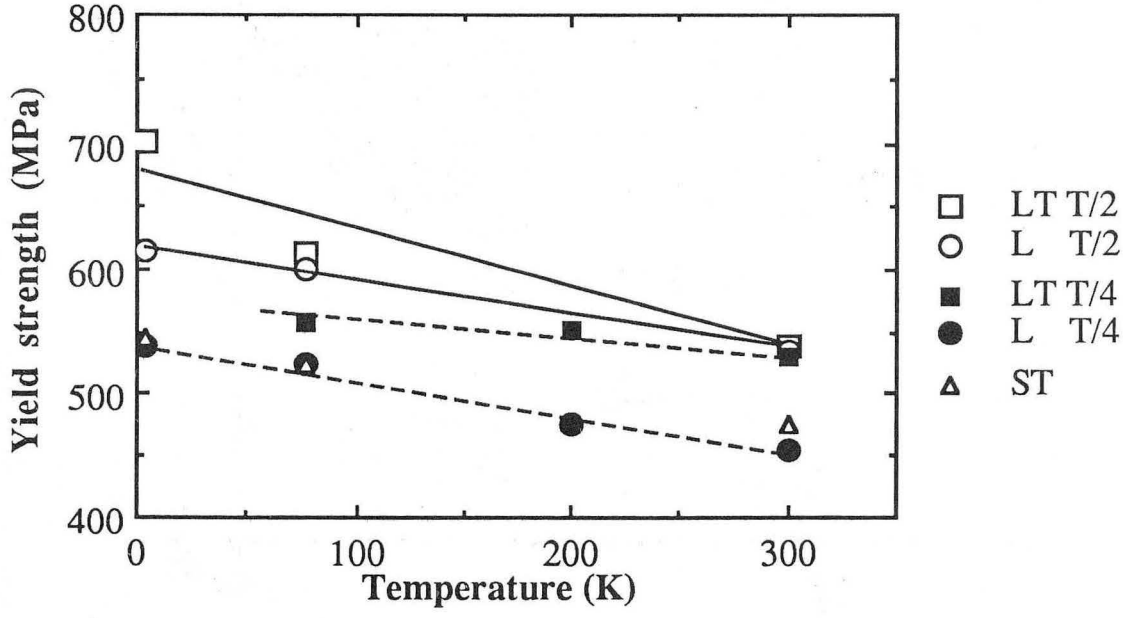

Figure 3.4 Yield strength anisotropy of 2090-T81 as a function of test temperture and test orientation.

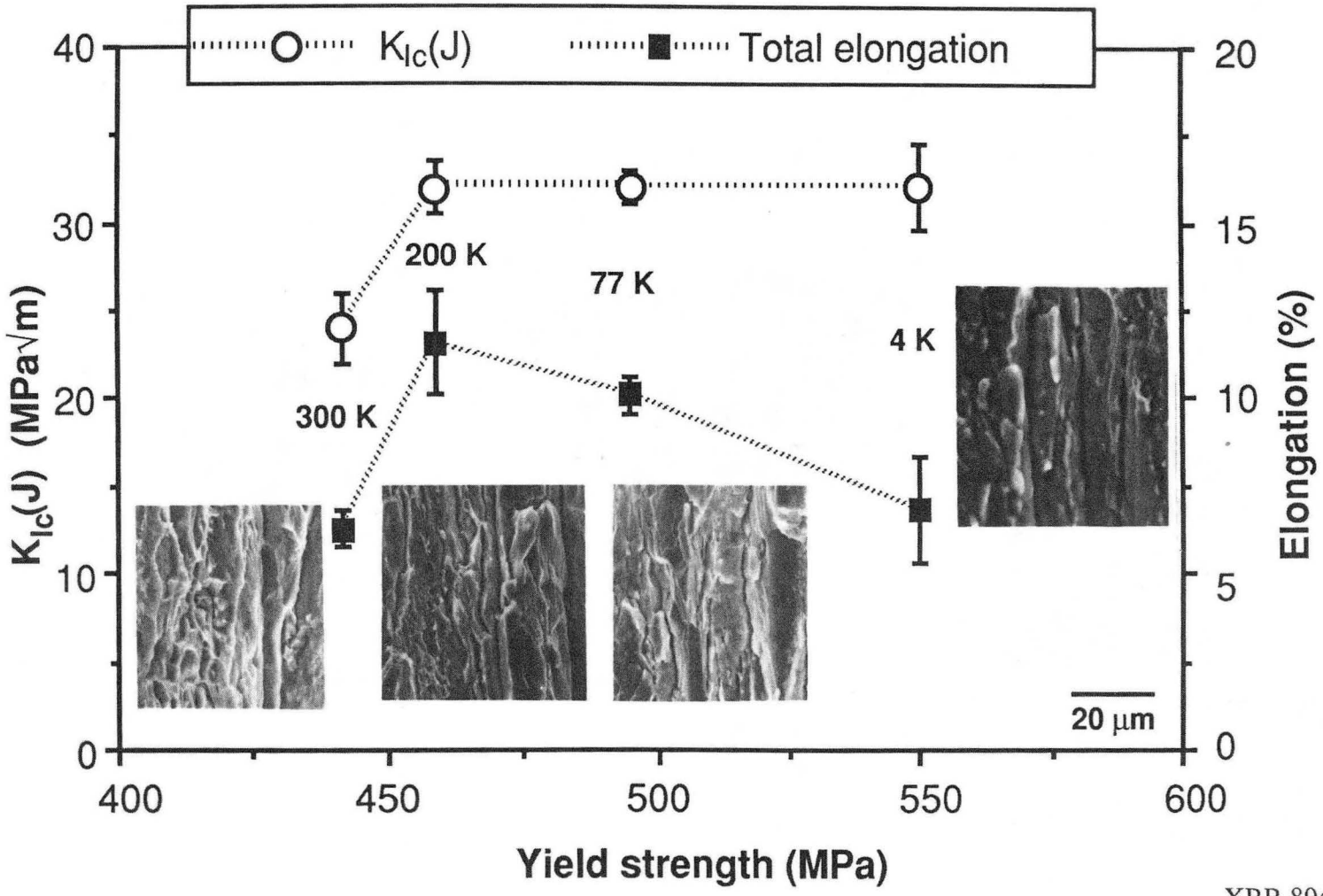

XBB 894-3136

Figure 3.5 Summary of 2091-T8 L strength and L-T toughness combination as a function of temperature. Error bars represent scatter in data. Insets are scanning electron micrographs of fracture surfaces of J_{Ic} specimens used to determine fracture toughness.

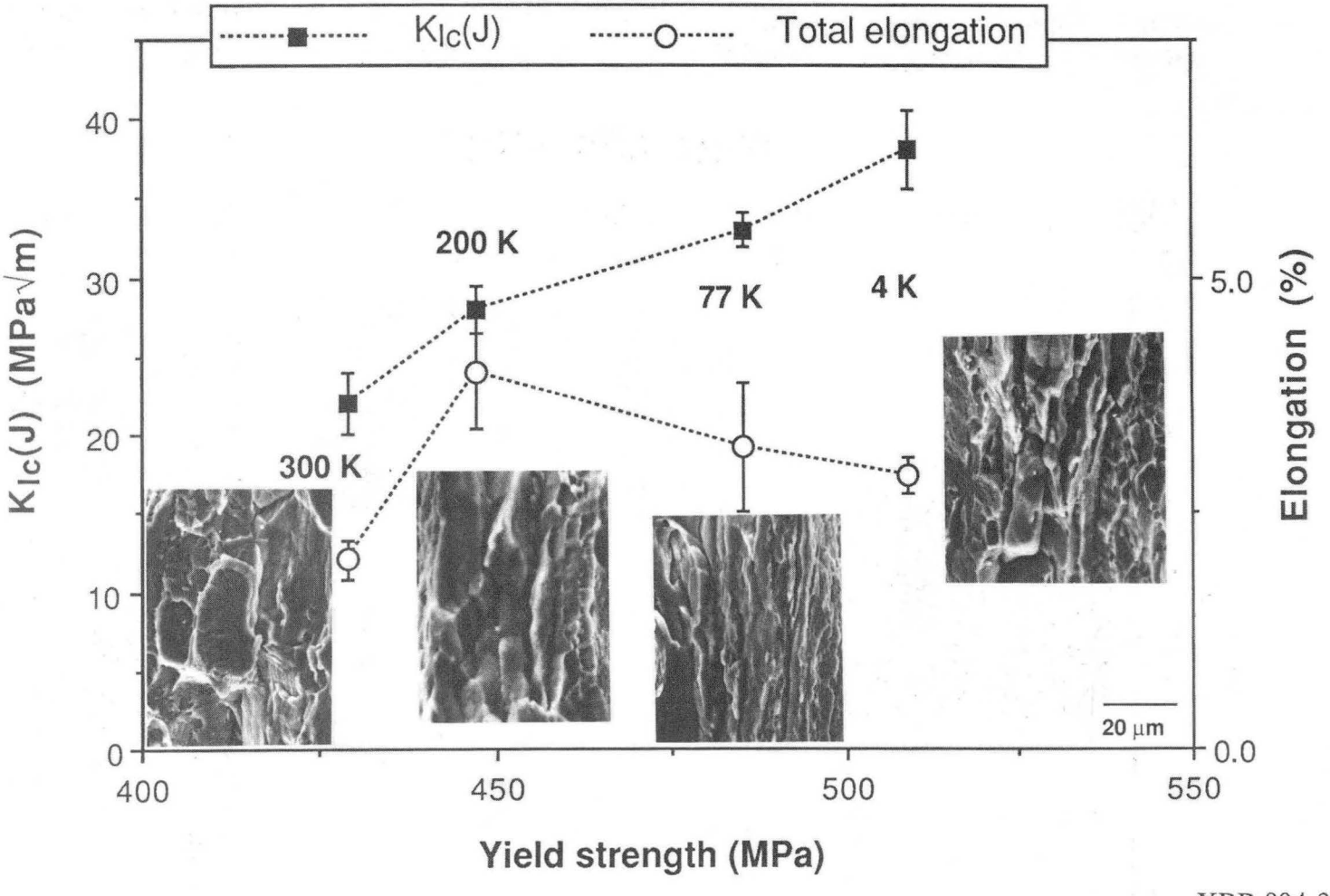

XBB 894-3138

Figure 3.6 Summary of 2091-T8 LT strength and T-L toughness combination as a function of temperature. Error bars represent scatter in data. Insets are scanning electron micrographs of fracture surfaces of J_{Ic} specimens used to determine fracture toughness.

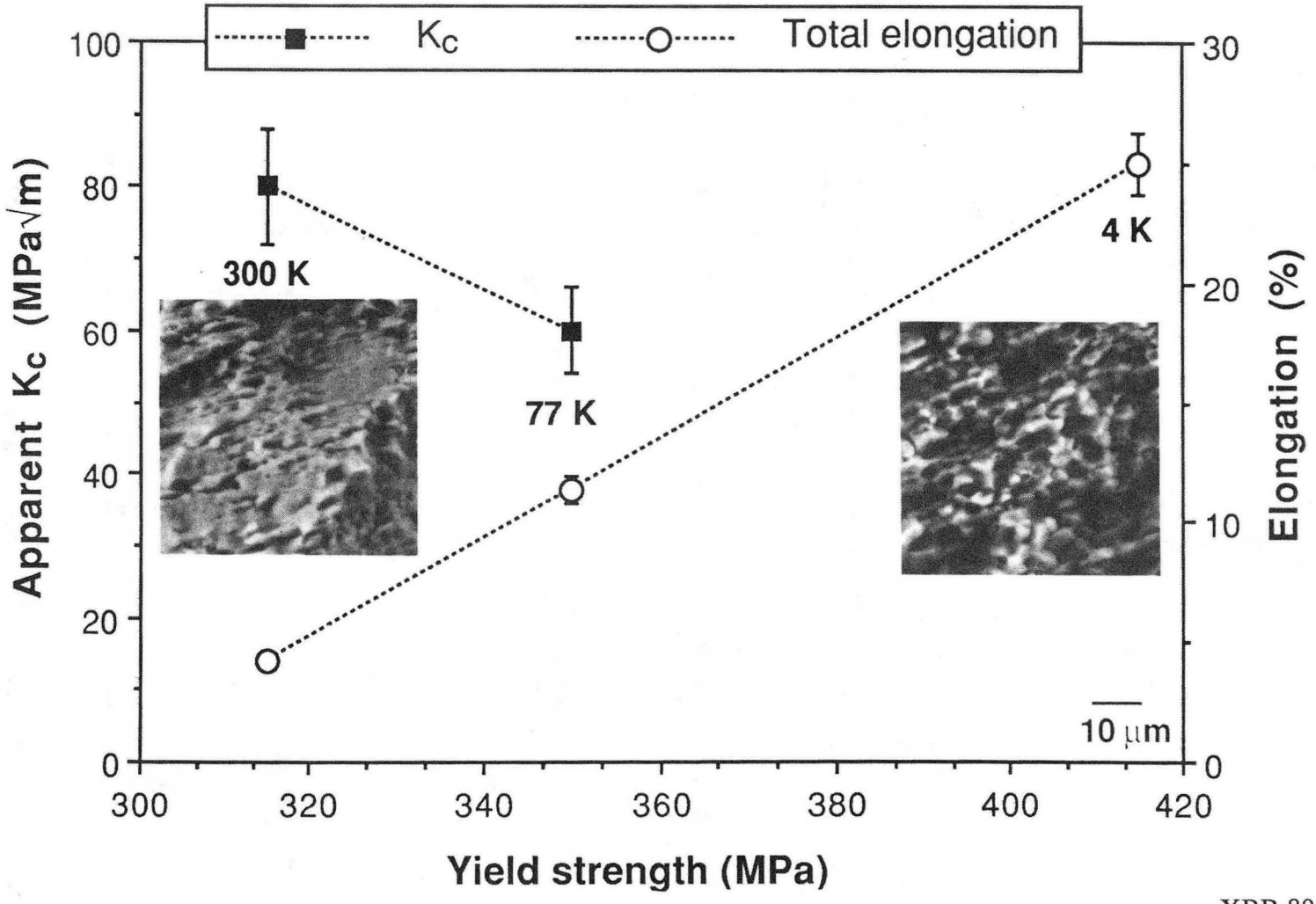

XBB 894-3135

Figure 3.7 Summary of strength-toughness combination for superplastically formable 2090 sheet aged to peak strength. Insets are scanning electron micrographs of failure appearance of tensile specimens. The basis for determining the apparent toughness is described in the text.

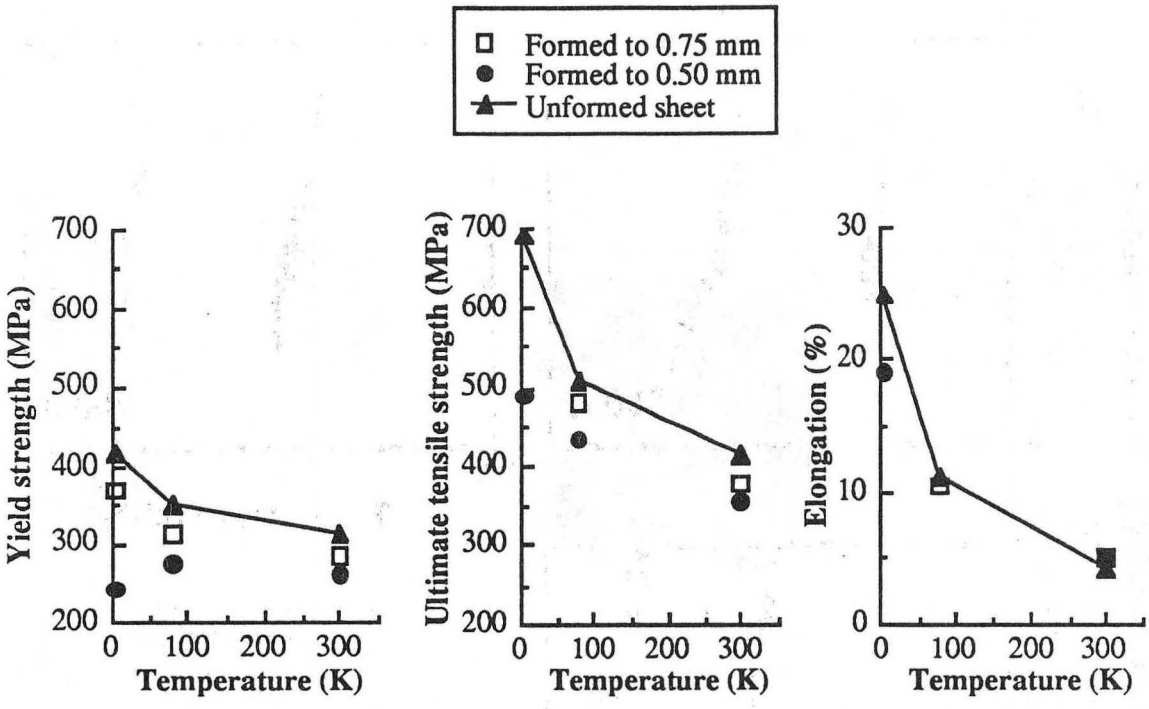

Figure 3.8 Comparison of tensile data for unformed superplastic 2090-T6 sheet with properties of formed and heat-treated sheet.

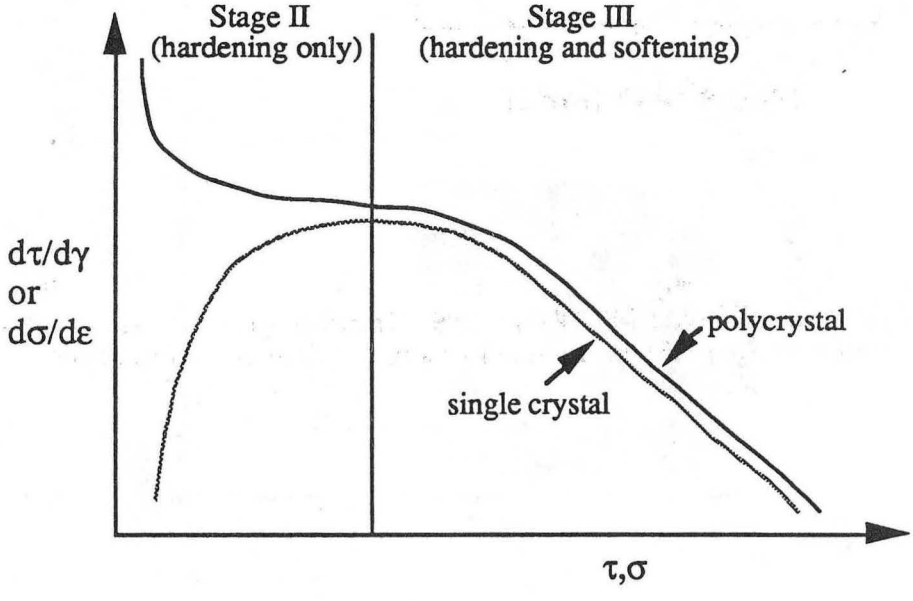

Figure 4.1 Schematic illustration of strain hardening behavior as a function of true stress σ (polycrystal) or true shear stress τ (single crystal) in Stages II and III of deformation. ε and γ are the true strain (polycrystal) and true shear strain (single crystal), respectively. (After Mecking, 1975.)

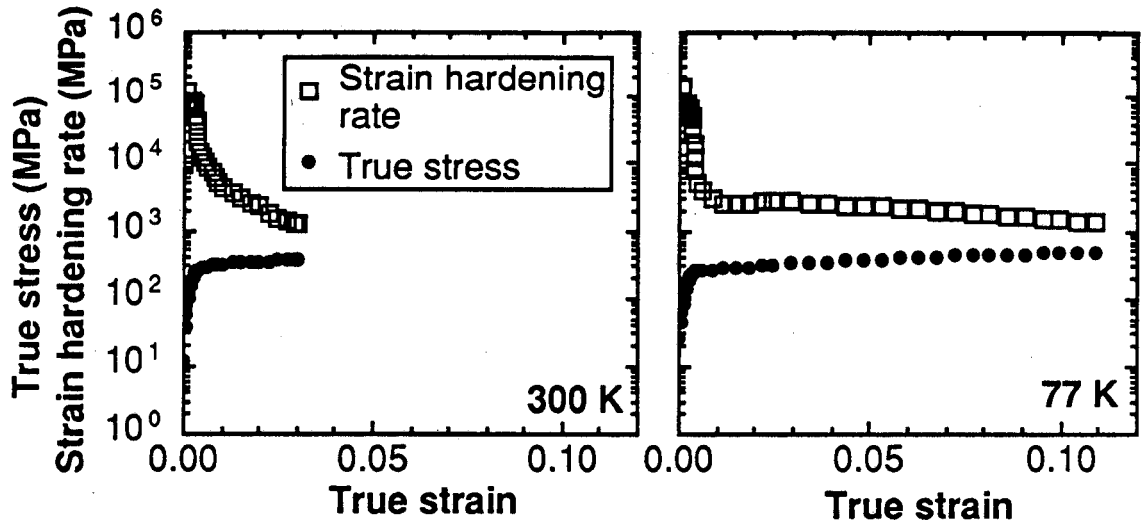

Figure 4.2 Comparison of true stress and strain hardening rate as a function of true strain for L-oriented tensile specimnes of Al-2.4Li-0.1Zr alloy.

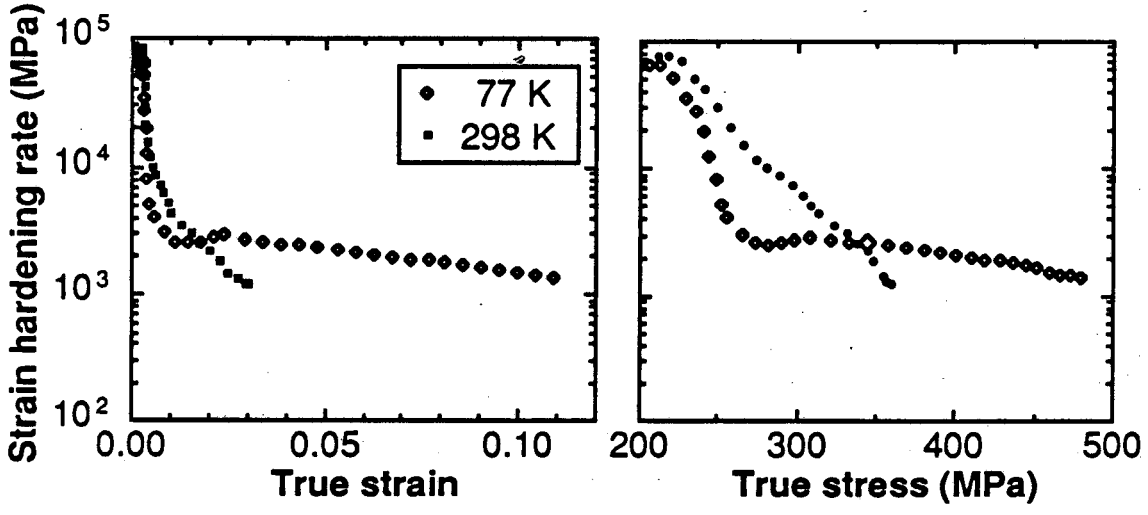

Figure 4.3 Comparisons of strain hardening rates at 300 K and 77 K as a function of true strain and true stress for L-oriented tensile specimens of Al-2.4Li-0.1Zr alloy.

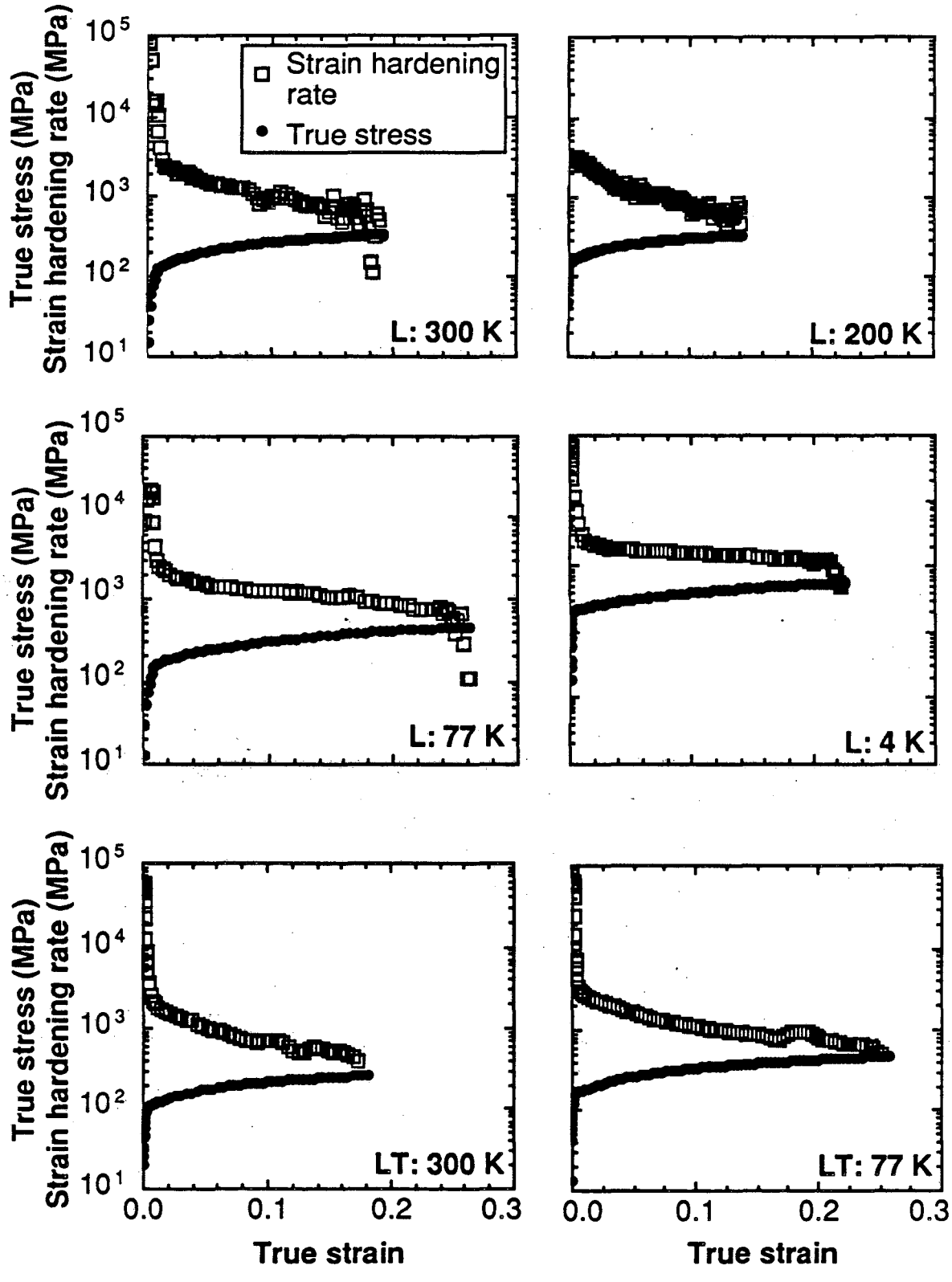

Figure 4.4 Comparison of true stress and strain hardening rate as a function of true strain for L-oriented (top) and LT-oriented (bottom) 2090-T4 tensile specimens tested at various temperatures.

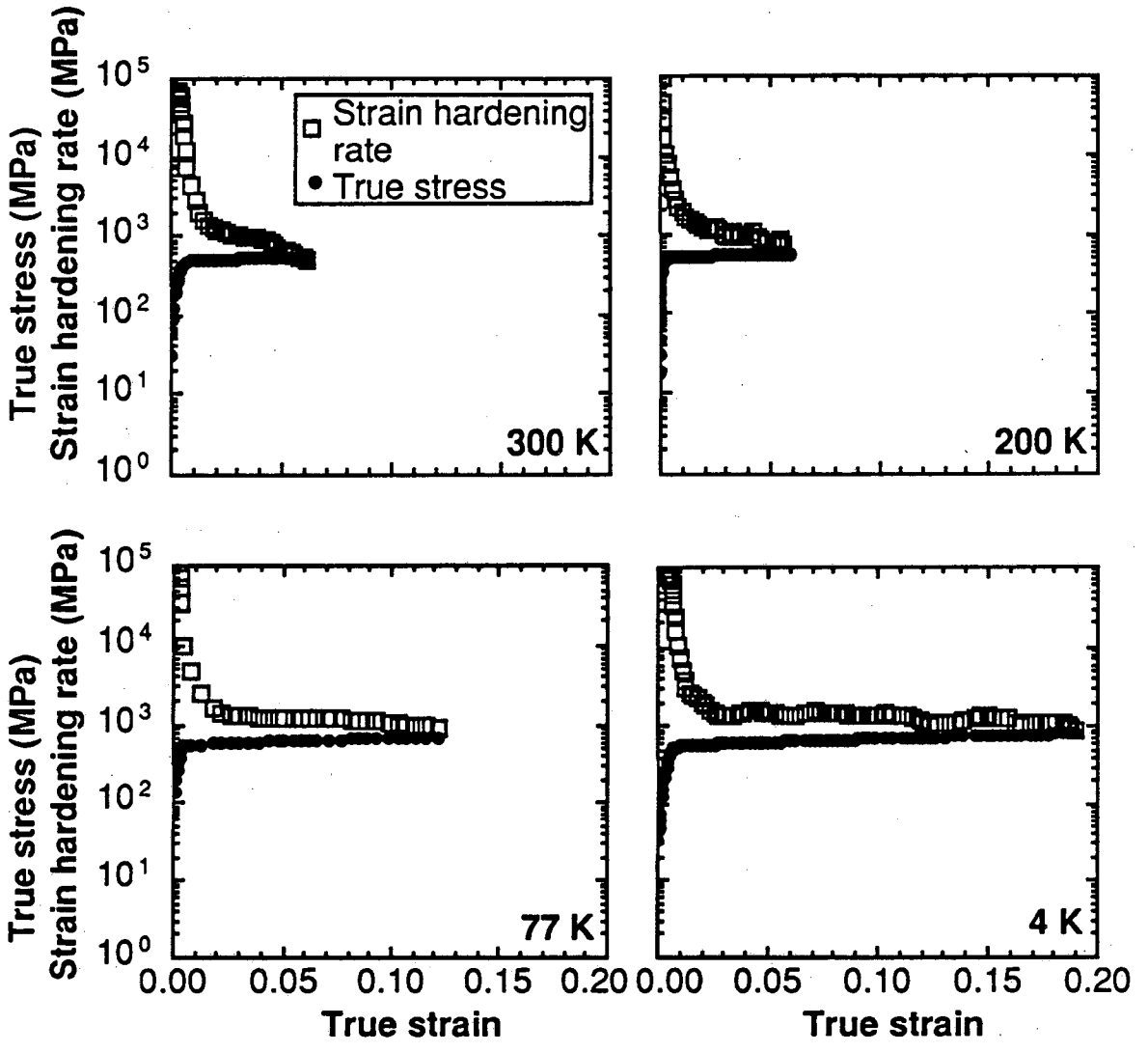

Figure 4.5 Comparison of true stress and strain hardening rate as a function of true strain for L-oriented 2090-T81 tensile specimens taken at T/4.

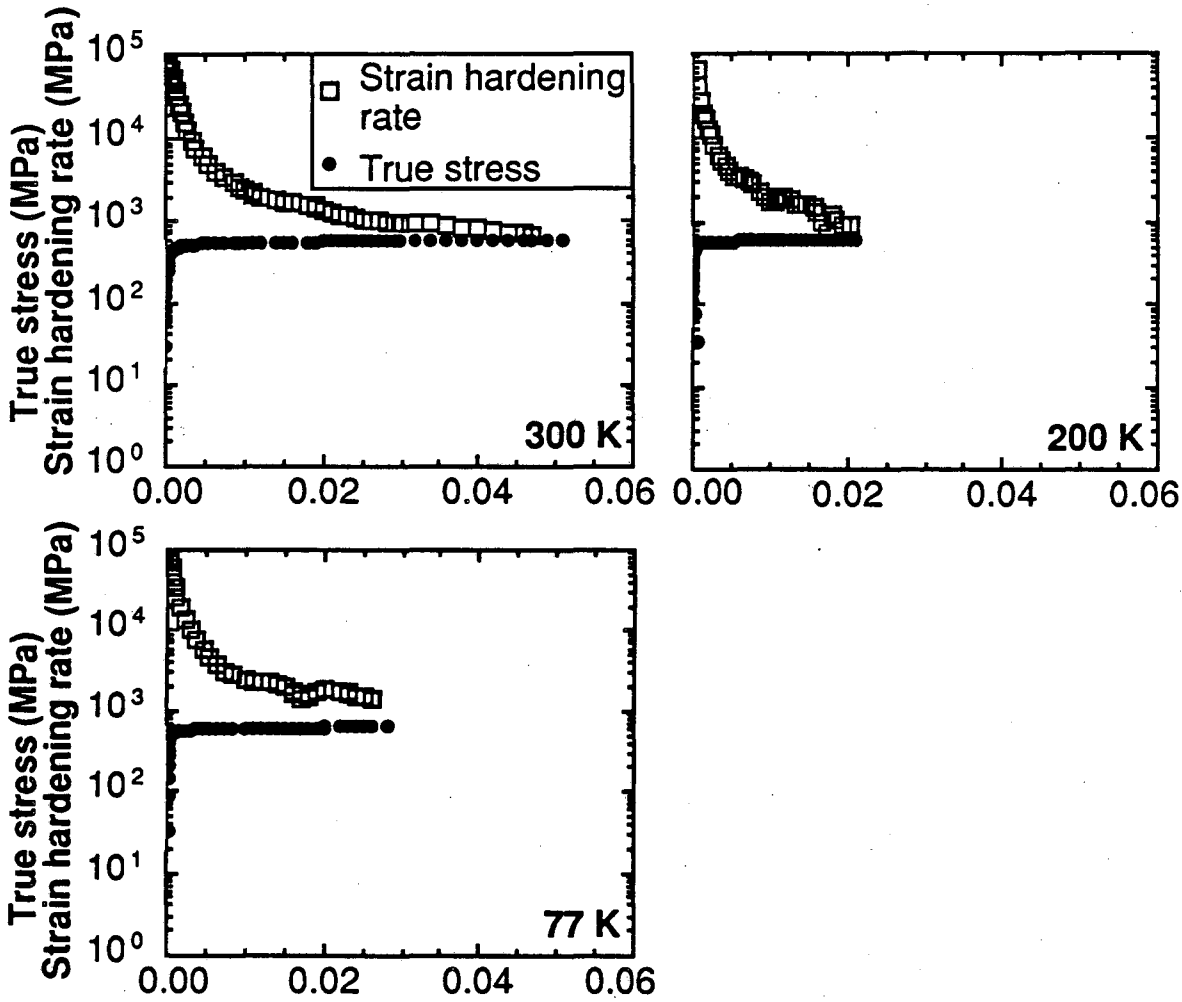

Figure 4.6 Comparison of true stress and strain hardening rate as a function of true strain for LT-oriented 2090-T81 tensile specimens taken at T/4.

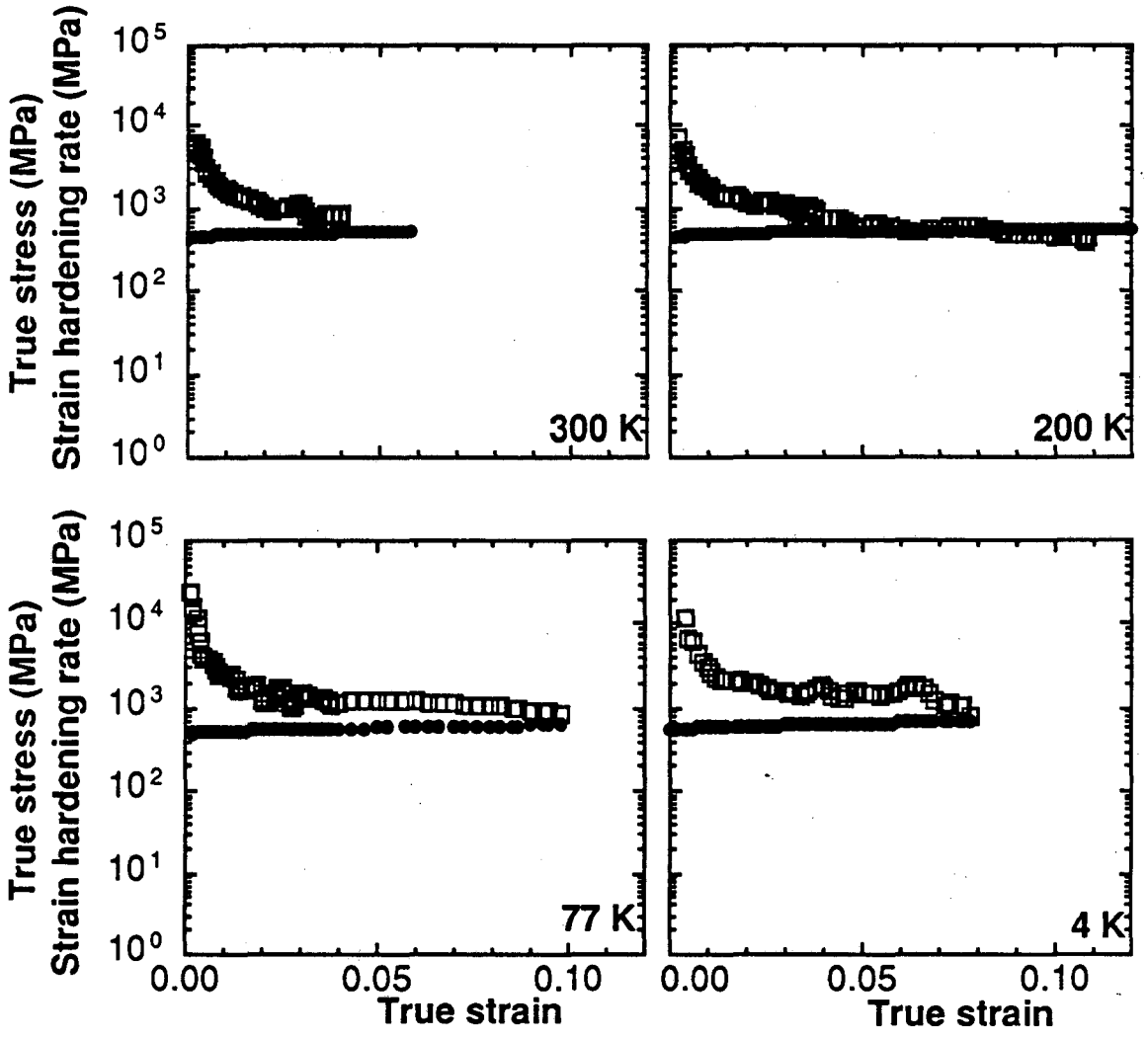

Figure 4.7 Comparison of true stress and strain hardening rate as a function of true strain for L-oriented 2091-T8 tensile specimens.

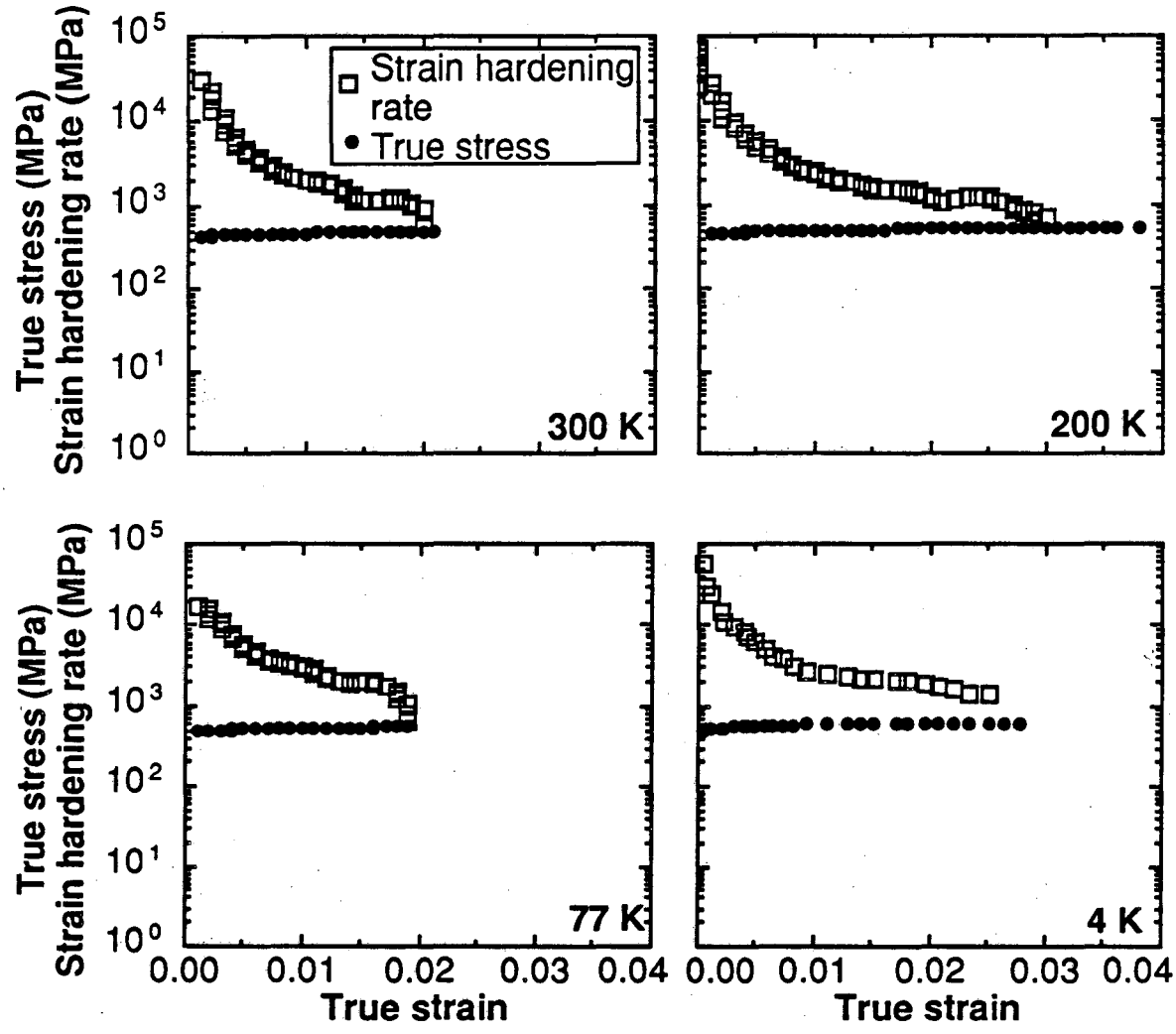

Figure 4.8 Comparison of true stress and strain hardening rate as a function of true strain for LT-oriented 2091-T8 tensile specimens.

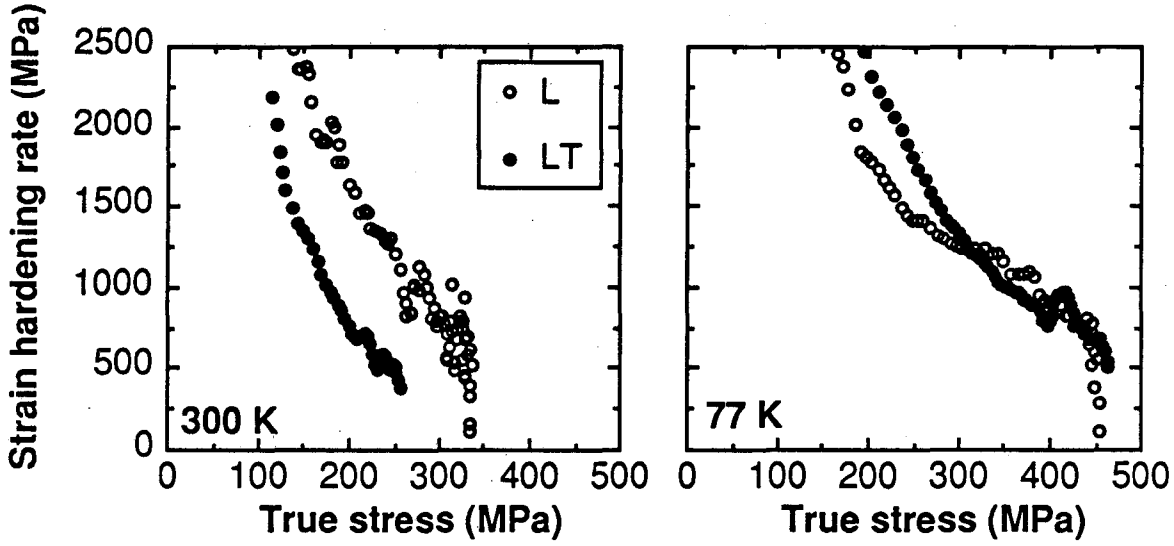

Figure 4.9 Comparison of strain hardening rates as a function of true stress for L and LT-oriented 2090-T4 tensile specimens.

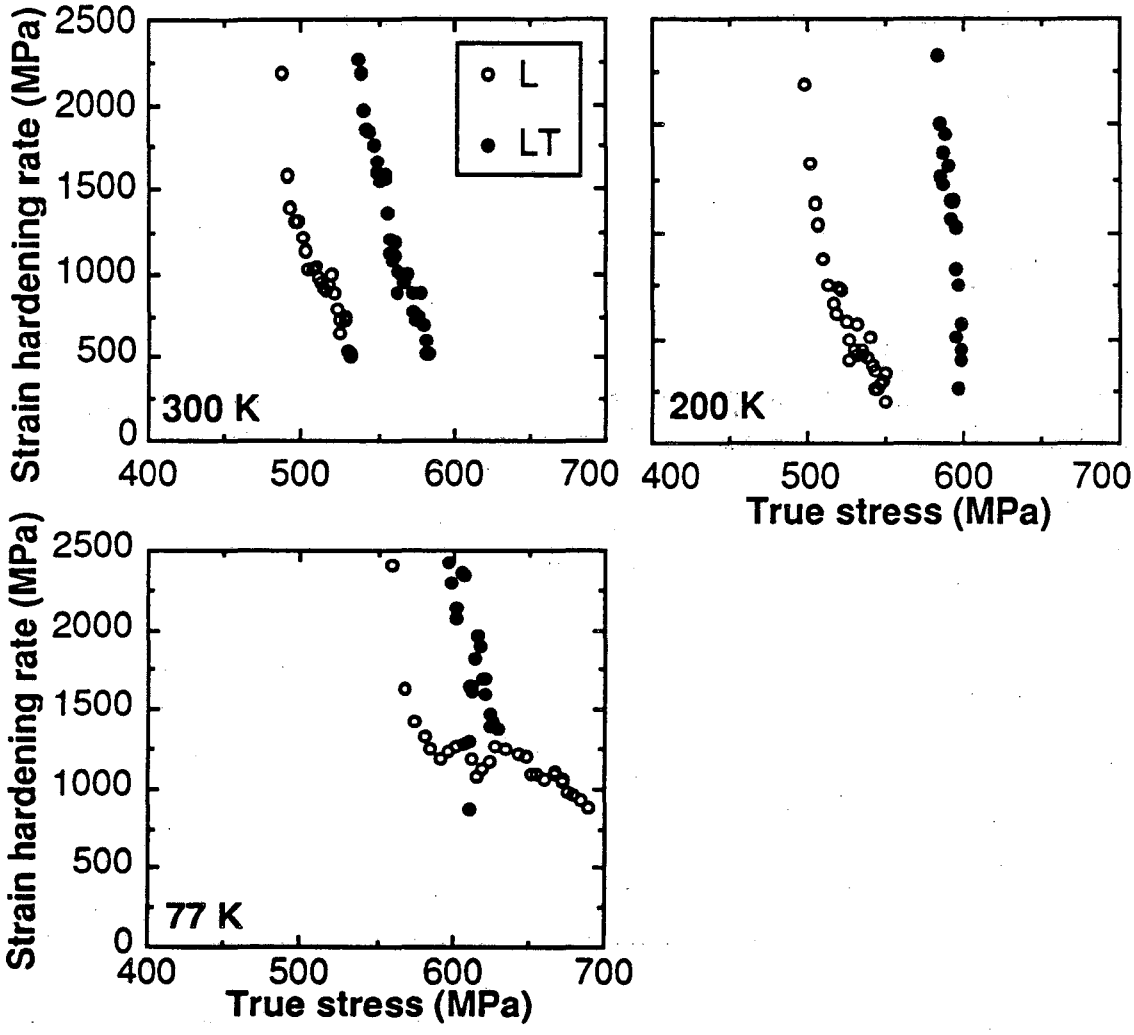

Figure 4.10 Comparison of strain hardening rates as a function of true stress for L and LT-oriented 2090-T81 (T/4) tensile specimens.

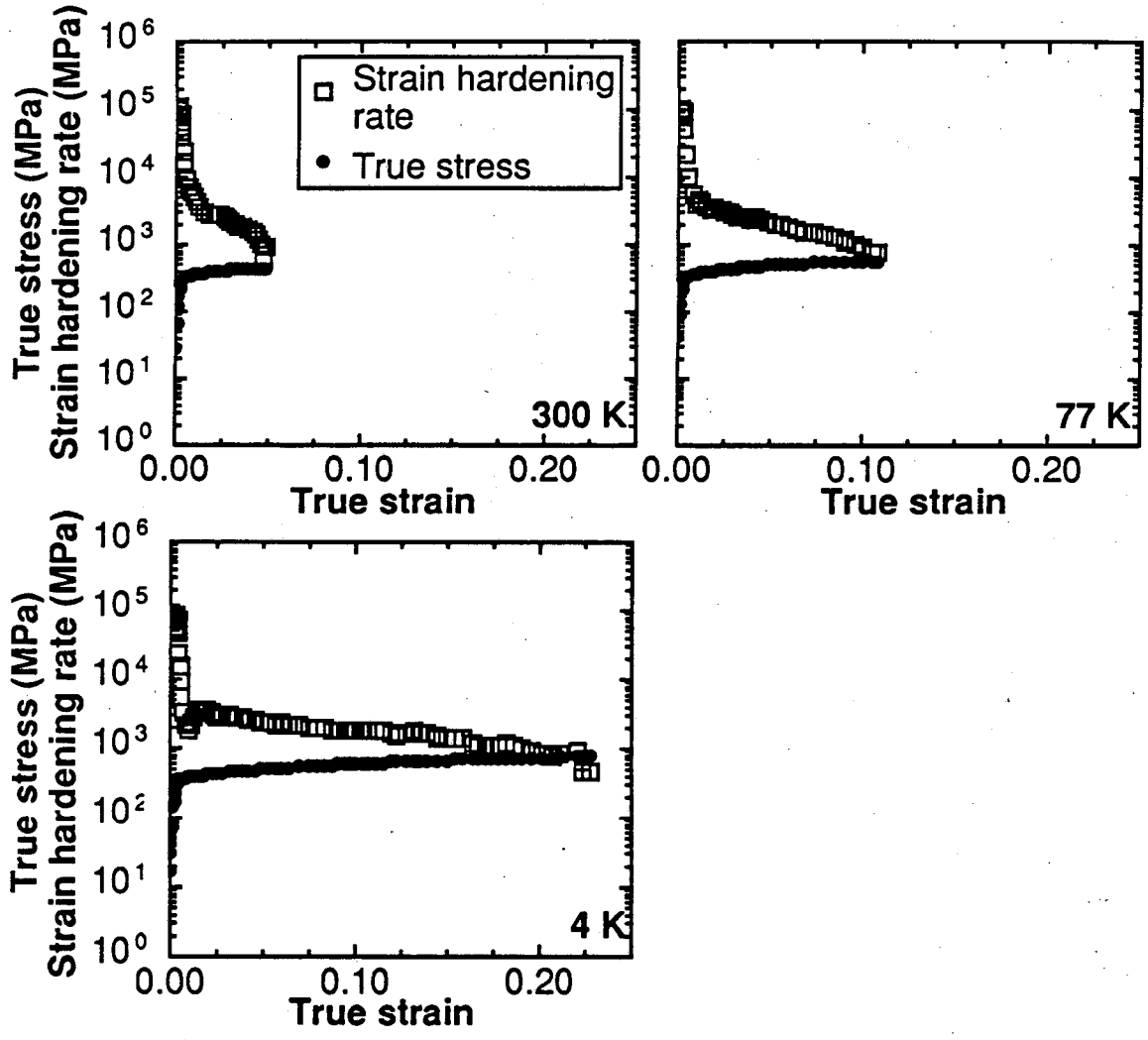

Figure 4.11 Comparison of true stress and strain hardening rate as a function of true strain for superplastically formable (unformed) 2090-T6 tensile specimens.

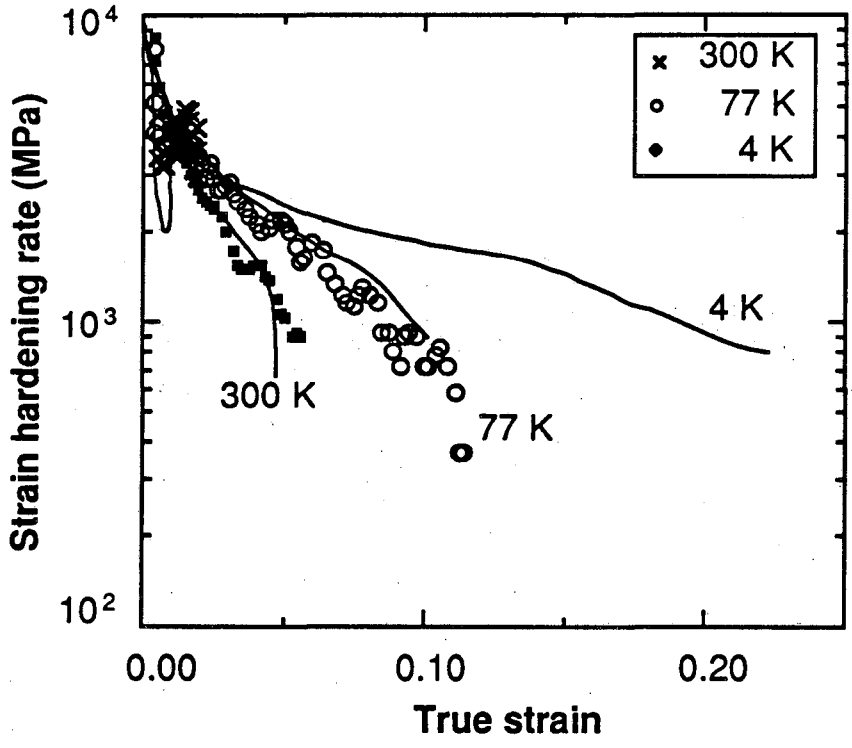

Figure 4.12 Comparison of strain hardening rates of unformed superplastically formable 2090-T6 sheet and sheet formed to 0.75 mm before heat treatment. Solid lines represent trend lines for unformed sheet; data points are for formed sheet.

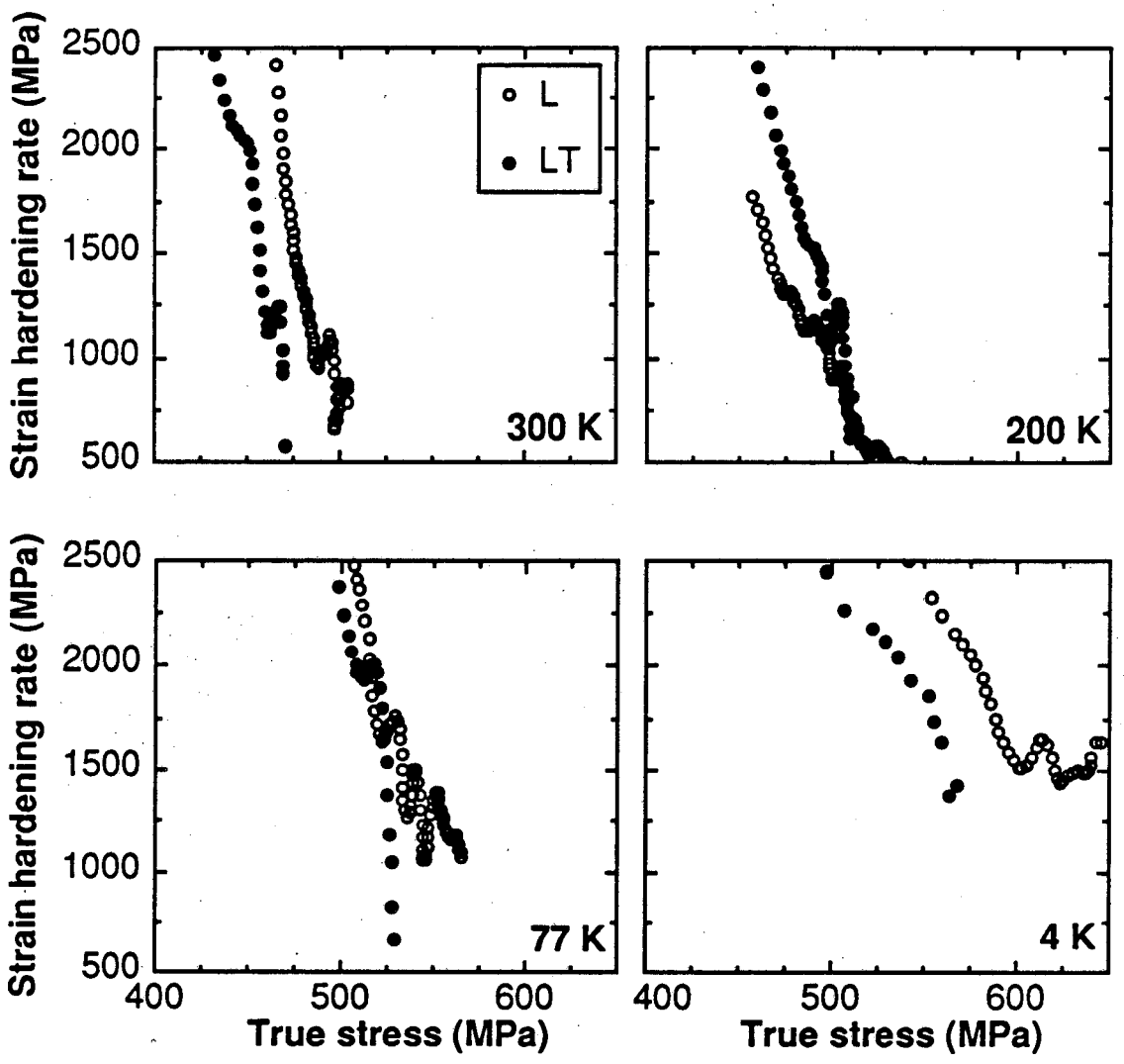

Figure 4.13 Comparison of strain hardening rates as a function of true stress for L and LT-oriented 2091-T8 tensile specimens.

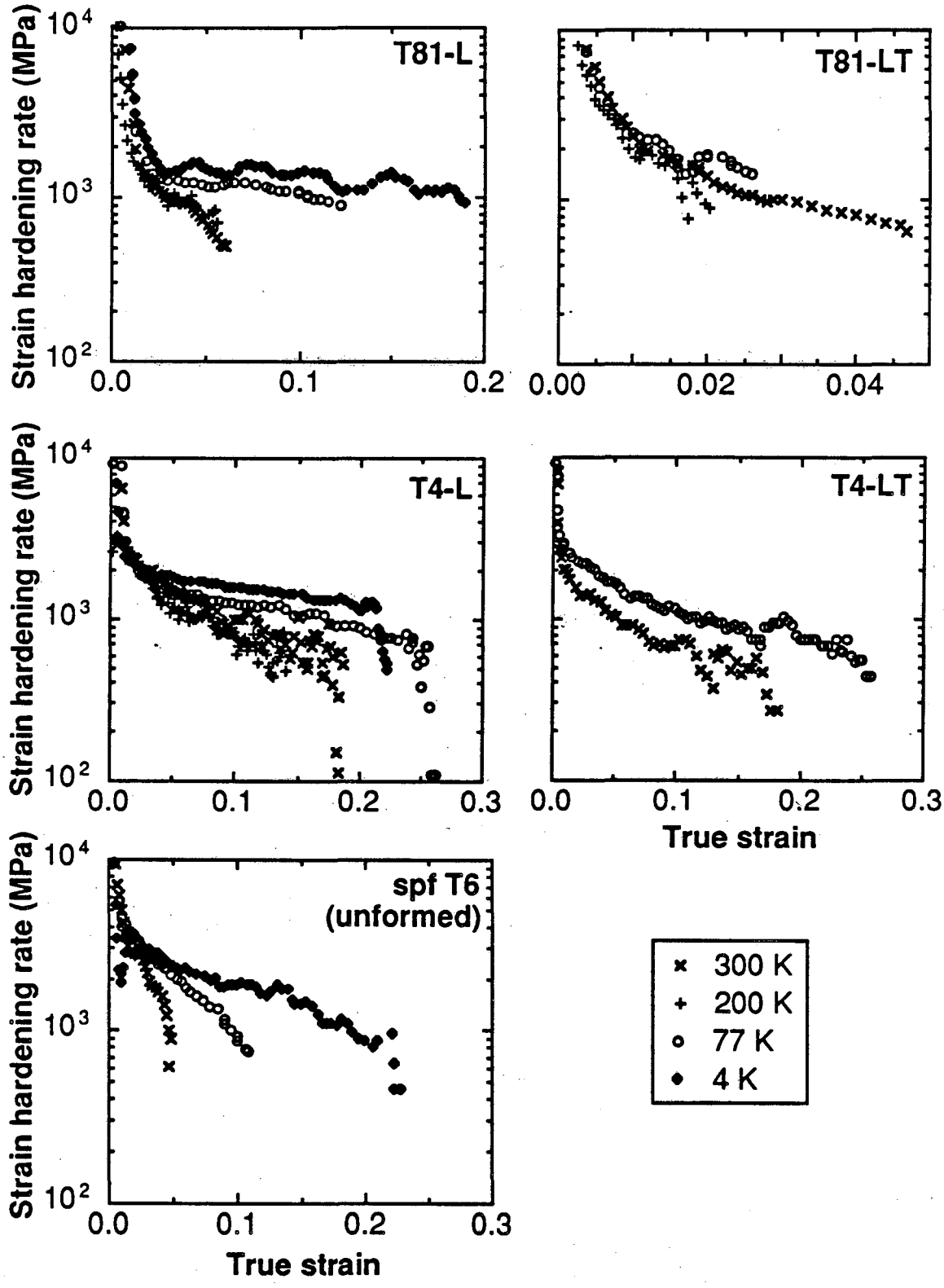

Figure 4.14 Temperature variation of strain hardening rate as a function of true strain for 2090 materials.

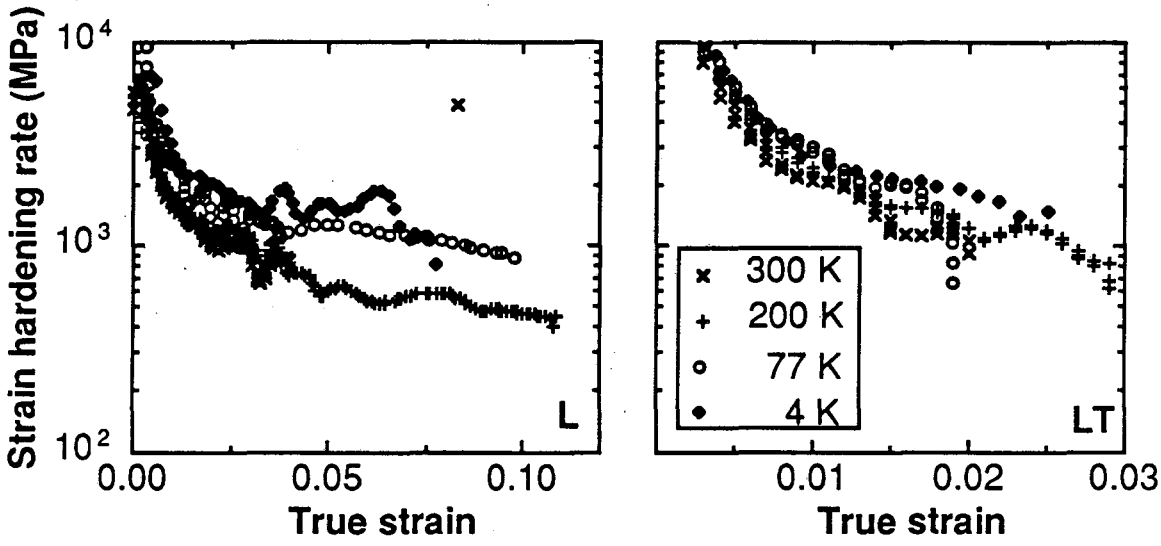

Figure 4.15 Temperature variation of strain hardening rate as a function of true strain for 2091-T8.

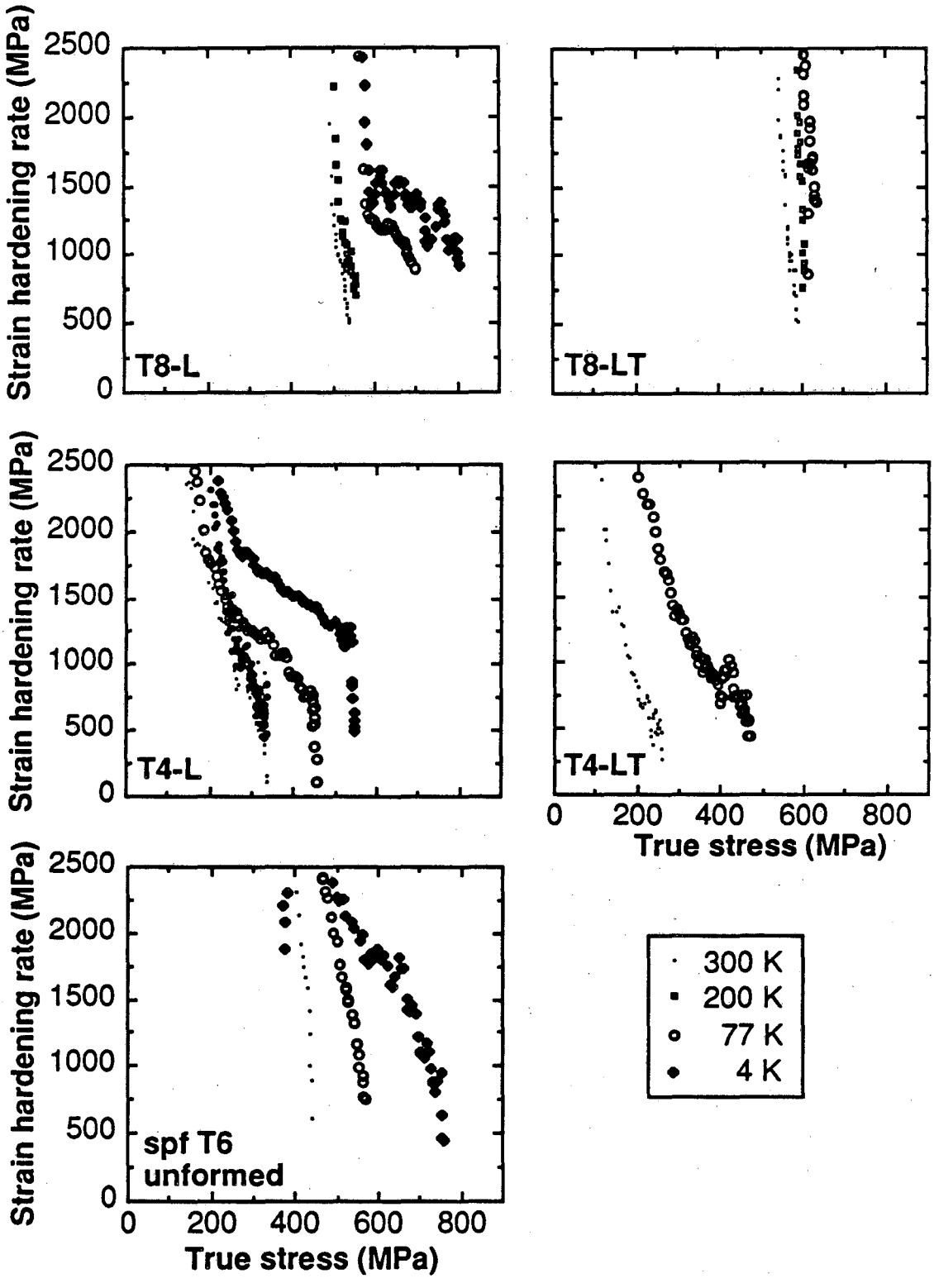

Figure 4.16 Temperature variation of strain hardening rate as a function of true stress for 2090 materials.

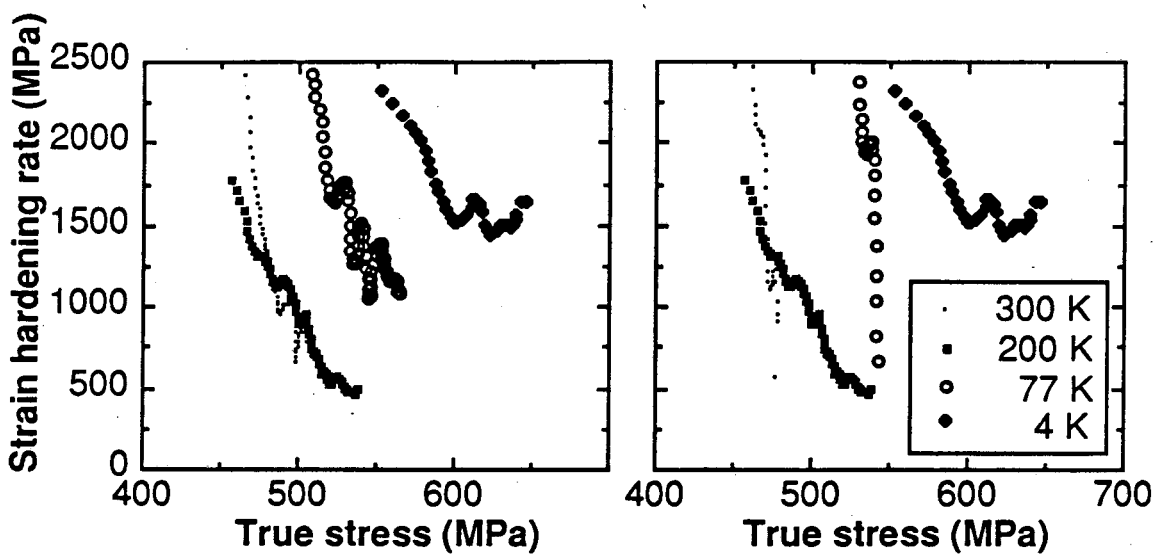

Figure 4.17 Temperature variation of strain hardening rate as a function of true stress for 2091-T8.

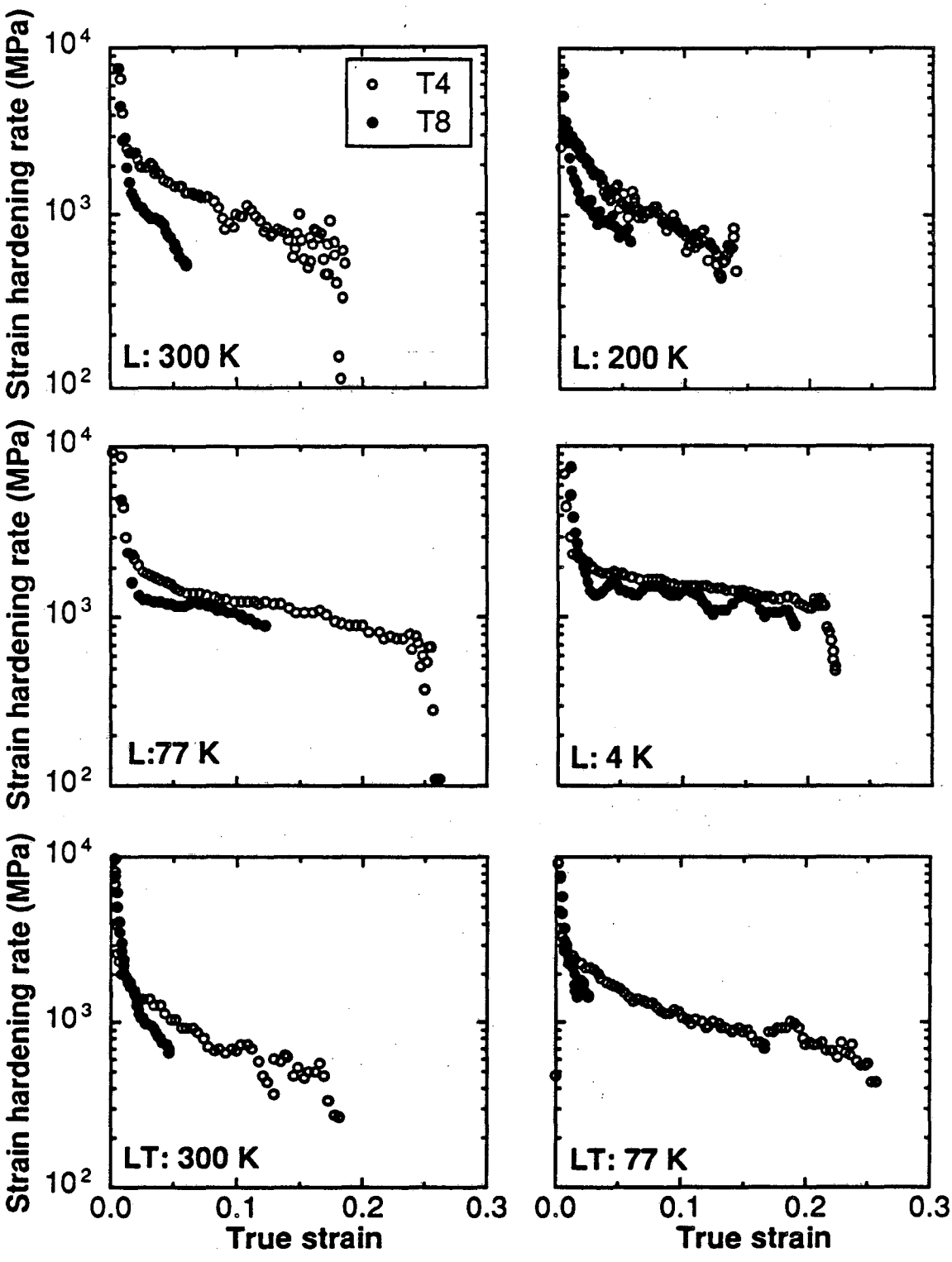

Figure 4.18 Comparison of strain hardening rates as a functin of true strain for 2090-T4 and -T81 tempers.

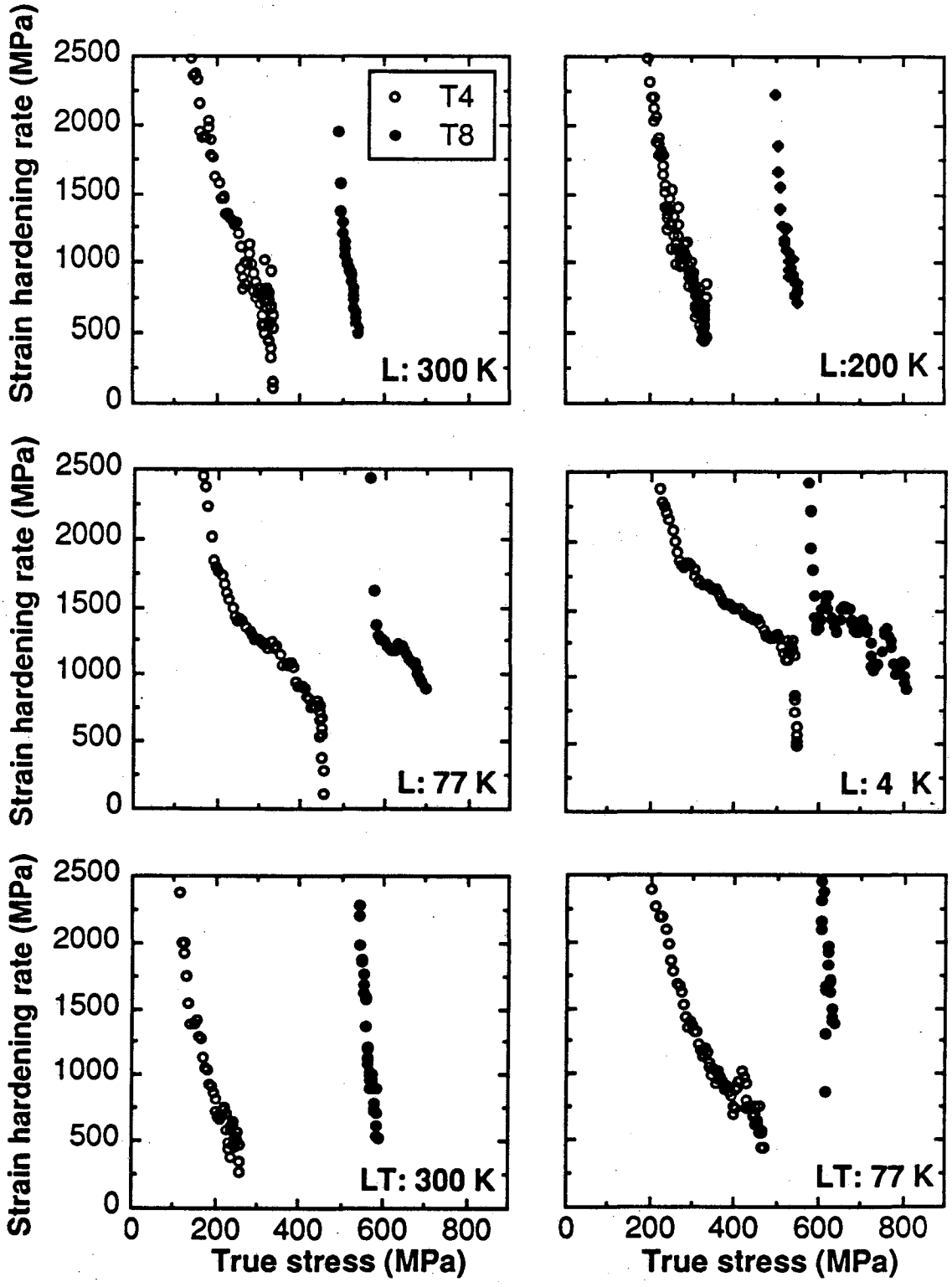

Figure 4.19 Comparison of strain hardening rates as a function of true stress for 2090-T4 and -T81 tempers.

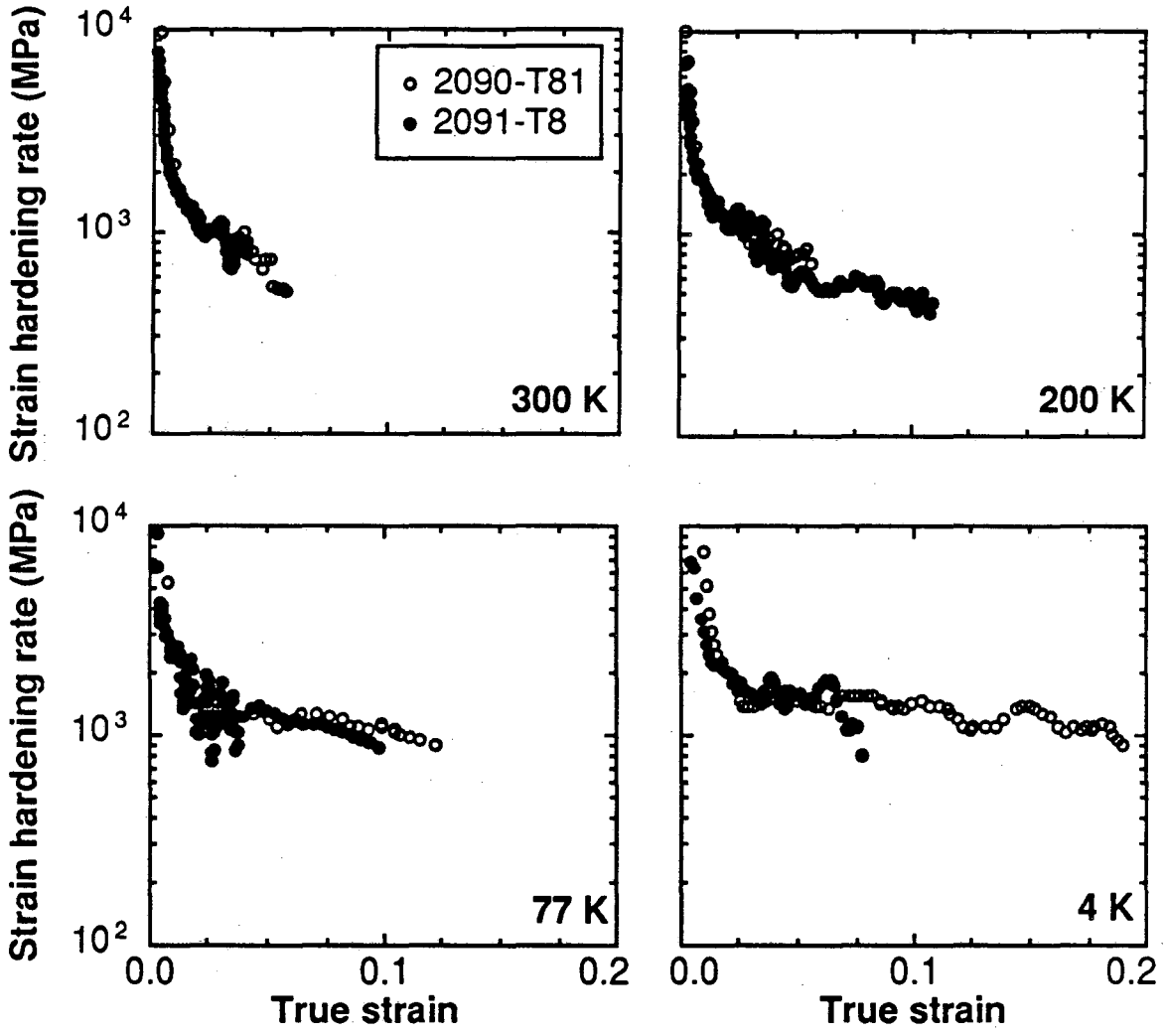

Figure 4.20 Comparison of 2090-T81 and 2091-T8 strain hardening rates at various test temperatures as a function of true strain. L-oriented specimens.

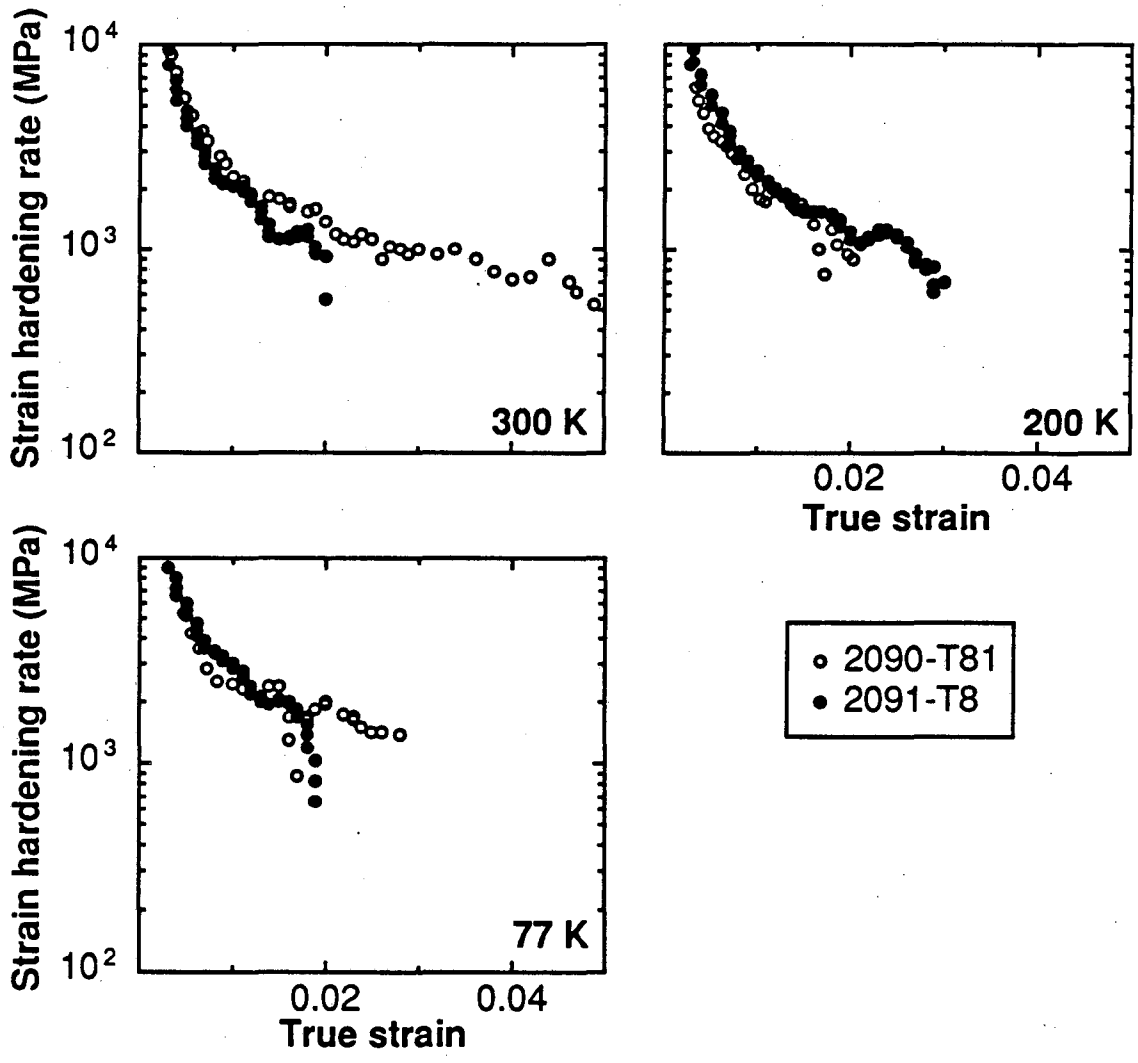

Figure 4.21 Comparison of 2090-T81 and 2091-T8 strain hardening rates at various test temperatures as a function of true strain. LT-oriented specimens.

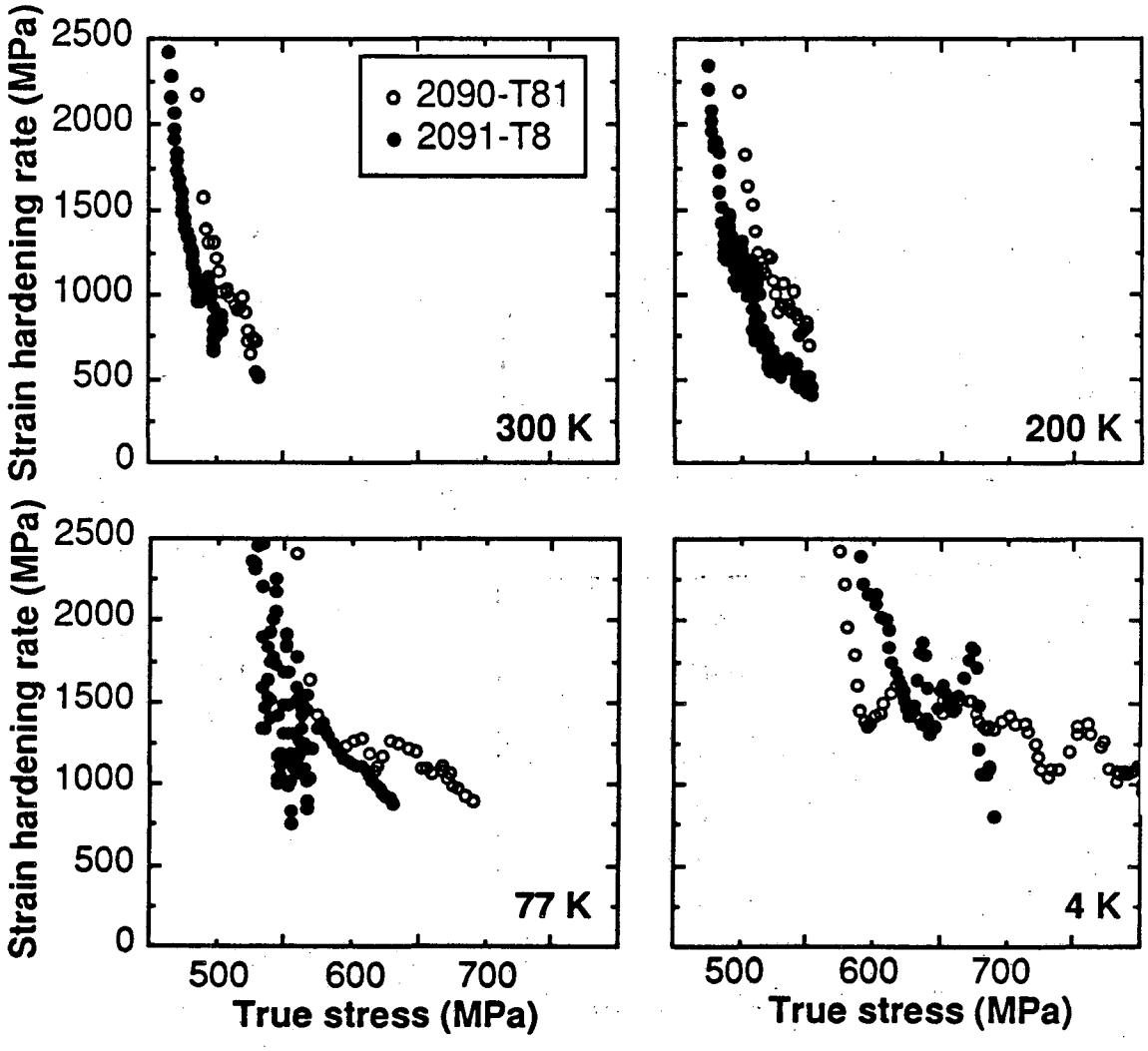

Figure 4.22 Comparison of 2090-T81 and 2091-T8 strain hardening rates at various test temperatures as a function of true stress. L-oriented specimens.

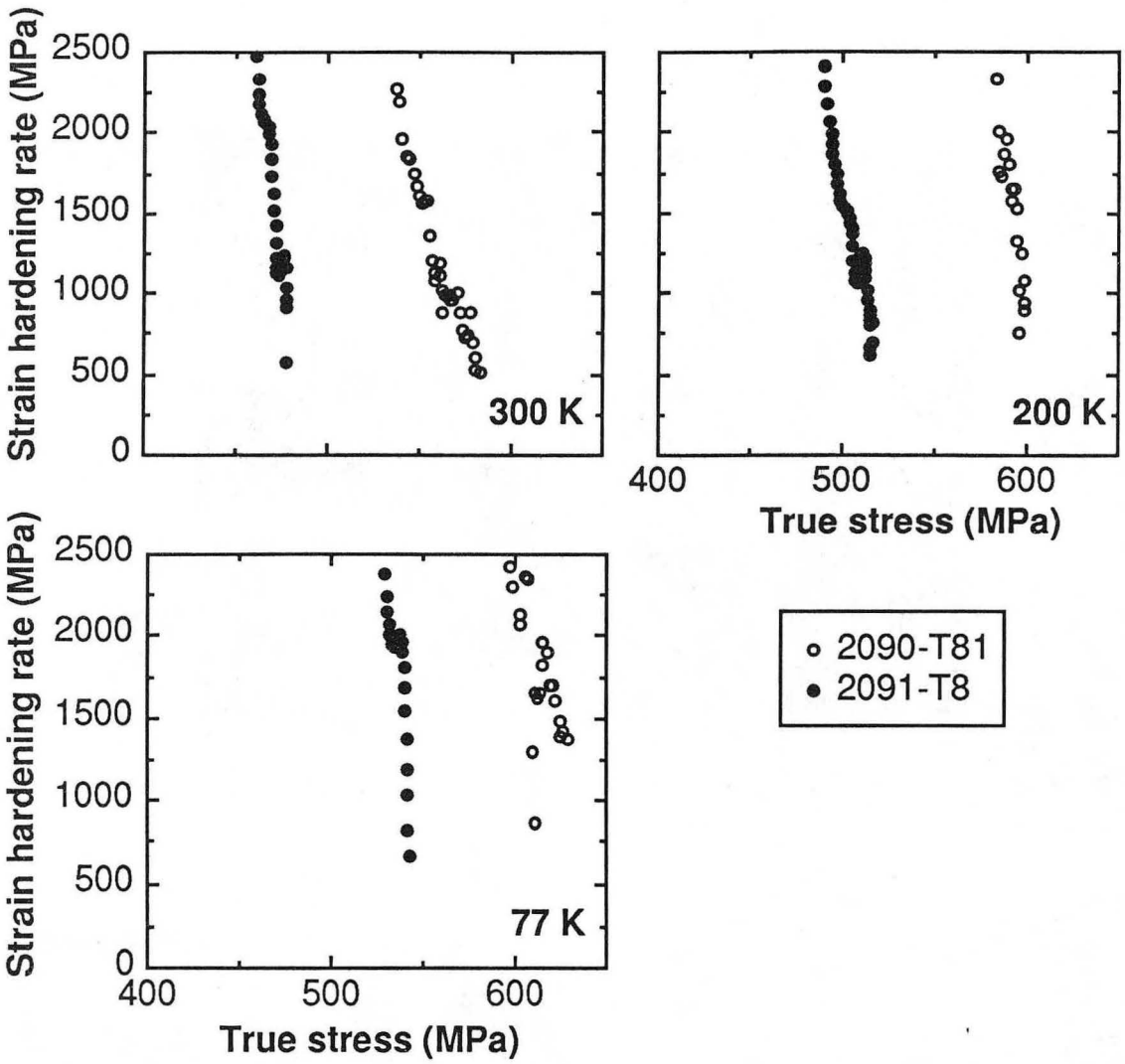

Figure 4.23 Comparison of 2090-T81 and 2091-T8 strain hardening rates at various test temperatures as a function of true stress. LT-oriented specimens.

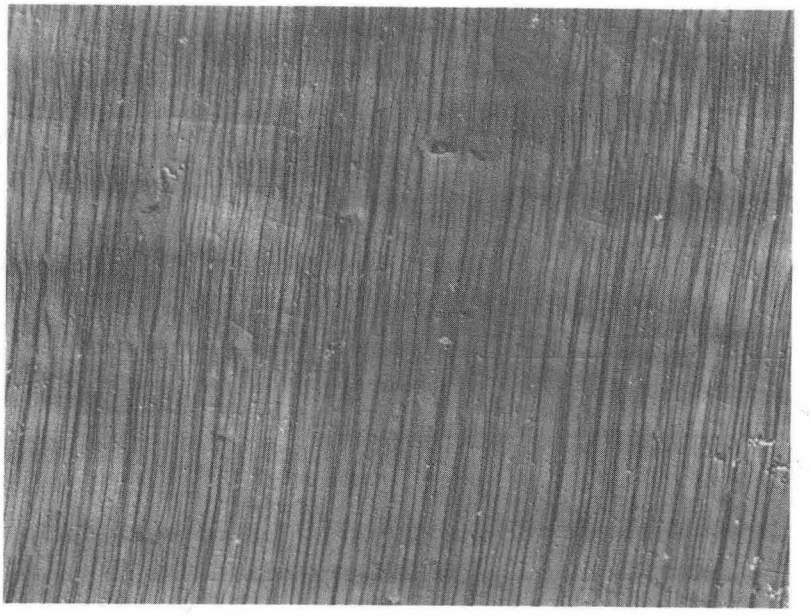

XBB 896-4750

Figure 4.24 Optical micrograph using Nomarski interference contrast of a pre-polished 2090-T81 L-oriented tensile specimen after 2% deformation at room temperature.

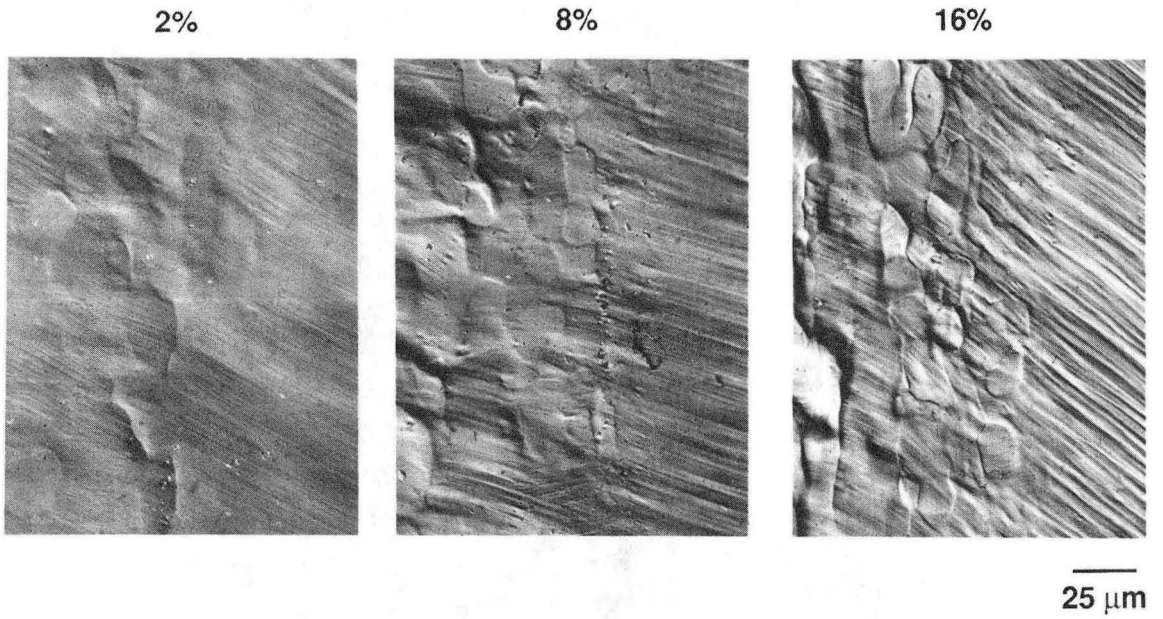

Figure 4.25 Optical micrographs using Nomarski interference contrast of pre-polished 2090-T4 L-oriented tensile specimens deformed various amounts at 77 K

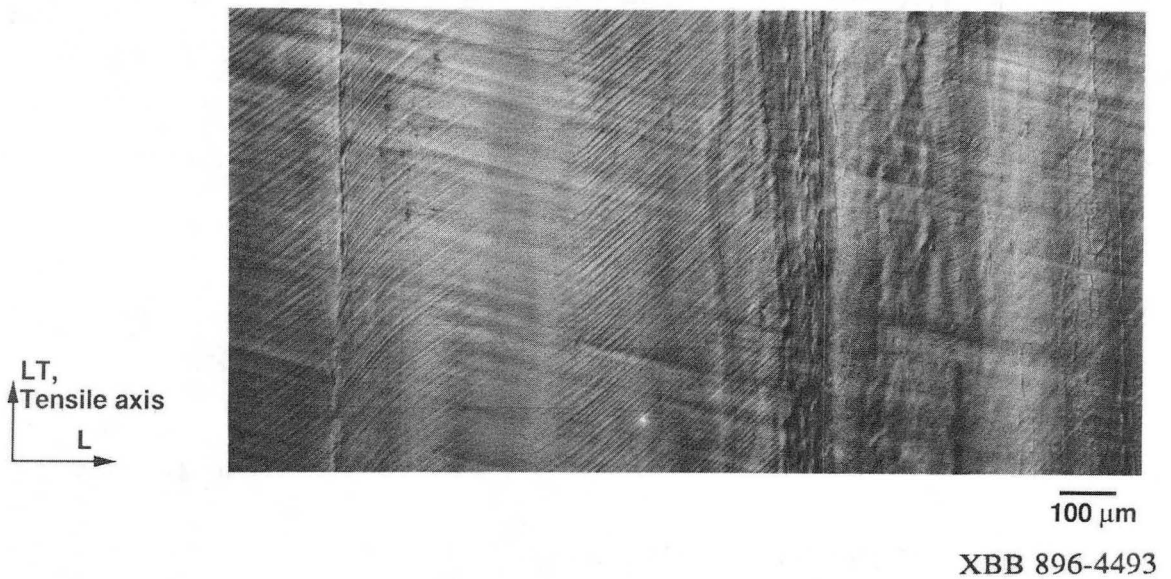

Figure 4.26 Optical micrograph using Nomarski interference contrast of pre-polished 2090-T81 LT-oriented tensile specimen deformed 5.5% at room temperature.

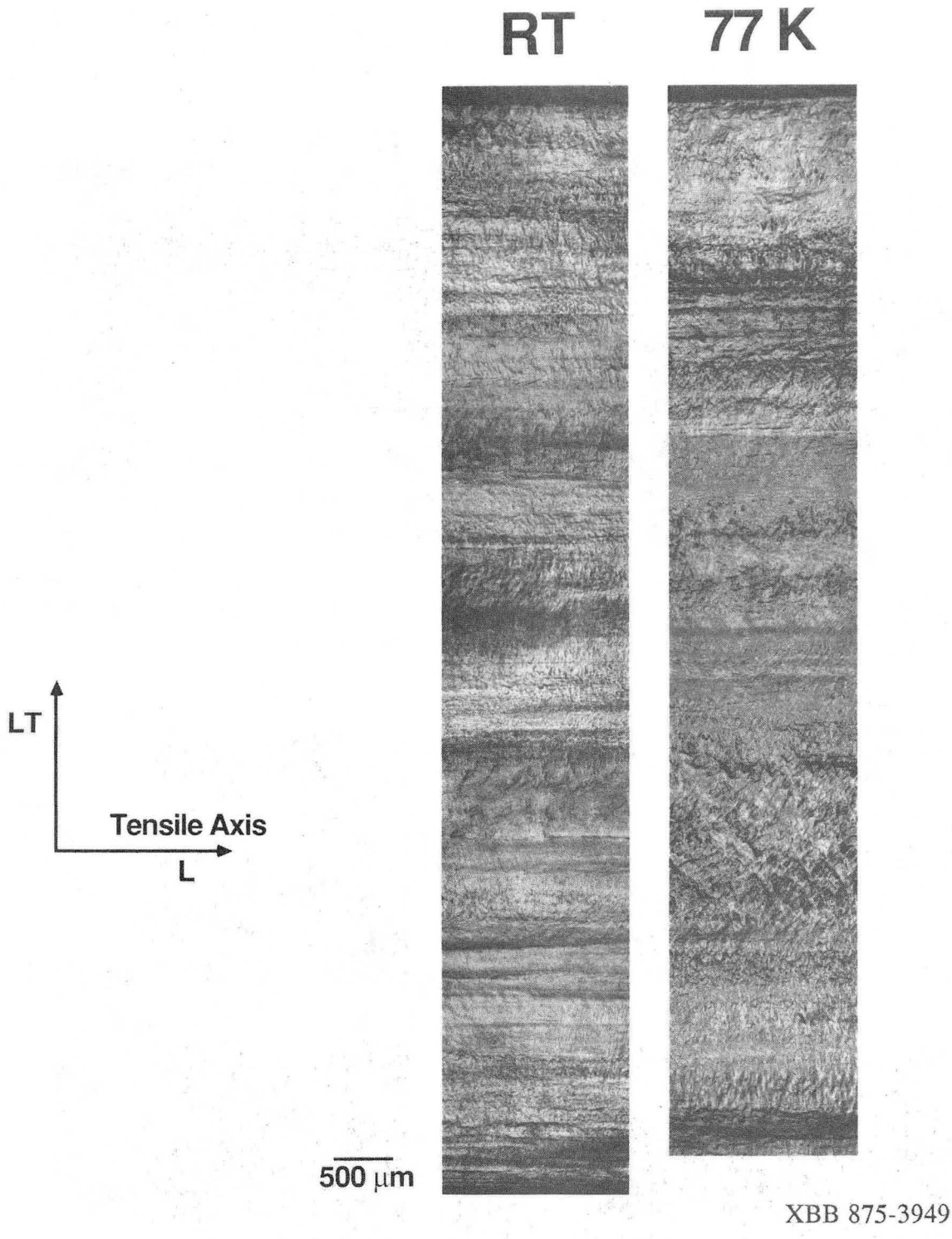

Figure 4.27 Optical micrographs using Nomarski interference contrast comparing surface slip line patterns after straining of pre-polished 2090-T4 specimens deformed 16% at 300 and 77 K.

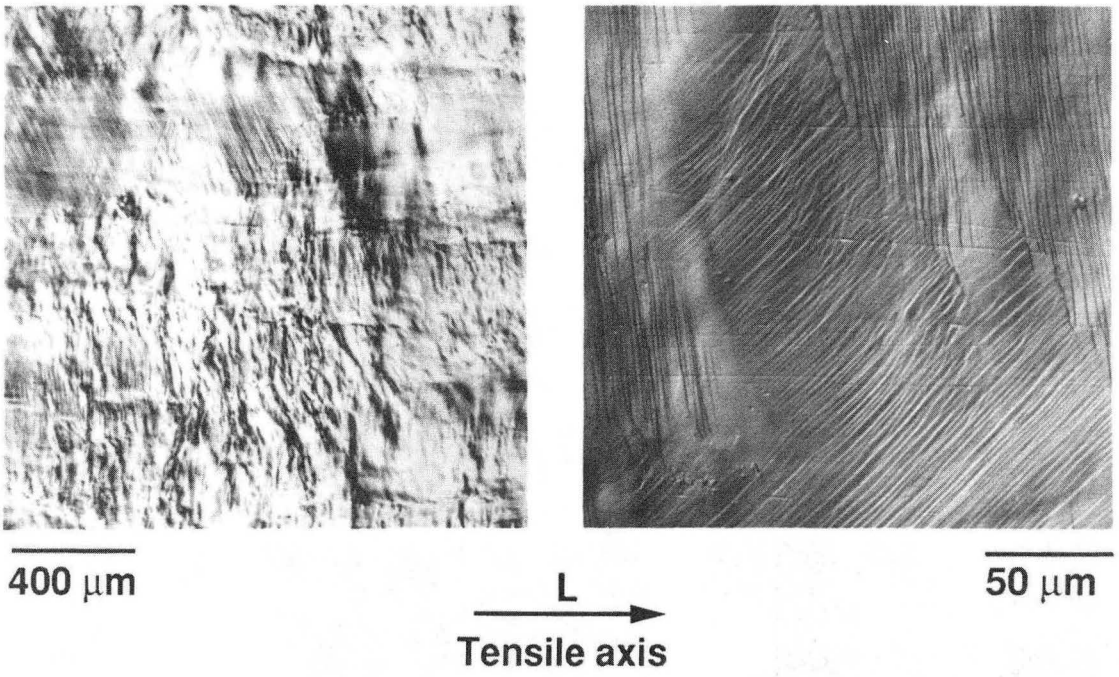

XBB 896-4895

Figure 4.28 Optical micrographs using Nomarski interference contrast of pre-polished 2091-T8 L-oriented tensile specimen strained 5% at 300 K.

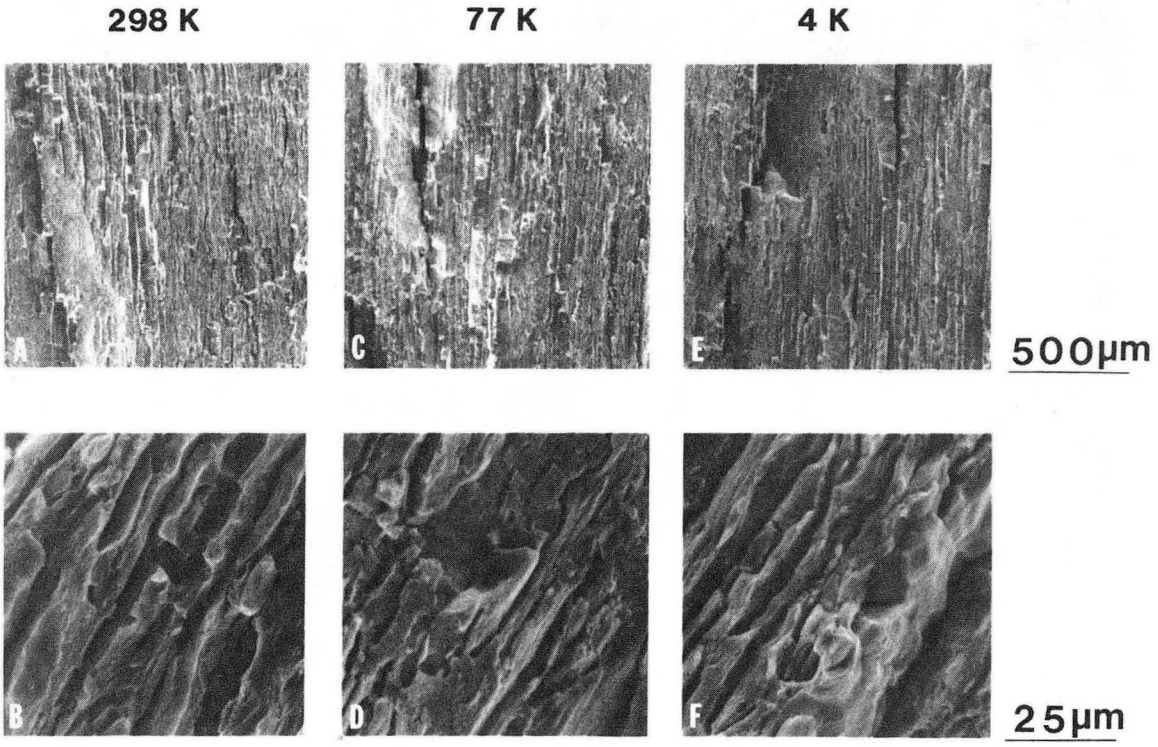

XBB 858-5979

Figure 5.1 Scanning electron micrographs of fracture surfaces of 2090-T81 J_{Ic} specimens tested in the L-T orientation broken at a),b) 298 K, c),d) 77 K and e),f) 4 K.

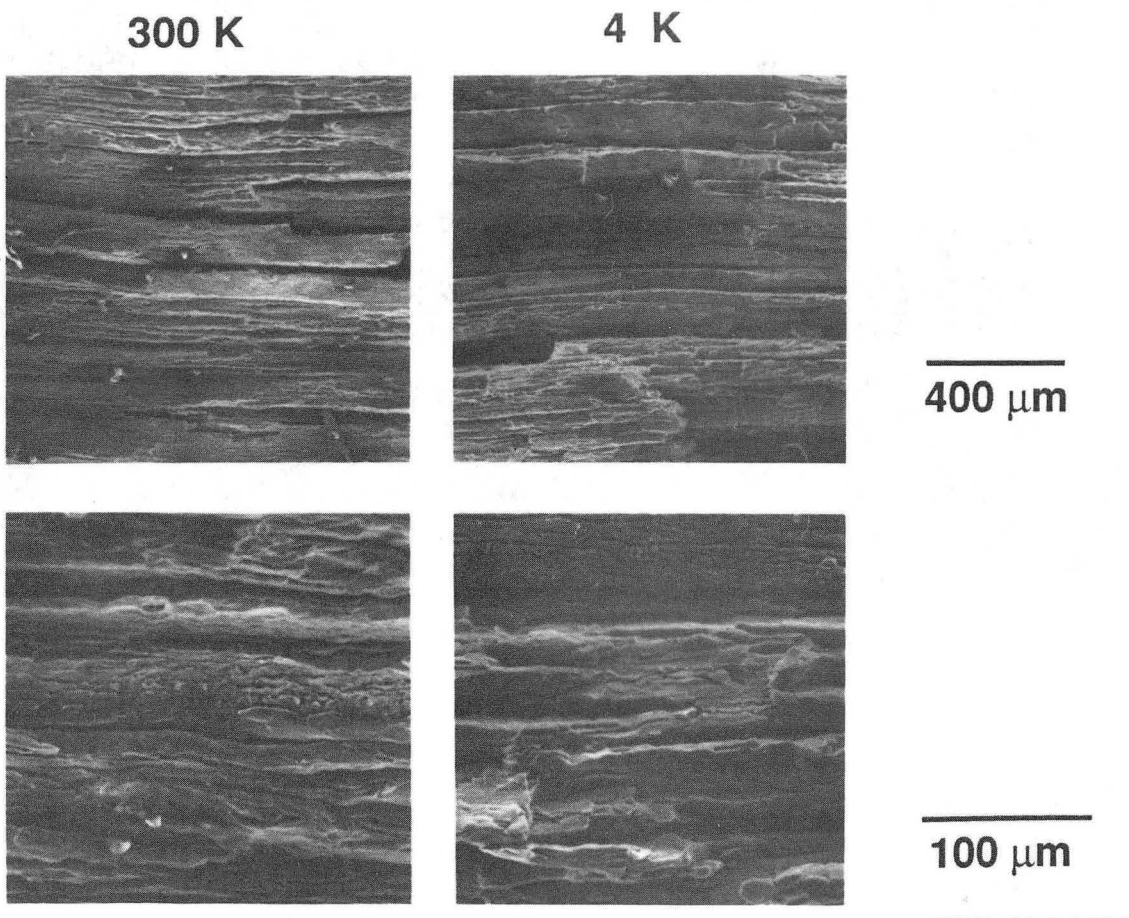

Figure 5.2 Scanning electron micrographs showing failure appearance of 2090-T81 L-oriented tensile specimens tested at T/4. Specimens broken at 200 and 77 K not shown due to extensive intergranular splitting.

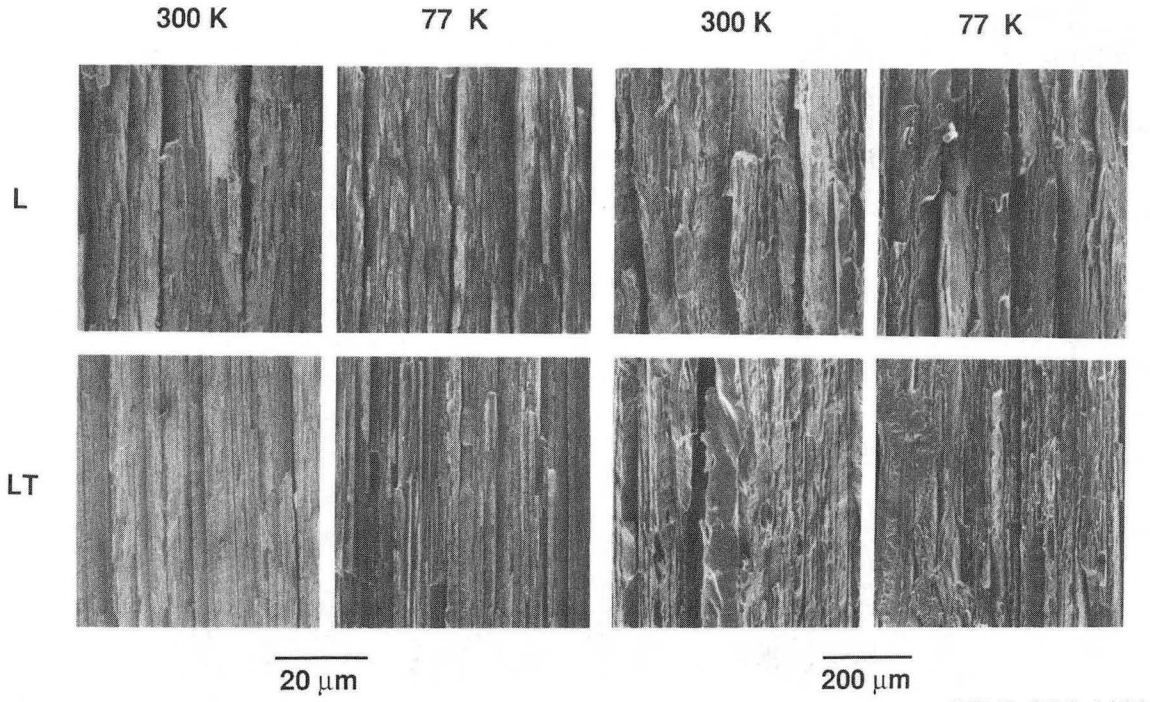

Figure 5.3 Scanning electron micrographs comparing fracture appearance of 2090-T81 notched tensile specimens centered at T/2.

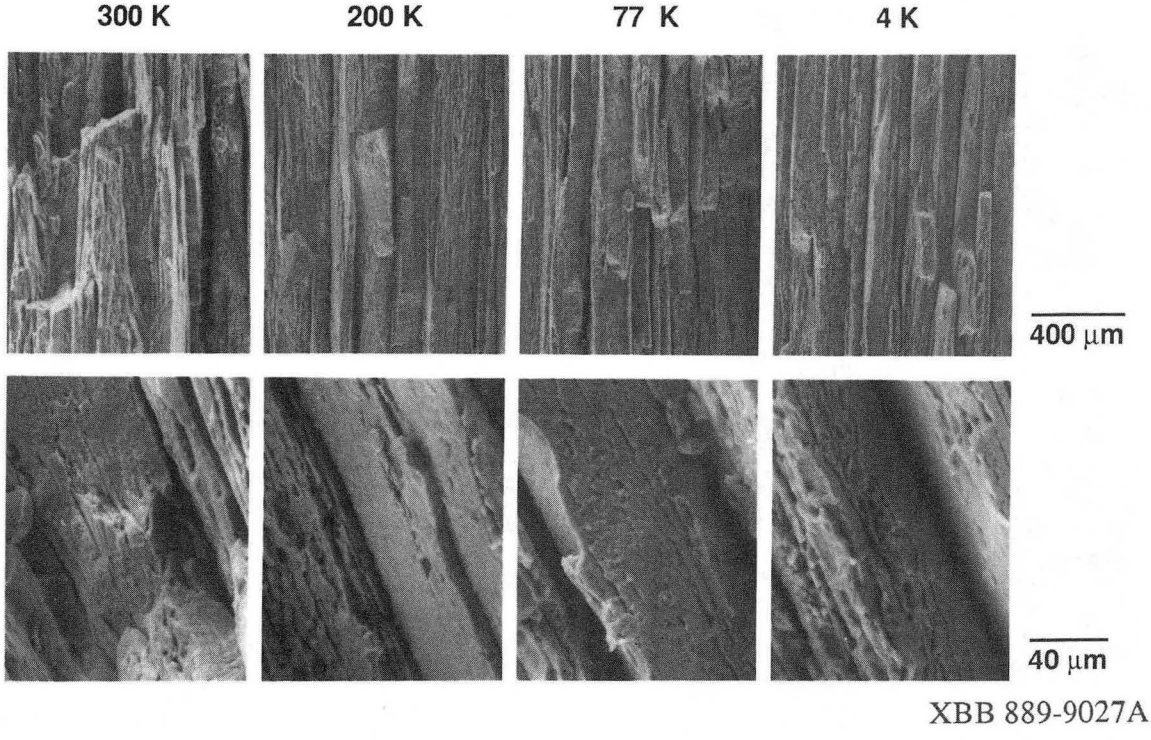

Figure 5.4 Scanning electron micrographs comparing failure appearance of LT-oriented 2091-T8 tensile specimens broken at various test temperatures.

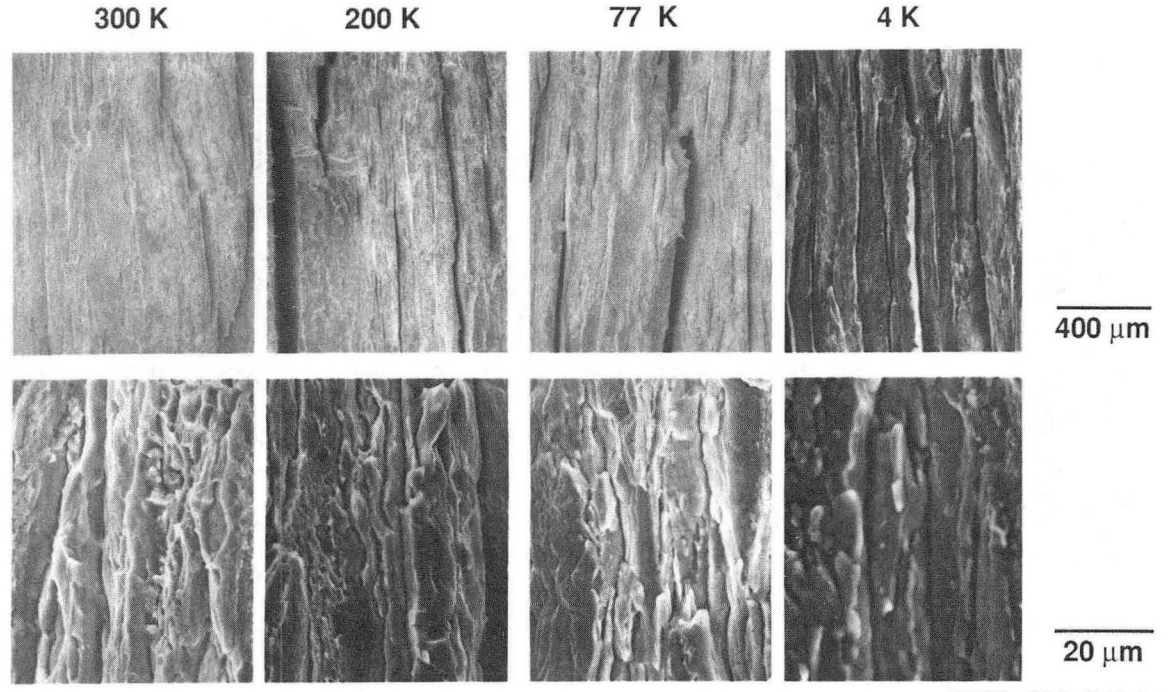

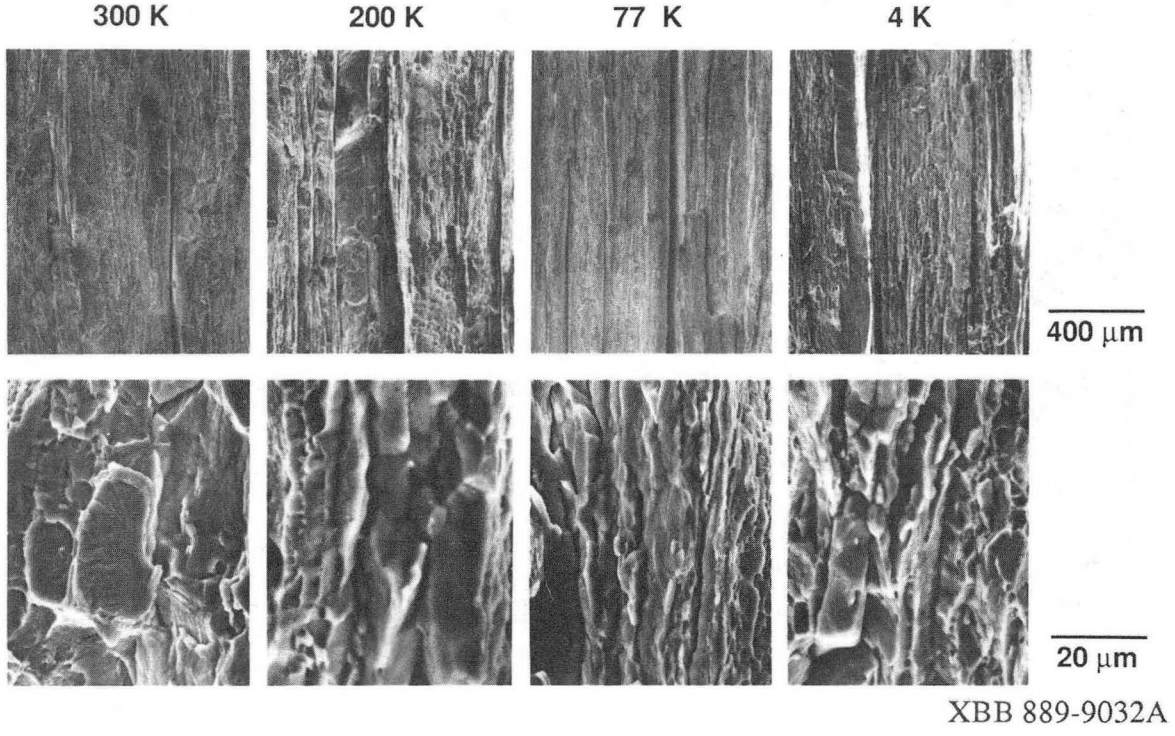

Figure 5.6 Scanning electron micrographs comparing fracture appearance of T-L oriented 2091-T8 J_{Ic} specimens broken at various test temperatures.

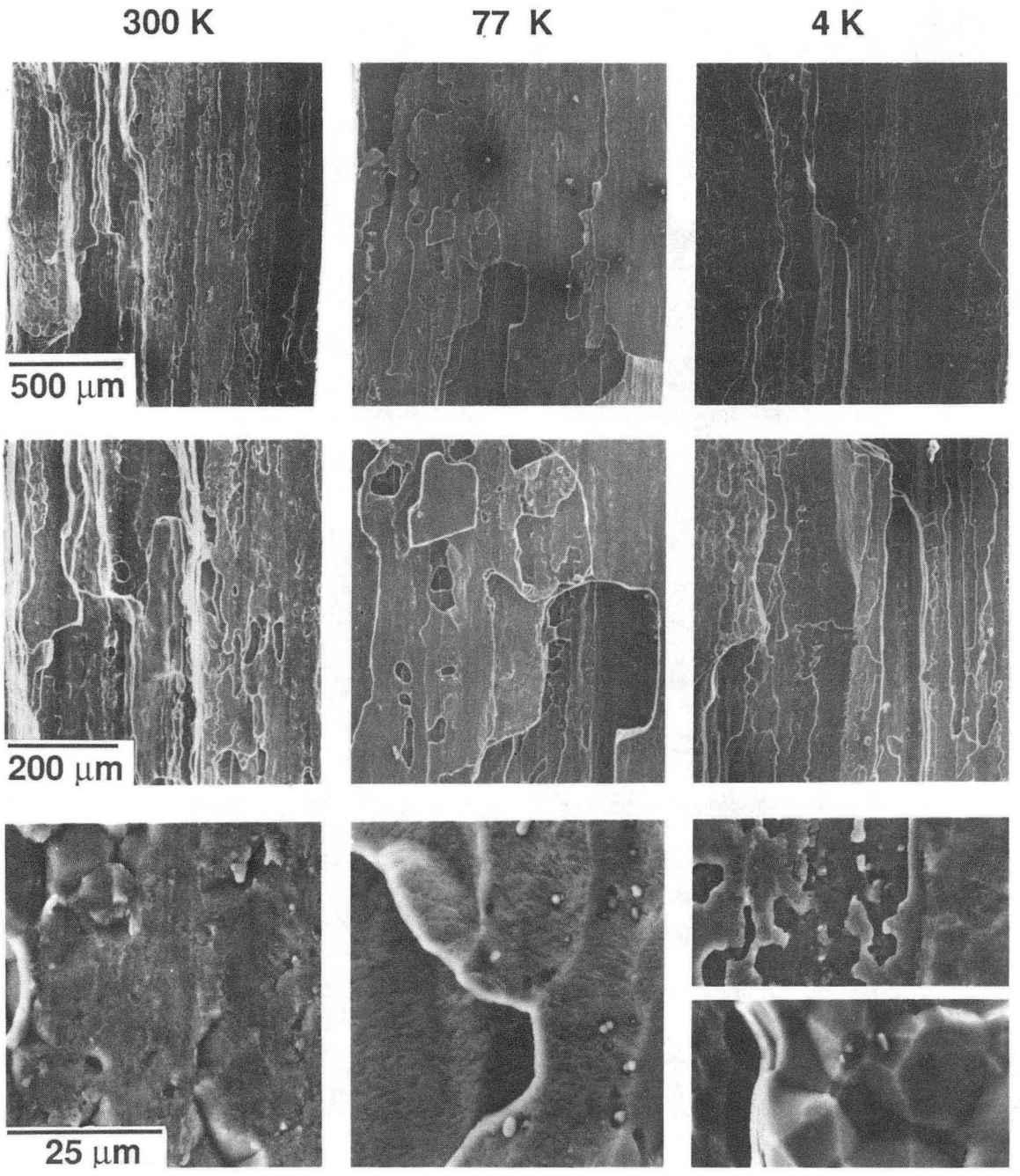

Figure 5.7 Scanning electron micrographs comparing the failure appearance of ST-oriented 2090-T81 tensile specimens.

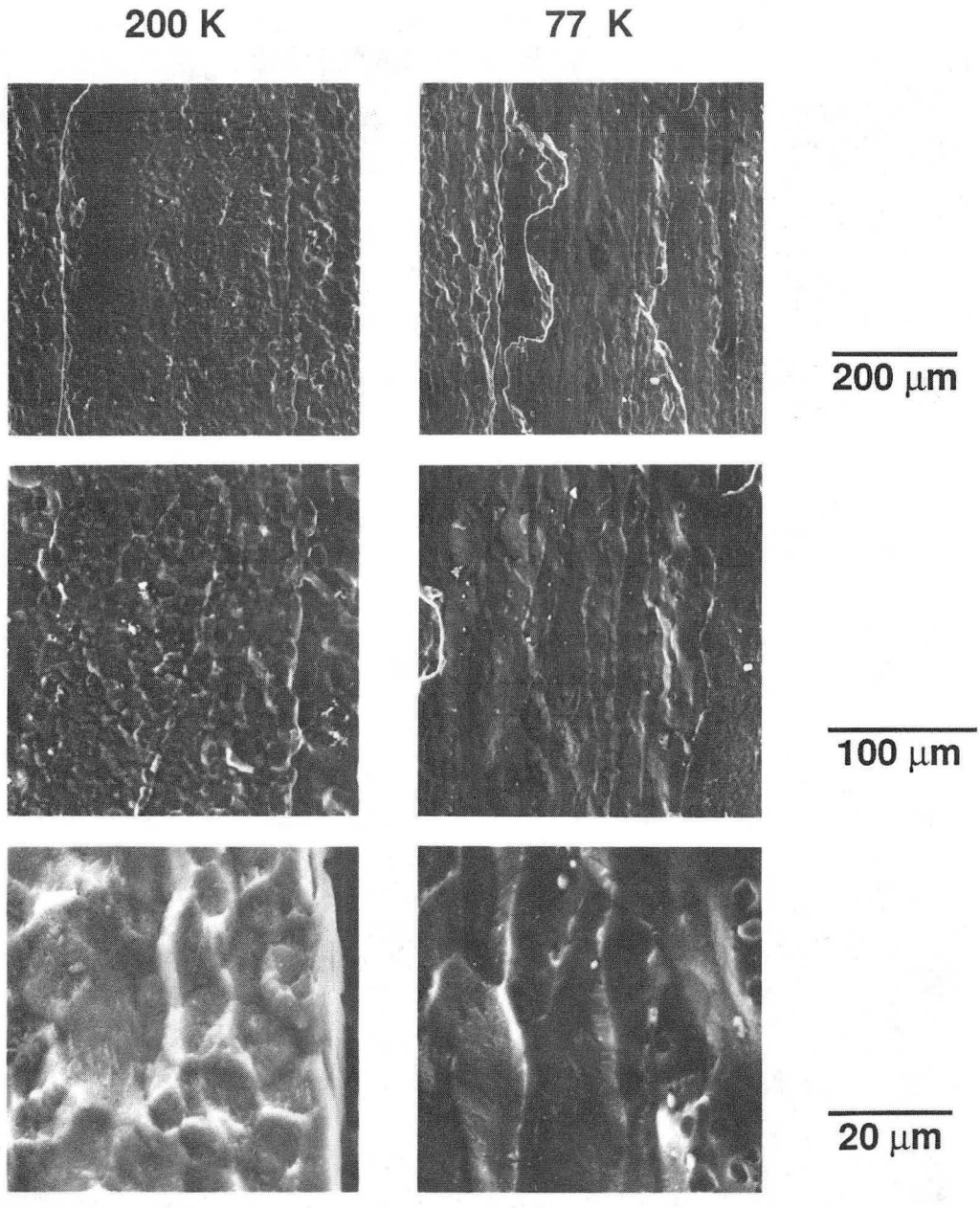

Figure 5.8 Scanning electron micrographs illustrating the appearance of the surfaces along which delamination occurs in 2090-T81 L-oriented tensile specimens centered at T/4.

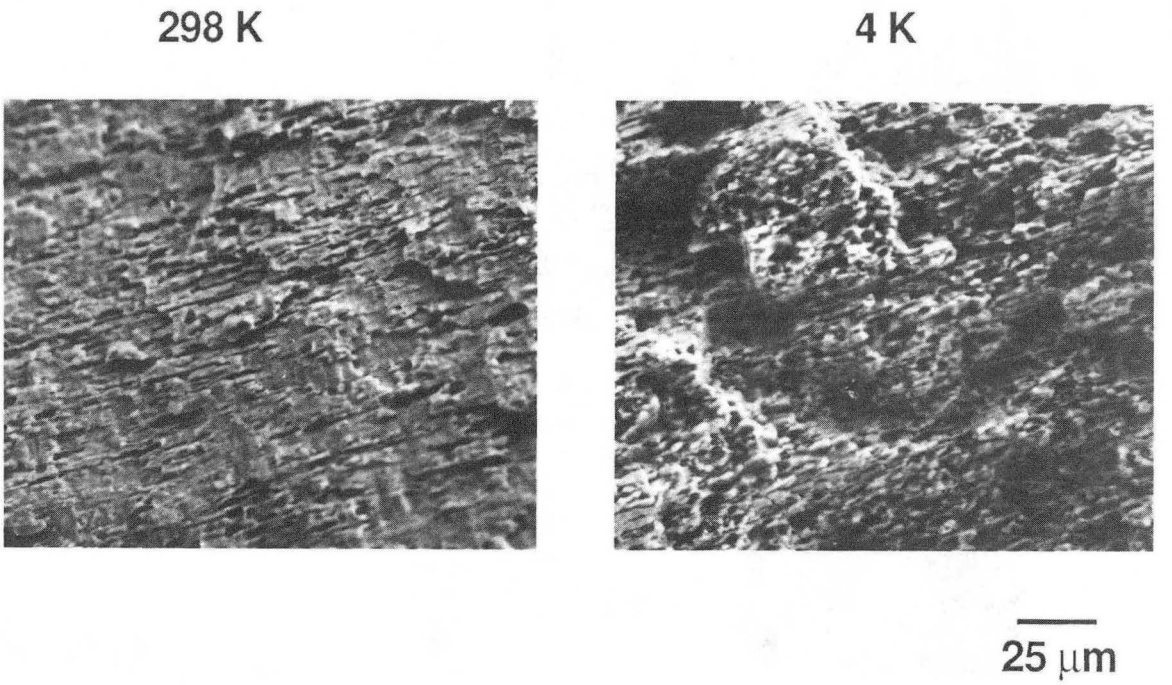

Figure 5.9 Scanning electron micrographs illustrating the change in failure surface appearance in tensile specimens of superplastically formable 2090-T6 tested at various temperatures.

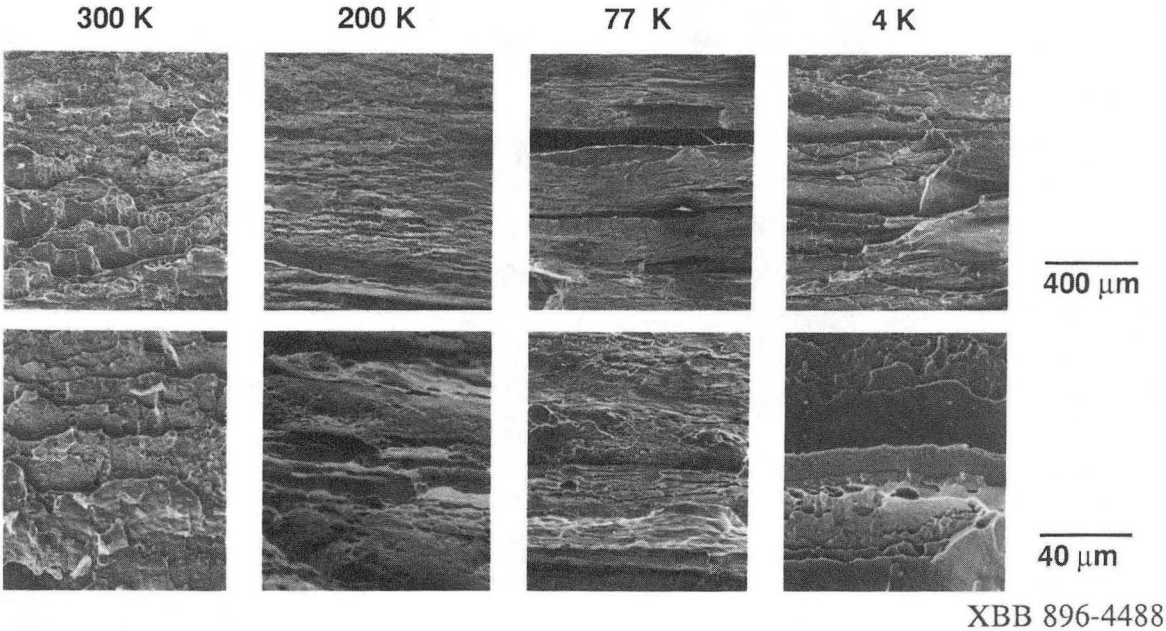

Figure 5.10 Scanning electron micrographs of tensile failure surfaces of L-oriented specimens of 2090-T4 (centered at T/4).

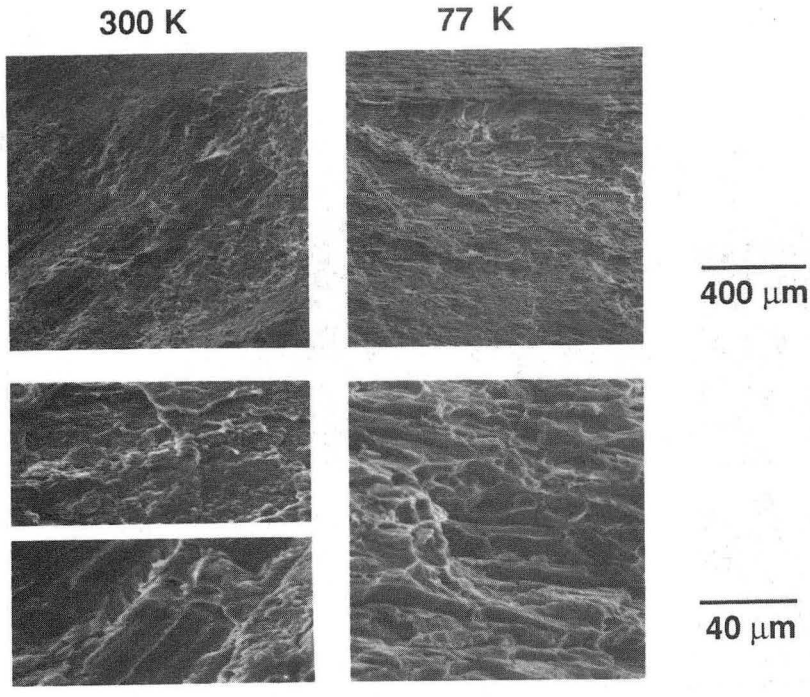

Figure 5.11 Scanning electron micrographs of tensile failure surfaces in L-oriented specimens of peak-aged Al-2.4 Li-0.12 Zr.

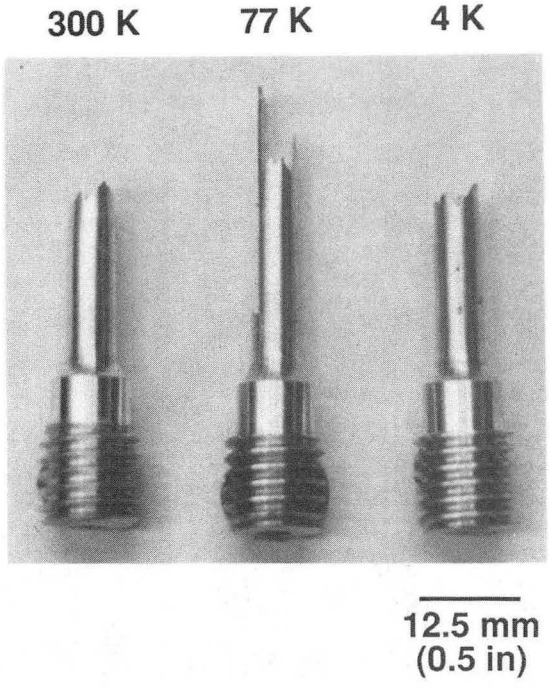

Figure 5.12 Optical micrograph of failed 2090-T81 tensile specimens centered at T/2. Note extensive splitting at 77 K.

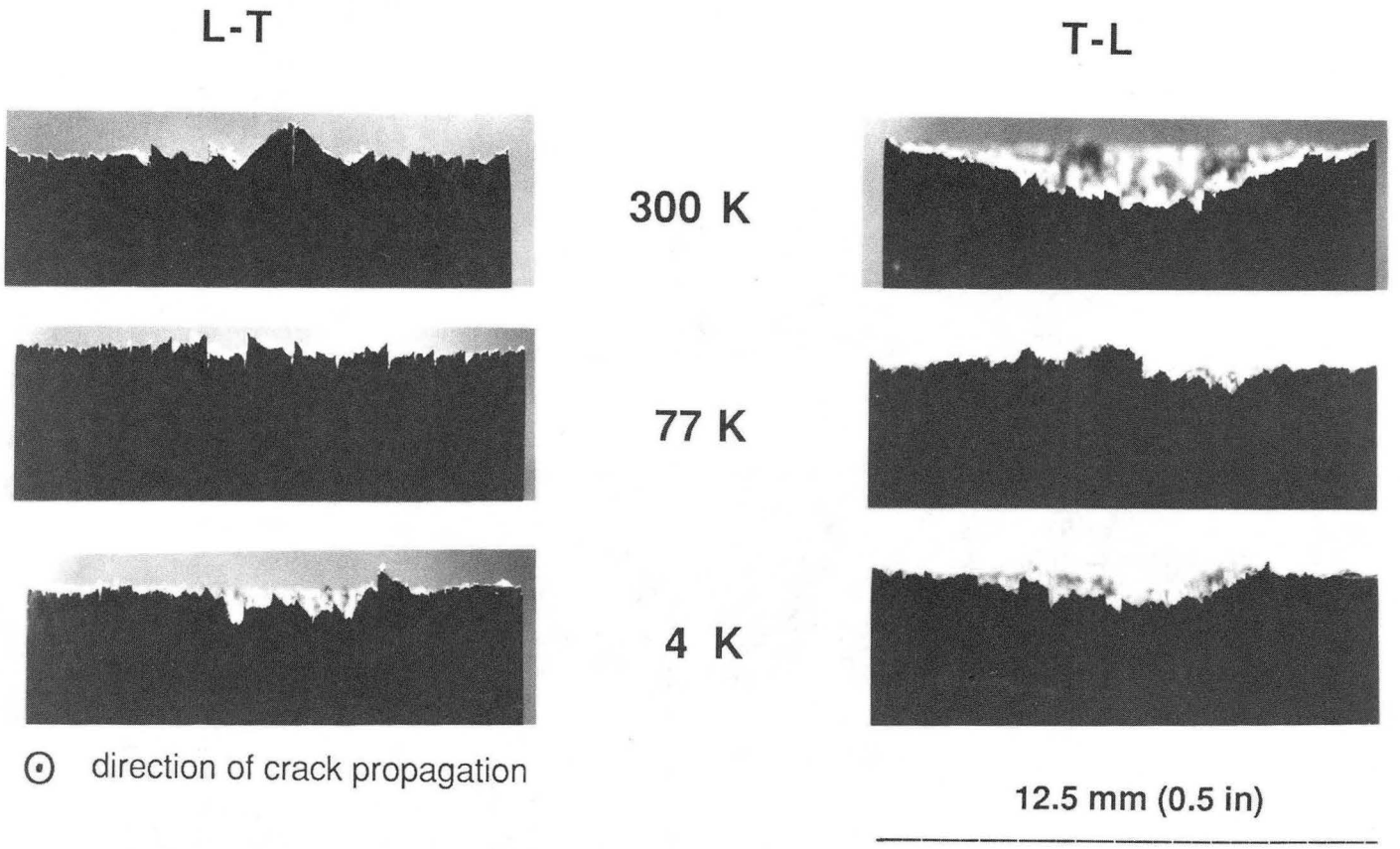

Figure 5.13 Optical micrographs showing fracture profile and splitting in 2090-T81 J_{Ic} specimens. Specimens were sectioned perpendicular to crack path near the crack initiation point. Cross section shown is the entire thickness of specimen.

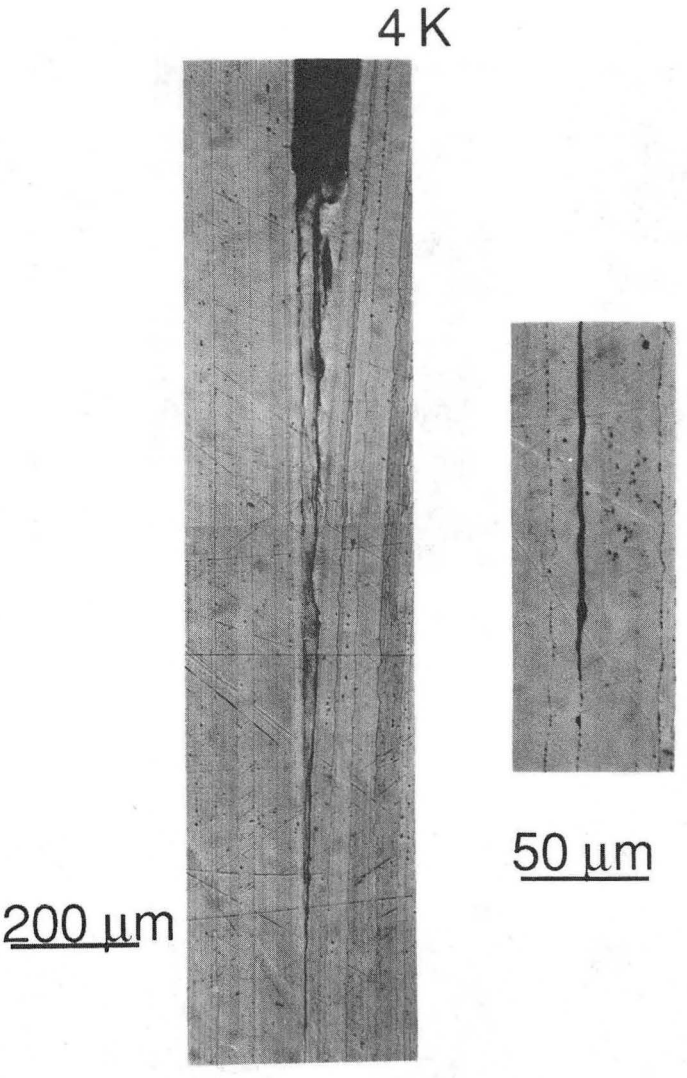

XBB 875-3629

Figure 5.14 Optical micrograph of polished and etched cross section perpendicular to crack path of 2090-T81 J_{Ic} specimen broken at 4 K. Splits appear to follow grain boundaries.

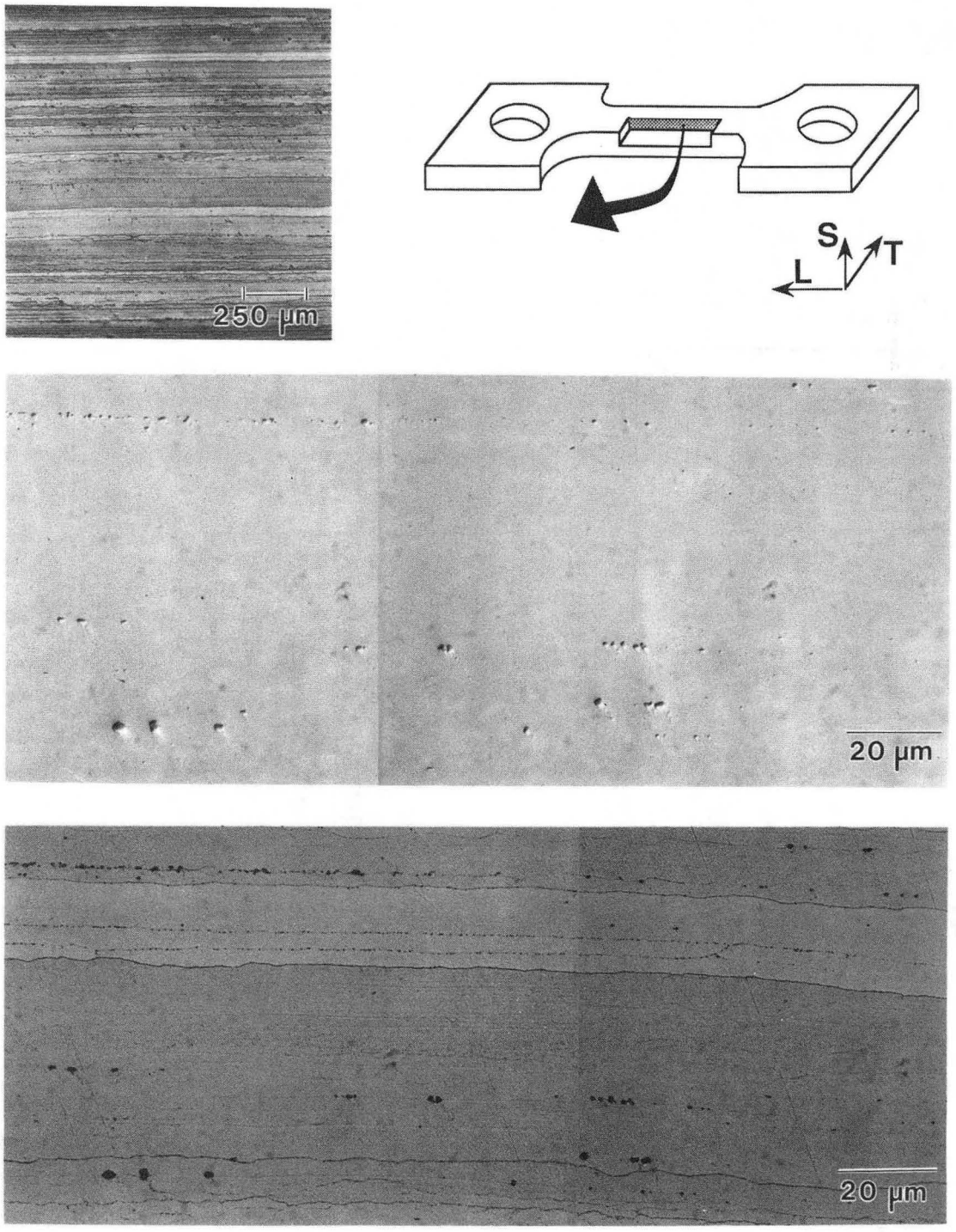

XBB 892-742

Figure 5.15 Optical micrographs of polished (all) and etched (top and bottom, only) cross section of 2090-T81 tensile specimen centered at T/4. Specimen was strained at 77 K to an engineering strain of 8%. Although there is extensive splitting in specimens broken at this temperature, no splits are observed in this strained but unbroken specimen.

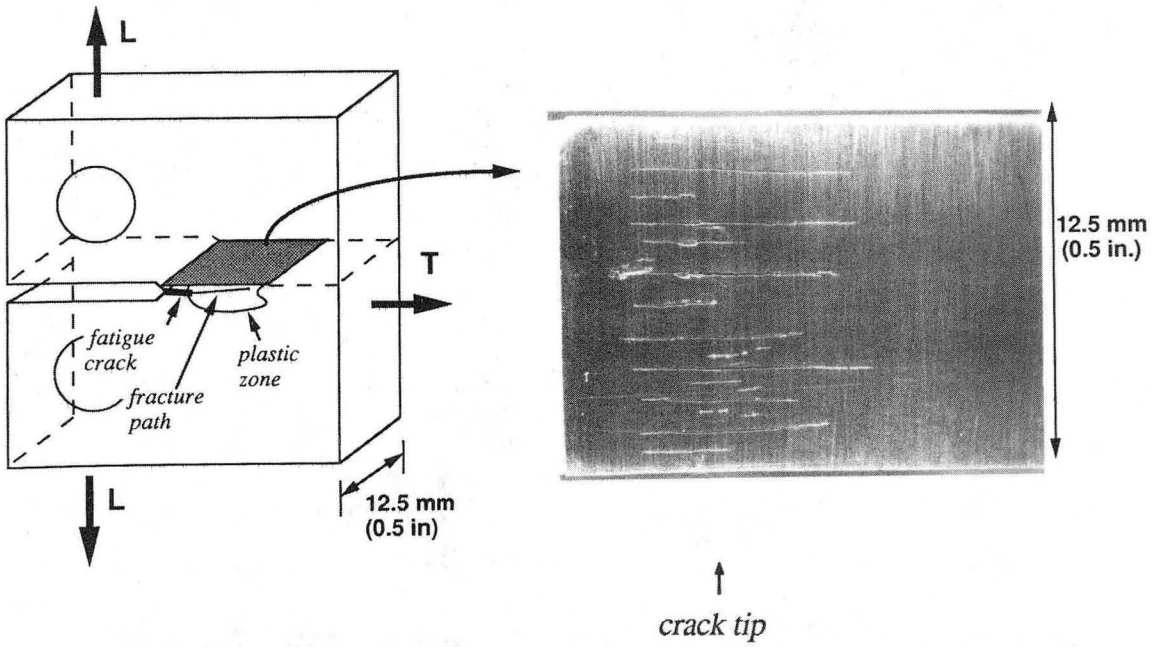

XBB 889-9029

Figure 5.16 Optical micrograph of polished cross section of 2090-T81 J_{Ic} specimen tested at 77 K. After crack had propagated a few millimeters, the specimen was sectioned about one millimeter from the crack plane and parallel to it. White lines are splits. The crack tip location is marked.

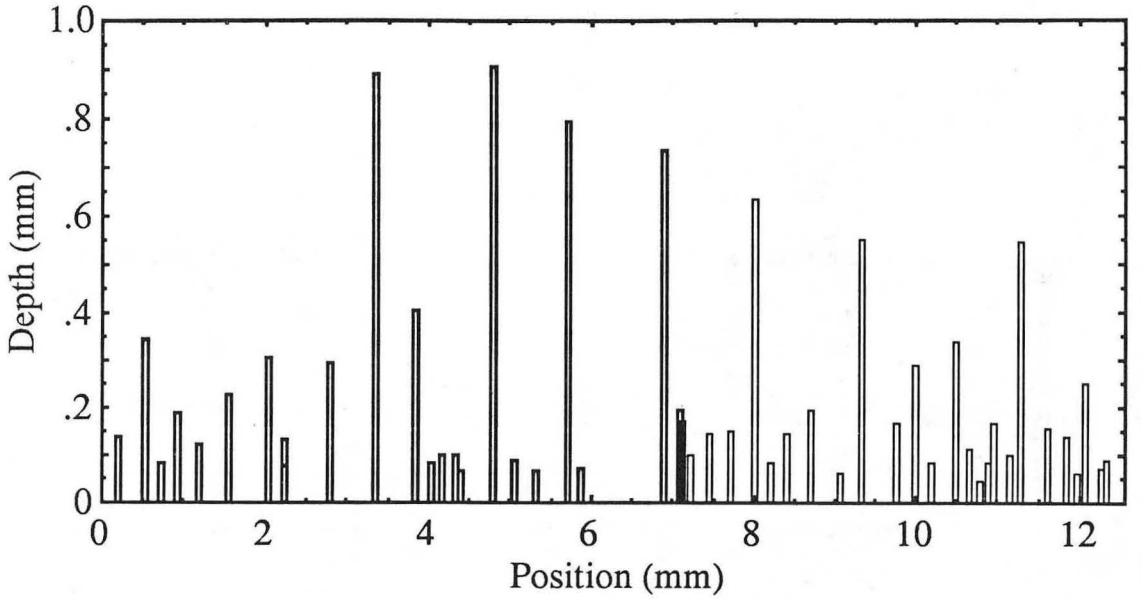

Figure 5.17 Schematic split profile obtained after digitizing splits in optical micrographs of polished cross section of J_{Ic} specimen. Data shown are for a 2090-T81 specimen tested at 77 K in the L-T orientation.

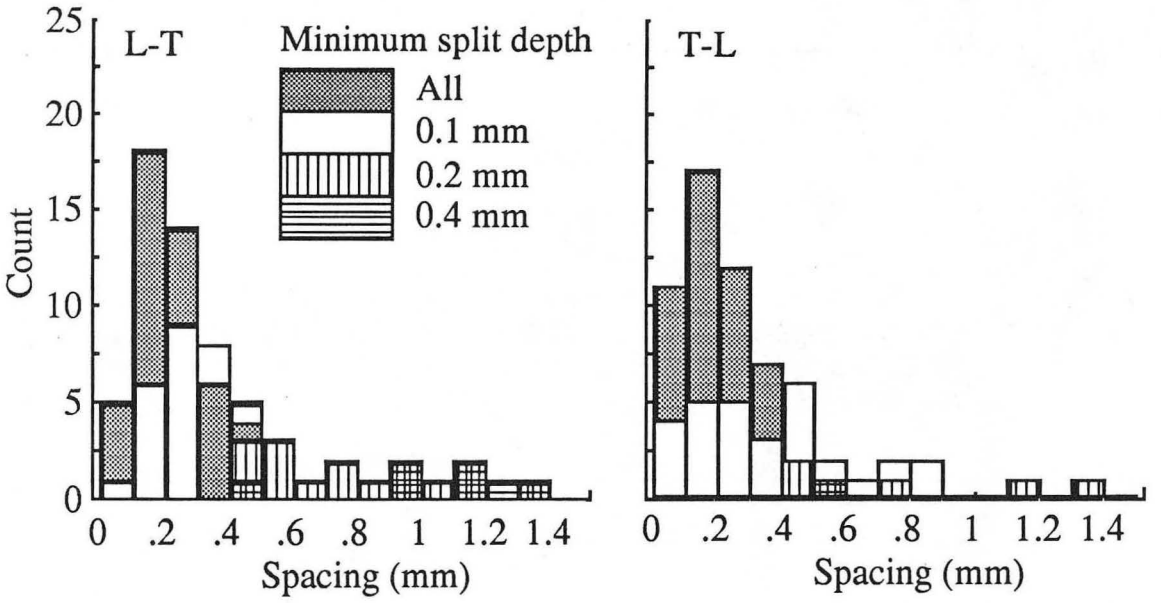

Figure 5.18 Histograms of split spacing for 2090-T81 specimens tested at 77 K in L-T and T-L orientations. Separate histograms were computed for splits deeper than the specified values.

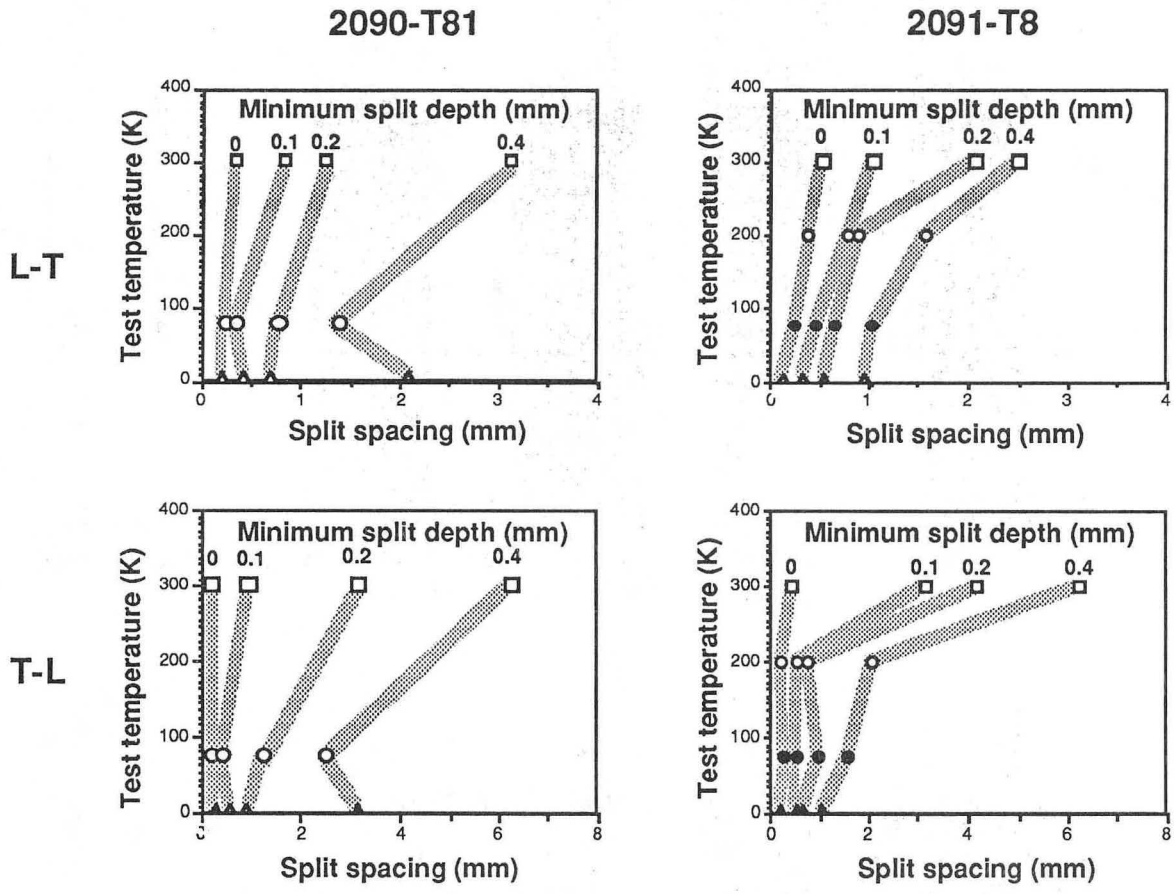

Figure 5.19 Variation in mean split spacing with test temperature and minimum split depth for 2090-T81 and 2091-T8 J_{Ic} specimens in the L-T and T-L orientations. Note the change in the horizontal scale for L-T and T-L orientations.

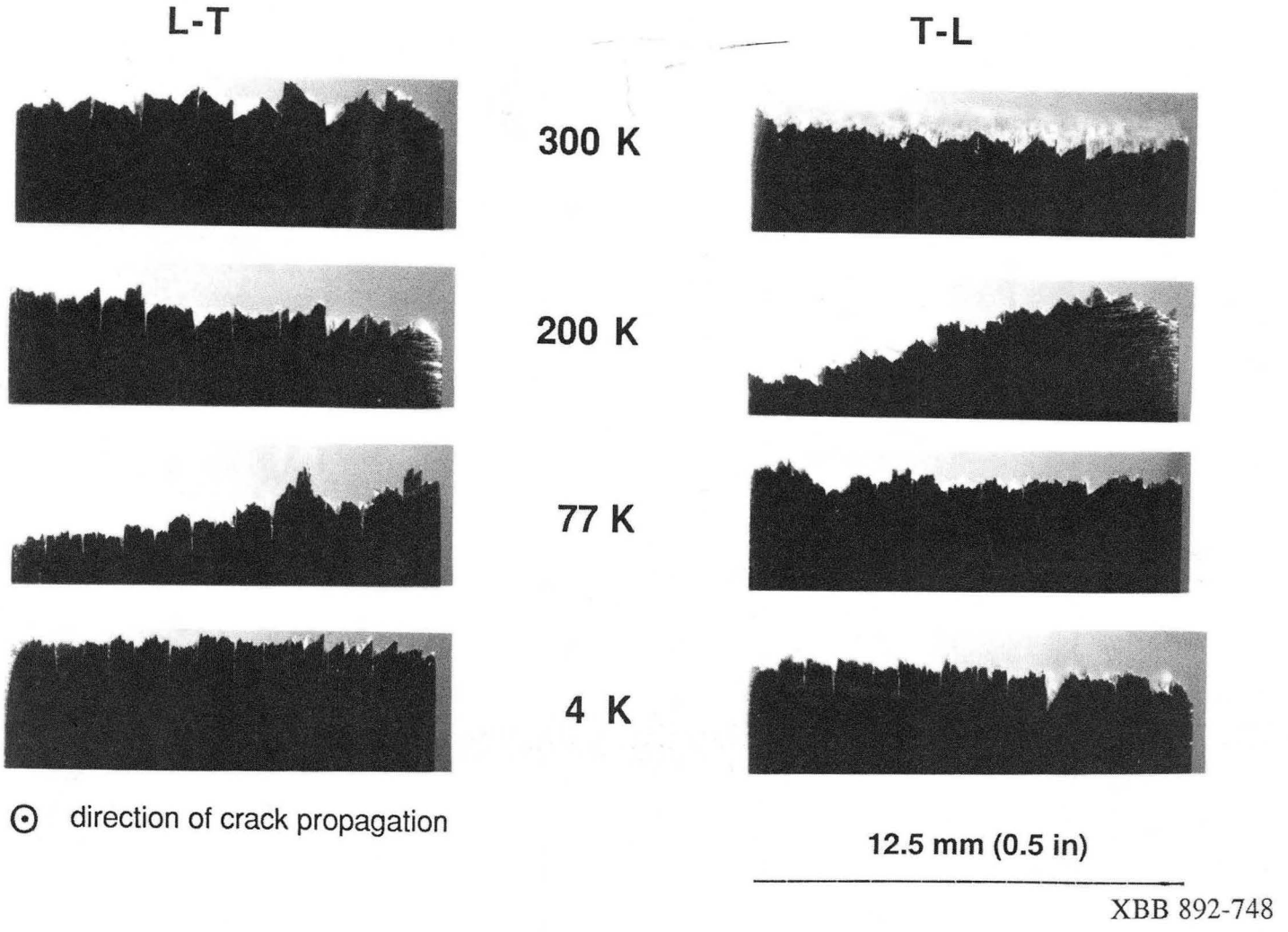

Figure 5.20 Optical micrographs showing fracture profile and splitting in 2091-T8 J_{Ic} specimens. Specimens were sectioned perpendicular to crack path near the crack initiation point. Cross section shown is the entire thickness of specimen.

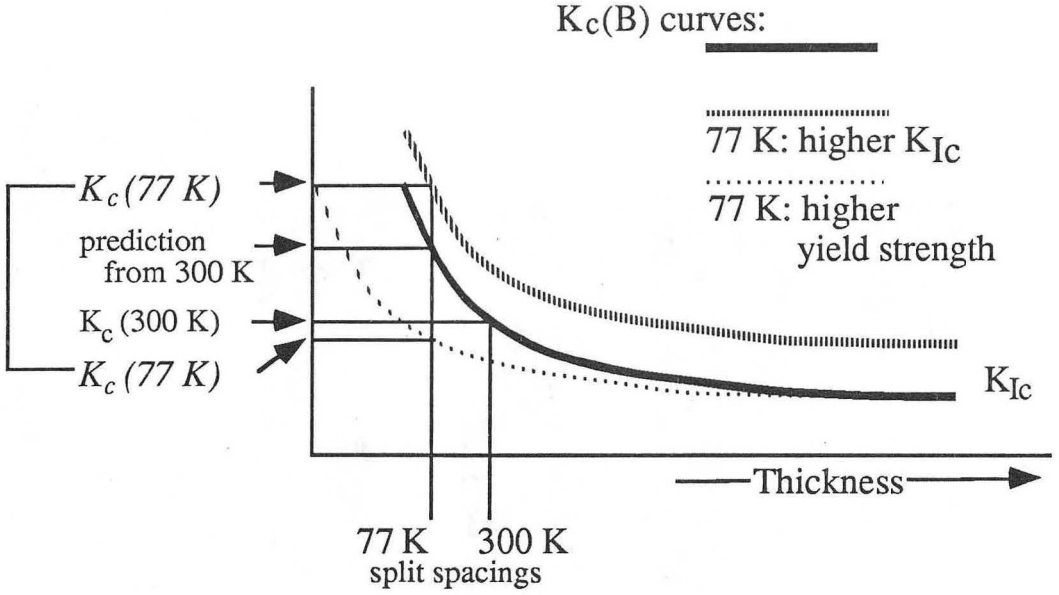

Figure 6.1 Schematic illustration of possible effects of temperature on apparent K_{Ic} in specimens that split. Possible effects on the K_c vs. specimen thickness curve and predicted toughness for various split spacings are shown. It is experimentally observed that the split spacing at 77 K is lower than at 300 K for both 2090-T81 and 2091-T8 in both test orientations.

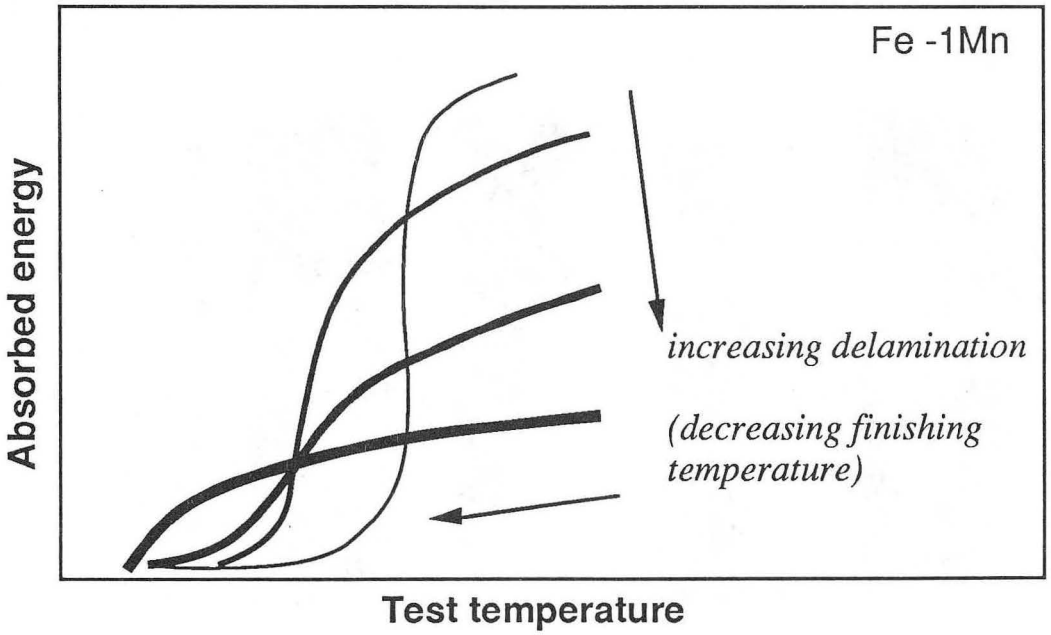

Figure 6.2 Effect of intergranular delamination in crack-divider orientation on Charpy impact energy in an Fe-1 Mn steel. Both the ductile-brittle transition temperature and the upper shelf toughness decrease with increasing amounts of splitting. (From Bramfitt and Marder, 1977.)

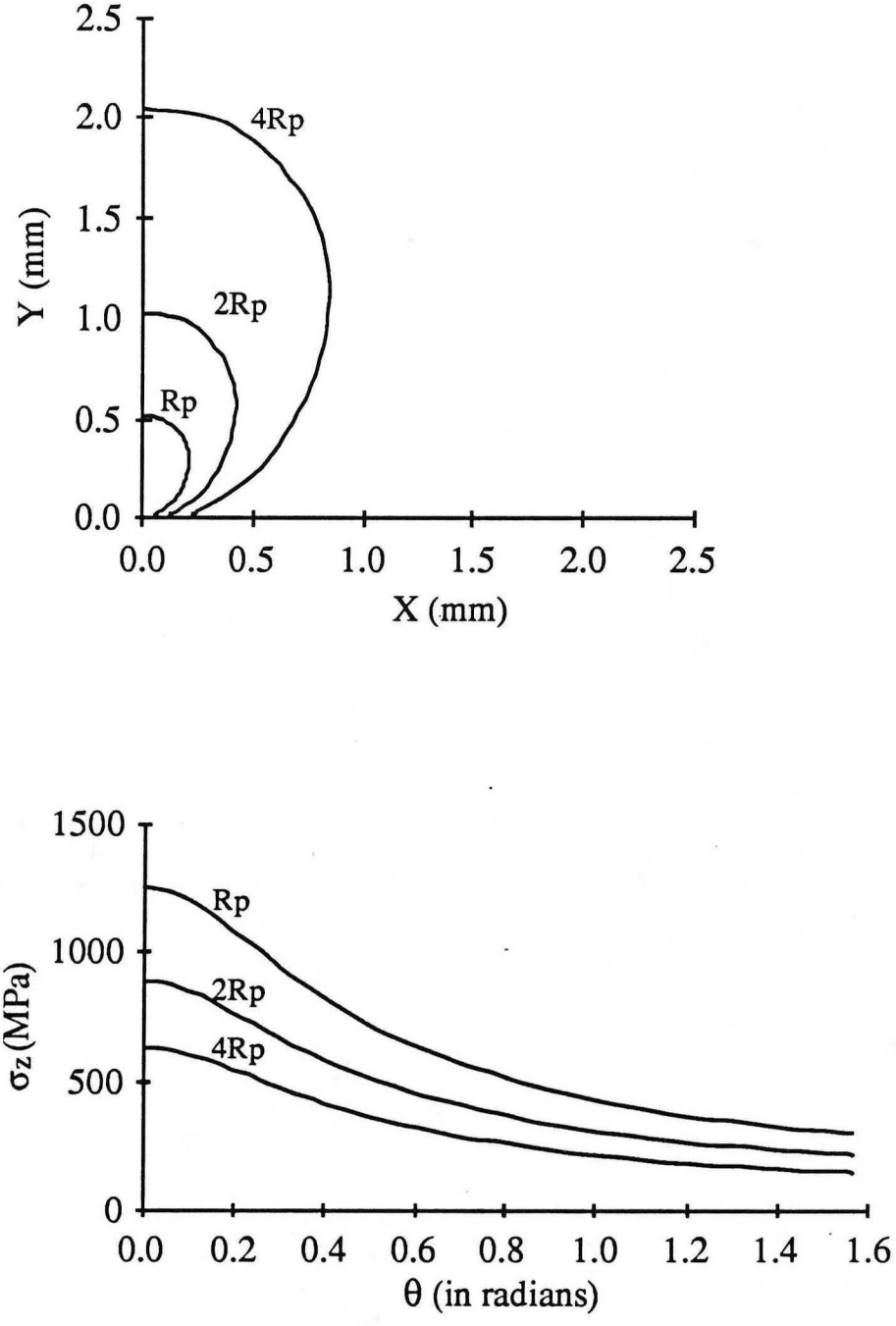

Figure 6.3 Calculated stress under linear elastic fracture mechanics for 2090-T81, L-T, tested at 300 K when the stress intensity is equal to K_{Ic}. It is assumed that plane strain conditions prevail. The origin is the crack tip. Top: Equivalent von Mises' stress contours parameterized by the plastic zone size R_p. Bottom: Calculated values of through-thickness stress σ_z along equivalent von Mises' stress contours shown above.

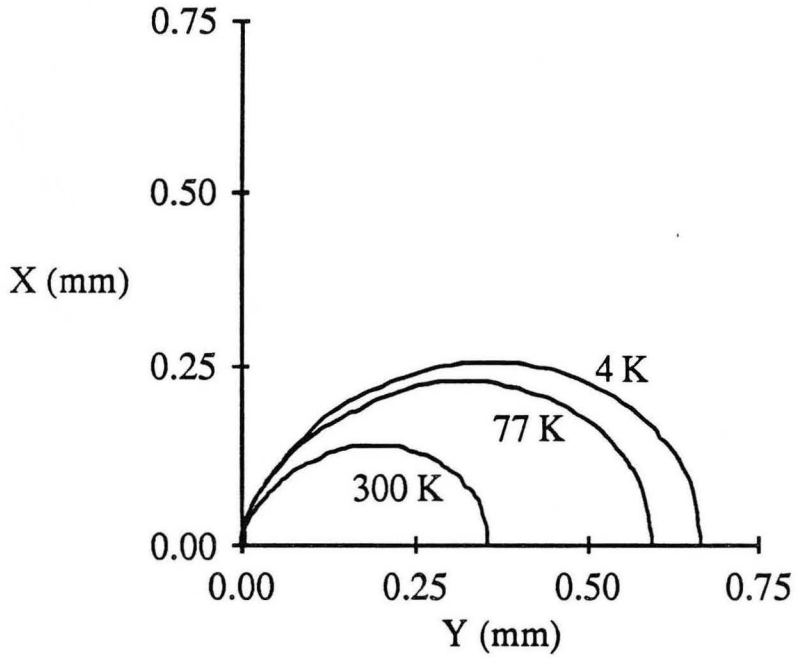

Figure 6.4 Calculated regions in which the through-thickness stress σ_z due to the applied stress intensity K_{Ic} exceeds the ST tensile fracture stress σ_f of 2090-T81 tested in the L-T orientation. The origin is the crack tip. The calculation assumes that plane strain linear elastic fracture mechanics apply.

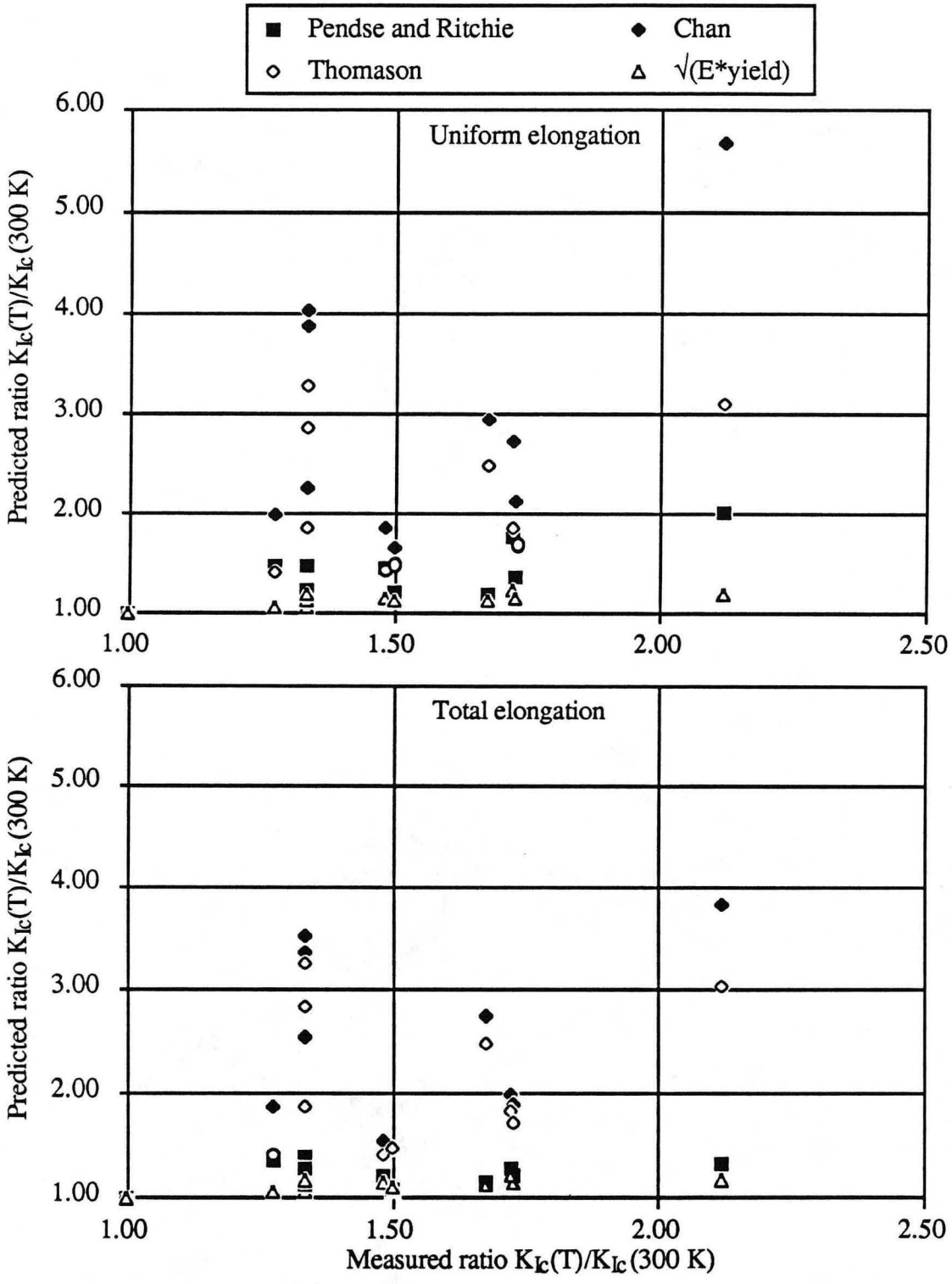

Figure 6.5 Comparison of experimental results and predictions of various fracture theories for relative variation in fracture toughness K_{Ic} below room temperature due to changes in other material properties. Data are for 2090-T81 and 2091-T8 in the L-T and T-L orientations. Top: ε_f taken as uniform elongation; bottom: ε_f taken as total elongation. Equations are given in the text.

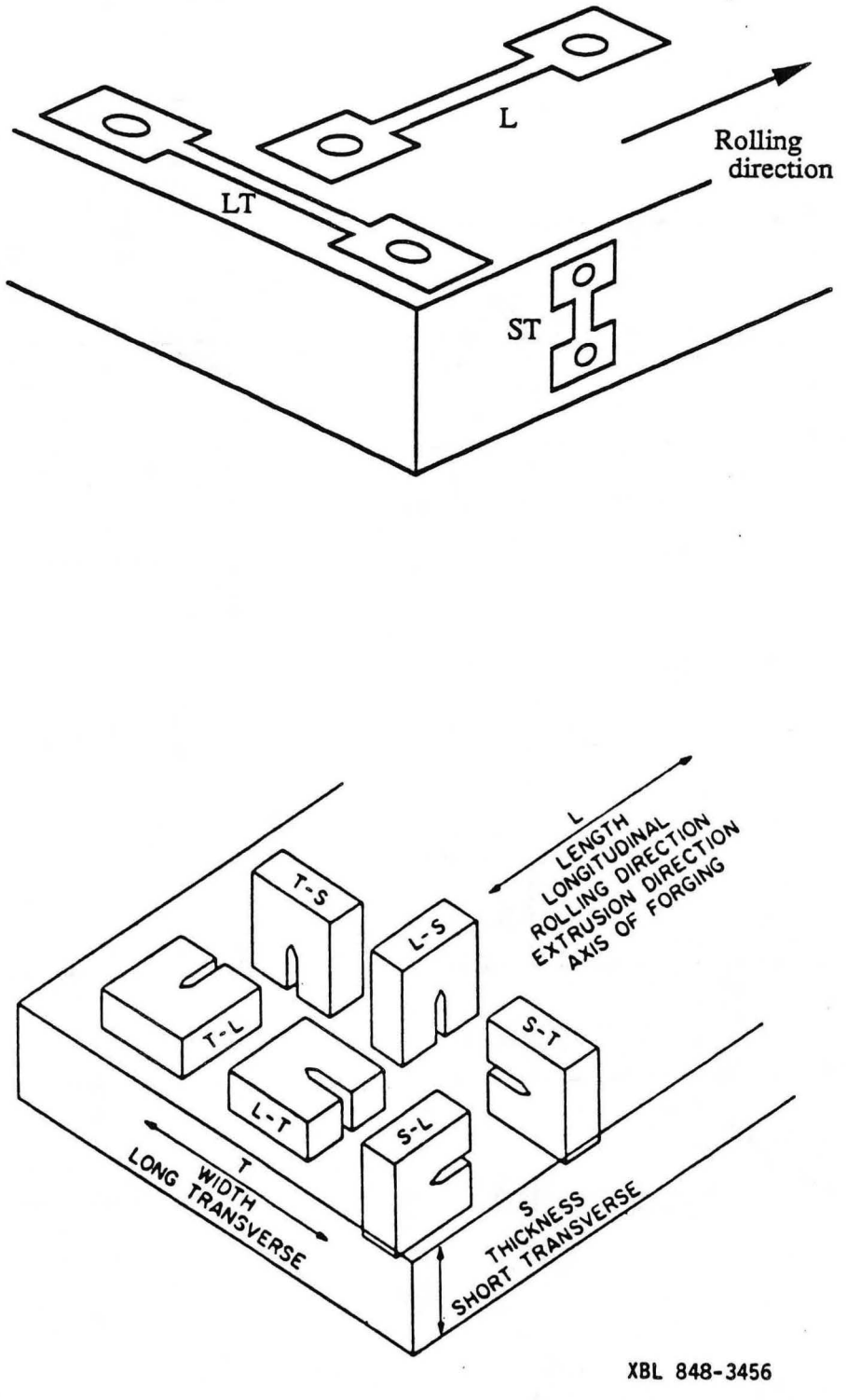

Figure A1.1 Orientation codes for tensile (top) and fracture toughness (bottom) specimens.

LAWRENCE BERKELEY LABORATORY
CENTER FOR ADVANCED MATERIALS
1 CYCLOTRON ROAD
BERKELEY, CALIFORNIA 94720